142 171

50376
2001
53-2

N° d'ordre :

THESE
(LABEL EUROPEEN)

Présentée à

l'Université des Sciences et Technologies de Lille

pour obtenir le titre de

DOCTEUR DE L'UNIVERSITE
Spécialité : ELECTRONIQUE

par

Marta FERNANDEZ DIEGO

NONLINEAR TRANSMISSION LINES FOR FREQUENCY MULTIPLIER APPLICATIONS

(MULTIPLICATEURS DE FREQUENCE A BASE DE LIGNES DE TRANSMISSION NON LINEAIRES)

soutenue le 6 Juillet 2001 devant la commission d'examen

Membres du jury :	M. Y. Crosnier	Président
	M. D. Lippens	Directeur de thèse
	M. G. Angénieux	Rapporteur
	M. M. Baquero	Rapporteur
	M. R.E. Miles	Rapporteur
	M. P. Ferrari	Examinateur
	M. F. Martín	Examinateur

A Papá, Carmina, Meli, Titín y Dani.

Acknowledgements/Remerciements

Ce travail a été effectué au Laboratoire Central de l'Institut d'Electronique et de Microélectronique du Nord (IEMN) dirigé par Monsieur G. Salmer. Je le remercie de m'avoir accueilli dans ce laboratoire.

Je remercie Monsieur Y. Crosnier, professeur de l'Université de Lille, qui me fait l'honneur de présider cette commision d'examen.

Monsieur D. Lippens a assuré l'encadrement de ce travail. Son intérêt, son dynamisme et sa gentillesse ont été d'une aide précieuse lors de ces quelques années à Lille. Qu'il trouve ici ma plus profonde reconnaissance et gratitude.

Je suis particulièrement reconnaissante à Monsieur M. Baquero, de l'Université Polytechnique de Valencia, de s'être intéressé à ce travail malgré la distance et d'en être le rapporteur. Mes plus vifs remerciements aussi pour Monsieur G. Angénieux, de l'Université de Savoie, et Monsieur R.E. Miles, de l'Université de Leeds, pour avoir accepté de juger ce travail et d'en être les rapporteurs.

Je remercie également Monsieur P. Ferrari, de l'Université de Savoie, et Monsieur F. Martín, de l'Université de Barcelona, qui me font l'honneur de participer à ce jury.

Bien sûr, mes sincères remerciements pour Monsieur O. Vanbésien pour avoir toujours été disponible et avoir suivi ce travail avec intérêt. De la même façon, je remercie Monsieur P. Mounaix.

Je tiens à exprimer toute ma reconnaissance aux membres de la centrale de technologie, en particulier à Madame C. Legrand, et à Mesdames S. Lepilliet et E. Delos de la centrale de caractérisation, cette dernière m'ayant beaucoup aidé à la fin de ce travail. Et comment ne pas oublier Monsieur M. Sénéchal, qui a su se montrer toujours disponible pour résoudre d'innombrables problèmes informatiques, et Madame V. Gysembergh, qui m'a fourni absolument tous les articles dont j'avais besoin. Je tiens à remercier aussi Madame J. Louchard qui a assuré la reproduction de ce manuscrit.

Maintenant, je ne prétend pas résumer ce qui s'est passé chaque jour pendant ces années, mais il faut quand même que je dise quelquechose.

Je commencerai par Jérôme qui fut le premier dans l'équipe à m'offrir son aide et son amitié et qui est le seul à présent à être venu à Valencia. Je ne desespère pas encore pour les autres. Eric m'aida à me plonger dans mon sujet de thèse, ce qui aurait été plus difficile autrement. Il dû me quitter trop vite, je suis sûre que c'était malgré lui, malgré moi en tout cas. Heureusement, après Eric, arriva Xavier. Il m'a appris tout ce que je sais sur la centrale de technologie. Ensemble, nous formions un bon binôme. Comme d'habitude et sans aucun problème, nous avons été sauvés par Steve au dernier moment.

Ensuite, il y a Tahsin, qui devrait maintenant savoir que la vie n'est pas toujours facile, Emilien, que j'ai un peu ennuyé avec la fréquence de Bragg et Thibaut, qui a voulu m'apprendre ce qu'est un peigne.

Quant aux filles, toujours en infériorité numérique, mais pourtant dont le nombre ne reflète pas l'aide qu'elles m'ont apportée, je tiens à remercier leur disponibilité à l'extérieur du laboratoire. Florence, je ne sais pas ce que j'aurais fait de mes weekends sans elle, Valérie, avec qui j'ai partagé beaucoup, et enfin Rocío, avec toutes ses histoires.

Et finalement, merci aussi à la relève de l'équipe, Thibaut, David et Hervé.

Je ne veux pas oublier ni Stéphane, que j'ai beaucoup ennuyé avec mes problèmes et qui ne s'est jamais plaint, ni Vincent, que malheureusement j'ai rencontré trop tard, mais c'est comme s'il avait été là depuis le début.

Non seulement à Lille, mais aussi à Leeds j'ai rencontré de remarquables personnes. Mes sincères remerciements pour Messieurs R.E. Miles et P. Steenson qui ont assuré l'encadrement de mon stage, ainsi qu'à Andy, Jim et Arne. Mon plus gentil merci à Joan qui m'a soutenu depuis le premier jour jusqu'à la fin. Et enfin, je tiens à remercier toute la troupe de mexicains dans laquelle j'inclus les quelques 'gachupines'.

Surtout, merci à ceux qui n'étant pas physiquement avec moi à Lille m'ont donné leur soutient tout au long de ces années. Je pense à mes amis de Valencia et plus particulièrement à ma famille, qui par mail ou par téléphone a été tous les jours avec moi. Bien sûr, j'ai reçu aussi tout le soutient de la part de Dani, mais ce que je voudrais souligner, qui n'est pas du tout évident, c'est qu'il a suivi ce travail depuis le premier jour. A la fin, il s'est aussi occupé du coté artistique de ce manuscrit.

Contents

List of Tables xi

List of Figures xii

General Introduction 1

I Background and Context 3

I.1 Historical Background 3

I.1.1 Solitary Waves 3

I.1.1.1 Hydrodynamic Analogy 3

I.1.1.2 Soliton Definition 4

I.1.2 Soliton Propagation 5

I.1.2.1 Soliton Fundamental Properties and Equation 5

I.1.2.2 Interaction between Two Solitons 6

I.1.2.2.1 Two Solitons Moving in the Same Direction 6

I.1.2.2.2 Two Solitons Moving in Opposite Directions 8

I.1.3 NLTL Background 11

I.2 Theoretical Description 13

I.2.1 The Dispersion Equation 13

I.2.2 The Bragg Frequency 17

I.2.3 The Korteweg-de Vries Equation 18

I.3 NLTL Modes of Operation 19

I.3.1 Shock Wave 20

I.3.1.1 Intuitive Approach 20

I.3.1.2 State-of-the-Art 21

I.3.2 Pulse Sharpening 23

I.3.2.1 Principle 23

I.3.2.2 State-of-the-Art 25

I.3.3 Harmonic Generation 26
I.3.3.1 Basis 26
I.3.3.2 State-of-the-Art 28
I.4 Integrated NLTL-based Circuits 29

II Elements Integrating an NLTL **31**
II.1 Introduction 31
II.2 Lumped Nonlinear Devices 32
II.2.1 Schottky Barrier Varactor Diode 32
II.2.1.1 Basic Principle 32
II.2.1.2 Bottlenecks and Possible Device Improvements 33
II.2.1.2.1 Generation of Higher Order Harmonics 33
II.2.1.2.2 Improvement in Conversion Efficiency 34
II.2.2 Heterostructure Barrier Varactor Diode 34
II.2.2.1 Basic Principle 34
II.2.2.2 Attractive Characteristics 37
II.2.2.2.1 Symmetry 37
II.2.2.2.2 Pump and Bias Signal 38
II.2.2.2.3 Breakdown Voltage 38
II.2.2.2.4 Nonlinearity 39
II.3 Transmission Lines 40
II.3.1 Coplanar Waveguide 40
II.3.2 Microstrip Line 41
II.3.3 Finline 42
II.3.4 Further Extensions 43
II.4 Modeling an NLTL Frequency Multiplier 44
II.4.1 Harmonic Balance Technique 44
II.4.2 HBV Diode Model 45
II.4.3 Electromagnetic Analysis 47
II.5 Conclusion 48

III Design Rules for NLTL Harmonic Generation **51**
III.1 Preliminary Analytical Results 51
III.1.1 Modeling the NLTL 51
III.1.2 The Semi-Lumped Approach 53

III.1.3 Considerations about the Bragg Frequency 57
III.2 Harmonic Generation 61
III.2.1 Generalities 61
III.2.2 The Bragg Frequency 62
III.2.3 The Characteristic Impedance 63
III.3 One Particular Approach: The MULTIS Project 66
III.3.1 Study Context 66
III.3.2 Configuration 67
III.3.3 Parameters 67
III.3.4 Electromagnetic Analysis 71
III.3.5 Network Analysis 74

IV Large Signal S Parameter Simulation of an NLTL **83**
IV.1 Introduction 83
IV.2 Large Signal S Parameters 84
IV.3 Small Signal and Large Signal Bragg Frequency 85
IV.4 Influence of the Diode C-V Characteristics 86
IV.4.1 Influence of the Area of the Diodes 88
IV.4.2 Influence of the Input Power 88
IV.4.3 Influence of the Number of Sections 89
IV.4.4 The Abrupt Transition 89
IV.4.5 Influence of the Diode C-V Relationship 90
IV.4.5.1 By Keeping *Cmax* Constant 93
IV.4.5.2 By Keeping *Cmin* Constant 93
IV.4.5.3 By Keeping both *Cmax* and *Cmin* Constant 93
IV.5 Large Signal S Parameters and Harmonic Balance 97
IV.6 The S_{12} Parameter 100
IV.7 Conclusion 101

V Technology and Characterization of the CPW NLTL **103**
V.1 Introduction 103
V.2 Technology of the CPW NLTL 104
V.2.1 Active Epitaxial Structure 104
V.2.2 Mask Set 105
V.2.3 Device Fabrication 108

V.2.3.1 Upper Ohmic Contact 108
V.2.3.2 Reactive Ion Etching 112
V.2.3.3 Lower Ohmic Contact 115
V.2.3.4 Ground Plane Formation 115
V.2.3.5 Isolation 116
V.2.3.5.1 Mesa Isolation 116
V.2.3.5.2 Diode Isolation 117
V.3 Characterization of the CPW NLTL 119
V.3.1 Linear Regime 119
V.3.1.1 Nonlinear Device Assessment 119
V.3.1.2 Unloaded Transmission Line Assessment 119
V.3.1.3 NLTL Assessment 122
V.3.2 Nonlinear Regime 124
V.3.2.1 Experimental Set-Up 124
V.3.2.2 Multiplier Performance 130
V.3.2.2.1 Number of Sections 130
V.3.2.2.2 Broad-Band Behavior 130
V.3.2.2.3 Input Power 131
V.4 Conclusion 134

Conclusion and Prospects **135**

Bibliography **139**

Summary **155**

List of Tables

III.1 Circuit parameters for different values of non-loaded transmission line impedance 63

III.2 The most salient results for each value of non-loaded transmission line impedance 66

III.3 Circuit parameters of the NLTL 67

III.4 Circuit parameters for different values of Bragg frequency 69

III.5 Physic parameters of the CPW (see figure III.13(a)) 69

III.6 Line elements of the CPW (see figure III.14) 70

List of Figures

I.1 Solitary wave observations performed by John Scott Russell 4

I.2 Traces of two solitons moving in the same direction 7

I.3 Space-time trajectories of the collision of two solitons having different amplitudes and traveling in the same direction (from reference [HS73]) 8

I.4 Space-time trajectories of the collision of two solitons having similar amplitudes and traveling in the same direction (from reference [HS73]) 9

I.5 Traces of two solitons moving in opposite directions 10

I.6 Space-time trajectories of the collision of two solitons having the same amplitude and traveling in opposite directions (from reference [HS73]) 11

I.7 Unit cell of the lossless lumped-constant transmission line 13

I.8 Lossless lumped-constant transmission line where the space variable is discretized 15

I.9 Shock wave formation and propagation along an NLTL (from reference [Cas93]) 22

I.10 Diagram of the effect of pulse sharpening along an NLTL 24

I.11 Pulse sharpening along an NLTL (from reference [Cas93]) 24

I.12 Harmonic generation along a 32-diode NLTL 27

II.1 Schematic of the conduction band and related conduction mechanisms in an HBV diode 35

II.2 Single barrier InP-based HBV epitaxial structure 36

II.3 Capacitance-voltage and current-voltage characteristics for an SBV diode and HBV diode 37

II.4 Photographs of an eight barrier-integrated HBV diode (from reference [Mél99]) 39

II.5 Schematic of a coplanar waveguide 41

II.6 Schematic of a microstrip line 42

II.7 Schematic of a finline 43

II.8 Measured and simulated capacitance-voltage characteristic of a double barrier InP-based HBV diode 46

II.9 Magnitude of the S_{11} parameter of a CPW as a function of the frequency for the whole structure and half the structure 48

III.1 Circuit and equivalent circuit diagrams of an NLTL 52
III.2 T models for the NLTL unit cell 54
III.3 Characteristic impedance as a function of the frequency for the lumped and semi-lumped model 56
III.4 Magnitude of the S_{21} parameter as a function of the frequency for the lumped and semi-lumped model 57
III.5 Layout of a CPW for an NLTL configuration 58
III.6 Magnitude of the S_{21} parameter as a function of the frequency varying the length of the discontinuity 59
III.7 Magnitude of the S_{21} parameter as a function of the frequency varying the width of the discontinuity 59
III.8 Three different semi-lumped unit cells 60
III.9 Magnitude of the S_{21} parameter as a function of the frequency for the cases of figures III.8(b) and III.8(c) 60
III.10 Phase of the S_{21} parameter as a function of the frequency for the cases of figures III.8(a) and III.8(b) 61
III.11 Conversion efficiency as a function of the input frequency for the fundamental and the three first non-zero harmonics 62
III.12 Conversion efficiency as a function of the number of sections for the fundamental and the two first non-zero harmonics varying the Z_l/Z_{ls} ratio 65
III.12 (continued) 66
III.13 Top view and transverse cross sectional views of a CPW NLTL 68
III.14 Diagram of the CPW NLTL and its equivalent loss circuit 70
III.15 Heinrich program input and output data 71
III.16 Characteristic impedance as a function of the frequency for the non-elevated and elevated center strip HFSS CPW 72
III.17 Magnitude of the S_{21} and S_{11} parameters as a function of the frequency for the non-elevated and elevated center strip HFSS CPW 73
III.18 Magnitude of the S parameters as a function of the frequency for the HFSS CPW with n^+ access areas 73
III.19 Magnitude of the S_{21} and S_{11} parameters as a function of the frequency for the HFSS CPW with and without n^+ access areas 74

III.20 Conversion efficiency to the third harmonic as a function of the diode area varying the number of diodes for the tripler configuration 75
III.21 Conversion efficiency to the fifth harmonic as a function of the diode area varying the number of diodes for the quintupler configuration 75
III.22 Conversion efficiency to the third harmonic as a function of the diode area varying the number of diodes for the quintupler configuration 76
III.23 Conversion efficiency to the third harmonic as a function of the diode series resistance 77
III.24 Conversion efficiency to the third and fifth harmonic as a function of the input frequency 78
III.25 Conversion efficiency to the third harmonic as a function of the input frequency for the lossless case and for $Rs = 1\Omega$ 78
III.26 Conversion efficiency to the third harmonic as a function of the number of sections for a loss case 79
III.27 Instantaneous voltage as a function of the time at the output of different NLTLs with different number of sections 80
III.27 (continued) 81
III.28 Conversion efficiency to the third harmonic as a function of the input power for a loss case 82

IV.1 Large signal and small signal S_{21} parameter ($P_{input} = 20dBm$) as a function of the frequency in a lossless case 86
IV.2 Large signal S_{21} parameter as a function of the frequency for different losses 87
IV.3 Small signal S_{21} parameter as a function of the frequency for different losses 87
IV.4 Large signal S_{21} parameter ($P_{input} = 20dBm$) as a function of the frequency varying the diode area 88
IV.5 Large signal S_{21} parameter as a function of the frequency varying the input power 89
IV.6 Large signal S_{21} parameter ($P_{input} = 20dBm$) as a function of the frequency varying the number of basic sections 90
IV.7 Magnitude of the large signal and small signal S_{21} parameter as a function of the frequency for different basic sections 91
IV.8 Large signal S_{21} parameter ($P_{input} = 18dBm$) as a function of the frequency varying the non linearity of the diode 92

IV.9 Large signal S_{21} parameter ($P_{input} = 18dBm$) as a function of the frequency varying the non linearity of the diode by keeping $Cmax$ constant 94
IV.10 Large signal S_{21} parameter ($P_{input} = 18dBm$) as a function of the frequency varying the non linearity of the diode by keeping $Cmin$ constant 95
IV.11 Large signal S_{21} parameter ($P_{input} = 18dBm$) as a function of the frequency varying the non linearity of the diode by keeping both $Cmax$ and $Cmin$ constant 96
IV.12 Large signal S_{21} parameter ($P_{input} = 20dBm$) and conversion efficiency as a function of the frequency in the lossless case 97
IV.13 More examples of the large signal S_{21} parameter and the conversion efficiency in the lossless case 98
IV.13 (continued) 99
IV.14 Large signal and small signal S_{21} parameter ($P_{input} = 20dBm$) as a function of the frequency in the presence of loss 100
IV.15 Magnitude of the large signal S_{21} and S_{12} parameters ($P_{input} = 20dBm$) as a function of the frequency in the lossless case 101

V.1 Double barrier InP-based HBV epitaxial structure 104
V.2 Mask set general view 106
V.3 CPW NLTL fabrication sequence 109
V.3 (continued) 110
V.3 (continued) 111
V.4 Optical views of the upper ohmic contact 112
V.5 Laser reflectometer plot announcing the barrier 114
V.6 SEM photographs after the RIE process 114
V.7 Etch depth as a function of etch time 115
V.8 $AZ - 5214$ resist on the wafer once developed 116
V.9 Optical views of an NLTL 117
V.10 SEM photographs of an NLTL 118
V.11 Visible air gaps under the center strip in a SEM photograph 118
V.12 Measured capacitance-voltage and current-voltage characteristics of a double barrier InP-based HBV diode 120
V.13 S parameters as a function of the frequency for the access line 121
V.14 S parameters as a function of the frequency for the non-loaded transmission line 121

V.15 Smith chart representation of the S parameters as a function of the frequency ($500MHz - 64.5GHz$) for the access line and the non-loaded transmission line . . . 123
V.16 Losses as a function of the frequency for the access line and the non-loaded transmission line . . . 124
V.17 Measured capacitance-voltage and current-voltage characteristics of an NLTL 125
V.18 S_{21} parameter as a function of the frequency for an NLTL varying the bias point of the diodes . . . 126
V.19 Schematic of the large signal experimental set-up . . . 126
V.20 Photograph of the large signal experimental set-up . . . 127
V.21 Photograph of the probe station . . . 128
V.22 Photograph of the radio-frequency probes . . . 128
V.23 Photograph of the spectrum analyzer system . . . 129
V.24 Measured conversion efficiency as a function of the number of sections . . . 130
V.25 Measured conversion efficiency as a function of the input frequency . . . 131
V.26 Conversion efficiency peak shown at the spectrum analyzer . . . 132
V.27 Measured conversion efficiency to the fifth harmonic as a function of the input power . . . 133
V.28 Conversion efficiency peak of the fifth harmonic shown at the spectrum analyzer . . . 133
V.29 Measured conversion efficiency as a function of the input power . . . 134

General Introduction

Despite extensive mathematical studies of nonlinear phenomena in recent years, it is now well recognized that computers allow us to solve interesting problems posed by many nonlinear equations. The reason for emphasizing nonlinearity is that it constitutes an important issue in many fields of science, pointing up chaos, fractals and solitons, as perhaps the most exciting.

Solitons, which are very stable solitary waves in a solution of the Korteweg-de Vries equation, have been shown to occur in a variety of nonlinear phenomena in physics. In particular, NonLinear Transmission Lines (NLTLs) enable the use of nonlinear solitary wave concepts in electrical transmission lines. The effects of nonlinearity, introduced by the loaded nonlinear elements, and dispersion, resulting of the periodic structure, counterbalance each other in such a way that solitons preserve their shape through propagation. Nowadays, nonlinear wave propagation is used extensively in the field of optical communications, notably in transatlantic under-sea optical cables, and will play a major role in the next generation of optical communication systems.

Besides, the limits of high-frequency technologies are explored and extended by research in ultrafast electronics and optoelectronics. Indeed, millimeter and submillimeter bands are rich in opportunities both for remote-sensing applications and for emerging industrial and commercial activities. With the advent of semiconductor technology, devices capable of generating fast-response electrical transitions have been reported for high-speed digital and analogue applications. Also, such devices are essential to obtain the wide bandwidth found in high-speed instrumentation. On the other hand, discrete devices have been traditionally used in communication systems by typically designing a resonant response in the band of interest, thus restricting the operating bandwidth. In this sense, distributed devices are subject of great interest in high-frequency electronics. Indeed, distributed circuits permit broad bandwidths with efficient coupling to semiconductor devices. Thus, NLTLs, as distributed networks, have the bandwidth necessary to support the propagation of picosecond signals.

When going up to millimeter and submillimeter frequencies, an additional difficulty consists in providing local oscillator sources with enough power levels by direct generation. Frequency multiplication can alleviate the problem of power sources for high frequencies. In this context, this thesis deals with the potential of NLTLs for harmonic generation on the basis of InP-based Heterostructure Barrier Varactors (HBVs). In particular, the HBV diode has been demonstrated to be a promising device for high efficiency frequency multipliers.

Chapter one of this thesis provides the necessary historical background to introduce the concept of an NLTL. A theoretical study of such lines allows us a further understanding of the

fundamental characteristic properties. Also, this introductory chapter describes all variety of applications found in the literature.

Chapter two reviews the two key elements integrating an NLTL, namely the nonlinear device and the non-loaded transmission line. In addition, different commercial software packages used in the simulation of such lines are introduced briefly.

Chapter three is devoted to the design rules for harmonic generation. After a certain number of preliminary considerations, this chapter discusses one particular approach. The study was carried out within the MULTIS (MUltiplicateur à Lignes de Transmission Intégrant des hétérostructures de Semiconducteurs) project research context in the framework of a CNRS (Centre National de la Recherche Scientifique) Télécom contract, in collaboration with the Laboratory of Microwaves and Characterization at the University of Savoie, France. The aim of this project is to prove the potential of NLTLs for frequency multiplication applications on the basis of InP-based HBV diodes monolithically integrated along the line. In practice, the aim is the fabrication of a V-band frequency multiplier prototype.

Chapter four deals with the influence of the diode capacitance-voltage characteristics on the transmission behavior of an NLTL. In particular, a special consideration has been paid to the determination of the Bragg frequency, by Large Signal S Parameter simulation, and the rejection above this frequency. This work was mainly performed in the Institute of Microwaves and Photonics of the School of Electronic and Electrical Engineering at the University of Leeds, UK, under the supervision of Robert Miles and Paul Steenson.

Finally, chapter five concerns the fabrication of the MULTIS prototype in a monolithic coplanar technology and its characterization. A detail description of the process steps involved in the fabrication is first presented, coming last the characterization under small signal and large signal conditions.

Chapter I

Background and Context

Chapter I

Background and Context

I.1 Historical Background

I.1.1 Solitary Waves

I.1.1.1 Hydrodynamic Analogy

In 1834 John Scott Russell (1808-1882), a Scottish shipbuilder and engineer in the late 19th century, provided the first description of solitons. Russell observed a wave which, guided through a canal, seemed to travel without losing its shape. This incident took place on the Union Canal at Hermiston, very close to Heriot-Watt University, Edinburgh. Following this preliminary observation, Russell built a wave tank and made important advances in the properties of the solitary wave, which were reported to the British Association for the Advancement of Science.

The early ideas of Russell started to be appreciated not until the mid 1960's. By then, applied scientists began to use modern digital computers to study nonlinear wave propagation. In 1973, the soliton was presented as a new concept in applied science by Scott *et al.* [SCM73]. Nowadays, the solitary wave concept enables to formulate the complex dynamical behavior of wave systems throughout a variety of fields. Not only have solitons been shown to occur in hydrodynamics and nonlinear optics, they have also appeared in descriptions of plasmas, protein models, atmospheric events, magma flow, general relativity, high energy physics and solid state physics.

One of the most promising applications of soliton theory is in the field of optical communications. With sufficient intensities from a separate pump laser, optical fibers can channel a light pulse of photons in the same way Russell saw the canal carry a water wave. In 1973, Akira Hasegawa of AT&T Bell Laboratories Electromagnetic Phenomena Research department was the first to suggest that solitons could exist in optical fiber and proposed the idea of soliton-based transmission systems. Since then, optical soliton propagation has been used

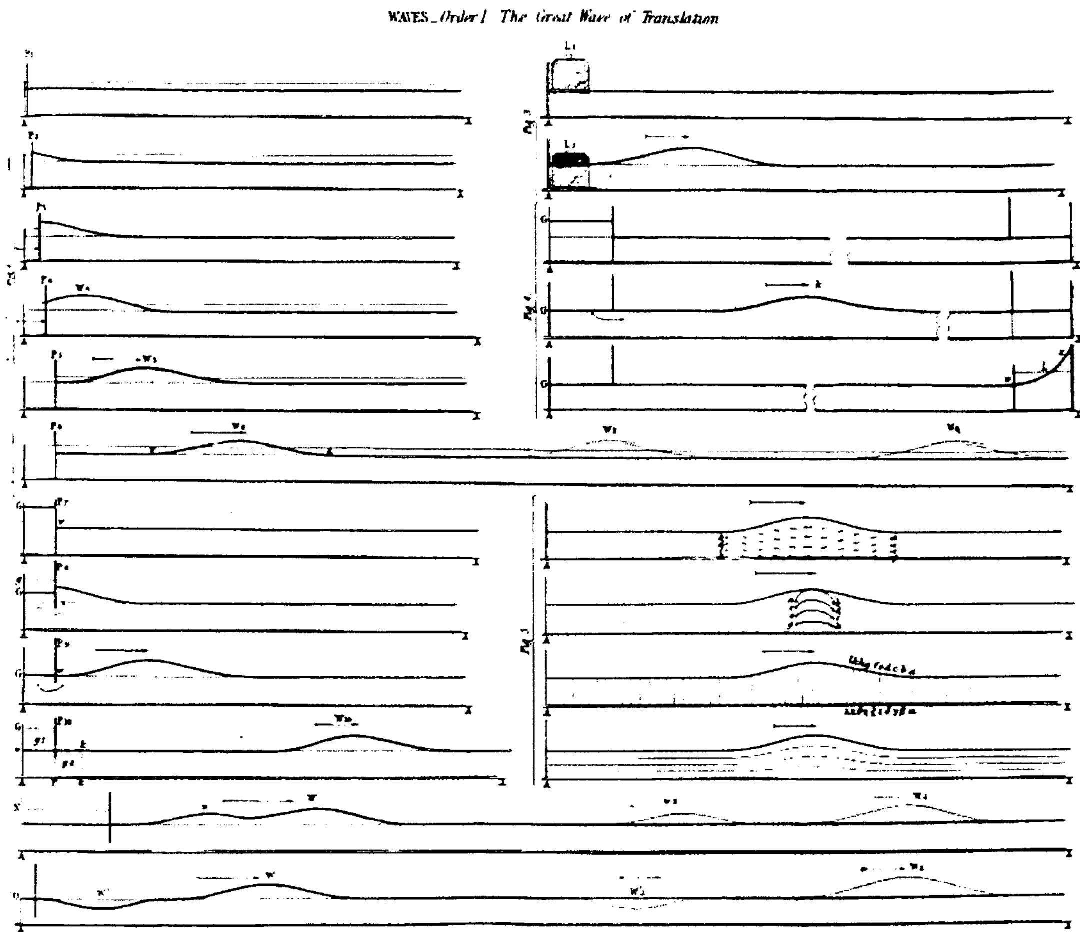

Figure I.1: Solitary wave observations performed by John Scott Russell

for dispersion-less signal propagation in fiber-optic transmission.

I.1.1.2 Soliton Definition

A soliton is a wave form that does not broaden, lose its shape and weaken as it travels along a particular medium.

The term soliton was introduced in the 1960's by Zabusky and Kruskal from numerical experiments of the Korteweg-de Vries equation while studying the heat conductivity of solids. In computer experiments they found that a sinusoidal initial condition broke up into a train of pulses, which later recombined to almost reproduce the initial shape, similar to the surprising results that Fermi, Pasta and Ulam had previously found in 1955. The Korteweg-de Vries equation was derived by Korteweg and his student de Vries late in the 19th century as a water wave equation, and after a long period, revived as one of the most fundamental equation of soliton phenomena. Solitons are very stable solitary waves in a solution of this equation.

The stability of solitons stems from the continual interaction of the nonlinearity and dispersion. If this delicate balance of nonlinearity and dispersion is lost, solitons become unstable and, eventually, cease to exist. The nonlinearity modifies the dispersion law in such a way that the amplitudes and the phase velocities of generated harmonics remain constant. Nonlinearity drives a solitary wave to concentrate further while dispersion is the effect to broaden such a localized wave. In the right situation, these opposing effects will complement each other, leaving the wave to propagate without any distortion.

I.1.2 Soliton Propagation

I.1.2.1 Soliton Fundamental Properties and Equation

The following unique properties of solitons have been observed by Hirota and Suzuki [HS73] in a nonlinear lumped LC network:

- An initial pulse-like wave packet breaks into a finite train of solitons, each of which travels at its own velocity, and a low-amplitude oscillatory tail.
- A soliton of high amplitude propagates faster than one of low amplitude and the width of the soliton is inversely proportional to its amplitude.
- Solitons preserve their identities after interacting with each other.

This nonlinear lumped circuit is equivalent to an anharmonic one-dimensional lattice, where Toda previously proved these fundamental properties. Also, Toda found an analytical solution to the equation of motion for the anharmonic one-dimensional lattice. Hirota provides the following solitary-wave pulse or lattice solution, which corresponds to the one found by Toda:

$$V_n(t) = V_{max} sech^2\left(\frac{A(t - nT_D)}{T_{FWHM}}\right) \tag{I.1.1}$$

where $V_n(t)$ is the time dependent voltage at the nth diode, V_{max} is the peak voltage, T_{FWHM} is the soliton's full width at half maximum duration given by:

$$T_{FWHM} = \frac{A}{\pi f_B \sqrt{\ln(1 + \frac{V_{max}}{V_o})}} \tag{I.1.2}$$

and T_D, the time delay through each section of line, is given by:

$$T_D = \frac{1}{\pi f_B \sqrt{\ln(1 + \frac{V_{max}}{V_o})}} \sinh^{-1}\left(\sqrt{\frac{V_{max}}{V_o}}\right) \tag{I.1.3}$$

By the way, f_B is the Bragg frequency and V_o is a constant voltage, parameters which will be introduced later on. Finally, the larger the parameter A is, the larger the local maximum is and the faster the wave travels.

Since the soliton represented by equation I.1.1 is very stable in the NonLinear Transmission Line (NLTL), most of the waves will decompose into a train of solitons after propagating long enough. Once the soliton is produced in the NLTL, it can propagate without any change of its temporal shape. In the formation process of the soliton, electromagnetic energy which is distributed spatially and temporally is compressed into the soliton.

I.1.2.2 Interaction between Two Solitons

A theoretical and experimental description of soliton-soliton interaction has been carried forward by Hirota and Suzuki in reference [HS73]. This section focuses on their experimental observations.

I.1.2.2.1 Two Solitons Moving in the Same Direction

The upper traces of figure I.2 show two input voltage pulses having greatly disparate amplitudes and moving in the same direction, where the larger amplitude pulse is preceded by the smaller amplitude one. The pulses are introduced into the network observing an input spacing, which will be narrowed from figure I.2(a) to figure I.2(c). Owing to their initial shape, each one will be transformed into a unique soliton as they travel through the nonlinear lumped circuit. Therefore, at a distance from the input, two solitons can be observed in the lower trace of figure I.2(a). The higher soliton, which travels faster, is still behind the lower one at this observation point. In figure I.2(b) the input pulse spacing is such that the larger amplitude soliton just overlaps the smaller amplitude one at the same observation point. It can be seen how, during the overlap time interval, their joint amplitude decreases. The resulting nonlinear superposition has a smaller amplitude and longer duration than the higher of the two interacting solitons. In the lower trace of figure I.2(c), still at the same observation point, the larger amplitude soliton has overtaken the smaller amplitude one and is now ahead. It can be observed how the two solitons come out of the collision unaltered. Actually, the amplitudes are detached once the larger soliton absorbs the smaller one.

The space-time trajectories of the collision of two solitons having different amplitudes and traveling in the same direction are shown in figure I.3. For the sake of clarity, the collision takes place at $t = 0$ and $z = 0$. Since $t_A < t_B$ for each distance $z < 0$, soliton B is initially retarded in relation to soliton A. Furthermore, the slope of its trajectory reveals that it travels faster. When it consequently approaches the smaller amplitude soliton, the larger amplitude one is accelerated , while the smaller soliton is correspondingly slowed down. After the collision, once soliton B is clearly ahead, it can be seen how the velocities of both solitons are restored. Soliton B is advanced with regard to the position it would have if no collision had occurred, contrary to what happens with soliton A.

In the case where, traveling in the same direction, the amplitudes of the two solitons are comparable, the interaction between them differs from the behavior described before. The

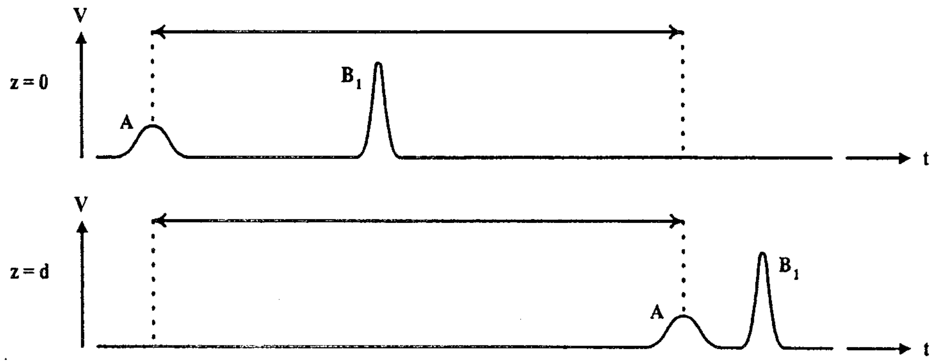

(a)

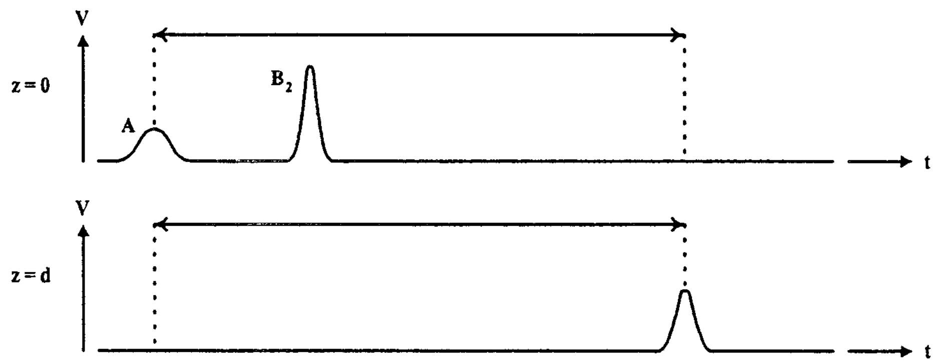

(b)

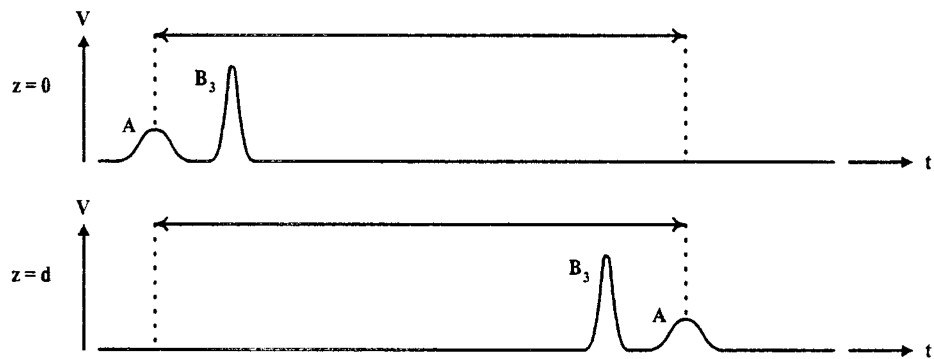

(c)

Figure I.2: Traces of two solitons moving in the same direction

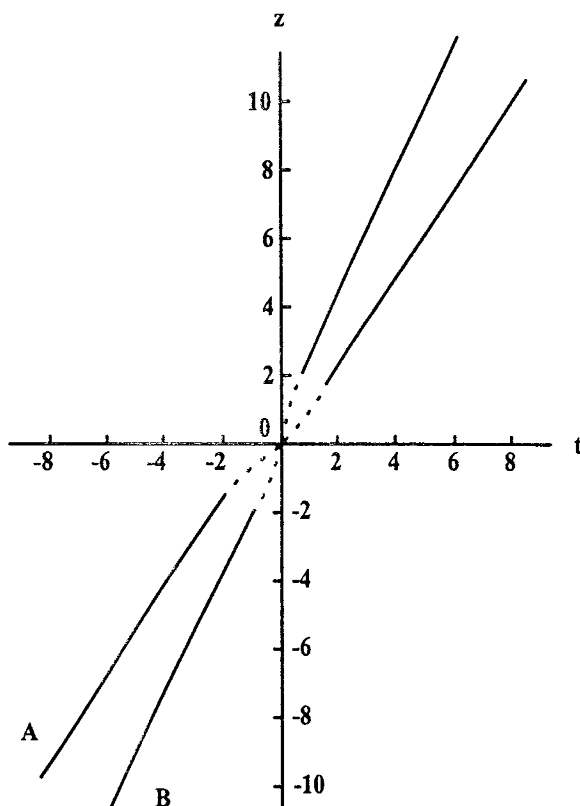

Figure I.3: Space-time trajectories of the collision of two solitons having different amplitudes and traveling in the same direction (from reference [HS73])

higher one (B) shrinks and the lower one (A) grows as soon as the higher comes close enough to the smaller. Nevertheless, figure I.4 shows no intersection in the space-time trajectories of both solitons. Once the larger amplitude soliton collides with the smaller amplitude one, its velocity is reduced until reaching the velocity of soliton A. As was to be expected, the opposite behavior happens in the case of soliton A. Thus, the two waves interchange their roles and after which they separate.

I.1.2.2.2 Two Solitons Moving in Opposite Directions

Figure I.5 shows two voltage pulses having the same amplitude and moving in opposite directions. The pulses are introduced into the network from each end, the pulses on the right (B) being excited after the pulse on the left (A). In this way, the pulse spacing in the upper traces of figure I.5 corresponds to the sum of the input spacing pulse injection and the time required by the pulse introduced from the end to reach the input. This former time allows to reduce the time delay between the two pulses from figure I.5(a) through figure I.5(c). Note that in the three situations displayed the observation point in between the two ends is the same. The lower trace of figure I.5(a) shows soliton A before the collision and soliton B_1 after

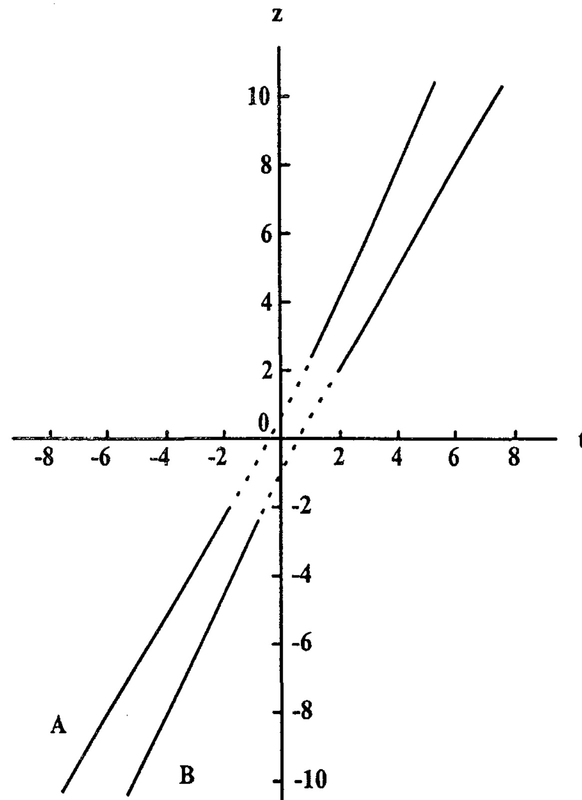

Figure I.4: Space-time trajectories of the collision of two solitons having similar amplitudes and traveling in the same direction (from reference [HS73])

the collision. Actually, the soliton which is first observed has not yet suffered collision. The other, once it is observed, has necessary passed through the first one, as they travel in opposite directions. Therefore, the lower trace of figure I.5(c) shows soliton B_3 before the collision and soliton A after the collision. From these traces, it can be stated that solitons propagate undistorted after collision. Finally, the lower trace of figure I.5(b) shows the collision of solitons A and B_2 with a significant increase in amplitude. At this point, their joint amplitude is greater than the sum of their amplitudes.

Figure I.6 shows the head-on collision of two solitons having the same amplitude (same slope value of the space-time trajectories) and traveling in opposite directions (opposite slope sign of the space-time trajectories). When the two waves approach one each other, both are accelerated. After collision, their velocities are restored. Different from what has been described for two solitons of different amplitudes propagating in the same direction, in this case, both pulses are advanced with regard to the position they would have if no collision had occurred.

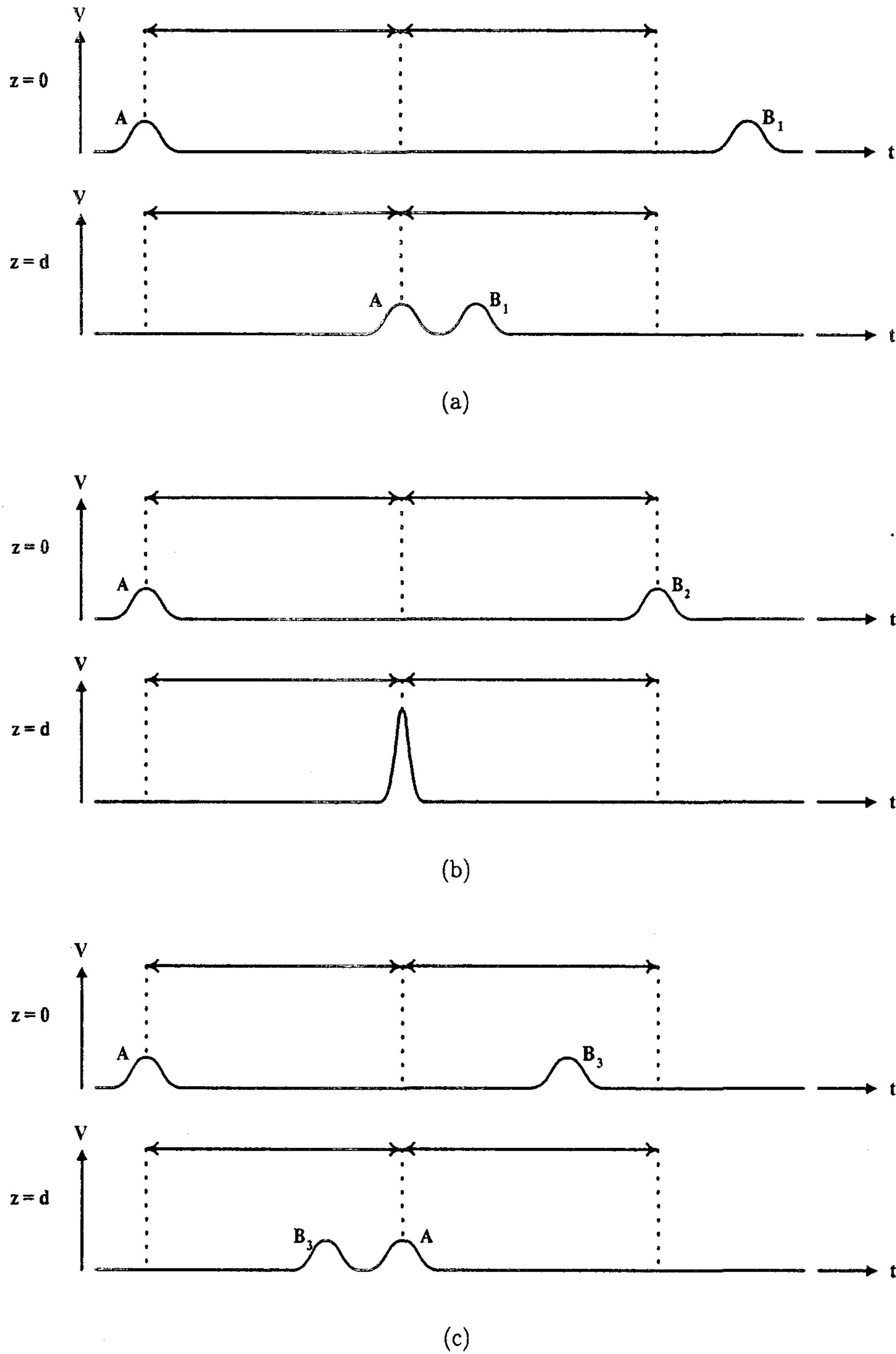

Figure I.5: Traces of two solitons moving in opposite directions

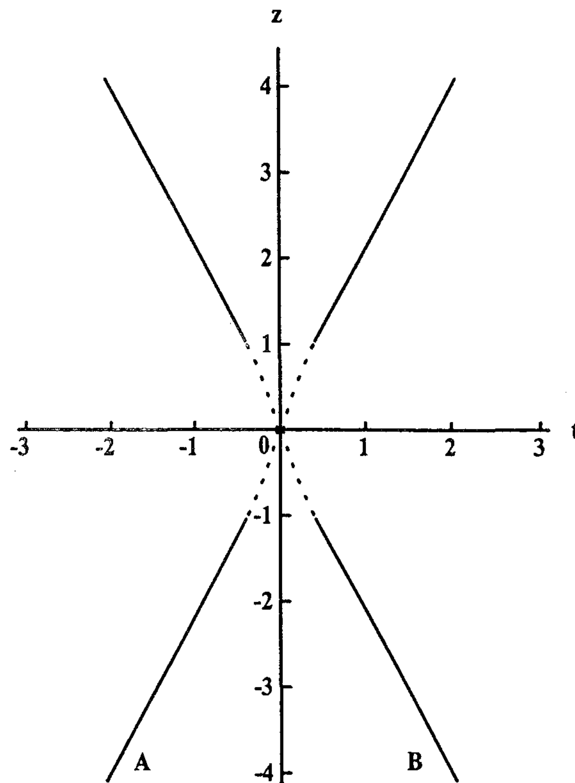

Figure I.6: Space-time trajectories of the collision of two solitons having the same amplitude and traveling in opposite directions (from reference [HS73])

I.1.3 NLTL Background

After this brief description of soliton propagation in a nonlinear lumped LC network, this section will focus on the NLTL background.

The nonlinear charge-voltage relationship of a reverse-biased semiconductor junction (variable capacitance diode) is used at high frequencies for many applications. If the junction is instead incorporated somehow into a transmission line, the resulting structure takes the form of a NonLinear Transmission Line (NLTL). Two types of interaction line-diode can be considered: a located, periodic interaction, and a distributed interaction all along the transmission line.

Investigation into the properties of NLTLs for high frequency applications began in the early 1970's. The advent of semiconductor fabrication processes motivated the need for a general analysis of fully distributed NLTL structures. The basic structures which have been discussed in the earlier literature are the Metal-Insulator-Semiconductor (MIS) and Schottky-contact for applications as delay lines or phase shifters. The transmission line consisted in microstrips [Jäg76, JB77] or coplanar waveguides [FI82, SLS84] forming a continuous distributed contact to a semiconductor layered substrate.

Even if second harmonic generation along MIS and Schottky-contact lines was also identified by Günther and Voges [GV73] and by Everszumrode *et al.* [EBJ77] as a possible application, they were faced with high values of conversion loss due to the losses associated with the use of semiconductor substrates as transmission media. In reference [EBJ77], a maximum value of 1% for power efficiency of frequency doubling is derived if Schottky-contact microstrip lines with optimum performance are designed on n-type silicon. Operation at liquid nitrogen temperatures increases the efficiency up to 6%. As a result of progress in the understanding of nonlinear wave phenomena and due to the improvements of stripline technology for Monolithic Microwave Integrated Circuit (MMIC) applications, in 1985 Jäger [Jäg85] attempted a general and also practical analysis of nonlinear slow-wave propagation on planar MIS and Schottky-contact striplines in order to enhance the small values of measured efficiency. The propagation of a sinusoidal input wave is a process which experiences the influence of dissipation and dispersion, the low-pass filter dispersion being absolutely necessary in harmonic generation applications.

Devices in which the active medium is semiconducting, namely have a poor resistivity, are intrinsically lossy. In reference [Rod87], Rodwell concluded that the loss introduced by the semiconductor substrate is the limiting factor in these fully distributed structures. At present, NLTLs developed for high frequency applications are usually of the lumped element varactor type.

Periodic NLTLs are usually constructed from fixed series inductors and voltage-varying shunt capacitors (varactor diodes) in cascade, because it is difficult, in practice, to obtain strongly nonlinear current-varying inductors having good Q factors at high frequencies. Experimentally, a transmission line is loaded periodically by varactor diodes to make up an NLTL.

At first, lumped element NLTLs were utilized at low frequencies as a powerful means for research into solitary wave behavior. As a nonlinear and dispersive medium, an NLTL is a convenient and inexpensive tool to study the propagation of solitons.

The experiment on a soliton in an NLTL was carried out first by Hirota and Suzuki [HS73]. They showed experimentally the basic properties of solitons in the electrical analogue of the Toda lattice. The transmission line has provided fundamental information about soliton propagation such as head-on and overtaking collisions of solitons, decomposition of a broad input pulse into a train of solitons, ... Later, Nagashima and Amagishi [NA78] obtained experimentally the velocity and the width of a soliton and also the interaction of two solitons in a quantitative agreement with the theoretical prediction.

Soliton formation and propagation in NLTLs have been also studied by, for example, Watanabe [Wat82], who considered an LC-ladder with constant inductance and expanded the voltage in Taylor's-series expansion around the bias DC voltage. By connecting a linear capacitor parallel to the nonlinear capacitor, the nonlinearity is deviated from that of the Toda lattice. However, even though the inverse of the differential capacitance does not depend linearly on the voltage, a soliton can propagate stably in the circuit.

The formation process of solitons in a dispersive medium has been studied in detail by Tsuboi [Tsu90] who observed a rectangular pulse fed into the nonlinear, lumped LC transmission line to be steepened by the nonlinear effect at the early stages, then to decrease and

broaden during propagation along the line and eventually change into solitons by a delicate balance between nonlinearity and dispersion. Tsuboi had previously reported in reference [Tsu89] the observation of a phase shift at the soliton collision which had been expected theoretically by Hirota and Suzuki [HS73].

Lately, theoretical studies about soliton propagation have been carried out by, for example, Ramos [Ram95], who showed by means of perturbation methods that solitons governed by the nonlinear Korteweg-de Vries equation may propagate along a nonlinear, lossless transmission line. Also in 1995, Burger [Bur95] illustrated a model believed to be the minimum necessary to analyze solitary waves on a practical transmission line.

I.2 Theoretical Description

I.2.1 The Dispersion Equation

Consider initially an analysis of the generic lossless lumped-constant transmission line, having a series inductance of l henrys per unit length and a shunt capacitance of c farads per unit length. Its unit cell is depicted in figure I.7.

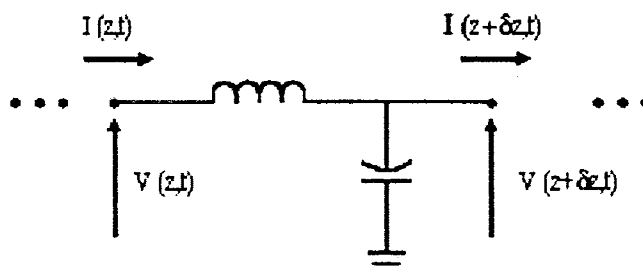

Figure I.7: Unit cell of the lossless lumped-constant transmission line

Applying Kirchhoff's voltage law to an elemental length δz of the transmission line gives:

$$\frac{\delta V}{\delta z} = -l\frac{\delta I}{\delta t} \tag{I.2.1}$$

Similarly, from Kirchhoff's current law:

$$\frac{\delta I}{\delta z} = -c\frac{\delta V}{\delta t} \tag{I.2.2}$$

In all the works dealing with transmission lines, it is assumed that one can proceed to the

limit $\delta z \to 0$, thus obtaining the following pair of partial differential equations:

$$\frac{\partial V}{\partial z} = -l\frac{\partial I}{\partial t} \tag{I.2.3}$$

$$\frac{\partial I}{\partial z} = -c\frac{\partial V}{\partial t} \tag{I.2.4}$$

Equations I.2.3 and I.2.4 can also be written as:

$$lc\frac{\partial^2 V}{\partial t^2} = \frac{\partial^2 V}{\partial z^2} \tag{I.2.5}$$

$$lc\frac{\partial^2 I}{\partial t^2} = \frac{\partial^2 I}{\partial z^2} \tag{I.2.6}$$

By substituting into these equations the reverse traveling-wave solutions:

$$V(z,t) = V_o e^{j(\omega t + kz)} \tag{I.2.7}$$

$$I(z,t) = I_o e^{j(\omega t + kz)} \tag{I.2.8}$$

where V_o and I_o are complex amplitudes,

the well-know dispersion equation is obtained:

$$\boxed{\omega^2 = \frac{k^2}{lc}} \tag{I.2.9}$$

that is, the phase and group velocities are identical. Therefore, equations I.2.3 and I.2.4 or equations I.2.5 and I.2.6 are not dispersive.

The numerical analysis of such a structure implies the discretization of both independent variables, the space variable and the time variable. Next, let us consider the effect of the discretization of the space variable, for example. Figure I.8 shows a lossless lumped-constant transmission line where the space variable is discretized.

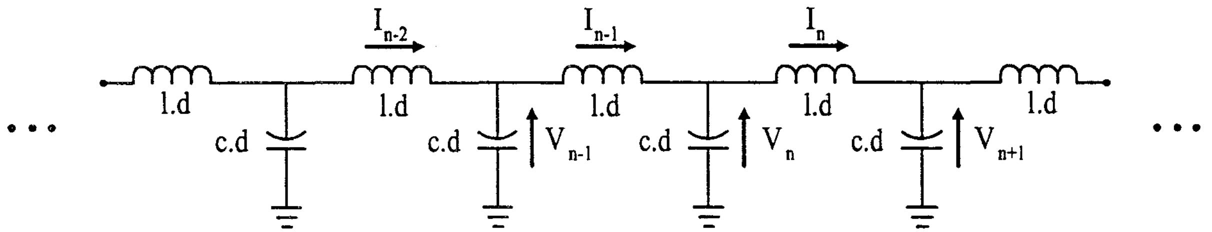

Figure I.8: Lossless lumped-constant transmission line where the space variable is discretized

Assume now that the time variable in equations I.2.3 and I.2.4 is kept continuous while the space variable is discretized. The so-called Method of Lines is used here to discretize the spatial variable. This discretization reduces equations I.2.3 and I.2.4 to ordinary differential equations in time:

$$l\frac{dI_n}{dt} = -\frac{V_{n+1} - V_n}{d} \tag{I.2.10}$$

$$c\frac{dV_n}{dt} = -\frac{I_n - I_{n-1}}{d} \tag{I.2.11}$$

$V_n = V(z_n, t)$ where $z_n = nd$, d denoting the spatial step size and n the nth grid point.

Equations I.2.10 and I.2.11 may be combined to give:

$$lc\frac{d^2V_n}{dt^2} = \frac{V_{n+1} + V_{n-1} - 2V_n}{d^2} \tag{I.2.12}$$

By expressing V_{n+1} and V_{n-1} in terms of Taylor expansions:

$$V_{n+1} = V_n + d\frac{\partial V}{\partial z} + \frac{1}{2}d^2\frac{\partial^2 V}{\partial z^2} + \frac{1}{6}d^3\frac{\partial^3 V}{\partial z^3} + \frac{1}{24}d^4\frac{\partial^4 V}{\partial z^4} + ... \tag{I.2.13}$$

$$V_{n-1} = V_n - d\frac{\partial V}{\partial z} + \frac{1}{2}d^2\frac{\partial^2 V}{\partial z^2} - \frac{1}{6}d^3\frac{\partial^3 V}{\partial z^3} + \frac{1}{24}d^4\frac{\partial^4 V}{\partial z^4} - ... \tag{I.2.14}$$

it can be shown that:

$$lc\frac{\partial^2 V}{\partial t^2} = \frac{\partial^2 V}{\partial z^2} + \frac{d^2}{12}\frac{\partial^4 V}{\partial z^4} \tag{I.2.15}$$

This equation differs from equation I.2.5 in the terms involving fourth and higher order spatial derivatives.

A Fourier analysis similar to the one employed before yields to the following dispersion equation:

$$\boxed{\omega^2 = \frac{k^2}{lc}(1 - \frac{d^2k^2}{12})} \tag{I.2.16}$$

which indicates that equation I.2.15 is dispersive, that is, the phase and the group velocities are different.

Note that:

$$lim_{d\to 0}\frac{k^2}{lc}(1 - \frac{d^2k^2}{12}) = \frac{k^2}{lc} \tag{I.2.17}$$

which corresponds to equation I.2.9.

The modified equation I.2.15 can be saved by substituting the following expressions into equations I.2.10 and I.2.11:

$$V_n = V_o e^{j(\omega t + knd)} \tag{I.2.18}$$

$$I_n = I_o e^{j(\omega t + knd)} \tag{I.2.19}$$

This substitution leads to the following dispersion equation:

$$\boxed{\omega^2 d^2 = 2\frac{1 - \cos kd}{lc}} \tag{I.2.20}$$

which can be expanded in Taylor's series as:

$$\omega = \frac{k}{\sqrt{lc}}\sqrt{1 - \frac{d^2k^2}{12}} \tag{I.2.21}$$

which corresponds exactly to equation I.2.16, an even more approximate version of the dispersion relationship I.2.20.

So as to finish with this analysis, consider only the two first terms of the Taylor's series expansion of $\cos kd$. Equation I.2.20 simplifies to:

$$k = \omega\sqrt{lc} \tag{I.2.22}$$

where the phase and group velocities are identical, leading again to the dispersionless case.

In conclusion, this problem is intimately related to numerical analysis. Frequency dispersion results from the periodic structure, which causes frequencies close to the cut-off frequency of the ladder network to propagate more slowly than other frequencies. However, in an NLTL, which may be formed by replacing the shunt elements of a conventional lumped-constant transmission line by nonlinear elements, this discretization of the space variable does not appear from the numerical analysis, but corresponds physically to the periodic introduction of the nonlinear elements.

I.2.2 The Bragg Frequency

Actually, all experimental NLTLs are lumped-parameter lines where the spatial variable is discretized. Therefore, there is an upper limit to the pump frequency, owing to the nature of the transmission line, as they have all the properties of low-pass filters. The cut-off frequency forms the upper limit of the system, above which neither pump signal nor harmonic components may be efficiently transmitted.

Due to the discretization of the spatial derivatives, equation I.2.20 indicates that the maximum wave number that can be resolved corresponds to $kd = \pi$. That is, the shortest wavelength for which a real solution of this equation is obtained is two sections long, $d = \lambda/2$. This wavelength corresponds to the following cut-off frequency:

$$\omega_B = \frac{2}{d\sqrt{lc}} \tag{I.2.23}$$

$$\boxed{f_B = \frac{1}{\pi d\sqrt{lc}}} \tag{I.2.24}$$

Hence, there are no traveling-wave solutions for frequencies above the cut-off frequency. This frequency is also called the Bragg frequency since the reflections from this one-dimensional electrical lattice bear a similarity to the reflections seen in a periodic crystal lattice. In particular, let us draw an analogy with Distributed Bragg Reflectors (DBRs), commonly called Bragg's mirrors, where the same condition of phase matching is imposed between the forward and the reverse traveling-waves. Indeed, a DBR is a periodic multilayer structure so that each layer exhibits a different refractive index. Thus, at each interface, the optical incident wave is in part reflected due to the index change in such a way that the direct emission and all the reflected waves are in phase producing a constructive interference phenomenon.

I.2.3 The Korteweg-de Vries Equation

First, consider the linear case (constant capacitance) where it is even difficult to incorporate the dispersion relation into the characteristic propagation equations, as shown in section I.2.1. Later, nonlinearity will be introduced by a voltage-dependent capacitance, leaving the dispersion term unaffected. Note that dissipation is ignored in this analysis.

The introduction of the expression I.2.23 of the Bragg frequency into equation I.2.16 leads to the following equation:

$$\boxed{\omega^2 = (\frac{\omega_B}{2})^2[(kd)^2 - \frac{(kd)^4}{12}]} \tag{I.2.25}$$

By assuming linear wave propagation, that is, allowing forward and backward traveling-waves to propagate independently on the transmission line, and using operator notation, where the operator D_a represents partial differentiation with respect to variable a, it can be proved that equation I.2.25 represents the characteristic equation for the differential equation:

$$[D_t^2 - (\frac{\omega_B d}{2})^2 D_z^2 - \frac{1}{12}(\frac{\omega_B d^2}{2})^2 D_z^4]V(z,t) = 0 \tag{I.2.26}$$

where $V(z,t) = V_{forward}e^{j(\omega t - kz)} + V_{reverse}e^{j(\omega t + kz)}$.

In this equation, it has been assumed that the term $(\omega_B d^3/48)^2 D_z^6 V(z,t)$ is small in comparison to the term corresponding to the first order dispersion. The equation can be broken into two differential equations, for the forward and reverse directions of propagation:

$$(D_t - \frac{\omega_B d}{2}D_z - \frac{\omega_B d^3}{48}D_z^3)(D_t + \frac{\omega_B d}{2}D_z + \frac{\omega_B d^3}{48}D_z^3)V(z,t) = 0 \tag{I.2.27}$$

For the forward wave, the following equation is obtained:

$$(D_t - \frac{\omega_B d}{2}D_z - \frac{\omega_B d^3}{48}D_z^3)V(z,t) = 0 \tag{I.2.28}$$

Assuming a differential equation equivalent to equation I.2.28 in the linear case:

$$\frac{1}{C}\frac{\partial Q}{\partial t} - \frac{\omega_B d}{2}\frac{\partial V}{\partial z} - \frac{\omega_B d^3}{48}\frac{\partial^3 V}{\partial z^3} = 0 \tag{I.2.29}$$

one can introduce nonlinearity by setting $Q(V) = C_o V_o \ln(1+V/V_o)$, so that the capacitance given by the derivative of its charge stored with respect to voltage:

$$\boxed{C(V) = \frac{C_o}{1+\frac{V}{V_o}}} \qquad \text{(I.2.30)}$$

results in the Hirota model for capacitance [HS73].

Then, equation I.2.29 results in:

$$\frac{C_o}{C}\frac{\partial V}{\partial t} - (1+\frac{V}{V_o})\frac{\omega_B d}{2}\frac{\partial V}{\partial z} - (1+\frac{V}{V_o})\frac{\omega_B d^3}{48}\frac{\partial^3 V}{\partial z^3} = 0 \qquad \text{(I.2.31)}$$

Assuming that the nonlinear factor present in the dispersion term (the third order term) can be neglected:

$$\boxed{\frac{C_o}{C}\frac{\partial V}{\partial t} - (1+\frac{V}{V_o})\frac{\omega_B d}{2}\frac{\partial V}{\partial z} - \frac{\omega_B d^3}{48}\frac{\partial^3 V}{\partial z^3} = 0} \qquad \text{(I.2.32)}$$

which is a form of the well-known Korteweg-de Vries equation. This equation contains the first order dispersion and first order nonlinearity effects.

One of the phenomena in dealing with nonlinear partial differential equations and of major interest are the solitary waves. Nowadays, there is a better knowledge of the underlying mathematical properties. Indeed, solitons are governed by the famous nonlinear Korteweg-de Vries equation.

I.3 NLTL Modes of Operation

There is a constant tendency in all communications to higher frequencies and higher bandwidths. Actually, to overcome the disadvantages of narrow-band techniques, systems are evolving towards wide bandwidths and greater time domain character. From the point of view of information theory or wave propagation, these wide bandwidth techniques are far superior and are attracting wide interest.

The advantage of the NLTL in millimeter and submillimeter applications over discrete devices, such as Schottky diodes and High-Electron-Mobility-Field-Effect-Transistors (HEMFETs), is high frequency operation over a wider bandwidth. Even though such lumped devices need an input and output matching network, they can have cut-off frequencies as high as several THz, while the NLTL is self matched over a much wider frequency range.

NLTLs can be designed to generate picosecond transition impulses, picosecond duration pulses and millimeter-wave harmonics, which performance exceeds that of conventional electrical wave shaping devices. As will be shown in the following sections, the transmission line behavior is defined depending on the interaction between the effects of dispersion and nonlinearity. The relationship between the input signal harmonic components and the Bragg frequency determines one of the three modes of operation, namely one of the three main applications. In addition, the effect of parasitics is of significant consideration in these three types of NLTLs.

I.3.1 Shock Wave

I.3.1.1 Intuitive Approach

Impulse compression on NLTLs has been widely studied by Rodwell *et al.* [RKY+91]. The formation of shock waves can be intuitively understood from the expression of the phase velocity per section of an NLTL:

$$v_p = \frac{1}{\sqrt{L_l(C_l + C_d(V))}} \tag{I.3.1}$$

where L_l and C_l are the inductance and capacitance of the NLTL section respectively, and $C_d(V)$ represents the voltage-dependent diode capacitance.

Note that the LC equivalent circuit of an NLTL is obtained by replacing the shunt elements of a conventional lumped-constant transmission line by nonlinear elements, resulting in the following capacitance: $C_T(V) = C_l + C_d(V)$.

If $C_d(V)$ decreases with increasing voltage, the higher portion of the input falling step function, where V_h and V_l are the initial and final voltages respectively, will travel faster than the lower amplitude portion, resulting in the reduction of the fall time of waves propagating on the NLTL. In other terms, the effect is to steepen the falling edge of a waveform to some asymptotic limit.

The voltage at the nth diode can be expressed as:

$$V_n(t) = V_{in}(t - nT(V)) \tag{I.3.2}$$

$$T(V) = \sqrt{L_l(C_l + C_d(V))} \tag{I.3.3}$$

where $T(V)$ is the propagation delay, the inverse of the phase velocity per section.

At first, the fall time $T_{f,n}$ will decrease linearly with distance:

$$T_{f,n} = T_{f,in} - n(T(V_h) - T(V_l)) \tag{I.3.4}$$

The generation of high frequency components brings about the minimum fall time $T_{f,min}$. However, when these generated frequencies are comparable to the Bragg frequency, dispersive effects become more important than the compression arising from the voltage-dependent propagation velocity, leading to the formation of solitons. Therefore, pulse compression must be achieved inhibiting the generation of multiple solitons.

In conclusion, the absence of dispersion and loss, where the LC equivalent circuit is considered well below the Bragg frequency, excites shock wave formation and propagation. Figure I.9 illustrates how the shock builds up and how it maintains the edge velocity once the minimum fall time is attained. Three different situations are displayed:

- (a) When the diode cut-off frequency limits the shock velocity ($f_{c,diode} = f_B$), the waveform shows uniform shock formation over the impulse's leading edge. Note also the complete absence of ringing in the waveform.
- (b) A large amount of ringing, nearly the same frequency as f_B, can be noted in the waveform when the diode has a very high cut-off frequency ($f_{c,diode} = 20f_B$). The shock formation is still uniform over the leading edge.
- (c) When the effects of the diode and the Bragg frequency are nearly the same, that is $f_{c,diode} = 4f_B$, the ringing is not pronounced but the shock formation is not uniform, gradually growing over the entire leading edge. This partial shock formation occurs when the propagation delay $T(V)$ is not linear with the voltage, but the input impulse varies linearly with the time.

The effects of the diode cut-off frequency on shock wave propagation have also been studied by Wang and Hwu in reference [WH99] and have been easily explained by their distributed model.

I.3.1.2 State-of-the-Art

The importance of the phenomenon of shock wave formation on fully distributed varactor lines to transmission of digital signals was discussed for the first time by Landauer [Lan60], who also pointed out that it is possible to obtain any useful gain from an NLTL used as a parametric amplifier.

Freeman and Karbowiak [FK77], who used varactor diodes and an LC-ladder network with constant inductances, investigated experimentally and numerically shock wave formation and propagation in NLTLs. They resolved the paradox of energy loss associated with a shock wave on a distributed structure by stating that the sum of the DC energy of the pulse and

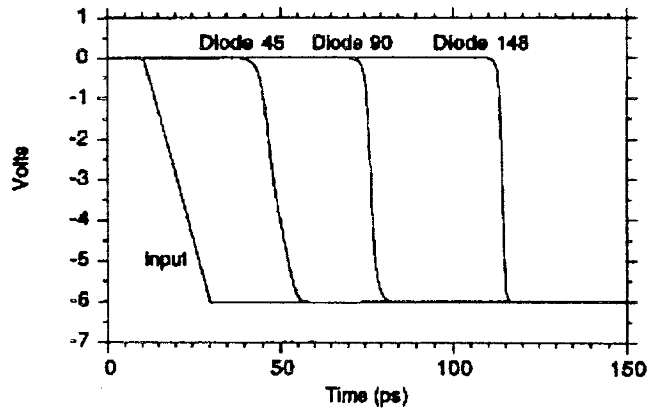

(a) $f_{c,diode} = f_B$

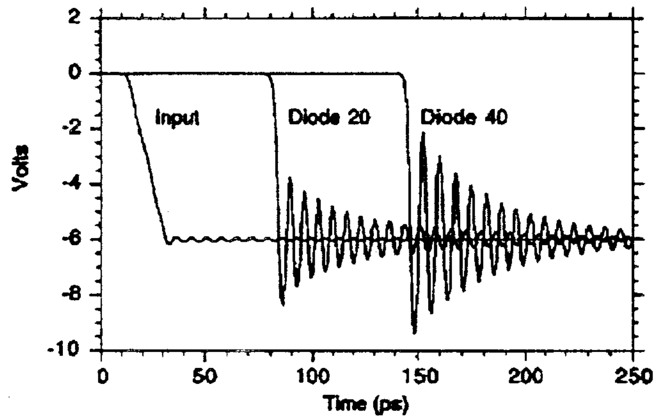

(b) $f_{c,diode} = 20 f_B$

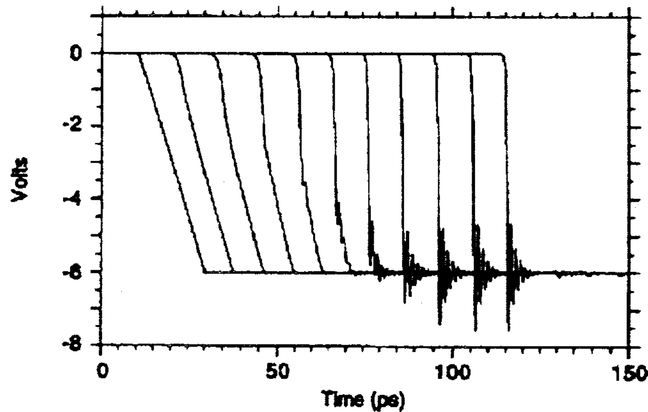

(c) $f_{c,diode} = 4 f_B$

Figure I.9: Shock wave formation and propagation along an NLTL (from reference [Cas93])

the Root-Mean-Square (RMS) energy associated with the oscillations is constant and equal to the input energy except for the losses incurred in R and G parameters.

Research on the use of lumped element NLTLs for shock wave formation was initiated to generate pulses with picosecond rising transients for wide bandwidth test instrumentation applications. The generation of picosecond rise times from shock waves propagating on an NLTL was first proposed by Riley in 1961. In 1987, Rodwell *et al.* [RBA87] demonstrated that fall times on the order of $4ps$ were possible using Schottky varactors with uniform doping monolithically integrated with transmission lines on GaAs. The varactor series resistance introduces a varactor cut-off frequency limiting the compressed fall time. Madden *et al.* [MMR+89] reported the generation of voltage waveforms with $6V$ amplitude and $1.6ps$ fall time, which were generated by voltage shock wave formation on a hyperabrupt-doped Schottky diode monolithic GaAs NLTL. In reference [RKY+91], Rodwell *et al.* studied in detail the shock wave formation during the compression phase as well as the shock wave propagation. In practice, the shock fall time will asymptotically approach a minimum compressed fall time of $1.4ps$, at which wavefront compression is balanced by the wavefront spreading. Subsequent development has resulted in pulse rise times of $480fs$ [Wei94] and $680fs$ [BAR95], the best reported transient results.

In order to generate shock waves having shorter fall times and larger amplitudes, NLTLs can be also manufactured on thin GaAs membrane. In this way, the linear capacitances of the CoPlanar Waveguide (CPW) lines decrease, which leads to the possibility to increase the nonlinear capacitance of the diodes without changing the input impedance and the Bragg frequency. In fact, the ratio between the maximum and minimum capacitance affects strongly the minimum fall time of the shock wave and due to the linear capacitance introduced by the CPW line, this parameter decreases. The first NLTLs on GaAs membranes for picosecond and large amplitude shock wave generation have been simulated by Simion *et al.* [SBM+97].

Finally, there are also many applications which require pulses with amplitudes greater than several hundred volts and rise times in the picosecond regime. In reference [BHJ+93], an NLTL is used to generate a $1.5kV$ pulse with a rise time of $500ps$ from the output of a power Metal-Oxyde-Semiconductor-Field-Effect-Transistor (MOSFET) pulse generator.

I.3.2 Pulse Sharpening

I.3.2.1 Principle

Shock wave formation and propagation in NLTLs has been investigated by Turner *et al.*, who employed uniform ladder networks for sharpening electrical pulses using either nonlinear capacitors or nonlinear inductances. In reference [TBS91], the mechanism by which electrical pulses can be sharpened by propagation along NLTLs is described.

Sharpening of the front or the tail of an electrical pulse is caused by the amplitude dependence of the phase velocity of signals propagating along the NLTL, as seen before. Therefore, the production of pulses with very fast leading or trailing edges depends on the configuration. When nonlinear inductors are used, the phase velocity is largest at the top of the pulse, which catches up with the start of the leading edge. This causes the leading edge of the pulse to

sharpen into a shock wave. When nonlinear capacitors are used, a shock wave forms on the trailing edge of the pulse, as the phase velocity decreases with increasing pulse amplitude. In fact, these situations represent a steep-fronted voltage shock wave and are displayed in figure I.10.

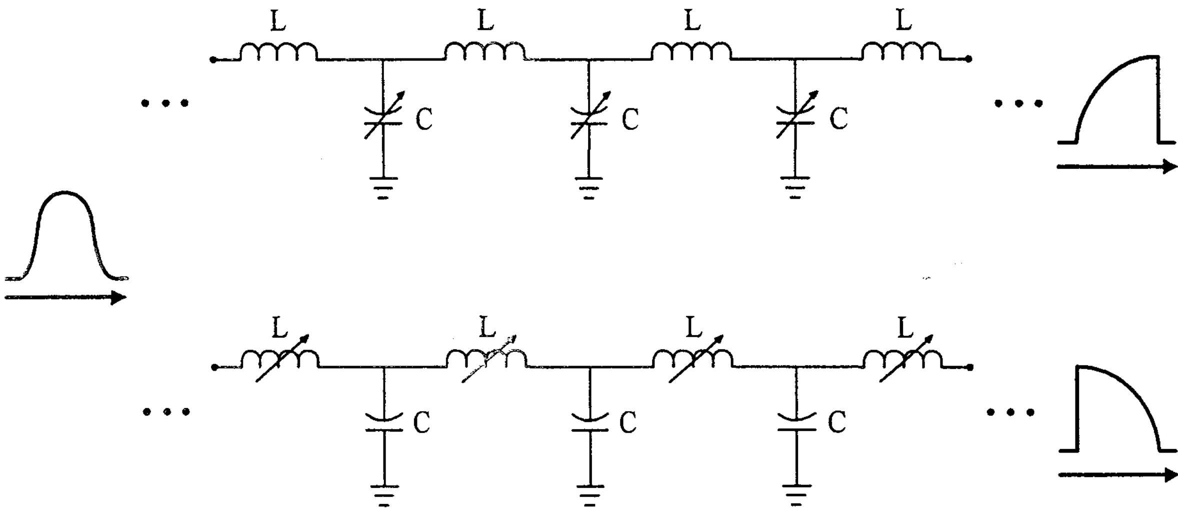

Figure I.10: Diagram of the effect of pulse sharpening along an NLTL

An example of pulse sharpening is shown in figure I.11.

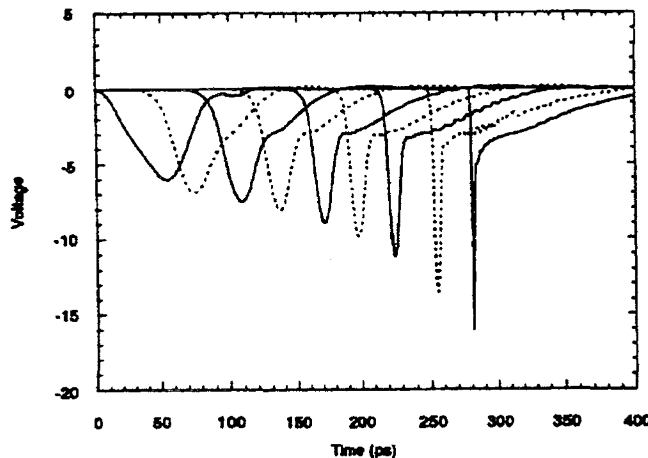

Figure I.11: Pulse sharpening along an NLTL (from reference [Cas93])

The limitations of this very simple 'catch-up' theory are also discussed in reference [TBS91]. Actually, the rise time of a sharpened pulse will depend on the balance between amplitude and frequency dispersion. The Bragg frequency of the line is usually maintained just above the major harmonic components of the signal. This means that impulse compression lines are

very much like tapered shock lines, where the Bragg frequency is increased towards the end of the line to become diode limited.

The main application of the homogeneous NLTL is the generation of higher order harmonics and shock wave propagation. Pulse signal can be generated using the homogeneous NLTL, but band-pass filters and phase shifters are required to adjust harmonic phases. However, nonhomogeneous NLTLs (tapered shock lines) generate pulse signals from sinusoidal inputs without the need of band-pass filters or phase shifters.

I.3.2.2 State-of-the-Art

In 1991, Wilson *et al.* [WTS91] proposed pulse sharpening effect of an NLTL with ferroelectric ceramic capacitors as nonlinear capacitors to generate short rise-time high voltage pulses. Impulse compression on NLTLs was also demonstrated by Tan *et al.* [TSA88] and Case *et al.* [CKY+91] using soliton propagation effects. Tan experimentally measured a compression factor greater than 7 on a low frequency scale model compressor. The inhomogeneous NLTL was built by loading a 300Ω twin lead cable with silicon hyperabrupt varactors. This device compressed a wide, low amplitude pulse into a larger amplitude, narrow width output pulse. The increase in amplitude and pulse compression effect of the leading soliton in a uniform nonlinear line inhomogeneously loaded by linear capacitors have also been observed by Muroya and Watanabe [MW81] and Watanabe and Yajima [WY84]. In his turn, Case demonstrated the generation of $5.5ps$ pulses through soliton effect compression on a tapered monolithic GaAs NLTL.

Ibuka *et al.* [IOY+97] proposed a new scheme of high voltage pulse generation based on the voltage amplification effect of the head-on collision of two solitons in an NLTL with ferroelectric ceramic capacitors. A fast high voltage pulse of $11kV$ amplitude and $76ns$ width has been successfully obtained from a $3.6kV$ amplitude and $300ns$ width initial pulse. In addition, they employed stacked NLTLs to obtain the much higher voltage amplification ratio of 3.78.

Van Der Weide [Wei93] generated saw-tooth waves along NLTLs. Driven with a $70MHz$ and $3W$ source, the circuit was able to produce a $16V$ saw-tooth waveform with a fall time lower than $70ps$. Then, any harmonic (more than 200 harmonics generated) can be selected from the spectrum within a YIG (Yttrium-Iron Garnet)-tuned output band-pass filter, resulting in sinusoidal output signals. This YIG-tuned NLTL multiplier showed that practical millimeter-wave multipliers can be realized with NLTLs when the output filter of the multiplier presents a short circuit to unwanted harmonics. Later, Birk *et al.* [BLG+00] described a new technology for a fast Return-Zero (RZ) pulse source in the picosecond range at several gigabit repetition rates using an NLTL, which was achieved using a low cost silicon integrated circuit with a pulse forming network at the output of the NLTL and an electrical modulation gate. In this application, the input sine-wave was also transformed through nonlinear wave propagation to a saw-tooth waveform at the output of the NLTL.

So far, NLTLs were fabricated on GaAs, as the advantage of GaAs compared to Si is a better carrier mobility and a higher breakdown field. However, this is in contrast to the superior mechanical properties of Si. In 1998, Birk *et al.* [BKW+98] demonstrated the first

working NLTL on silicon substrate, an airbridge NLTL with 40 diodes and 160 pillars, where the fall time of $74ps$ of a $4GHz$ sine-wave was compressed to $32ps$ at the output. In reference [TBMA00] is presented a global finite difference time domain analysis of a silicon NLTL using optimized varactors. The fall time was compressed approximately to $15ps$.

Another application of the NLTL discussed in reference [IWW+88] is the generation of high-power microwave bursts based on the creation of a soliton pulse train. The generation of high-frequency oscillations ($100GHz$, $5 - 10V$) is also presented in reference [BK98]. In this case, the front of the shock wave, caused by the application of a voltage step to the NLTL input, can be considered as a traveling source of radiation leaving behind an increasing tail of oscillations. Once these oscillations behind the shock wave front arise, the train of generated oscillations can be transmitted into a matched load connected at the output port of the NLTL.

In short, theoretical studies based on soliton formation and propagation properties have promoted the applications just described. This work is still necessary. In 1998, Cai *et al.* [CGJB+98] developed a perturbation theory to study the soliton dynamics. They investigated the system's ability to perform reliable pulse sharpening from a train of non solitonic pulses as the input signal and shaped a very noisy signal of pulses into a very ordered one using a perturbed Toda lattice.

I.3.3 Harmonic Generation

I.3.3.1 Basis

Hirota and Suzuki [HS73] analyzed the soliton-soliton interaction, establishing an analytical expression which represents a collision between two lattice solitons. However, the interaction between more than two lattice solitons is quite complicated analytically. Further studies should allow to better understand, among other applications, harmonic generation in NLTLs.

The soliton characteristics are completely determined by its amplitude, a given amplitude imposing a specific full width at half maximum. A larger amplitude soliton travels faster and has a shorter duration than a smaller amplitude one. This fundamental property of solitons on NLTLs can be used to achieve harmonic conversion, in such a way that a waveform with longer duration than that given by equation I.1.2 for its amplitude will decompose into two or more solitons of different amplitudes and propagation velocities. At least one of these decomposed solitons will have a larger amplitude and shorter duration than the initial disturbance. This phenomenon is shown in figure I.12, where the NLTL was excited by an input sine-wave.

In these lines, the Bragg frequency is typically kept at a small ratio to the signal. Higher orders of harmonic generation can be achieved, but efficiencies drop as harmonics increase.

As harmonic generation is the main application developed in this thesis, this section will be studied in detail in the following chapters. Reference [Tho99] is also dedicated only to frequency multiplication.

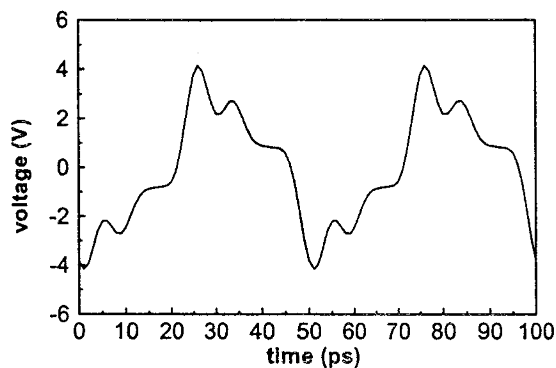

(a) after 12 diodes

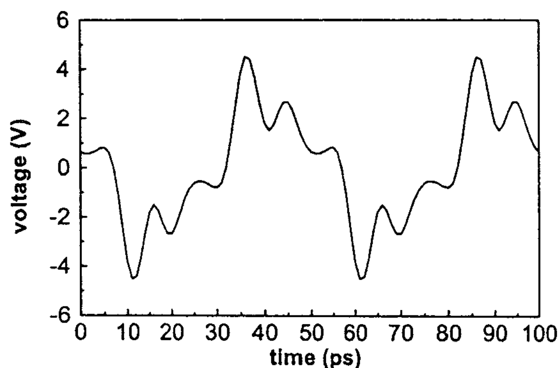

(b) after 16 diodes

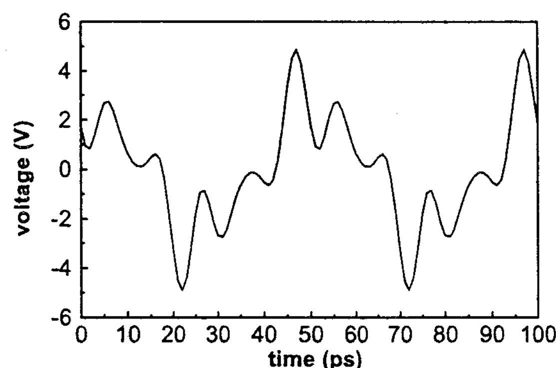

(c) after 20 diodes

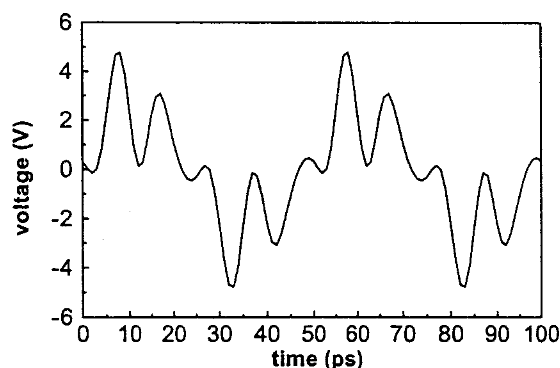

(d) after 24 diodes

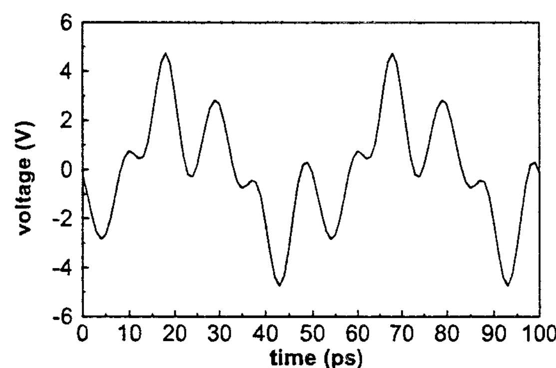

(e) after 28 diodes

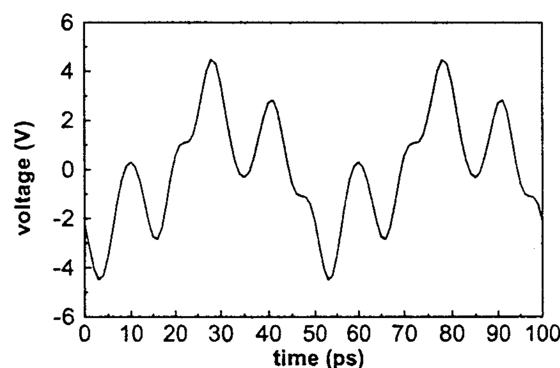

(f) after 32 diodes

Figure I.12: Harmonic generation along a 32-diode NLTL

I.3.3.2 State-of-the-Art

Early research concerning lumped element NLTLs led to the identification of harmonic generation as a possible application for this type of circuits. In 1965, Benson and Last [BL65] performed a study of harmonic generation with particular reference to efficiency and bandwidth. The existence of a spatially periodic pattern of harmonic amplitudes was stated, with an energy interchange between fundamental and harmonic components. A transmission line was constructed having a small signal cut-off frequency of $4MHz$ to study the performance of an NLTL and to confirm the theoretical predictions.

At the time when lumped element NLTLs were being used at low frequencies for research into solitary wave behavior, Jäger [Jäg78] performed in 1978 a study of soliton propagation along a periodic loaded transmission line. Then, a novel NLTL was presented by Jäger and Tegude. It consisted in a semi-lumped line where only varactor diodes were used as lumped elements, thus leading to excellent high frequency characteristics. The influence of dispersion on second harmonic frequency generation, yielding large values of the efficiency, was specially addressed in reference [JT78].

Since then, the interest in harmonic generation through soliton propagation at microwave frequencies is manifest. In 1991, this resulted in a distributed harmonic generator, a GaAs MMIC NLTL with Schottky diodes. A $9.3dB$ minimum conversion loss to the second harmonic for input frequencies from $13.5GHz$ to $18GHz$ at $20dBm$ input power was reported in reference [CGC+91]. Carman *et al.* [CCK+92] improved their previous results by reducing skin losses and by introducing devices for V-band and W-band output, resulting in a minimum conversion loss of $11.5dB$ to the third harmonic over the $80GHz-105GHz$ range. In 1995, Shi *et al.* [SZD+95] investigated three new device concepts in order to improve the performance of NLTLs. These devices, the Multi-Quantum Barrier Varactor, the Schottky Quantum Barrier Varactor and the Schottky Superlattice Quantum Barrier Varactor, were shown to be useful in high power harmonic generation applications.

As it has been already noticed in reference [EBJ77], fully distributed Schottky varactor NLTLs were excessively lossy. However, Li *et al.* [LH98, LKH98] explored NLTLs based on fully distributed Heterostructure Barrier Varactor (HBV) and showed that such NLTLs could provide efficient tripling over input frequencies in the range $25GHz - 35GHz$, with a $5.1dB$ maximum conversion loss for an input frequency of $29GHz$. Furthermore, it was shown that these fully distributed HBV structures could act as frequency quintuplers.

The design of novel microstrip-based GaAs MMIC NLTL harmonic and pulse generators was reported in reference [SL99a]. The microstrip NLTL provides an alternative to CPW NLTLs when a compromise has to be made between performance, MMIC size, aspect ratio, bandwidth and output power. A wide bandwidth doubler operating over the $5GHz-10GHz$ input frequency range was fabricated with a measured conversion efficiency of 5.5%. Experimental work has also been undertaken to measure the output waveform of a microstrip-based GaAs MMIC tapered NLTL pulse generator.

As a promising alternative, Hollung *et al.* [HSD+00] fabricated a distributed frequency tripler, consisting of a finline section periodically loaded with 15 HBV diodes. A 7% of conversion efficiency was demonstrated at $130.5GHz$, taking advantage of the properties of the HBV diodes employed and that offered by finlines in terms of concentration of fields on

small diode dimensions.

Harmonic generation at high frequencies with the lumped element varactor type circuit has been demonstrated using different approaches. One of them is the phase matching between the input and second harmonic frequencies, which prevents shock wave formation and suppresses higher order harmonics. Wedding and Jäger [WJ81] have predicted and confirmed experimentally efficiencies of 90% for fundamental to second harmonic conversion. Therefore, in terms of conversion loss, this technique potentially offers the best performance, but at the cost of limited tunability. Further studies regarding conversion efficiency have been carried out by Champlin and Singh [CS86]. The phase matching technique involves matching the velocity of fundamental and generated harmonic signals during propagation, restricting the applicability of this configuration for broad-band frequency multiplier applications. However, increased operational bandwidth has been achieved by Marsland *et al.* [MSB90] through parametric coupling of forward waves on an NLTL. With an input of $20dBm$ at $50GHz$, amplitudes up to $1V$ at $100GHz$ have been measured.

I.4 Integrated NLTL-based Circuits for Instrumentation Applications

NLTLs have direct applications in a variety of high speed, wide bandwidth systems as it will be shown in this section. However, the limiting factor in these devices is the loss introduced by the nonlinear elements. Thus, future generations of high speed and wide bandwidth electronics will require distributed devices with lower loss but equivalent nonlinearity. This will enable the use of nonlinear solitary wave concepts in electrical transmission lines.

Over other electrical circuits, NLTLs have the significant advantage of their integrability with other circuitry. Indeed, NLTLs have evolved from single prototypes capable of generating picosecond transition time signals into integrated circuits, the NLTL having proved to be the most suitable circuit for extending the frequency bandwidth of the present high speed sampling instrumentation. In short, these circuits are interesting not only for their intrinsic ultrafast physics, resulting in the generation of picosecond electrical signals, but also for their applications in detecting other high-speed and broad-band signals. In 1994, Rodwell *et al.* [RAY+94] described active and nonlinear wave propagation devices in ultrafast electronics and optoelectronics for the generation and detection of millimeter wave and picosecond signals.

The primary application of NLTLs is in sampling circuits. In 1991, Rodwell *et al.* [RKY+91] described the circuit design and diode design requirements for NLTL-driven diode sampling bridge circuits. Marsland *et al.* [MVM+89], Yu *et al.* [YCK+90] and Shakouri *et al.* [SBAB93] have reported other NLTL-gated sampling circuits. NLTL-gated sampling circuits for high speed on-wafer waveform measurements have attained a $3dB$ bandwidth of $725GHz$ [BAR95] by using an elevated coplanar waveguide technology. In addition, monolithic photodiode/sampling circuits combining a photodetector and an NLTL-based sampling circuit have been reported in references [KGK+91, OLB91] for picosecond optical waveform measurements.

In fact, sampling oscilloscopes and microwave network analyzers use diode sampling bridges

to down-convert the signal under test to a lower frequency before acquisition. Using such narrow pulses with sampling bridges, the frequency bandwidth of the oscilloscopes and vector network analyzers has been extended in the past few years.

On one hand, the frequency bandwidth of sampling oscilloscopes has been extended up to $300GHz$ [RKY$^+$91]. On the other hand, in reference [MMW$^+$90], integrated circuits for network analysis have been fabricated combining the millimeter-wave NLTL signal sources and sampling circuits. Active probes have been developed by Yu *et al.* [YKC$^+$91, YPK$^+$92, YRP$^+$95] for on-wafer millimeter-wave vector network analysis to $200GHz$. Wohlgemuth *et al.* [WAP$^+$98, WRR$^+$99] demonstrated the first NLTL-based integrated circuit for network analysis within $70 - 230GHz$, which can be used as a S-parameter test set for the broad-band commercial S-parameter set-up $HP - 8510$ operating up to $120GHz$.

Applications include both on-wafer and in free space instrumentation for millimeter-wave waveform and network circuit measurements. In references [KG91, KKC$^+$92], NLTLs and sampling circuits have been used for gain-frequency measurements in free space. Van Der Weide *et al.* [WBAB93] reported a similar system for broad-band measurements, with bow-tie antennas as interfaces.

Finally, note that NLTLs have also applications beyond the area of instrumentation. For example, Pullela *et al.* [PBAR96] have developed an NLTL-based multiplexer/demultiplexer integrated circuit for $100Gb/s$ fiber-optic transmission.

Chapter II

Lumped Nonlinear Devices and Transmission Lines Integrating an NLTL

Chapter II

Lumped Nonlinear Devices and Transmission Lines Integrating an NLTL

II.1 Introduction

In order to realize a NonLinear Transmission Line (NLTL), a transmission line is periodically loaded with varactor diodes. Thus, a nonlinear device and a non-loaded transmission line are the two key elements integrating an NLTL and will have a special consideration in this chapter.

From the main three NLTL applications described in chapter I, harmonic generation is the one developed in this thesis. The key issue when going up to millimeter and submillimeter frequencies is the availability of reliable local oscillator sources to generate enough power levels at these frequencies. This can be achieved either by direct generation or by frequency multiplication from a lower fundamental source. Power sources for high frequencies are much more difficult to realize than for lower frequencies. This being the case, the solution is to use a frequency multiplier.

Frequency multiplication requires a nonlinear device, such as a diode. The transistor is also used in frequency multipliers, the intrinsic gain acting as a counterbalance to losses. Even overall conversion gain potential can be obtained, which is its main advantage. Diodes present two sources of nonlinearity, resistive (varistor) or reactive (varactor). In the first case, a nonlinear resistance or conductance is used. Note that the nonlinearity is here evident in the I-V curves. Resistive devices suffer from the dissipative nature of the nonlinearity. Consequently, poor conversion efficiency can be achieved. Indeed, the conversion efficiency limit can be estimated to $1/n^2$ according to Page [Pag58], where n is the order of the output harmonic. In the second case, a nonlinear reactive element, usually a nonlinear capacitance, is used. Relying on varactor diodes, very low loss conversion efficiency can be achieved. Manley

and Rowe [MR56] demonstrated a maximum conversion efficiency of 100%. In practice, the limitation stems from the device series resistance. However, such lumped devices need an input and output matching network in order to cancel reactive power components, with the subsequent limitation in bandwidth.

In conclusion, common multipliers are limited in either conversion efficiency or bandwidth. NLTLs use varactor diodes as nonlinear devices. The advantage of NLTLs over discrete devices is a high frequency operation over a broader frequency range, the NLTL being self matched.

II.2 Lumped Nonlinear Devices

II.2.1 Schottky Barrier Varactor Diode

II.2.1.1 Basic Principle

One of the most widely used device in frequency multiplication is the Schottky varactor diode. In the same way, NLTLs were mainly realized loading transmission lines with Schottky varactor diodes.

A Schottky Barrier Varactor (SBV) is a rectifying metal to semiconductor junction resulting in an asymmetric capacitance dependent on the applied voltage. This one-sided device consists of a junction between a metal and a lightly doped thin epitaxial layer grown on a heavily doped buffer layer. Under reverse bias, the SBV exhibits a progressive depletion in the vicinity of the metal to semiconductor junction. The heavily doped buffer layer allows to minimize series resistance losses.

The most common C-V fitted expression for the SBV diode is:

$$C_j(V) = \frac{C_{j0}}{(1 - \frac{V}{\phi})^M} \tag{II.2.1}$$

where C_{j0} is the zero-bias junction capacitance, ϕ is the barrier potential and M is the grading coefficient.

The asymmetric C-V and I-V characteristics can be observed in figure II.3(a). The C-V characteristic depends on the epitaxial structure of the diode. Among all the parameters involved, let us make stand out the doping profile as it can be adjusted to provide a strongly varying depletion capacitance, as described in section II.2.1.2.2. Rodwell *et al.* [RKY+91] already emphasized that such a property, with high breakdown voltages and high cut-off frequencies, are greatly desirable for picosecond shock generation.

Diode loss is a limiting factor in the three NLTL applications having an effect on the transition speed, the pulse duration, as well as the conversion efficiency. Indeed, small parasitics

are essential in order to increase the bandwidth. As a result, the diode cut-off frequency is one of the most important parameters in NLTL performance, thus determining its application. The diode small signal RC cut-off frequency, at bias voltage V, is defined as:

$$f_{c,diode} = \frac{1}{2\pi C_j(V)Rs} \tag{II.2.2}$$

where Rs is the diode series resistance.

II.2.1.2 Bottlenecks and Possible Device Improvements

II.2.1.2.1 Generation of Higher Order Harmonics

With the recent interest in direct frequency tripling, new Schottky varactor structures with symmetric C-V characteristics have been proposed, leading to an absence of even harmonic generation. This absence of even harmonic generation simplifies the realization of higher order multipliers.

In 1995, Shi *et al.* [SZD+95] investigated new devices in order to improve the performance of NLTLs. Actually, the use of a Schottky diode as a one-sided device restricts the performance of an NLTL. The improved compression effect of a two-sided device, driven by both negative and positive voltage components, was demonstrated through the Multi-Quantum Barrier Varactor and the Schottky Quantum Barrier Varactor. The Multi-Quantum Barrier Varactor is a stacked Quantum Barrier Varactor which operates as a varactor under both forward and reverse bias due to its symmetric structure. The Schottky Quantum Barrier Varactor is essentially a Multi-Quantum Barrier Varactor with an additional Schottky barrier. The epitaxial profiles as well as the corresponding equivalent circuits are shown in reference [SZD+95].

It is also possible to fabricate devices with a symmetric C-V characteristic by connecting two diodes back-to-back. Therefore, devices which naturally do not have a symmetrical C-V characteristic can be mounted in a back-to-back configuration (two facing diodes in series), but complicating the fabrication process. In addition, Bradley *et al.* [BKE97] proved that the $Cmax/Cmin$ ratio measured under small signal conditions is not an adequate indication of the large signal behavior of the back-to-back diode in a tripler circuit. Indeed, this configuration is more complex than first expected. Due to the self-biasing effect, at the terminals of the back-to-back uniformly doped varactor there is no capacitance variation produced by the pump signal. However, when the doping profile is not uniform, the pump signal does modulate the capacitance of the pair of diodes and frequency multiplication is then possible.

Even if the back-to-back configuration has been used in frequency tripling applications, at the moment no NLTL includes such integrated devices. In reference [LTFM92], Lieneweg *et al.* compared the back-to-back Barrier-Intrinsic-n^+ (bbBIN) diode and the back-to-back Barrier-n-n^+ diode (bbBNN) as planar varactor frequency multiplier devices. The limitations of the bbBIN diode frequency tripler were also discussed in reference [HS92]. While operating back-to-back, $Cmax$ is approximately half of a single diode, and $Cmin$ is slightly smaller,

resulting in a smaller $Cmax/Cmin$ ratio and smoother C-V characteristic. However, such devices with undoped drift regions have a broad range of power operation. In other terms, the symmetry is achieved at the expense of nonlinearity. Later, Choudhury *et al.* [CSS+95] obtained a tripling efficiency of 7% at $220GHz$ using a bbBNN varactor diode tripler integrated in a split-waveguide block.

Finally, note that the back-to-back configuration is also free from external bias, simplifying the circuitry.

II.2.1.2.2 Improvement in Conversion Efficiency

A nonuniform diode doping profile is required for high nonlinearity. Thus, NLTL performance is strongly affected by the diode doping profile. High nonlinearity can be achieved by using an exponential graded or delta-doped profile.

In 1989, Madden *et al.* [MMR+89] proposed the use of diodes having a larger variation in capacitance to minimize the required line length. An exponentially graded diode doping profile provides much higher fractional change in capacitance than a uniformly doped structure. Therefore, they reported the generation of voltage waveforms by shock wave formation on a hyperabrupt-doped Schottky diode monolithic GaAs NLTL. The term hyperabrupt is applied when the doping decreases with increasing depth for Schottky-up devices. Hyperabrupt doping always provides better performance than the uniform doping, even though hyperabrupt doping profiles increase the reflection loss.

Taking hyperabrupt doping to its extreme results in a delta-doped profile. In 1994, Van Der Weide [Wei94] proposed delta-doped Schottky diodes better than hyperabrupt diodes as, over the central bias range, the delta-doped Schottky diode offers a more drastic change in the C-V characteristic, resulting in a greater transmission line phase velocity modulation than the hyperabrupt varactor. Indeed, a planar doping profile diode presents a step-like transition in its C-V characteristic but also a high series resistance through the intrinsic region.

Later, Salameh and Linton [SL99b, SL99c] performed a detail study of the relation between Gaussian doping profiles and diode C-V characteristics. The effect of diode C-V characteristics on NLTL performance was also investigated.

II.2.2 Heterostructure Barrier Varactor Diode

II.2.2.1 Basic Principle

The Heterostructure Barrier Varactor (HBV), first proposed by Kollberg and Rydberg [KR89], has received considerable attention as a promising device for high efficiency frequency multiplication at millimeter and submillimeter wavelengths. In the same way, its use in NLTLs should become generalized because of its attractive characteristics and flexible design parameters. At the moment, several configurations using micromachined waveguides [TSM98], finline waveguides [HSD+00] and coplanar waveguides [FDM+01] have been proposed for frequency

multiplier applications. In addition, Li *et al.* [LH98] explored NLTLs based on fully distributed HBV. Each approach showed that such NLTLs could provide efficient tripling.

In contrast to Schottky varactor diodes where the blocking condition is guaranteed by the metal-semiconductor potential barrier, the principle of operation in the case of an HBV diode is based on a heterostructure blocking barrier. Such a barrier is obtained by creating a potential discontinuity both in the valence and conduction band.

A single barrier HBV diode consists of a large band gap semiconductor sandwiched between symmetric moderately doped modulation regions of smaller band gap semiconductor. The potential barrier, thus formed, prevents conduction through the structure, so that each cladding layer can be depleted according to bias conditions.

The conduction band of such a structure is schematically depicted in figure II.1, as well as the related conduction mechanisms.

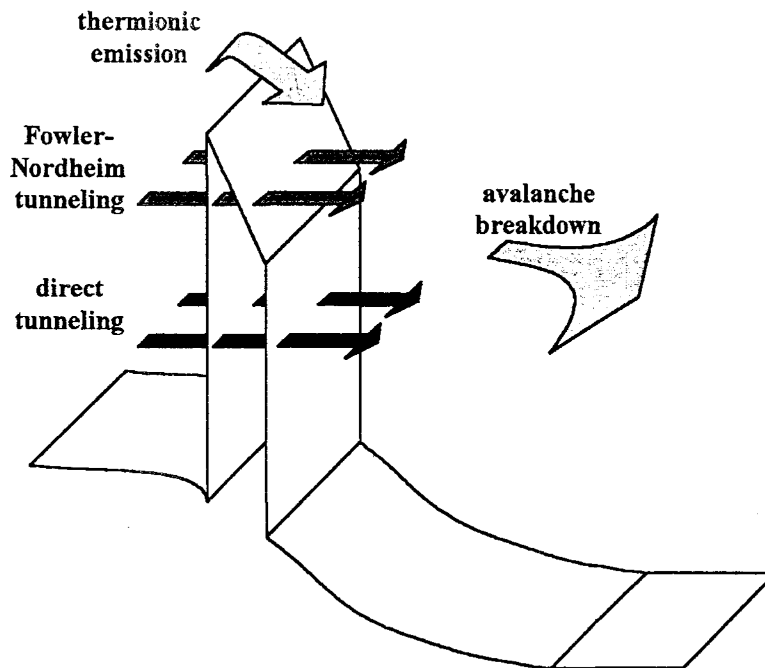

Figure II.1: Schematic of the conduction band and related conduction mechanisms in an HBV diode

The leakage current is caused both by thermionic emission over the barrier and direct tunneling of carriers through the barrier. At higher voltages, the leakage current is dominated by Fowler-Nordheim tunneling, namely tunneling through the triangular-shaped barrier. The transport mechanism at breakdown is related to impact ionisation in the depleted layer.

In reference [LMS+96], a lattice matched $In_{0.53}Ga_{0.47}As/In_{0.52}Al_{0.48}As$ system on InP substrate provided high performance HBV diodes. As a consequence of the parasitic conduction mechanisms just described, the barrier must be thick enough so that the leakage current does not tunnel through it. In addition, thermionic emission can be alleviated by incorporating

a very high band gap layer of AlAs in the middle of the barrier, as demonstrated in references [HLV+98, MCH+98, MMM+98]. The increase of the effective barrier height by placing a thin AlAs layer in the middle of an AlGaAs barrier was first proved by Krishnamurthi *et al.* [KNH94]. The active epitaxial structure depicted in figure II.2 corresponds to a single barrier InP-based HBV diode.

Layer	Doping	Thickness
InGaAs	$1 \times 10^{19} cm^{-3}$	$5000 \AA$
InGaAs	$1 \times 10^{17} cm^{-3}$	$3000 \AA$
InGaAs	undoped	$50 \AA$
InAlAs	undoped	$50 \AA$
AlAs	undoped	$30 \AA$
InAlAs	undoped	$50 \AA$
InGaAs	undoped	$50 \AA$
InGaAs	$1 \times 10^{17} cm^{-3}$	$3000 \AA$
InGaAs	$1 \times 10^{19} cm^{-3}$	$1 \mu m$
InP substrate		

Figure II.2: Single barrier InP-based HBV epitaxial structure

Over the past, HBV diodes were grown on GaAs substrates accordingly with mature processing techniques. However, HBV diodes on InP substrate exhibit a higher potential barrier, which leads to a reduced leakage current. Indeed, excellent InP-based HBV tripler results have been reported by Mélique *et al.* in references [MMF+00, MMM+99]. In reference [MMM+99], record performances in terms of output power ($9.5 dBm$) and maximum efficiency (12.3%) have been demonstrated for a $250 GHz$ HBV tripler. These high performance results have motivated in this thesis the insertion of HBV diodes grown on InP substrate in the NLTLs manufactured.

On the processing device side, HBV diodes on InP substrate offer significant advantages at the expense of less standard processing techniques. Since semiconductor alloys, layer thicknesses, doping profiles, as well as device geometries and areas can be easily varied, this technology involves important flexibility in the design.

II.2.2.2 Attractive Characteristics

II.2.2.2.1 Symmetry

Among the device characteristics, the most attractive is the symmetric nonlinear capacitance-voltage characteristic about zero volt bias. The symmetric C-V and anti-symmetric I-V characteristics are a direct consequence of the epitaxial structure of the device, which does not require any rectifying contact. The differences between a Schottky diode and an HBV diode concerning the C-V and I-V characteristics are manifest in figure II.3.

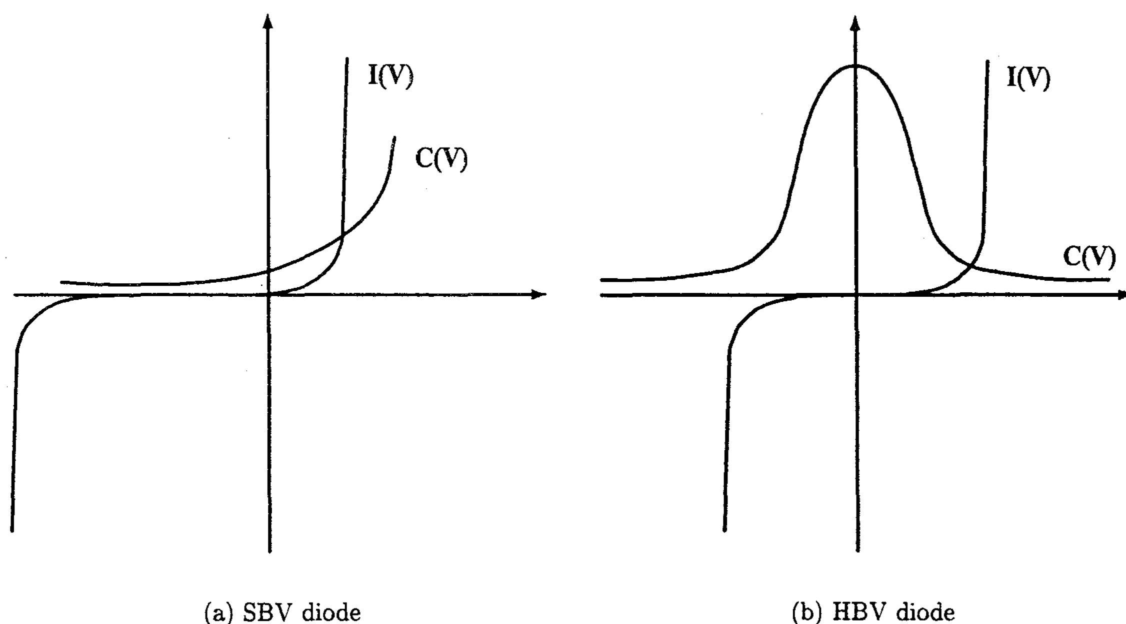

(a) SBV diode (b) HBV diode

Figure II.3: Capacitance-voltage and current-voltage characteristics for an SBV diode and HBV diode

This symmetric C-V characteristic confers to the device a natural potential for odd harmonic generation. As a result, the HBV diode offers significant benefits for odd harmonic multiplier applications since idler circuits at the even harmonics are not required. In the case of an HBV tripler no idler is required, while in a frequency quintupler application, only the idler at the third harmonic has to be considered, compared to the three idlers needed in a Schottky varactor quintupler.

In particular, a two-sided NLTL can be driven by a symmetric signal with respect to positive and negative voltages. As a result, the even harmonics are cancelled while the odd harmonics are doubled while compared to a single-sided NLTL. In fact, the use of HBV diodes improves the performance of an NLTL in terms of compression and harmonic efficiency.

In the same way, HBV diodes open up new horizons in NLTL high order harmonic generation. Indeed, the key problem concerning high order harmonic generation is the energy sharing between the generated harmonics, which results in a lower conversion efficiency for the higher harmonic.

II.2.2.2.2 Pump and Bias Signal

On the other hand, the C-V characteristic of the device is peaked around zero volt bias. Thus, the device does not require external DC bias, minimizing the number of off-chip circuit connections. In addition, the sharp C-V characteristic close to zero volt bias condition allows for potentially high multiplication efficiency at low input power levels. This is an advantage at higher frequencies where the available input power is usually quite low.

High efficiency frequency multipliers, which do not require DC bias and which require fewer idlers than the standard Schottky diode multiplier, can then be realized. Thus, the HBV diode is ideally suited for use as the multiplier element in a high order NLTL.

II.2.2.2.3 Breakdown Voltage

The breakdown characteristics of GaAs Schottky varactors have limited the magnitude of shock waves. In addition, hyperabrupt diodes which exhibit larger nonlinearities are required for improved compression efficiency, but at the expense of lower breakdown voltage. In 1995, Shi *et al.* [SZD+95] proposed the stacking of several quantum barriers first and second a back-to-back device configuration in order to increase the voltage handling capability of a Schottky-based NLTL. It was noted in reference [SZD+95] that these solutions only fit two-sided devices.

In this way, HBV diodes, as two-sided devices, permit both epitaxially and laterally stacking. By epitaxially stacking several single barrier HBV diodes in series, further advantages are obtained, including higher impedances for a given device area and higher cut-off frequencies due to reduced capacitances, higher power handling capabilities due to sharing of the pump power over several series devices, and higher heat dissipation capabilities for a given capacitance modulation range due to increased device areas.

On the other hand, the diode voltage range can be extended by stacking several devices laterally, in order to drive the NLTL with higher input power levels. Thus, eight barriers have been successfully integrated in reference [Mél99], four by epitaxial integration and two by planar integration. An optical view and a Scanning Electron Microscope (SEM) view are shown in figures II.4(a) and II.4(b) respectively.

In short, by employing stacking structures, the breakdown voltage is increased and thus the total effective depletion region can be extended. In this sense, the $Cmax/Cmin$ ratio is significantly enhanced to the detriment of the C-V characteristic slope.

Finally, stacking structures increase the effective series resistance. Therefore, there is a trade-off between breakdown voltage capabilities, which can be a limitation for high power applications, and losses, which can be a limitation for high frequency applications.

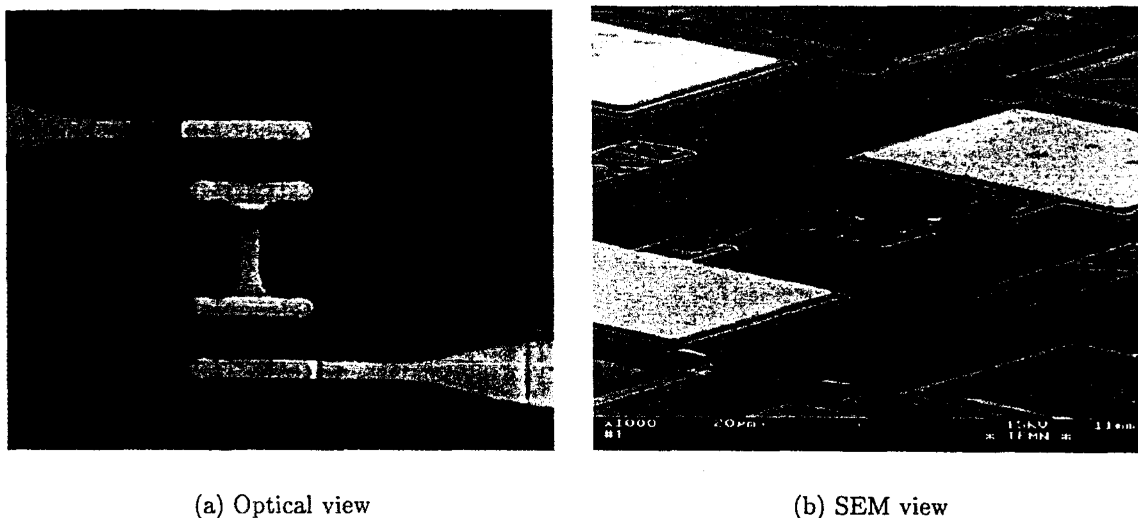

(a) Optical view (b) SEM view

Figure II.4: Photographs of an eight barrier-integrated HBV diode (from reference [Mél99])

II.2.2.2.4 Nonlinearity

As for a Schottky diode, a nonuniform HBV diode doping profile is required for high nonlinearity. Indeed, the capacitance nonlinearity can be improved with a planar doping profile as demonstrated in reference [LMM+98], where a single barrier InP-based HBV diode homogeneously doped and delta-doped are compared. At the same time, Dillner *et al.* [DSK97] investigated how the shape of symmetric C-V characteristics influences the maximum multiplier efficiency. In particular, they compared an homogeneously doped HBV diode to a delta-doped one. The delta-doped diode exhibits an increased $Cmax$ but the C-V characteristic is flatter near zero voltage values, the enhanced nonlinearity being shifted. Contrary to a delta-doped Schottky diode, the best efficiency here is obtained for an homogeneously doped HBV diode. The reason for this is that the strongest nonlinearity does not occur at the region near zero volt bias, where a two-sided device is mainly modulated. Thus, even if the HBV capacitance nonlinearity can be enhanced with a delta-doped profile, this does not involve a better multiplier efficiency.

On the other hand, nonlinearity can be improved with a quantum-well adjacent to the barrier. In fact, Jones *et al.* [JJT94] further improved the barrier height by using low band gap InGaAs spacer layers compared to the GaAs cladding layers. Due to electron confinement closer to the barrier, Duez *et al.* [DMV+98] reported an excellent $Cmax/Cmin$ ratio of 10 : 1. Buried InAs quantum-well barrier InP-based HBV diodes have also been successfully fabricated by Lheurette *et al.* [LMM+98]. In comparison with delta-doped HBV diodes, the nonlinearity is here centered on zero volt bias, with a large breakdown voltage. This being the case, rather than a delta-doped concentration a quantum-well configuration should be preferred in order to enhance the conversion efficiency.

In chapter IV (Large Signal S Parameter Simulation of an NLTL), section IV.4.5 deals with the influence of the shape of symmetric diode capacitance-voltage characteristics on the transmission behavior of the NLTL, since it is well known that a high derivative of the

capacitance with respect to voltage enhances the power transferred to higher order harmonics.

II.3 Transmission Lines

In general, the need to integrate active devices into a circuit makes the analysis and design of millimeter and submillimeter wave transmission lines an important issue. In this case more precisely, it is even a question of one of the two key elements integrating an NLTL. Although microstrip lines have been used extensively in integrated circuits, alternative transmission lines have potential advantages over the microstrip.

A transmission line consists of two or more parallel conductors. When the conductors are completely surrounded by a uniform dielectric medium, the principal wave that can exist on the transmission line is a Transverse Electro Magnetic (TEM) wave. However, most of the planar transmission lines does not have the dielectric medium completely surrounding the conductors and therefore does not support a pure TEM wave. In this case, the dominant mode of propagation approaches that of a TEM wave at low frequencies, which is called a quasi-TEM mode.

A planar transmission line is a transmission line with conducting metal strips that lie entirely in parallel planes, in this way compatible with integrated circuit fabrication. There are several types of monolithically integrable transmission lines, such as microstrip lines, coplanar lines and slotlines. The reasons for choosing a particular type of transmission line, amongst the configurations just mentioned, are discussed in the following sections. In fact, the motivations concerning an NLTL layout do not differ essentially from a general case.

Even if microstrip lines have been used extensively, coplanar lines have experienced a great interest with the advent of monolithical integrated circuits. The most significant advantage of a coplanar line over a microstrip line is the ability to connect components in shunt from the conducting strip to the ground plane on the same side of the substrate. In a microstrip line, a connection requires via holes drilled through the substrate. Finally, note that slotlines are less desirable. Wave propagation on this line is more strongly influenced by nearby conductors, as it is not balanced relative to a ground plane. As a result, the open slotline is not as widely used as the microstrip and coplanar lines. However, the shielded slotline, also called finline, has been found to be useful for many circuit applications.

II.3.1 Coplanar Waveguide

The coplanar line, often called a CoPlanar Waveguide (CPW), was proposed first by Wen [Wen69] in 1969. It consists of a single strip mounted between two ground planes on the same side of the dielectric substrate, as shown in figure II.5. Note that CPWs are commonly used in NLTLs.

In fact, the mount of lumped components in shunt or series configuration is much easier and the performance of coplanar lines is comparable to microstrip lines in terms of guide wavelength, dispersion and losses. It can be better sometimes. The main disadvantage is

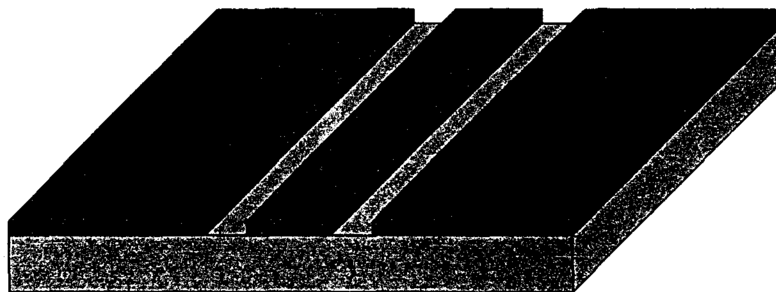

Figure II.5: Schematic of a coplanar waveguide

that CPWs occupy a significant Monolithic Microwave Integrated Circuit (MMIC) area and consequently have higher cost. Also, the aspect ratio between the longitudinal and transverse dimensions is significantly larger in comparison with a microstrip configuration.

At higher frequencies, the main problems encountered in CPWs are the presence of losses and the excitation of hybrid modes. The attenuation is caused by three different mechanisms, conductor losses, dielectric losses and radiation losses. The former is the dominant component, which can be reduced by increasing the center conductor width of the CPW. In this sense, inhomogeneous lines are required in order to achieve high orders of impulse compression or harmonic conversion. In particular, Case *et al.* [CKY+91] fabricated a tapered monolithic GaAs NLTL. Second, dielectric losses increase, as well, with frequency as the fields tend to be more concentrated in the dielectric substrate. Radiation, stemming essentially from discontinuities, is the last source of losses, less significant in an NLTL than the other two. However, radiation in the free space and in the substrate must be taken into account.

Finally, let us note that an open structure is very convenient for use in MMICs where lumped devices must be surface mounted in the circuit. However, the presence of the dielectric-air interface modifies the mode of propagation to a non-TEM hybrid mode at millimeter wave frequencies on high permittivity substrates, resulting in a surface-wave mode of propagation that consists of a field concentrated near the air-dielectric interface. Also, the coupled slotline mode may be excited in a CPW. To prevent the excitation of such an unbalanced mode, air bridges between the two ground planes are often used to reduce parasitic mode generation.

II.3.2 Microstrip Line

A microstrip line consists of a single conducting strip placed on a dielectric substrate and located on a ground plane, as shown in figure II.6. The mode of propagation in a microstrip line is almost TEM, which allows an easy approximate analysis and yields wide band circuits. That explains mainly why it is the most popular of the planar transmission structures. The quasi-static approach and the full-wave analysis aimed at determining the characteristic impedance, phase velocity and attenuation constant for a microstrip line can be found in reference [GGBB96]. Also, simple transitions to coaxial are feasible. In addition, microstrip lines can be fabricated using conventional techniques, which results in a low cost and good

mechanical tolerances.

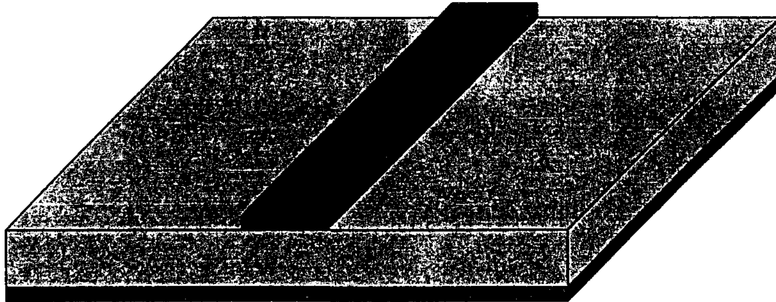

Figure II.6: Schematic of a microstrip line

In 1999, Salameh and Linton [SL99a] proposed microstrip GaAs NLTLs as an alternative to CPW NLTLs in the microwave region where a compromise has to be made between performance, MMIC size, aspect ratio, bandwidth and output power. In other terms, the advantages of microstrip-based NLTLs are compressed size and flexible aspect ratio. Notably, a meander is easily realized using a microstrip configuration. In addition, within a microstrip line, the metallic loss term is lower than in a CPW due to microstrip more uniform conductor current distribution. However, the major disadvantages are the need for via holes, causing limited bandwidth, and lower performances than in CPW-based NLTLs.

II.3.3 Finline

At the higher microwave frequencies, waveguides, which must be rather treated as electromagnetic boundary-value problems, are often preferred to transmission lines because of better electrical and mechanical properties. However, it is difficult to incorporate active devices as part of waveguide circuits. The solution is to use a finline, which was first proposed by Meier [Mei73]. Indeed, the finline is suitable for use in microwave circuits that incorporate two-terminal devices such as diodes.

The finline is a quasi-planar transmission line that can be considered as a shielded slotline. The fins are metal foils on a thin dielectric substrate mounted in the E plane of a rectangular waveguide, as shown in figure II.7. In addition, the finline can be matched to the rectangular waveguide by means of tapered sections.

The main characteristics of a finline are its large bandwidth of operation for the fundamental mode and the absence of radiation. The fins concentrate the field in the fin-gap region as, for the dominant mode, the current flows in the axial direction. Thus, any device connected to the fins will be subjected to larger power densities. The advantage offered by finlines in terms of concentration of fields on small diode dimensions has resulted in the realization of NLTLs in a finline configuration. A distributed HBV frequency tripler has been fabricated by Hollung *et al.* [HSD+00]. Actually, a finline can act as a substitute for CPWs in that the latter suffer from practical problems of tolerance conditions with the very narrow strip widths

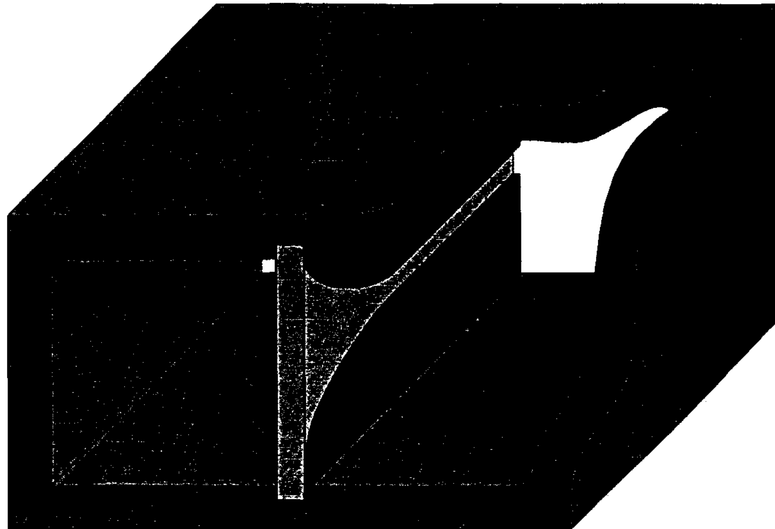

Figure II.7: Schematic of a finline

required at millimeter wavelengths. However, note that the field concentration also results in higher conductor and dielectric losses.

Finally, NLTLs thus manufactured have resulted in hybrid circuits. However, the current trend is towards the use of MMICs at the higher microwave frequencies.

II.3.4 Further Extensions

More recently, micromachined transmission lines fabricated on thin dielectric membranes have demonstrated outstanding performances at higher frequencies with respect to conventional planar transmission lines, which present severe drawbacks at millimeter and submillimeter wave frequencies. The problem stems essentially from the fact that, as the wavelength decreases, the substrate thickness becomes comparable to the guided wavelength, generating higher order modes of propagation as well as increased losses in the substrate. Thus, membrane supported structures have emerged as a novel and promising technology while preserving the advantage of planar transmission lines concerning the ease of integration. A membrane transmission line consists of metallic strips suspended in an almost homogeneous medium, resulting in an almost pure TEM mode with no dispersion up to very high frequencies. Micromachined or membrane transmission lines on silicon substrate were first analyzed by Dib *et al.* [DHK+91] in 1991. Later, membrane structures on GaAs substrate were demonstrated in references [SDH+96, DCM+99]. NLTLs can be also manufactured on thin GaAs membrane. The first NLTLs on GaAs membrane have been simulated by Simion *et al.* [SBM+97]. The linear capacitances of the CPWs decrease, which leads to the possibility to increase the nonlinear capacitance of the diodes without changing the input impedance and Bragg frequency. In this way, this technology opens up the way for new possibilities in NLTL technology.

In short, new transmission lines with low loss and low dispersion are needed in MMICs

for applications at millimeter and submillimeter wave frequencies. A new coplanar-like transmission line was proposed by Hofschen and Wolff [HW96] in 1996. They demonstrated by simulation that the distributed capacitance of an elevated CPW is four times lower in comparison to a normal CPW at $300GHz$ and the losses are at least divided by two. This new transmission line consisted on an elevated center conductor produced by airbridge fabrication processes as described in reference [RW98].

Apart from coplanar waveguides and finline waveguides, another NLTL configuration using micromachined waveguides has been studied in reference [TSM98]. The use of micromachined waveguides allows the integration of planar and discrete devices in a wide variety of circuit configurations.

In addition, Li *et al.* [LH98, LKH98] explored fully distributed NLTLs. The requirements here are quite different. In past years, microstrip lines and coplanar waveguides, specially microstrip lines, forming a continuous distributed contact to a semiconductor layered substrate have been under study.

Note that GaAs is the dielectric substrate material usually used in CPW-based NLTLs. For MMICs, germanium, silicon and gallium arsenide are the usual semiconductor materials. In 1998, Birk *et al.* [BKW+98] demonstrated the first working NLTL on silicon substrate. More recently, NLTLs have also been fabricated on InP substrate [FDM+01].

II.4 Modeling an NLTL Frequency Multiplier

After this previous description of the two key elements integrating an NLTL, this section will focus on the design of both the lumped nonlinear device and the transmission line, in particular the HBV diode and the CPW.

II.4.1 Harmonic Balance Technique

NLTLs are nonlinear circuits which modeling is not easy. The commercial software package Microwave Design System (MDS) from Hewlett-Packard is able to simulate such structures. Within the MDS harmonic balance simulator, the main limiting factors can be summed up into the number of sections required and the input power applied. However, it is possible to a large extent to avoid convergence problems.

In general, the harmonic balance technique consists in the multi-tone simulation of circuits that exhibit intermodulation frequency conversion, which includes frequency conversion between harmonics. One can determine how many mixing products are to be included in the simulation for each independent source corresponding to a fundamental frequency. The harmonic balance simulation is limited only by practical considerations, such as memory and simulation speed.

Harmonic balance is based on circuit analysis in both time and frequency domains. A generalized partitioning scheme for separating the nonlinear circuit into linear and nonlinear

subcircuits is used. The linear subcircuit is analyzed in the frequency domain, while the non-linear subcircuit is analyzed in the time domain. The harmonic components are extracted from the resulting time domain waveforms using the Fast Fourier Transform (FFT). The harmonic balance simulation is automatically preceded by DC and AC simulations that generate an initial guess. An iterative process is then repeated until the harmonic components converge to their steady-state values using a convergence test.

II.4.2 HBV Diode Model

This section will discuss the design of the diode model within MDS. An HBV diode model to be used in MDS simulations has been developed. The model neglects the leakage current, which is very low in practice, and only takes into account the nonlinear capacitance.

The HBV diode C-V characteristic is modeled using a Symbolically Defined Device (SDD). A quasi-empirical expression for the voltage-charge characteristic of homogeneously doped HBV diodes, derived by Dillner [Dil97], has been used. Besides all the advantages of a physics-based approximate form, it is even preferred to a polynomial function. Indeed, this expression is more stable and has fast convergence, since a polynomial function will require a considerable number of coefficients to obtain a proper fit.

The voltage across the nonlinear capacitor is expressed as a function of its charge as:

$$V(Q) = N\{\frac{bQ}{\epsilon_b A} + 2\frac{sQ}{\epsilon_d A} + Sign(Q)[\frac{Q^2}{2qN_d\epsilon_d A^2} + \frac{4kT}{q}(1 - e^{-\frac{|Q|}{2L_D A q N_d}})]\} \tag{II.4.1}$$

where N is the number of barriers,
b is the barrier thickness,
ϵ_b is the dielectric constant in the barrier material,
A is the device area,
s is the spacer layer thickness,
ϵ_d is the dielectric constant in the modulation layer,
q is the elementary charge,
N_d is the doping concentration in the modulation layer,
k is the Boltzmann constant,
T is the device temperature,
L_D is the extrinsic Debye length.

The fourth term in this modeling equation includes electron screening effects for small bias by introducing the extrinsic Debye length which expression is:

$$L_D = \sqrt{\frac{\epsilon_d kT}{q^2 N_d}} \tag{II.4.2}$$

The C-V characteristic can be directly simulated from expression II.4.1. However, the model requires a two port SDD, since the variables involved are three, the current through the capacitance, the voltage at the terminals of the capacitance and the charge stored in the capacitance, which is the third variable. Thus, port two is necessary to define the current through the capacitance as the derivative of the charge stored with respect to time.

At this stage, the C-V curves are fitted to experimental C-V characteristics. Certain parameters need little adjustment, in particular the barrier thickness and the doping concentration in the modulation layer. The former acts on the capacitance at zero volt bias, while the latter acts on the capacitance modulation.

Figure II.8 shows an excellent agreement between the simulated C-V characteristic and the measured C-V characteristic of a double barrier InP-based HBV diode, once this adjustment has been performed.

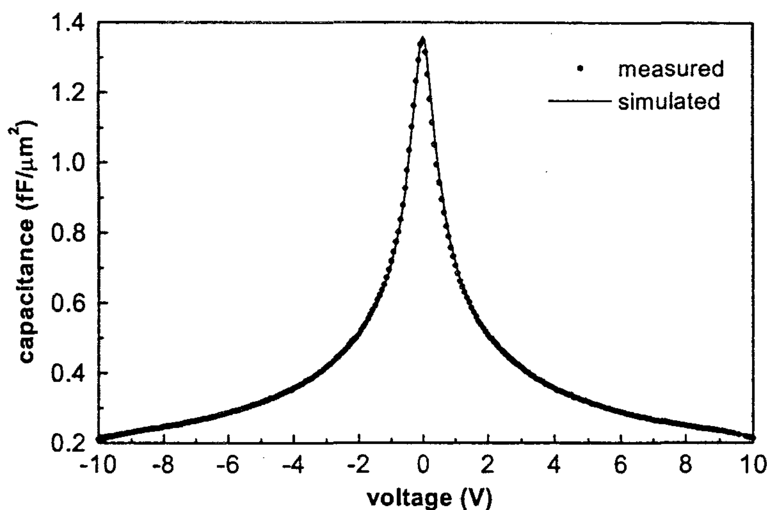

Figure II.8: Measured and simulated capacitance-voltage characteristic of a double barrier InP-based HBV diode

Diode losses are introduced with an equivalent resistance Rs in series with the nonlinear capacitance. Rather than establishing an expression, the resistance is swept accordingly to a safety range, since this parameter is difficult to predict. Also, the increase in HBV diode temperature, due notably to the effects of self-heating, was taken into account by Stake *et al.* [SDJ+98]. In reference [Mél99], a detailed thermal study was performed by Mélique.

Finally, the diode model includes a variable resistance in parallel with the nonlinear capacitance, which is swept from a value that guarantees convergence towards a very high value. This resistance helps the simulator to converge. Indeed, convergence problems are usually related with nonlinear effects. In this sense, the astuteness consists in increasing the nonlinear effects of the circuit progressively during the swept harmonic balance simulation. Thus, the circuit is almost linear at the beginning, as most of the current flows through the parallel resistance. At the end of the sweep, the solution does correspond exactly to the proper design. In between, MDS takes advantage of the previous steps in a recurrent computing process.

This technique provides a further convergence within the MDS harmonic balance simulator.

II.4.3 Electromagnetic Analysis

Most of the transmission lines described in section II.3 have today an equivalent model within MDS. Some of the models are more advanced as regards losses. In particular, the CPW model includes losses, both metallic and dielectric, while the finline model does not. Thus, it is absolutely necessary, in the modeling of a finline-based NLTL, to resort to electromagnetic analysis in order to include the effect of transmission losses in the design. On the other hand, it is also useful to resort to electromagnetic analysis in the modeling of a CPW-based NLTL. In fact, the CPW is wholly modeled using a chain parameter set within MDS. However, design limitations, such as transitions or discontinuities, make the use of electromagnetic tools desirable in any case. In addition, novel transmission lines, in particular the elevated coplanar waveguide, require the use of such tools.

Transmission lines can be analyzed and designed using commercial available high frequency electromagnetic tools. High-Frequency Structure Simulator (HFSS) from Hewlett-Packard is a commercial software package for electromagnetic modeling of passive, three-dimensional structures. It enables to compute Scattering matrix response at a given frequency for mono or multiple mode operations, electric field distributions including far-field antenna radiation patterns and impedance and propagation constants. HFSS solves Maxwell's equations in the frequency domain. The simulation technique used to calculate the full three-dimensional electromagnetic field inside a structure is based on the Finite Element Method (FEM).

Concerning the CPW model, one can create a geometric model of half of the structure only. In fact, the more complex a geometric model is, the greater the requirements for memory and processing power become. In the same way as air bridges eliminate unbalanced modes in the CPW forcing the two ground planes at the same potential, the fact of imposing a perfect H plane of symmetry to the structure leads to the same consequence. The symmetric H boundary condition forces the E field to be tangential and the H field to be normal to that surface. Such models have the same voltage differential but half the power flow of the full structure, resulting in impedances that are twice those for the full structure and thus requiring an impedance multiplier factor. For slot-type structures, such as CPW or finline, the impedance defined as $Z_{pv} = V \cdot V/2P$ is the most appropriate according to the manual of HFSS, where the power and voltage are computed directly from the simulated fields. Figure II.9 shows the simulated S_{11} parameter of a CPW as a function of the frequency for the whole structure and half the structure. For the whole structure, the plotted S_{11} parameter corresponds to the second mode excited, due to the dimensions contemplated, while for half the structure the desired coplanar mode is the first excited.

In the modeling of a finline-based NLTL, it is necessary to use electromagnetic analysis. As it has been just mentioned, the finline model from MDS does not include losses. One can include the effect of transmission losses in the NLTL design by simulating a section of finline in HFSS. Then, by means of a data linear device of two ports convenient for cascading circuits together, the HFSS S-matrix of the section of finline can be exported to MDS. Before the insertion of HFSS S-parameters in MDS, the generalized S-matrix must be first normalized to 50Ω within HFSS. The normalized S-matrix will be generalized within MDS before its use in

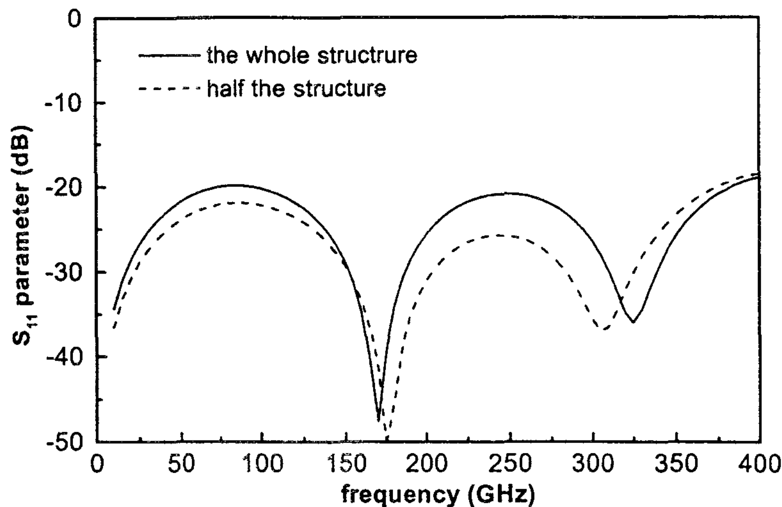

Figure II.9: Magnitude of the S_{11} parameter of a CPW as a function of the frequency for the whole structure and half the structure

the NLTL model.

Finally, note that source lines within HFSS allow internal ports in the structure, in such a way that the whole linear transmission line structure can be simulated within HFSS. Then, the nonlinear devices can be inserted in such ports within MDS, and the NLTL analyzed. However, the number of ports are limited to about ten.

II.5 Conclusion

Schottky diodes have been widely used in NLTLs. However, HBV diodes have demonstrated attractive characteristics in frequency multiplication applications. In particular, record performances in terms of output power and maximum efficiency have been reported by Mélique *et al.* [MMM+99] for a $250GHz$ InP-based HBV tripler. More recently, David *et al.* [DGA+01] have further improved these performances at $290GHz$. Owing to these high performance results, HBV diodes grown on InP substrate have been chosen here to be the nonlinear elements of the NLTLs manufactured.

On the other hand, after a series of preliminary results, one practical approach has been carried out in chapter III (Design Rules for NLTL Harmonic Generation), a CPW-based NLTL. In fact, the CPW-based NLTL design has resulted in a monolithic prototype. Therefore, chapter V (Technology and Characterization of the CPW NLTL) is devoted to the description of the process steps involved in the fabrication of the CPW-based NLTL and its characterization under small signal and large signal conditions. The novelty here arises from the use of InP-based HBV diodes.

Finally, note that a combination of different commercial software packages have been used

in order to analyze and design the NLTL circuits. MDS and HFSS from Hewlett-Packard have supplied complementary insights into circuit and electromagnetic analysis. In addition, Advanced Design System (ADS) from Agilent Technologies has been used in chapter IV in order to perform Large Signal S Parameter simulations for the frequency filtering analysis of a NLTL.

Chapter III

Design Rules for NLTL Harmonic Generation

Chapter III

Design Rules for NLTL Harmonic Generation

III.1 Preliminary Analytical Results

III.1.1 Modeling the NLTL

In order to realize a NonLinear Transmission Line (NLTL), a high impedance transmission line is periodically loaded with varactor diodes, as shown in figure III.1(a). The diodes reduce the characteristic impedance to 50Ω input impedance to improve matching. The equivalent circuit of this NLTL circuit diagram is shown in figure III.1(b).

The most important parameters which are involved in the design of an NLTL are first, those concerning the linear transmission line, its characteristic impedance Z_l and its velocity of propagation v:

$$Z_l = \sqrt{\frac{L_l}{C_l}} \tag{III.1.1}$$

$$v = \frac{d}{\sqrt{L_l C_l}} \tag{III.1.2}$$

where L_l and C_l are respectively the inductance in henrys and the capacitance in farads of the non-loaded transmission line section.

Then, once the nonlinear lumped elements are introduced, d represents the distance between the varactor diodes and C_{ls} the large signal capacitance. Previous theoretical analysis

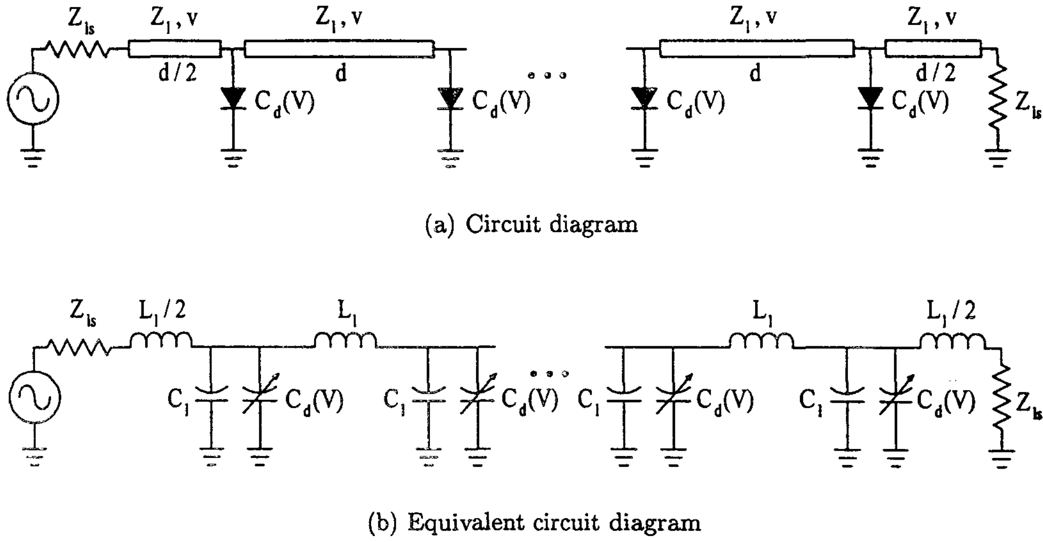

(a) Circuit diagram

(b) Equivalent circuit diagram

Figure III.1: Circuit and equivalent circuit diagrams of an NLTL

of NLTLs conducted by Rodwell *et al.* [RKY+91] introduced the concept of the large signal capacitance which is defined as:

$$C_{ls} = \frac{1}{V_h - V_l} \int_{V_l}^{V_h} C_d(V) dV \tag{III.1.3}$$

where V_h and V_l are the initial and final voltages of the input falling step function.

Finally, the nonlinear transmission line is supplied with a characteristic impedance Z_{ls}, with Z_l higher than Z_{ls}, and a Bragg frequency f_B resulting from the periodicity of the structure. The large signal diode capacitance can be used to represent the voltage dependent diode capacitance $C_d(V)$ in the linear regime. In this way, the large signal characteristic impedance is represented by:

$$Z_{ls} = \sqrt{\frac{L_l}{C_l + C_{ls}}} \tag{III.1.4}$$

And the resulting Bragg frequency in the lumped equivalent model can be expressed as:

$$f_B = \frac{1}{\pi\sqrt{L_l(C_l + C_{ls})}} \tag{III.1.5}$$

Consequently, for a required large signal characteristic impedance and Bragg frequency, the diode spacing must be:

$$\boxed{d = v\frac{Z_{ls}}{Z_l \pi f_B}} \tag{III.1.6}$$

Furthermore, the diodes must be chosen in order to exhibit a large signal capacitance given by the following expression:

$$\boxed{C_{ls} = \frac{1}{Z_{ls}\pi f_B}[1 - \frac{Z_{ls}^2}{Z_l^2}]} \tag{III.1.7}$$

Note that both parameters are expressed as a function of the non-loaded transmission line parameters. Therefore, once the linear transmission line is determined, as well as the parameters of the loaded NLTL, by imposing d and C_{ls} to the structure the design is achieved. The linear transmission line must be periodically loaded respecting the parameter d, while the diode junction area must be chosen to give a large signal capacitance of C_{ls}.

III.1.2 The Semi-Lumped Approach

In a semi-lumped NLTL only varactor diodes are used as lumped elements. This simple structure was proposed for the first time by Jäger and Tegude [JT78] as a high frequency NLTL. The analysis for such a line differs from the one described in section III.1.1, specially in the settling of the Bragg frequency. For the sake of a more accurate representation of the overall behavior of the NLTL, this distributed approach is preferred to the approximate lumped-element equivalent model, as in reference [WH99]. Actually, the approximation only works under the assumption that the per-section capacitance of the line is smaller than the average capacitance of the nonlinear loading devices. This being the case, Martín *et al.* [MFO+01] demonstrated that both models of NLTL for the simulation of frequency multiplication give equivalent results.

In the following, the formalism introduced by Jäger and Tegude [JT78] and adopted by Case in reference [Cas93] will be detailed. Let us consider initially the analysis of the lumped section of figure III.2(a), so that a symmetrical T section results. The wave analysis of periodic structures is described in reference [Col92]. The circuit analysis of a periodic structure involves constructing an equivalent network for a single basic section or unit cell of the structure first.

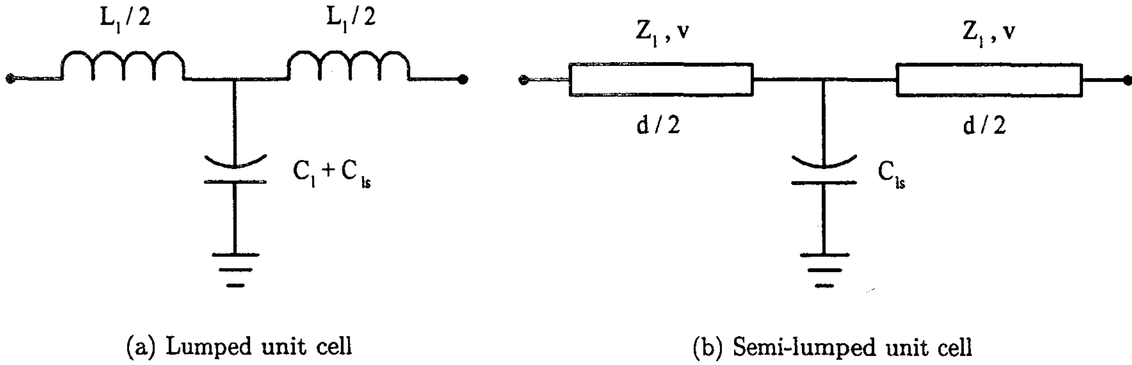

(a) Lumped unit cell

(b) Semi-lumped unit cell

Figure III.2: T models for the NLTL unit cell

The following expression III.1.8 simplifies greatly, analytically as well as practically, the determination of the characteristic impedance of the line:

$$Z_{ls} = \sqrt{Z_{oc} Z_{sc}} \tag{III.1.8}$$

where Z_{oc} and Z_{sc} are respectively the open-circuited impedance and the short-circuited impedance of the section:

$$Z_{oc} = j[\frac{L_l \omega}{2} - \frac{1}{(C_l + C_{ls})\omega}] \tag{III.1.9}$$

$$Z_{sc} = j\frac{L_l \omega}{2} + \frac{\frac{L_l}{2(C_l+C_{ls})}}{j[\frac{L_l \omega}{2} - \frac{1}{(C_l+C_{ls})\omega}]} \tag{III.1.10}$$

The resulting characteristic impedance can be expressed as:

$$Z_{ls} = \sqrt{\frac{1}{(C_l + C_{ls})}[1 - \frac{L_l (C_l + C_{ls})\omega^2}{4}]} \tag{III.1.11}$$

From equation III.1.11, the Bragg frequency of the lumped-element model can be derived. Indeed, if the characteristic impedance is cancelled out, the frequency obtained results in expression III.1.12, corresponding to the Bragg frequency:

$$Z_{ls} = 0 \Longleftrightarrow \omega = \frac{2}{\sqrt{L_l (C_l + C_{ls})}} = \omega_B \tag{III.1.12}$$

Thus, the Bragg frequency is the frequency which cancels out the large signal impedance. Consequently, the Bragg frequency of the semi-lumped model can also be obtained from $Z_{ls} = 0$, but graphically on this occasion. With this intention, the characteristic impedance is derived from the reciprocal two-port transfer matrix of the T section shown in figure III.2(b). The circuit for a unit cell may be broken down into three circuits in cascade, namely, a section of transmission line of length $d/2$, followed by a shunt susceptance, which in turn is followed by another length of transmission line. Transmission matrices (or ABCD matrices) are convenient for cascading circuits together.

For the lossless NLTL cell, the multiplication of:

$$\begin{pmatrix} \cos(\frac{\omega d}{2v}) & jZ_l \sin(\frac{\omega d}{2v}) \\ \frac{j}{Z_l}\sin(\frac{\omega d}{2v}) & \cos(\frac{\omega d}{2v}) \end{pmatrix} \begin{pmatrix} 1 & 0 \\ j\omega C_{ls} & 1 \end{pmatrix} \begin{pmatrix} \cos(\frac{\omega d}{2v}) & jZ_l \sin(\frac{\omega d}{2v}) \\ \frac{j}{Z_l}\sin(\frac{\omega d}{2v}) & \cos(\frac{\omega d}{2v}) \end{pmatrix} \tag{III.1.13}$$

results in the following characteristic ABCD matrix:

$$\begin{pmatrix} \cos(\frac{\omega d}{v}) - \frac{Z_l\omega C_{ls}}{2}\sin(\frac{\omega d}{v}) & jZ_l\sin(\frac{\omega d}{v}) - jZ_l^2\omega C_{ls}\frac{\cos(\frac{\omega d}{v})-1}{2} \\ \frac{j}{Z_l}\sin(\frac{\omega d}{v}) + j\omega C_{ls}\frac{\cos(\frac{\omega d}{v})+1}{2} & \cos(\frac{\omega d}{v}) - \frac{Z_l\omega C_{ls}}{2}\sin(\frac{\omega d}{v}) \end{pmatrix} \tag{III.1.14}$$

From equation III.1.14, the characteristic impedance and propagation constant of the periodic-loaded transmission line are derived. The characteristic impedance can be determined from $Z_{ls} = \sqrt{B/C}$, as a result of according the input impedance as a function of the output impedance, both impedances related to the transmission matrix elements:

$$\boxed{Z_{ls} = Z_l\sqrt{\frac{\sin(\frac{\omega d}{v}) + \frac{\omega Z_l C_{ls}}{2}(\cos(\frac{\omega d}{v}) - 1)}{\sin(\frac{\omega d}{v}) + \frac{\omega Z_l C_{ls}}{2}(\cos(\frac{\omega d}{v}) + 1)}}} \tag{III.1.15}$$

If the periodic structure is able to support a propagating wave, it is necessary for the voltage and current at the $(n+1)^{st}$ terminal to be equal to the voltage and current at the nth terminal, apart from a phase delay due to a finite propagation time. Therefore, the propagation constant can be determined from $\cos(kd) = (A+D)/2$:

$$\boxed{\cos(kd) = \cos(\frac{\omega d}{v}) - \frac{Z_l\omega C_{ls}}{2}\sin(\frac{\omega d}{v})} \tag{III.1.16}$$

where k is the propagation constant for the NLTL cell.

Equations III.1.15 and III.1.11 indicate evident differences between the two circuits. The approximate equivalent circuit is much easier to analyze than the transmission line circuit. However, even if the low frequency characteristics are very similar, the models differ significantly as frequencies approach the Bragg frequency. Figure III.3 shows the graphic determination of the Bragg frequency corresponding to both approaches.

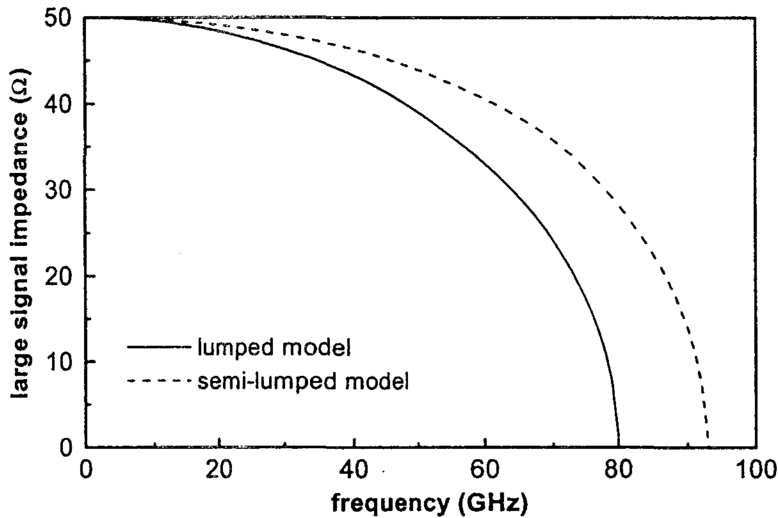

Figure III.3: Characteristic impedance as a function of the frequency for the lumped and semi-lumped model

The example proposed here consists of a high impedance line of characteristic impedance $Z_l = 80\Omega$ loaded at spacings $d = 292\mu m$ by varactor diodes exhibiting a large signal capacitance of $C_{ls} = 48.5fF$. The propagation velocity of the high impedance coplanar waveguide is $v = 1.18 \cdot 10^8 m/s$. The Heinrich program [Hei93] was used in order to work out the characteristics of the CoPlanar Waveguide (CPW), resulting in a line section inductance and capacitance of $L_l = 199pH$ and $C_l = 31fF$ respectively.

For the discrete model the loaded line impedance is zero for a frequency $f = f_B = 80GHz$, while for the semi-lumped model the impedance Z_{ls} falls to zero at a higher frequency. The new Bragg frequency is $f_B = 93GHz$.

At this stage and by means of Microwave Design System (MDS), the S_{21} parameter of an 8-diode structure is shown in figure III.4 for the discrete and semi-lumped models in order to determine by simulation the Bragg frequency corresponding to each approach.

Figure III.4 provides a good agreement between the theoretical and simulated values of Bragg frequency. The simulated Bragg frequencies for the discrete and semi-lumped models correspond to $f_B = 78GHz$ and $f_B = 91GHz$ respectively.

The dispersion relationship of the semi-lumped model has also been deduced. Note the difference between equations III.1.16 and I.2.20 (on page 16). This latter equation could be determined in the same way by comparing the matrix resulting of the three circuits in cascade with the ABCD matrix of a transmission line.

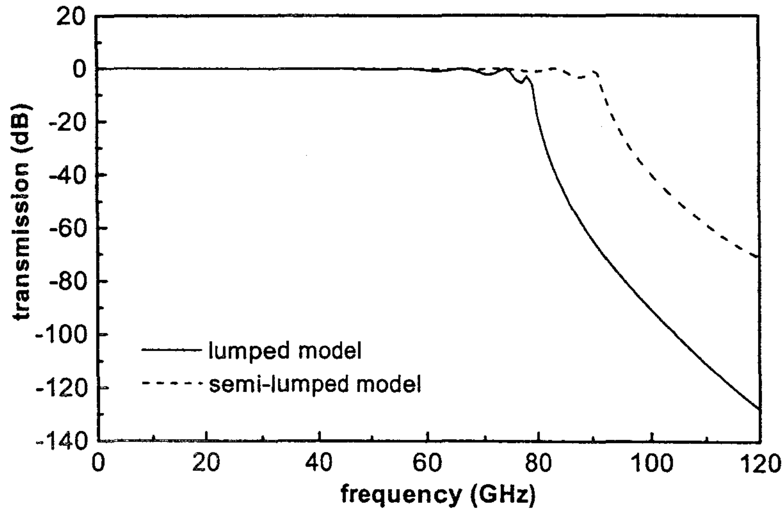

Figure III.4: Magnitude of the S_{21} parameter as a function of the frequency for the lumped and semi-lumped model

Furthermore, it is apparent from equations III.1.15 and III.1.16 that the line will exhibit several pass and stop-bands, frequency bands for which unattenuated propagation can take place separated by frequency bands in which the wave is attenuated. Based on the lumped-element model, an NLTL has the transmission characteristic of a low-pass filter with a cut-off frequency corresponding to the Bragg frequency. In the distributed model, the NLTL behaves like a pass-band filter resulting in a low-pass filter at low frequencies.

III.1.3 Considerations about the Bragg Frequency

The NLTL cell consists of a diode connected between the center conductor and ground at the junction between two sections of transmission line. There are many possibilities for a good layout. The one proposed by Rodwell *et al.* [RKY+91] is shown in figure III.5. The ground planes of a CPW are enlarged towards the center conductor, bringing the diode lower ohmic contacts nearer the center strip in order to decrease the diode series resistance. In addition, the undesired non CPW mode, that is the coplanar strip mode (the two ground planes at different potentials), is suppressed by interconnecting the two grounds together.

The periodicity of such a structure provides a resonance frequency given by:

$$f_R = \frac{1}{2d\sqrt{lc}} \qquad \text{(III.1.17)}$$

This resonance frequency results from the linear dispersion equation $k = \omega\sqrt{lc}$ (I.2.22 on page 17) by imposing $kd = \pi$, namely $d = \lambda/2$, while the Bragg frequency is obtained from the dispersion equation $\omega^2 d^2 = 2(1 - \cos kd)/(lc)$ (I.2.20 on page 16) by imposing the same

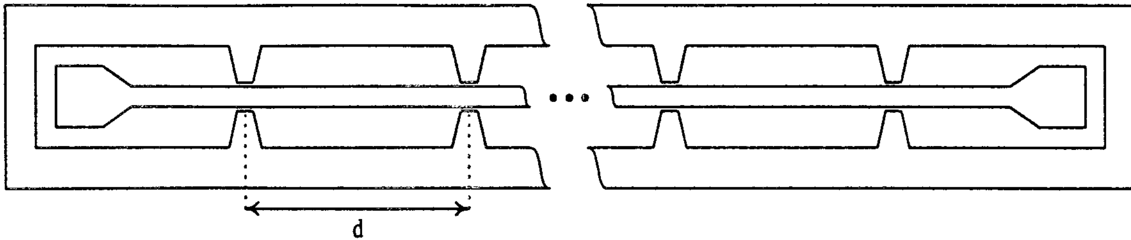

Figure III.5: Layout of a CPW for an NLTL configuration

condition. This way of determining the Bragg frequency was seen in section I.2.2, resulting in:

$$f_B = \frac{1}{\pi d\sqrt{lc}} \tag{III.1.18}$$

First of all, two simulations based on the periodic structure of figure III.5, have been performed by means of the network analysis code MDS with subsequent verification through High-Frequency Structure Simulator (HFSS) electromagnetic simulations. A unit cell of figure III.5, corresponding to half the structure in the longitudinal dimension, is depicted in figure III.8(a), where the length and the width of the discontinuity are also represented. The results show that the location of the resonance frequency depends exclusively on the inductance and capacitance per unit length of the CPW and the distance d between discontinuities. The length or width of the discontinuity do not affect the value of the resonance frequency but the transmission characteristic, so that the longer or the larger the discontinuity is, the worst transmission is obtained at this frequency. This is shown in figures III.6 and III.7 respectively.

In this example, the simulated $f_R = 208GHz$ is in good agreement with the calculated $f_R = 201GHz$.

At this stage, let us introduce the varactor diodes at the discontinuities. Thus, the unit cell of figure III.8(a) results in that of figure III.8(c). In addition, figure III.8(c) shows a more realistic representation of the semi-lumped NLTL unit cell than that of figure III.8(b), as the ground planes of the CPW are enlarged towards the center conductor as in figure III.8(a). From the results plotted in figure III.9, it can be stated that the two models differ at high frequencies well above the Bragg frequency. Consequently, it is not worthwhile to consider the semi-lumped NLTL unit cell of figure III.8(c) in future simulations, but that of figure III.8(b)
.

Finally, the phase of the S_{21} parameter is plotted as a function of the frequency for the cases of figures III.8(a) and III.8(b). Indeed, figure III.10 shows that the propagation constant is more linear in the case of figure III.8(a), so the semi-lumped unit cell of figure III.8(b) represents a more dispersive situation.

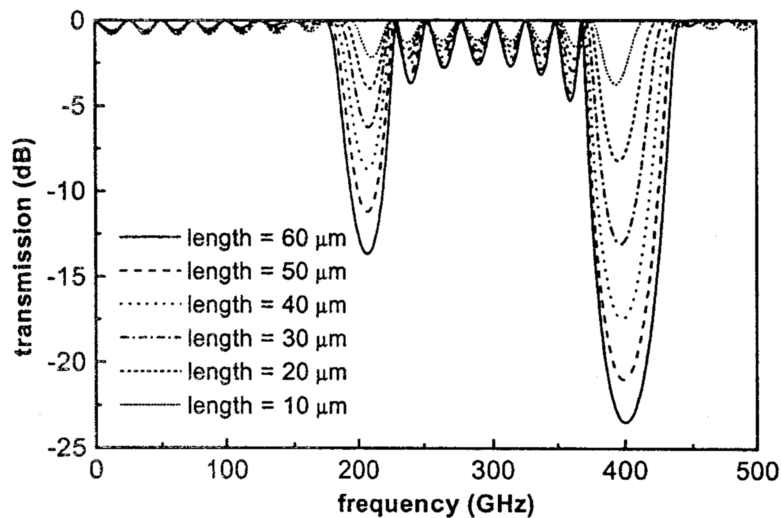

Figure III.6: Magnitude of the S_{21} parameter as a function of the frequency varying the length of the discontinuity

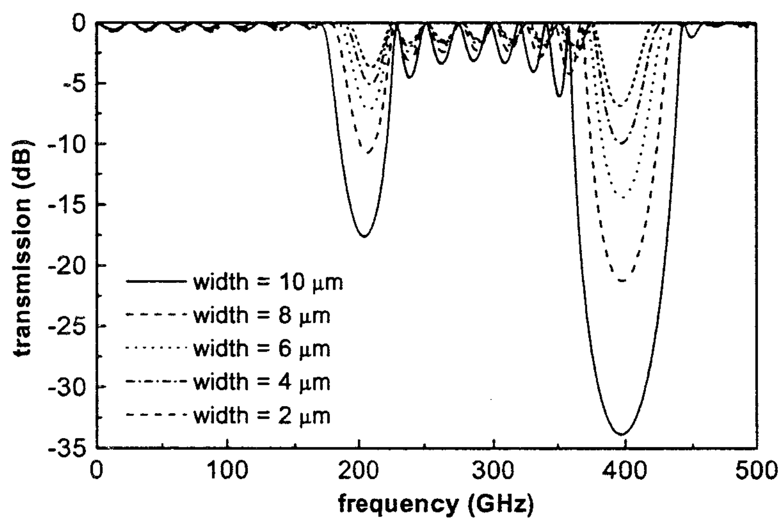

Figure III.7: Magnitude of the S_{21} parameter as a function of the frequency varying the width of the discontinuity

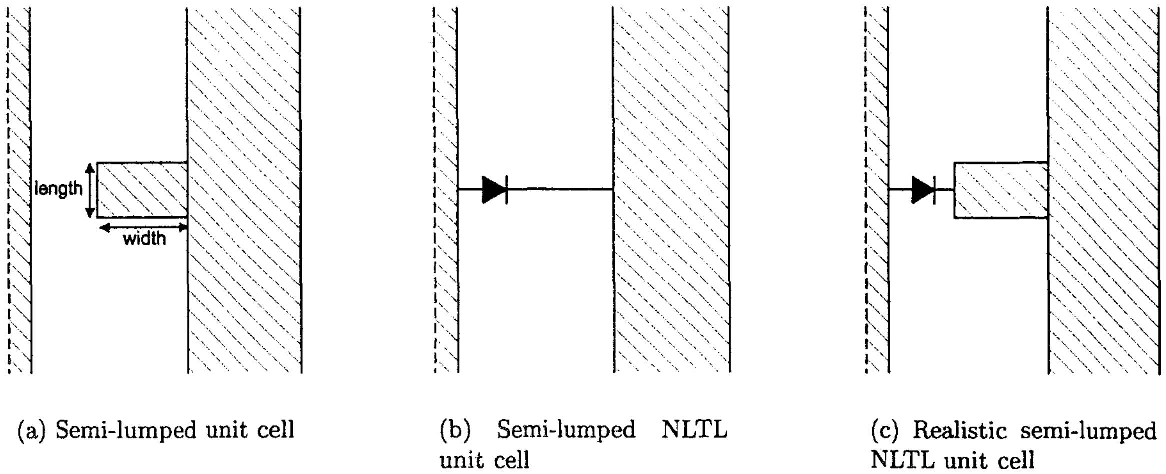

(a) Semi-lumped unit cell

(b) Semi-lumped NLTL unit cell

(c) Realistic semi-lumped NLTL unit cell

Figure III.8: Three different semi-lumped unit cells

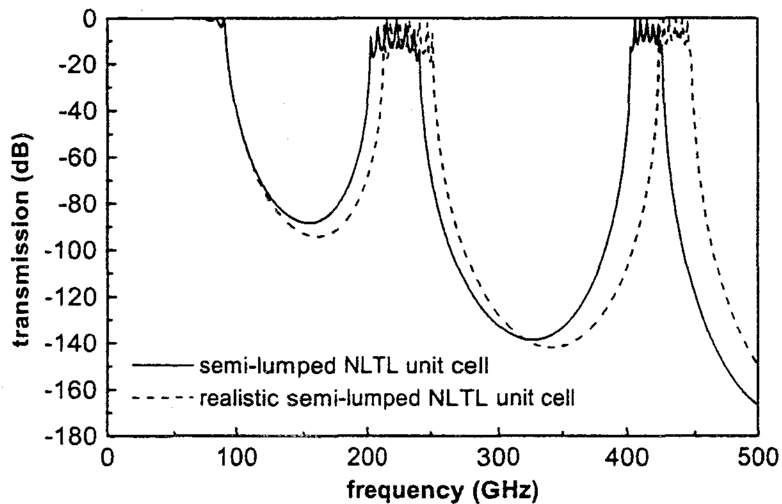

Figure III.9: Magnitude of the S_{21} parameter as a function of the frequency for the cases of figures III.8(b) and III.8(c)

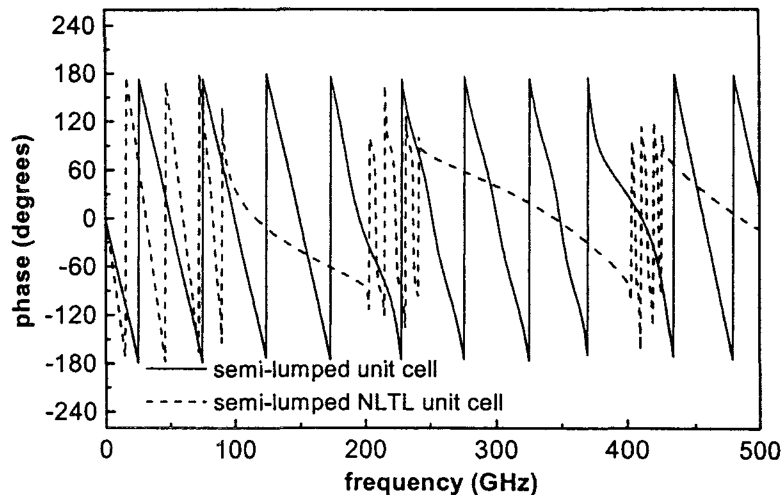

Figure III.10: Phase of the S_{21} parameter as a function of the frequency for the cases of figures III.8(a) and III.8(b)

III.2 Harmonic Generation

III.2.1 Generalities

NLTL harmonic generation can be described in terms of large signal nonlinear propagation and the resulting generation of sets of solitons. In this way, a waveform of multiple solitons per cycle is progressively produced, and hence harmonic generation achieved, as the shape of the wave may be related to its equivalent frequency components by Fourier analysis. Since frequency multipliers rely on the interaction between two or more solitons, this type of NLTL is quite difficult to understand in terms of soliton-like propagation.

This phenomenon can be observed by introducing an input sinusoidal signal. The voltage variation of the NLTL capacitance results in nonlinear wave propagation and harmonics of the input frequency are generated. The harmonic components generated accompany the diminishing fundamental component along the transmission line. As the waveform propagates, the distortion will increase. Moreover, harmonics at frequencies higher than the Bragg frequency do not propagate along the line. This effect can be used to select an output frequency.

As it has been already seen in section I.3, the type of NLTL can be determined depending on the f_B to f_{in} ratio. The Bragg frequency will set the peak conversion efficiency as well as the impulse transition time or the pulse width. Although the main parameter involved in the design of NLTL frequency multipliers is the f_B/f_{in} ratio, the Z_l/Z_{ls} ratio plays also an important role in the design of such a line. Other issues affecting conversion efficiency are impedance matching and driven amplitude related to the voltage dependent capacitance characteristic of the diodes, which will be discussed later on. Loss plays also a significant role in frequency multiplier NLTLs.

III.2.2 The Bragg Frequency

The order of harmonic conversion is related to the f_B/f_{in} ratio. The results of scanning the frequency of the input sine-wave in order to study conversion efficiency for the first three non-zero harmonics are plotted in figure III.11.

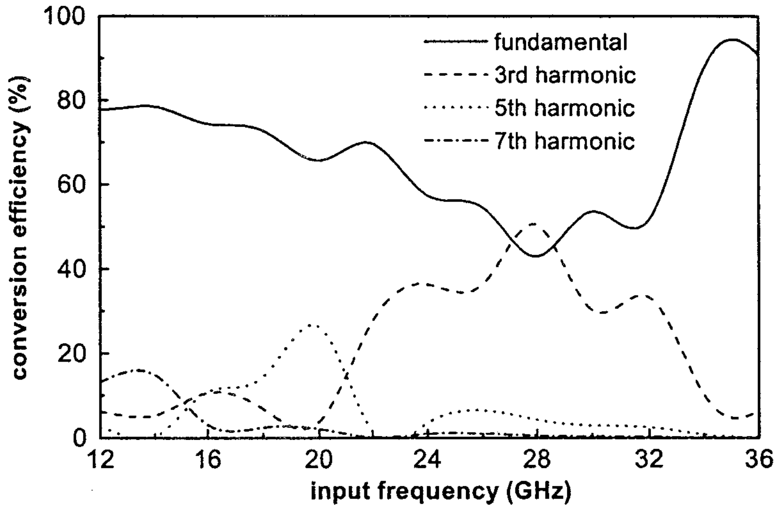

Figure III.11: Conversion efficiency as a function of the input frequency for the fundamental and the three first non-zero harmonics

The example proposed consists of a ladder-type LC circuit containing constant inductors of $L_l = 132.6pH$ and constant capacitors of $C_l = 20.7fF$, the latter in parallel with voltage dependent capacitors exhibiting a large signal capacitance of $C_{l_s} = 32.3fF$. These parameters result in a Bragg frequency of $120GHz$. A harmonic balance simulation has then been performed for a $3.3mm$ line length. Note that a $20dBm$ input power has been chosen to drive the circuit.

Although an NLTL harmonic multiplier could be theoretically used as any order converter, figure III.11 also shows that the optimum efficiency decreases for a higher harmonic. A higher f_B/f_{in} ratio means that more harmonics are involved in the multiplication process, but also implies the distribution of the energy over all these harmonics. Actually, to avoid power conversion into harmonics higher than desired, the Bragg frequency is set a few percent above the desired output frequency. Aspects about the safeguard taken in the specification of the optimum ratio between the Bragg frequency and the input frequency will be discussed in chapter IV (Large Signal S Parameter Simulation of an NLTL).

According to this, conversion to the third harmonic is most efficient in the frequency band where the fifth harmonic is above the Bragg frequency and the third harmonic is, of course, below the Bragg frequency, namely $3f_{in} < f_B < 5f_{in}$.

III.2.3 The Characteristic Impedance

By using equations III.1.6 and III.1.7 one can derive the diode spacing and the large signal diode capacitance for a required loaded transmission line impedance and Bragg frequency, as seen in section III.1.1. The values of Z_{ls} and f_B are fixed to 50Ω and $120GHz$ respectively. The choice of the large signal impedance in a MMIC-like technology (Monolithic Microwave Integrated Circuit) is usually 50Ω in order to make sure of a good matching with the input generator. Therefore, table III.1 is obtained for different values of non-loaded transmission line impedance, with $Z_l > Z_{ls}$. The calculations have been made assuming the propagation velocity resulting of a GaAs transmission medium, namely $v = 0.83 \cdot 10^8 m/s$.

$Z_l(\Omega)$	80	100	120	140	160	180	200	220
$d(\mu m)$	138.4	110.7	92.3	79.1	69.2	61.5	55.4	50.3
$C_{ls}(fF)$	32.3	39.8	43.8	46.3	47.9	49	49.7	50.3
$C_l(fF)$	20.7	13.3	9.2	6.8	5.2	4.1	3.3	2.7
$L_l(pH)$	132.6	132.6	132.6	132.6	132.6	132.6	132.6	132.6

Table III.1: Circuit parameters for different values of non-loaded transmission line impedance

Table III.1 shows that the higher the Z_l/Z_{ls} ratio, the lower the distance between the diodes and the higher the diode area. It is thus advantageous to work at high impedances as it implies a reduction of both transmission losses and diode losses, and efficient conversion requires low loss. However, reaching such non-loaded transmission line impedances is difficult in practice for certain technologies, such as CPWs, and a compromised value of Z_l must be chosen.

The choice of the characteristic impedance is critical in the design of an NLTL. This issue was fully addressed in reference [JFT+99] by using a simulation approach that included the skin effect losses of a CPW pulse compressor.

A harmonic balance simulation has been performed corresponding to the discrete approach, where the line section capacitance and inductance have also been derived in the table. Furthermore, the diode junction area has been chosen to give the large signal capacitance also specified thanks to a single barrier Heterostructure Barrier Varactor (HBV) diode of $Cmax = 2fF/\mu m^2$ and a $Cmax/Cmin$ ratio equal to 5.

Figure III.12 (on pages 65 and 66) shows the evolution of the simulated harmonic output power as a function of the number of diodes for different non-loaded transmission line impedances. The input frequency has been fixed to $20GHz$. This being the case, the fifth harmonic prevails initially. Later on with the distance, an inversion between the fifth and third harmonic trends can be observed.

For harmonic generation applications, one is primarily concerned with the harmonic conversion efficiency. From the results of figure III.12, it can be stated that an increase in the Z_l/Z_{ls} ratio not only leads to a reduction of both transmission and diode losses, but also to an improved performance in the efficiency conversion of the initially prevailing harmonic with respect to the number of sections. Actually, the peak conversion efficiency grows from 26% of the $20dBm$ input power in the case $Z_l = 80\Omega$ to 44% in the case $Z_l = 220\Omega$.

This behavior is not surprising as the Z_l/Z_{ls} ratio is related to the compression rate defined by Rodwell *et al.* [RKY+91] as the fall time compression rate normalized to the propagation delay of the non-loaded transmission line:

$$\kappa = \frac{T_{max} - T_{min}}{T} = \frac{\sqrt{L_l(C_l + C_d(V_h))} - \sqrt{L_l(C_l + C_d(V_l))}}{\sqrt{L_l C_l}} \tag{III.2.1}$$

$$\kappa = \sqrt{\xi}\left(\sqrt{\frac{1}{\xi} + \frac{C_d(V_h)}{C_{ls}}} - \sqrt{\frac{1}{\xi} + \frac{C_d(V_l)}{C_{ls}}}\right) \tag{III.2.2}$$

where

$$\xi = \frac{C_{ls}}{C_l} = \frac{Z_l^2}{Z_{ls}^2} - 1 \tag{III.2.3}$$

In this way, Rodwell *et al.* recommended in reference [RAY+94] to have $Z_l > 75\Omega$, such that the diode capacitance is still dominant over the CPW capacitance. Even though this normalized fall time compression rate is defined for an input falling step function, the concept can be applied to an input sinusoidal function and harmonic generation.

The peak conversion efficiency to the fifth harmonic occurs along the line after a number of nonlinear devices relatively constant, in fact between 24 and 28 diodes. However, the real transmission line length decreases from $3.3mm$ in the case $Z_l = 80\Omega$ to $1.4mm$ in the case $Z_l = 220\Omega$. Actually, when the compression rate is not sufficiently strong to efficiently compress the wave, a longer line is required and, as a result, additional losses are introduced.

Table III.2 summarizes the most salient results for each value of Z_l, namely, the conversion efficiency peak corresponding to the fifth harmonic and the distance from the input of the NLTL at which this peak is obtained. Note a saturation of the conversion efficiency above $Z_l = 140\Omega$.

On the other hand, line lengths can be adjusted to get the best conversion efficiency for a required harmonic. Furthermore, although the order of harmonic conversion is related to the f_B/f_{in} ratio, the line length plays an important role in which order of harmonic is emphasized. From this point of view, as the line length must be minimized because of transmission losses, the best conversion efficiency to the third harmonic is still obtained when the required harmonic is firstly predominant. If the line is too short, solitons will not separate completely. However, since the driven amplitude is repetitive, solitons will be combined if the line is too

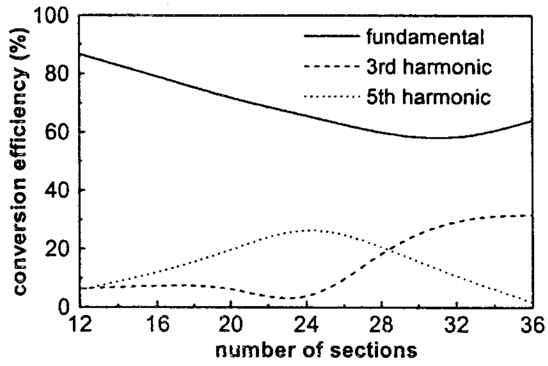

(a) $Z_l = 80\Omega$

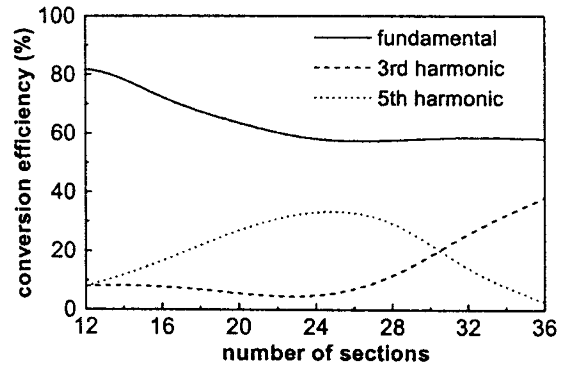

(b) $Z_l = 100\Omega$

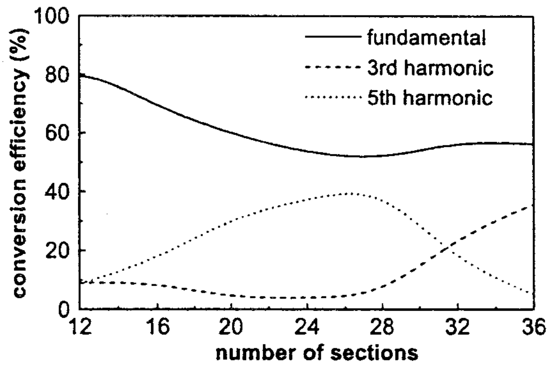

(c) $Z_l = 120\Omega$

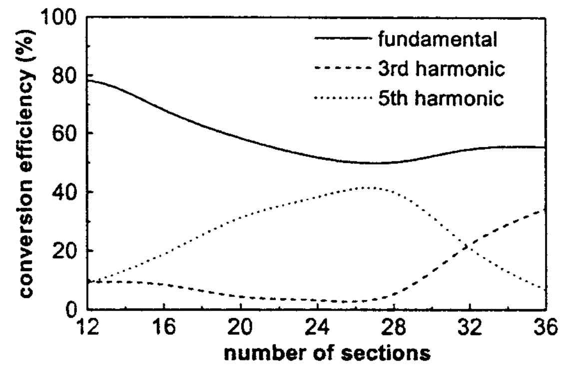

(d) $Z_l = 140\Omega$

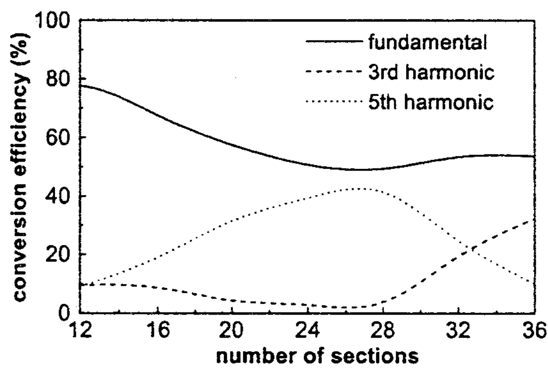

(e) $Z_l = 160\Omega$

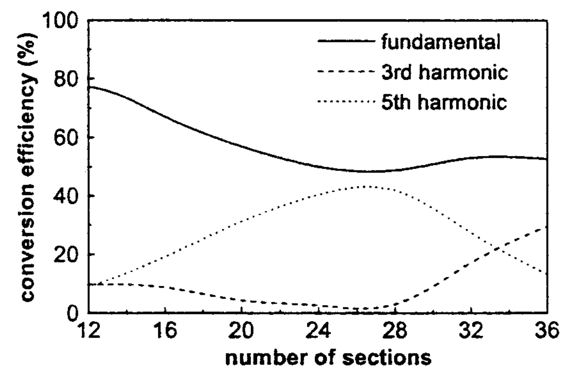

(f) $Z_l = 180\Omega$

Figure III.12: Conversion efficiency as a function of the number of sections for the fundamental and the two first non-zero harmonics varying the Z_l/Z_{ls} ratio

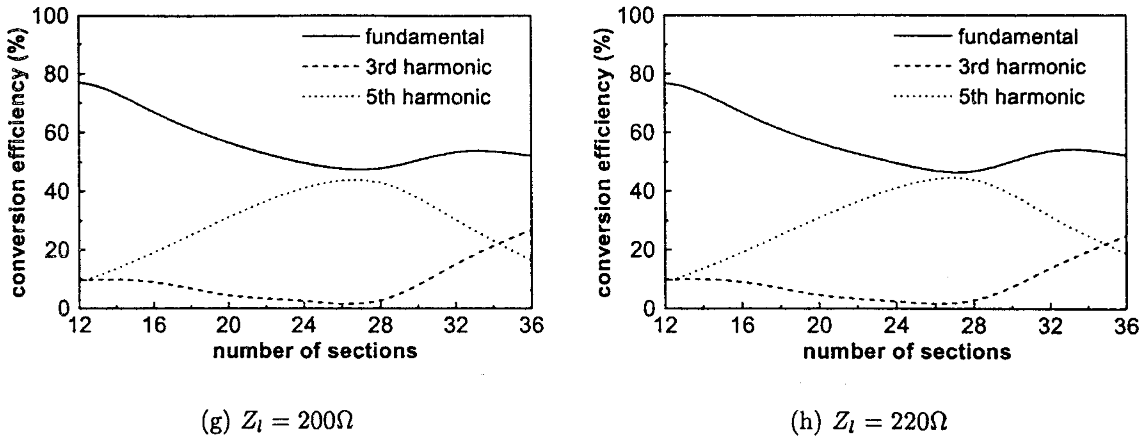

(g) $Z_l = 200\Omega$

(h) $Z_l = 220\Omega$

Figure III.12: (continued)

$Z_l(\Omega)$	80	100	120	140	160	180	200	220
$P_{out}/P_{in}(\%)$	26.288	32.979	37.308	39.972	41.357	41.966	42.833	43.783
$l(mm)$	3.322	2.657	2.215	2.215	1.938	1.722	1.551	1.408

Table III.2: The most salient results for each value of non-loaded transmission line impedance

long, originating a certain periodicity with distance concerning which order of harmonic is emphasized.

In reference [LFM+99], Lheurette *et al.* investigated the potential of NLTLs for harmonic generation on the basis of experimental capacitance and current-voltage characteristics of high performance InP-based HBV diodes. A large harmonic content in the propagating signal can be achieved depending on the number of cascaded sections, enabling the design of high efficiency quintuplers.

III.3 One Particular Approach: The MULTIS Project

III.3.1 Study Context

The following study was carried out within the MULTIS (MUltiplicateur à Lignes de Transmission Intégrant des hétérostructures de Semiconducteurs) project research context. In particular, the aim of this project is to prove the potential of NLTLs for frequency multiplication

applications on the basis of InP-based HBV diodes.

On the modeling side, the following sections are devoted to the study of a V-band frequency multiplier operating at $60GHz$. In addition, reference [DFF+01] provides complementary information. Let us recall that this project was carried out within the framework of a CNRS (Centre National de la Recherche Scientifique) Télécom contract in collaboration with the Laboratory of Microwaves and Characterization at the University of Savoie, France.

In practice, the design of the CPW-based NLTL multiplier has resulted in a monolithic prototype. Thus, chapter V (Technology and Characterization of the CPW NLTL) and reference [FDM+01] provide a description of the different steps involved in the prototype fabrication process and its characterization under small signal and large signal conditions.

III.3.2 Configuration

Figure III.13 shows the configuration chosen which will be justified throughout this section.

Considering the previously mentioned definition, a non-loaded transmission line and a nonlinear device are the two key elements integrating an NLTL, a CPW and an InP-based HBV diode in the present case.

The NLTL is fabricated on a semi-insulating InP epitaxial wafer. The CPW center strip is composed of the active epitaxial structure depicted in figure V.1 (on page 104), corresponding to a double barrier InP-based HBV diode. Different from the configuration proposed in figure III.5, the diodes are simply positioned within the center strip by means of trapezoidal-shaped access areas realized in the highly doped n^+ buried layer. All these configuration aspects will be discussed in detail in chapter V, devoted partly to the fabrication techniques, as well as the severe under-etching effect providing air gaps under the center strip, as shown in the cross sectional view A-A' of figure III.13.

III.3.3 Parameters

The values of Z_{ls} and f_B are fixed to 50Ω and $80GHz$ respectively. By using equations III.1.6 and III.1.7 one can derive table III.3, where Z_l has been fixed to 80Ω. Note that the calculations have been made assuming a 6.5 effective dielectric constant stemming from the Heinrich program [Hei93] and a resulting propagation velocity of $v = 1.17 \cdot 10^8 m/s$.

$Z_{ls}(\Omega)$	$f_B(GHz)$	$Z_l(\Omega)$	$d(\mu m)$	$C_{ls}(fF)$
50	80	80	292.4	48.5

Table III.3: Circuit parameters of the NLTL

Before going on, note that the choice of a $80GHz$ Bragg frequency can be justified as

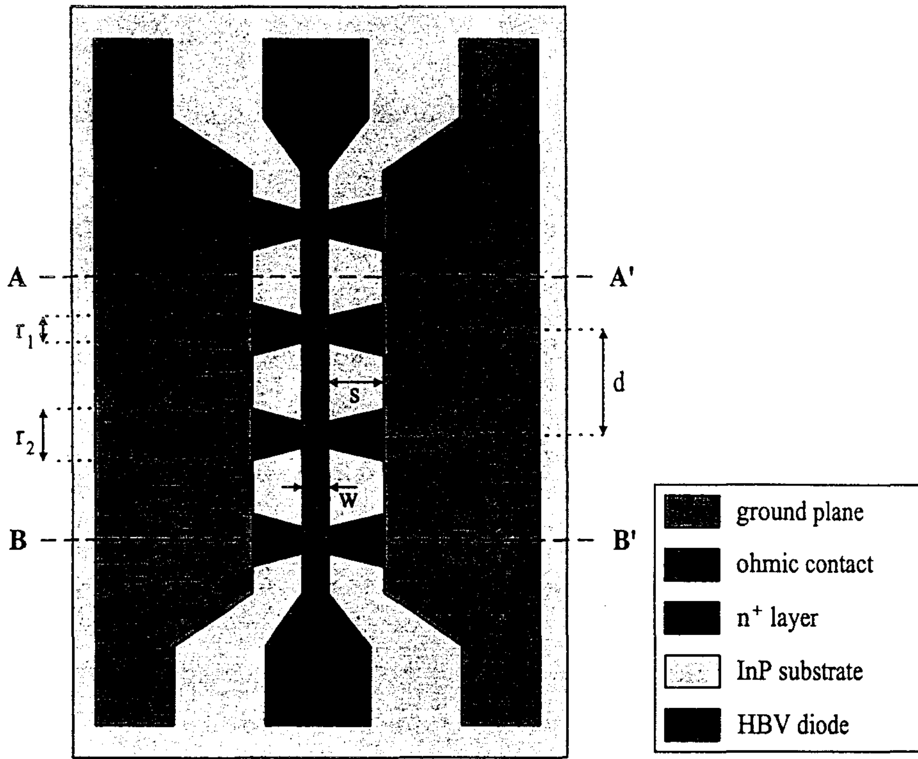

(a) Top view

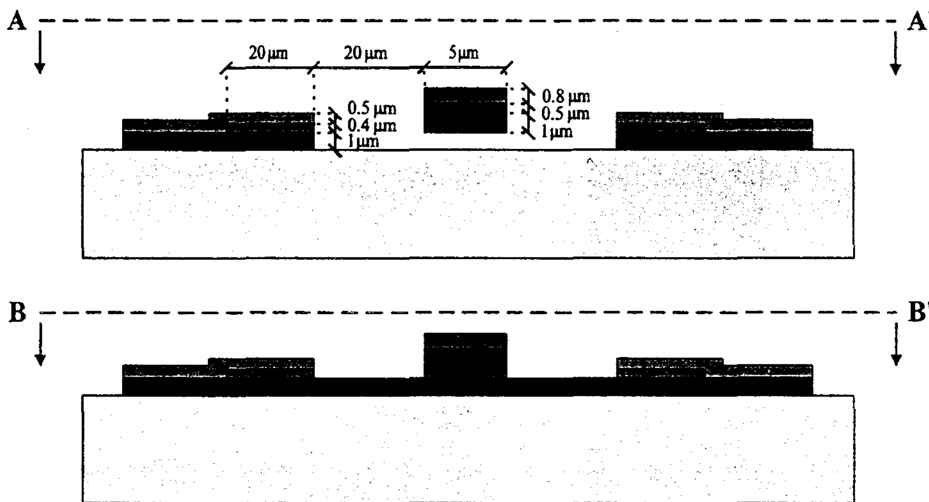

(b) Transverse cross sectional views

Figure III.13: Top view and transverse cross sectional views of a CPW NLTL

follows. The targeted device being a V-band frequency multiplier prototype operating at $60GHz$, a range extending from $60GHz$ to $100GHz$ is possible at first glance for the Bragg frequency, where conversion to the third harmonic is most efficient. In table III.4, the diode spacing and the large signal diode capacitance are reported for a required Bragg frequency in this range. The loaded impedance line and the non-loaded impedance line have been set to 50Ω and 80Ω respectively. From the results shown in table III.4, it seems interesting, in terms of transmission losses, to choose a Bragg frequency as high as possible, since the higher this frequency, the smaller the distance between the diodes. However, a Bragg frequency of $80GHz$ has been finally determined. In fact, the diode spacing and the large signal diode capacitance have been calculated from the lumped model. As it is shown in figure III.3, the large signal impedance falls to zero at a higher frequency for the semi-lumped model. The new Bragg frequency is $f_B = 93GHz$, which is still a value below the fifth harmonic. A more accurate analysis of the choice of the Bragg frequency value will be carried out in chapter IV.

$f_B(GHz)$	60	64	68	72	76	80
$d(\mu m)$	389.9	365.6	344.1	324.9	307.8	292.4
$C_{ls}(fF)$	64.7	60.6	57	53.9	51	48.5

$f_B(GHz)$	84	88	92	96	100
$d(\mu m)$	278.5	265.9	254.3	243.7	234
$C_{ls}(fF)$	46.2	44.1	42.2	40.4	38.8

Table III.4: Circuit parameters for different values of Bragg frequency

The Heinrich program can be used in order to work out the characteristics of the 80Ω non-loaded impedance CPW. The most interesting parameters are summarized in table III.5.

$Z_l(\Omega)$	$w(\mu m)$	$s(\mu m)$	ϵ_{eff}
80	5	20	6.5

Table III.5: Physic parameters of the CPW (see figure III.13(a))

Figure III.14 shows a top view diagram of the CPW NLTL and its equivalent loss circuit. The transmission line lumped elements are displayed in table III.6, assuming both metallic and dielectric losses. Thus, the effects of non-ideal conductors, as well as substrate loss and finite metallization thickness, are included.

$Z_l(\Omega)$	$L_l(pF)$	$C_l(fF)$	$R_l(\Omega)$	$G_l(\Omega)$
80	199	31.2	3.8	312500

Table III.6: Line elements of the CPW (see figure III.14)

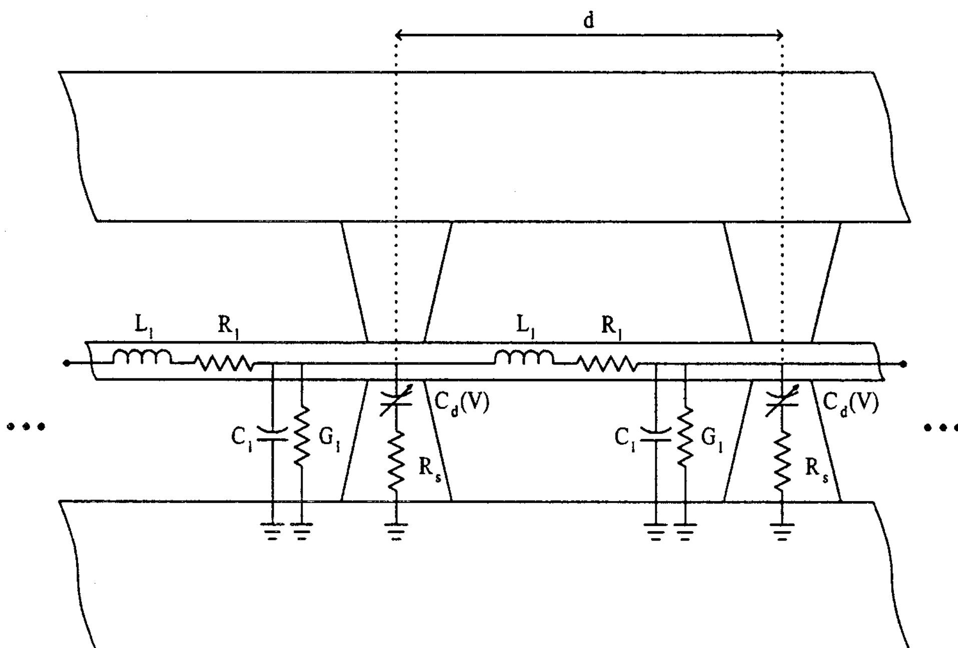

Figure III.14: Diagram of the CPW NLTL and its equivalent loss circuit

Moreover, note that the Heinrich program allows us to perform a frequency sweep, so as a description of the CPW as a function of the frequency can be easily obtained. Figure III.15 shows the input and output data at $60GHz$, the frequency at which these parameters have been calculated.

```
------------------------------------------------------------
Geometry (microns):
w  =  5.000D+00    s  =  2.000D+01    t =  1.000D+00
wg =  9.000D+01    hs =  4.000D+02
------------------------------------------------------------
Material Parameters:
substrate: eps(r) =   12.6        tan(de) =  3.000D-04
conductivity of metallizations:    kappa =  3.000D+07
------------------------------------------------------------

------------------------------------------------------------
Frequency: f =  6.000D+01 GHz

Line Elements:
inductance  L =  6.803D-07 Henry/m
capacitance C =  1.066D-10 Farad/m
resistance  R =  1.294D+04 Ohm/m
conductance G =  1.103D-02 Siemens/m  (mho/m)

Propagation Constants:
er(eff)       = 6.52435D+00       alpha   = 7.07094D-01 db/mm
beta          = 3.21203D+03 1/m   alpha   = 8.14072D+01 1/m
beta/beta(0) = 2.55428D+00

Characteristic Impedance:
Real(Z)       = 7.98958D+01 Ohm   Imag(Z) =-2.00300D+00 Ohm

------------------------------------------------------------
```

Figure III.15: Heinrich program input and output data

III.3.4 Electromagnetic Analysis

In order to further establish the CPW characteristics, one can simulate, by means of the electromagnetic code HFSS, an 8 times $292\mu m$ long structure with a cross sectional view all along the structure AA', as the one depicted in figure III.13(b). Simulation results of the transmission characteristics showed that the existence of the active layer under the center strip and the n^+ layer under the ground planes do not affect considerably the CPW characteristics.

The sequence of layers composing the diode, with an overall height of $0.95\mu m$, has been substituted by a layer of III-V GaAs/InP compounds, which has a typical dielectric constant of 13 and a loss tangent around 0.0016. Concerning the other layers, the gold resistivity

and the semiconductor highly doped n^+ layer resistivity have been fixed to $2.2 \cdot 10^{-8}\Omega m$ and $3.1 \cdot 10^{-6}\Omega m$ respectively.

The same structure with the two n^+ layers sandwiching the active layer has also been simulated. The former structure exhibits a characteristic impedance of 87.65Ω, while a characteristic impedance of 79.89Ω has been obtained for the latter structure. This impedance matches the 80Ω impedance announced by the Heinrich program. Indeed, the lower n^+ layer under the center strip acts as the center conductor itself. However, the former structure corresponds to an elevated center conductor CPW. The properties of such lines have been studied in detail in references [HW96, RW98]. In particular, Reichelt and Wolff [RW98] showed a considerable increase in the characteristic impedance. They also pointed out that coplanar-like waveguides with an elevated center conductor exhibit low loss and low dispersion. However, it should be noted that the elevation of the center conductor was more important than in the present work.

The simulation results of the whole structure, namely including the input and output 50Ω CPW access lines, are now presented. The center strip width and the slot width of the CPW access line have been set to $70\mu m$ and $50\mu m$ respectively. A linear transition from the access line to the high impedance line has been considered, providing a gradual variation of the taper geometry.

The characteristic impedance at the input of the structure is plotted in figure III.16 as a function of the frequency for both configurations, with and without the highly doped n^+ lower layer under the center strip.

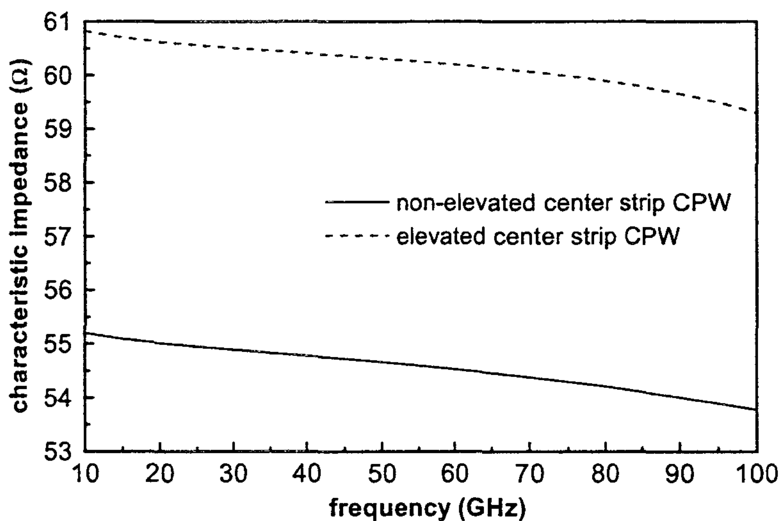

Figure III.16: Characteristic impedance as a function of the frequency for the non-elevated and elevated center strip HFSS CPW

The comparison between both configurations concerning the S_{21} parameter and S_{11} parameter is shown in figures III.17(a) and III.17(b) respectively.

Finally, even though HFSS can not consider the diode as an active element but rather as

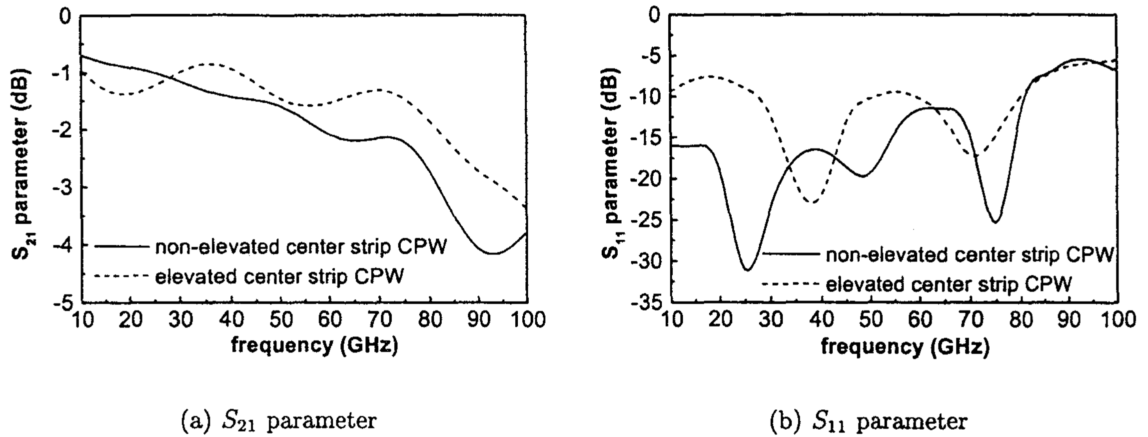

(a) S_{21} parameter

(b) S_{11} parameter

Figure III.17: Magnitude of the S_{21} and S_{11} parameters as a function of the frequency for the non-elevated and elevated center strip HFSS CPW

some stacked dielectric layers, it may be interesting to analyze the influence of the n^+ access areas in the transmission characteristics of the CPW. For this reason, the n^+ access areas, allowing us to link the 8 diodes to the transmission line which was analyzed previously, have been included locally (BB' transverse cross section). The S_{21} and S_{11} parameters are plotted in figure III.18. The comparison of the S parameters between the structures with and without the n^+ access areas is shown in figure III.19.

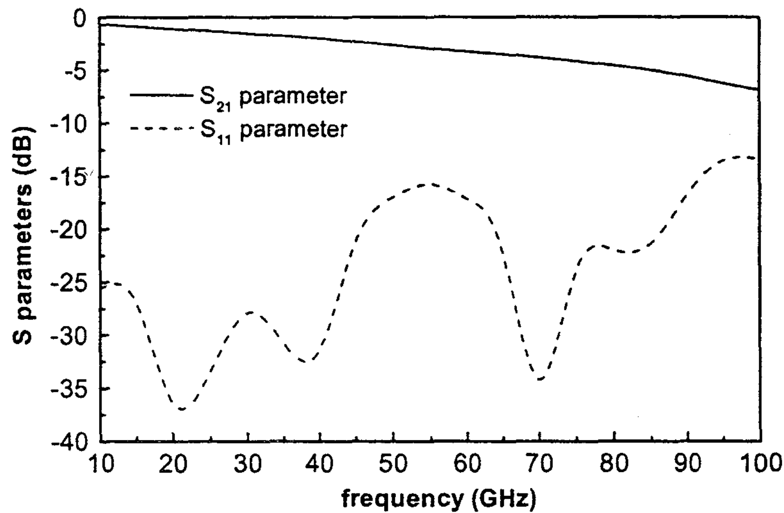

Figure III.18: Magnitude of the S parameters as a function of the frequency for the HFSS CPW with n^+ access areas

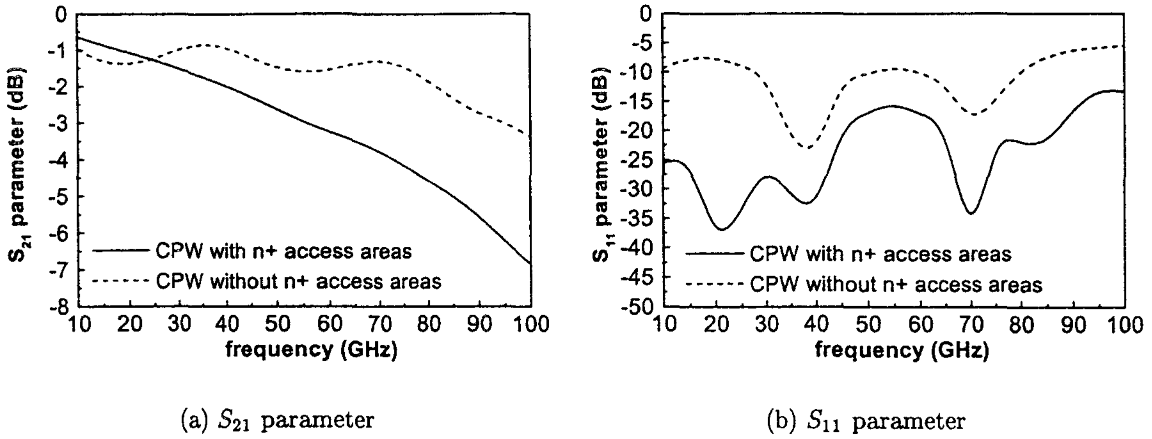

(a) S_{21} parameter

(b) S_{11} parameter

Figure III.19: Magnitude of the S_{21} and S_{11} parameters as a function of the frequency for the HFSS CPW with and without n^+ access areas

III.3.5 Network Analysis

The number of sections, the diode nonlinear capacitance and the pump frequency affect the power transferred to higher order harmonics in a complicated manner. Figures III.20, III.21 and III.22 have been obtained varying the diode area and keeping constant the other parameters. Each curve corresponds to a different diode number structure.

First, the semi-lumped NLTL has been pumped by a $30dBm$ $20GHz$ sinusoidal signal to study the effect of dynamic voltage range on the NLTL performance for a tripler configuration. Figure III.20 shows that different optimum areas result of diode number variation. Thus, a maximum conversion efficiency to the third harmonic is obtained for a diode area equal to $210\mu m^2$ in the case of a 10-diode structure, for a diode area equal to $180\mu m^2$ in the case of a 15-diode structure and for a diode area equal to $160\mu m^2$ in the case of a 20-diode structure.

On the other hand, the $30dBm$ input power brings about a peak driven amplitude of $10V$. With such a change in the amplitude, the double barrier HBV diode displays a capacitance per unit area of $0.47fF/\mu m^2$. As a consequence, one can determine the diode area optimized for a 50Ω input impedance by simply dividing the calculated value of the large signal capacitance by the capacitance per unit area regarding the chosen diode. Neglecting the fact that the voltage sweep across successive diodes changes due to nonlinear wave propagation, the optimum diode area has been estimated at $100\mu m^2$. However, the curves in figure III.20 show a shift in the optimum diode area. Note that, as the number of diodes is increased, the conversion efficiency is improved. Besides, the simulated optimum diode area tends to fit the calculated one.

In figures III.21 and III.22, a $30dBm$ $12GHz$ sinusoidal signal has been supplied to the NLTL. The diode spacing has been set to $334.2\mu m$ and the large signal capacitance to $55.4fF$, so as to determine a $81GHz$ semi-lumped Bragg frequency. This being the case, the behavior observed in figure III.21 for a quintupler configuration recalls the one demonstrated for the tripler configuration. However, as expected, a decrease in the peak conversion efficiency can be observed in each case.

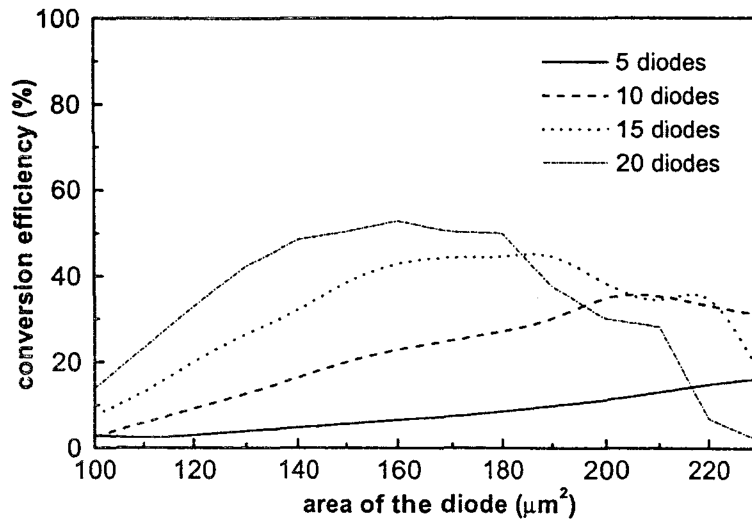

Figure III.20: Conversion efficiency to the third harmonic as a function of the diode area varying the number of diodes for the tripler configuration

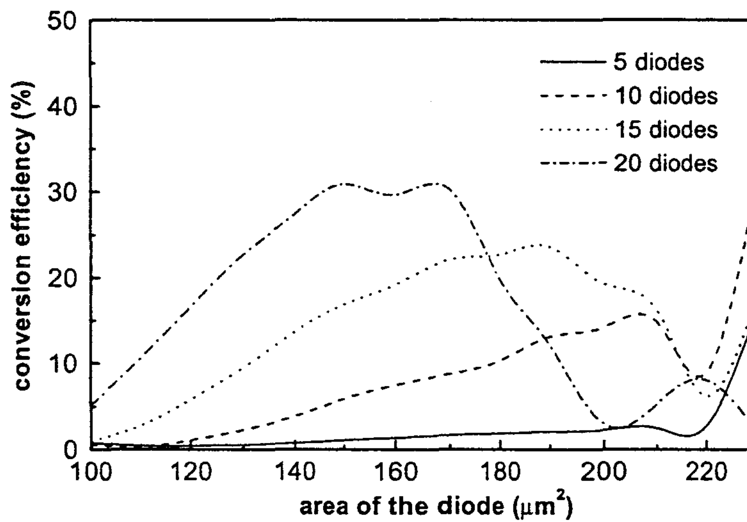

Figure III.21: Conversion efficiency to the fifth harmonic as a function of the diode area varying the number of diodes for the quintupler configuration

Figure III.22 shows the conversion efficiency to the third harmonic as a function of the diode area when the NLTL multiplier is designed as a quintupler by a proper choice of the Bragg frequency.

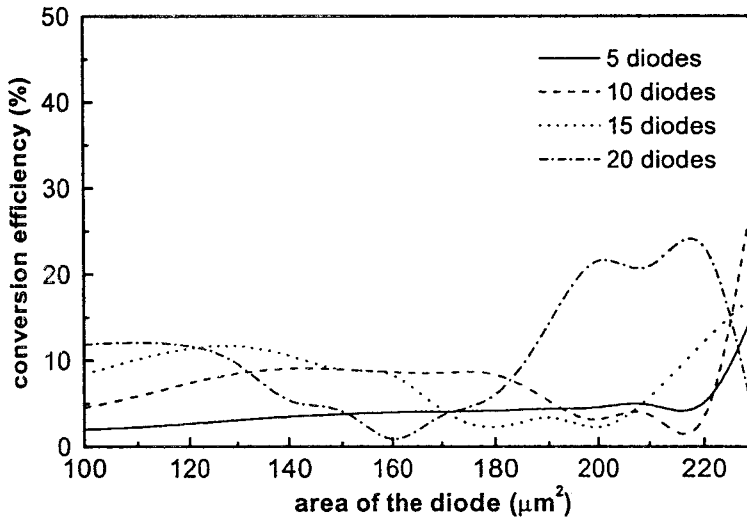

Figure III.22: Conversion efficiency to the third harmonic as a function of the diode area varying the number of diodes for the quintupler configuration

The problem of the variable dynamic range was addressed by Salameh and Linton in reference [SL99b], where variable diode areas were used to enhance matching. Actually, in figures III.20 and III.21 diode area variation implies diode large signal capacitance variation, and hence the loaded line impedance is subject to variation too. Nevertheless, large signal impedance variation is negligible for the areas considered here, and consequently the resultant impedance mismatching. Thus, the increase in the C_{ls}/C_l ratio can justify the behavior observed.

On the other hand, part of the power fed to the NLTL is lost through the HBV diodes and the CPW. Thus, due to losses, the maximum instantaneous voltage decreases as the waveform propagates through successive sections. A comparison between two different time domain approaches, Finite Difference Time Domain (FDTD) [Jra99] and SPICE [JTFT00] simulations, was carried out on lossy and dispersive NLTLs used for pulse compression. Here, loss effects are treated within MDS.

Let us now address the loss issue by considering first only the diode series resistance, which can be estimated between 1Ω and 5Ω. The influence of losses has been studied considering the diode areas which display a maximum conversion efficiency when the device is used as a tripler. The results are shown in figure III.23. It can be noted how the conversion efficiency values obtained tend towards the same limit when the series resistance increases. This means that structures with a limited number of diodes have to be considered.

At this stage, the results of scanning the frequency of the $30dBm$ input sine-wave in order to study the conversion efficiency for the first two non-zero harmonics are shown in figure III.24. The tripler has been exactly designed for a peak conversion efficiency at $60GHz$. Moreover,

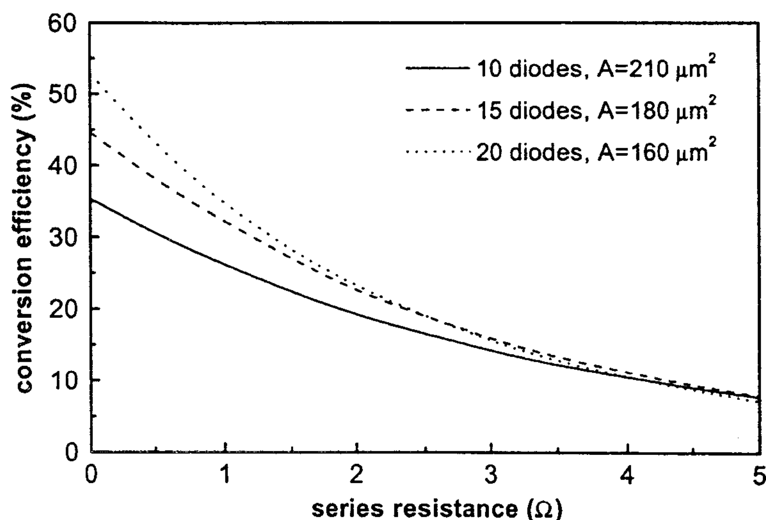

Figure III.23: Conversion efficiency to the third harmonic as a function of the diode series resistance

an input frequency of $14GHz$ will correspond to a maximum conversion efficiency to the fifth harmonic.

The input third harmonic bandwidth for the lossless case is shown in figure III.25, where the case corresponding to a 1Ω diode series resistance has been superimposed. A $6GHz$ input bandwidth (30%) largely confirms the device broad-band operation. As the Bragg frequency (equation III.1.5) and the large signal impedance (equation III.1.4) are expressed as a function of the diode large signal capacitance (equation III.1.3), and the diode large signal capacitance is determined by the input power, the overall matching is good independently from the frequency of the generator and the bandwidth is broad.

Finally, transmission line losses have been considered. CPW losses involve two contributions, the losses coming from the finite metallization thickness with a conductivity value equal to $3 \cdot 10^7 Scm^{-1}$ and the losses coming from the dielectric substrate with a loss tangent value equal to 0.0003. Note that the metallic loss contribution prevails over the dielectric one.

Figure III.26 shows the behavior of an NLTL periodically loaded with $200\mu m^2$ HBV diodes in terms of conversion efficiency to the third harmonic as a function of the number of sections. The simulation results, in a loss case, predict a maximum conversion efficiency of 10% for an 8-diode structure.

In order to explain this behavior, the instantaneous voltage at the output of different number of section structures has been plotted in figure III.27 (on pages 80 and 81). When the line is too short, the voltage waveform is not sufficiently distorted. However, as the voltage waveform propagates through successive sections, the instantaneous voltage tends to decrease due to losses. Thus, a trade-off must be found in practice concerning the number of sections in order to enhance conversion efficiency. Increasing the number of sections after the optimum deteriorates the performance, since the effect of losses becomes larger than the effect

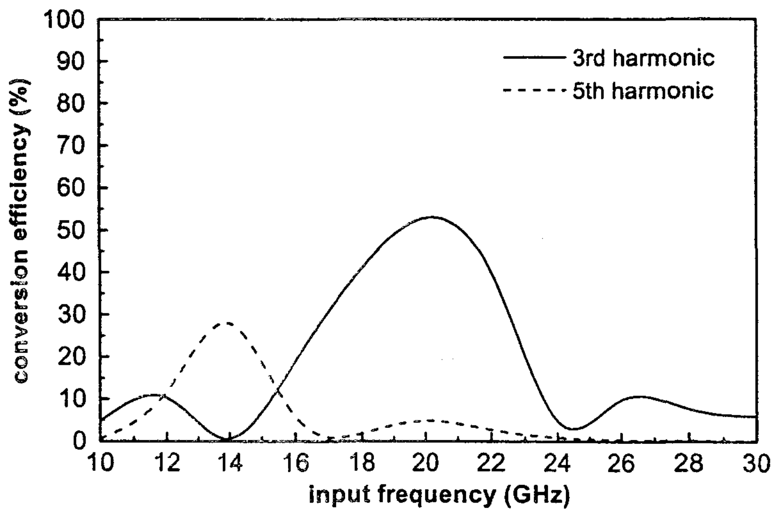

Figure III.24: Conversion efficiency to the third and fifth harmonic as a function of the input frequency

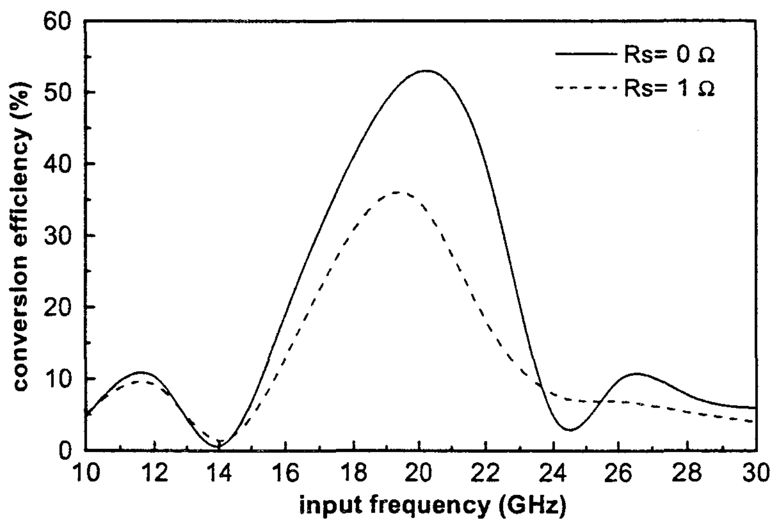

Figure III.25: Conversion efficiency to the third harmonic as a function of the input frequency for the lossless case and for $Rs = 1\Omega$

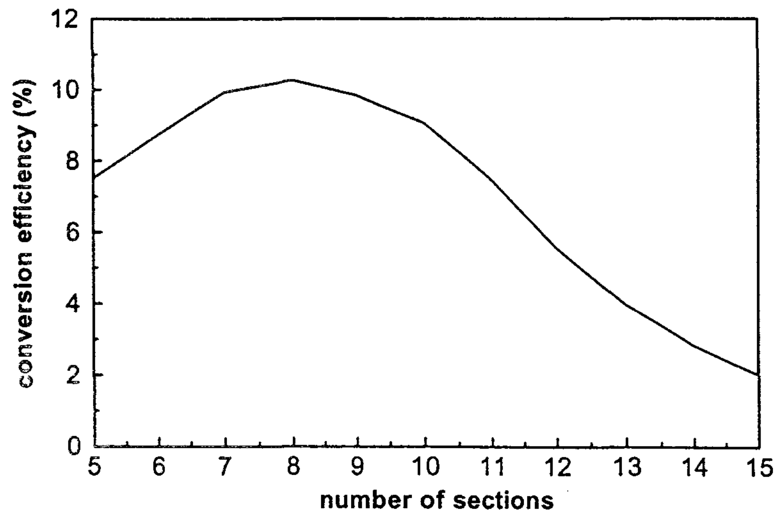

Figure III.26: Conversion efficiency to the third harmonic as a function of the number of sèctions for a loss case

of nonlinearity.

These simulations have been performed by injecting a $30dBm$ sinusoidal signal. An additional simulation has then been performed for the 8-diode structure varying the input power from $10dBm$ to $30dBm$. The results are displayed in figure III.28. A $30dBm$ input power pumps the diodes over the full voltage range, typically a $20V$ peak-to-peak value for proper operation. Under moderate pump conditions, one does not take entirely advantage of the nonlinearity of the diodes, which explains the behavior obtained. Furthermore, this is accompanied by impedance matching problems, as the design presumes a constant input power. The same arguments can be applied for the previous discussion.

In conclusion, loss problems imply the fact of considering structures with a limited number of diodes as the input signal amplitude must be sufficient to excite the nonlinearity of the diodes.

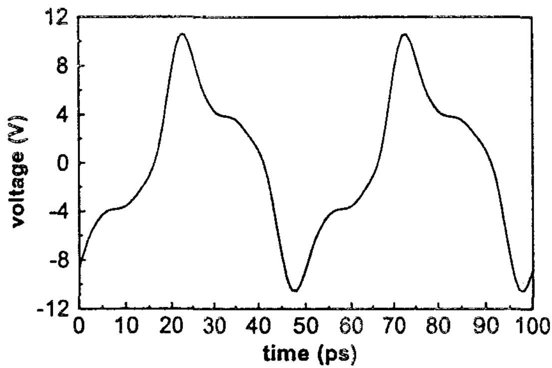

(a) 5 diodes

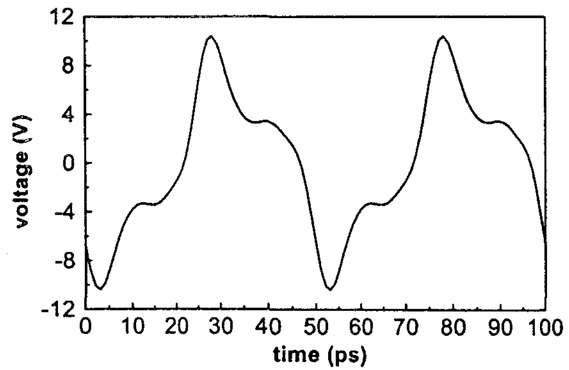

(b) 6 diodes

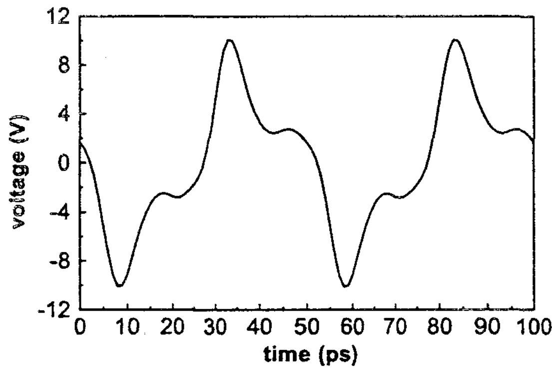

(c) 7 diodes

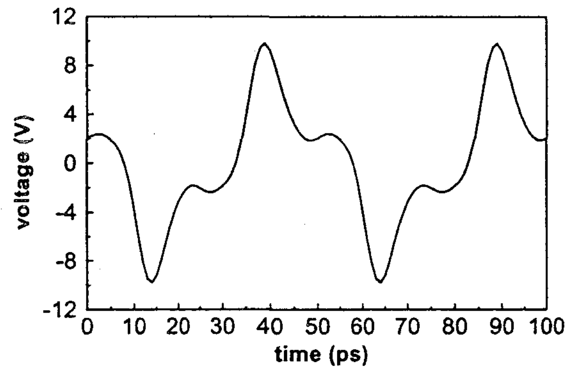

(d) 8 diodes

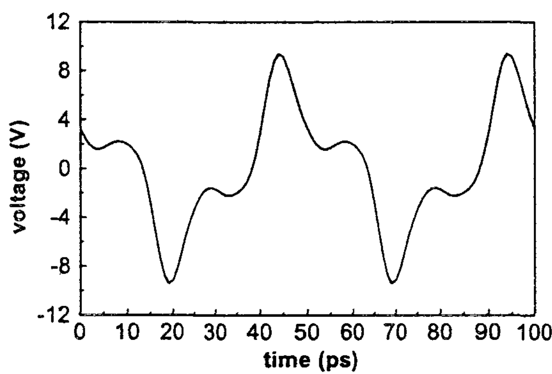

(e) 9 diodes

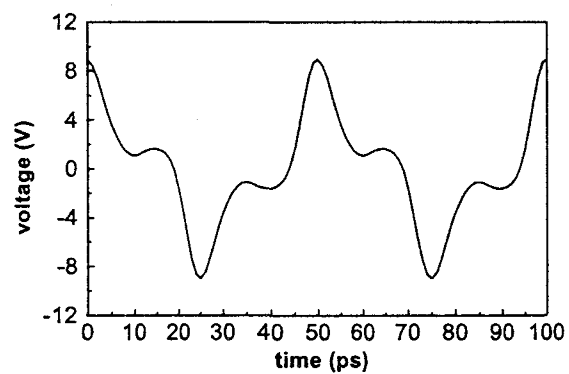

(f) 10 diodes

Figure III.27: Instantaneous voltage as a function of the time at the output of different NLTLs with different number of sections

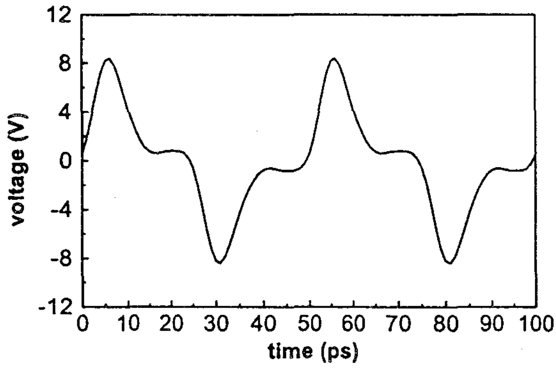

(g) 11 diodes

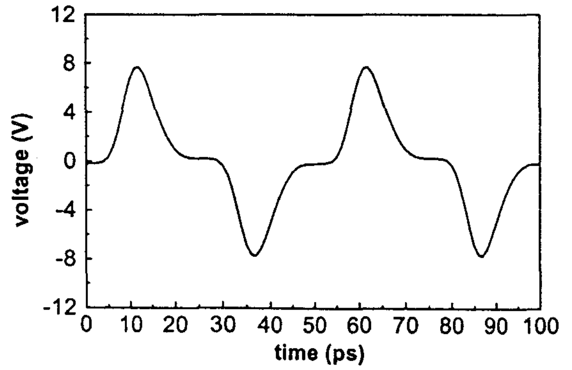

(h) 12 diodes

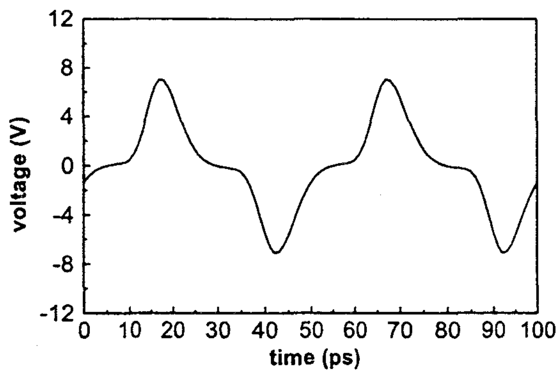

(i) 13 diodes

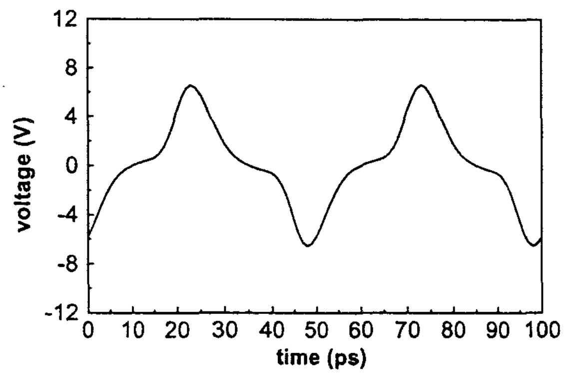

(j) 14 diodes

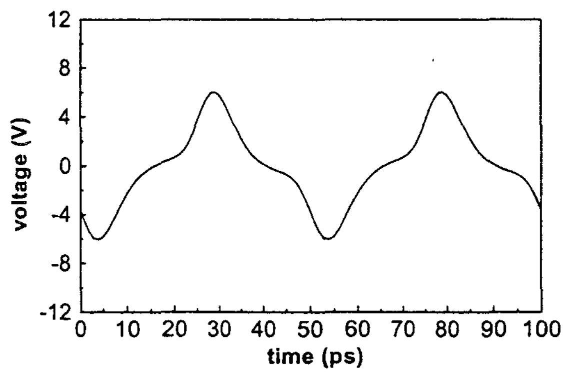

(k) 15 diodes

Figure III.27: (continued)

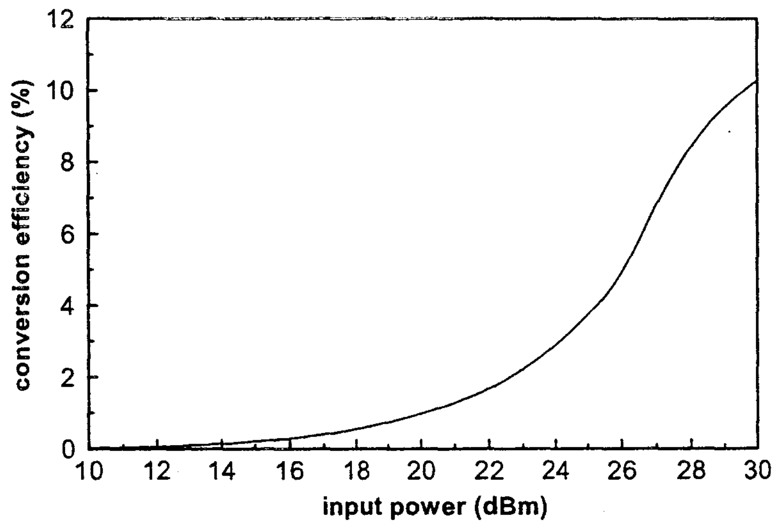

Figure III.28: Conversion efficiency to the third harmonic as a function of the input power for a loss case

Chapter IV

Large Signal S Parameter Simulation of an NLTL for the Frequency Filtering Analysis

Chapter IV

Large Signal S Parameter Simulation of an NLTL for the Frequency Filtering Analysis

IV.1 Introduction

As with all periodic structures, NonLinear Transmission Lines (NLTLs) exhibit pass-band/stop-band characteristics. In relation to this frequency filtering aspect, one of the most important parameters in the design of an NLTL is the Bragg frequency. The Bragg frequency determines the transition between the pass-band and the stop-band of the NLTL.

In this chapter, the S parameters are evaluated for large signal driving conditions using a powerful commercial software package, Advanced Design System (ADS), from Agilent Technologies.

The large signal simulation technique is based on a harmonic balance simulation of the full nonlinear circuit. The key advantage of this approach to study the transmission behavior of the NLTL is that, in the case of input and output matching conditions, the circuit can be analyzed without the restriction of linearizing it. In previous works, NLTLs were usually studied from two different points of view. In order to analyze the large signal behavior of the circuit, a harmonic balance simulation was performed. In terms of the transmission properties and the input and output matching conditions, the NLTL had to be analyzed using S parameters. This implies that the behavior of the intrinsically nonlinear circuit is approximated during the evaluation of the S parameters. In other words, the intrinsically nonlinear circuit was studied in the linear regime. As an alternative to the conventional S parameter analysis, the large signal technique enables us to simulate the circuit in a global way, including all nonlinear effects.

IV.2 Large Signal S Parameters

Concerning the transmission characteristics of the NLTL, the S parameter analysis was previously based on the conventional small signal simulation of the linearized circuit. In contrast to this approach, Large Signal S Parameters are based on a harmonic balance simulation of the full nonlinear circuit, which means that its solution includes nonlinear effects. Large Signal S Parameters are defined as:

$$S_{ij} = \frac{B_i}{A_j} \tag{IV.2.1}$$

where

$$A_j = \frac{V_j - Zo_j I_j}{2\sqrt{Ro_j}} \tag{IV.2.2}$$

and

$$B_i = \frac{V_i + Zo_i^* I_i}{2\sqrt{Ro_i}} \tag{IV.2.3}$$

V_i and V_j are the Fourier coefficients, at the fundamental frequency, of the voltages at ports i and j.

I_i and I_j are the Fourier coefficients, at the fundamental frequency, of the currents at ports i and j.

Zo_i and Zo_j are the reference impedances at ports i and j.

Ro_i and Ro_j are the real parts of Zo_i and Zo_j.

The definition of the Large Signal S Parameters is a generalization of the Small Signal S Parameter definition in that, V and I, rather than phasors, are Fourier coefficients of the voltages and currents at the fundamental frequency. This means that the definition simplifies to the small signal definition for a linear circuit.

In order to calculate the power dependent S parameters, as they are also called, the simulator performs basically the same steps followed in a Small Signal S Parameter simulation. For a two port device, once the port two is terminated with the complex conjugate of its reference impedance, a signal is applied at port one. This signal has a user specified power level and is generated by a source which impedance equals the complex conjugate of the reference impedance of the input port. The main difference arises from the use of a harmonic balance simulation to calculate the S_{11} and S_{21} parameters from the information of the currents and voltages at ports one and two. The benefits of this are discussed later.

The way the simulator calculates the S_{22} and S_{12} parameters will be discussed also later on.

IV.3 Comparison between Small Signal and Large Signal Bragg Frequency

Different from the Small Signal S Parameter simulation, the Large Signal S Parameter simulation can take into account the nonlinear effects of the NLTL. Namely, the propagation characteristics of the line are exposed for all the signals of interest. However, the Large Signal S Parameter simulation remains a S parameter simulation as the S_{21} parameter still represents the transmission from port one to port two when no conversion frequency is achieved. So, even if the transmission coefficient states the nonlinear effects of the NLTL, there is no explicitly information about the conversion efficiency.

In this chapter, a semi-distributed model for NLTLs is used as the results are deemed to be a more accurate representation of the overall behavior of the NLTL than the approximate lumped-element equivalent model. In particular, Wang and Hwu [WH99] performed a theoretical analysis confronted with simulations about this topic.

Concerning the magnitude, the comparison between the Small Signal and Large Signal S Parameter simulations for a lossless case is shown in figure IV.1(a) as a function of the frequency. The phase is plotted in figure IV.1(b). In these simulations, the lumped-element model of the Heterostructure Barrier Varactor (HBV) diode was implemented using a Symbolically Defined Device (SDD) in which the capacitance is related to the charge stored, analogous to the implementation carried out in Microwave Design System (MDS). The input power has been set to $20dBm$, the area of the diodes to $120\mu m^2$ and the number of sections to 6. To perform the Small Signal S Parameter simulation, each diode had to be biased to obtain the Bragg frequency corresponding to the average capacitance, in order to compare properly both simulations. In fact, if a Small Signal S Parameter simulation is performed directly, the Bragg frequency obtained would correspond to the capacitance at zero volt bias. Previous theoretical analysis of NLTLs conducted by Rodwell *et al.* [RKY+91] introduced the concept of the large signal diode capacitance or average capacitance, which is defined for an input falling step function. In this way, the large signal capacitance C_{ls} is used to represent the voltage dependent diode capacitance $C_d(V)$ in the linear regime.

Several features are manifest from these results:

- The same value of Bragg frequency is obtained in both cases, as can be deduced from the location of the low-pass filter transition. This result confirms the validity of the large signal capacitance approximation proposed by Rodwell *et al.* [RKY+91] and which expression is reported in equation III.1.3 (on page 52). In terms of Bragg frequency, it is equivalent to represent the diode capacitance $C_d(V)$ by this value when considered in the linear regime, that is C_{ls}. In addition, this average capacitance, usually defined for an input falling step function, can be applied with an input sinusoidal function, which is the case for a harmonic balance simulation.

- The most important difference between these two simulations appears in the shape of the transition between the pass-band and the stop-band. As it will be proved later, the more nonlinear the capacitance is, the more abrupt the transition becomes. In this case, a nonlinear capacitance is compared with a constant capacitance. Note that the

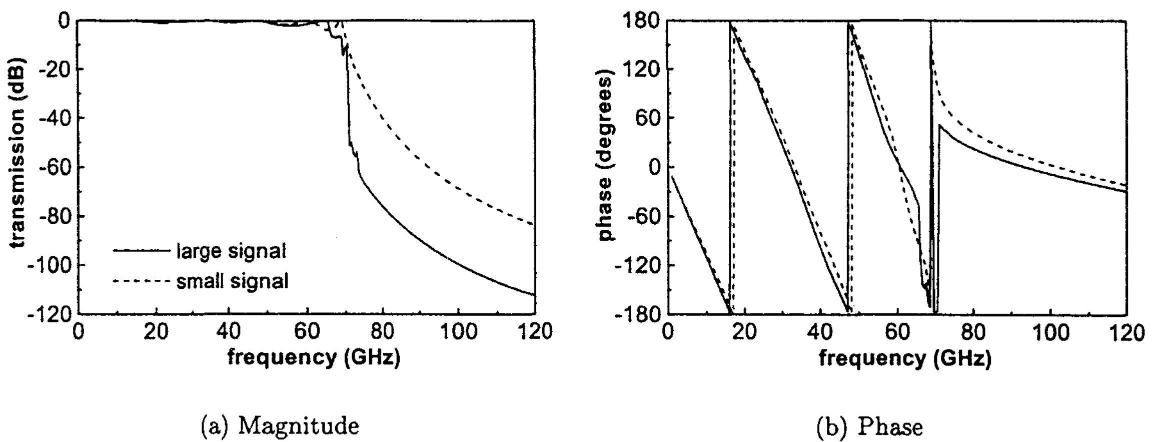

(a) Magnitude

(b) Phase

Figure IV.1: Large signal and small signal S_{21} parameter ($P_{input} = 20dBm$) as a function of the frequency in a lossless case

difference between the large signal and small signal S_{21} parameter can be more easily seen in the magnitude graphic.

- Related to the more abrupt transition in the large signal simulation, a more important fluctuation effect on the high frequency transmission behavior of the line can be seen preceding this transition. This pronounced fluctuation even makes the S_{21} parameter fall under $-3dB$ at some frequency ranges before what seems to correspond to the Bragg frequency (clearly defined by the transition). The observed behavior could justify the safeguard taken, even in the lossless case, in the specification of the optimum ratio between the Bragg frequency and the input frequency.

In figure IV.2(a), the magnitude of the large signal S_{21} parameter is plotted as a function of the frequency, where the transmission line losses and the series resistance of the diode have been included. The phase is shown in figure IV.2(b). In both plots, four different cases are displayed, the lossless case, when only the transmission line losses are included and, while considering both the transmission line losses and the series resistance, $Rs = 1\Omega$ or $Rs = 2\Omega$. As a consequence of the losses, the transition becomes less abrupt and is associated with a shift of the Bragg frequency to lower values.

Figures IV.3(a) and IV.3(b) show respectively the magnitude and the phase of the small signal S_{21} parameter with the purpose of comparing it with the previous graphics. It can be seen in the phase graphics how the influence of the losses, manifest from the separation of the curves, only appears after the Bragg frequency for the small signal parameter. However, this influence can be observed before for the large signal parameter.

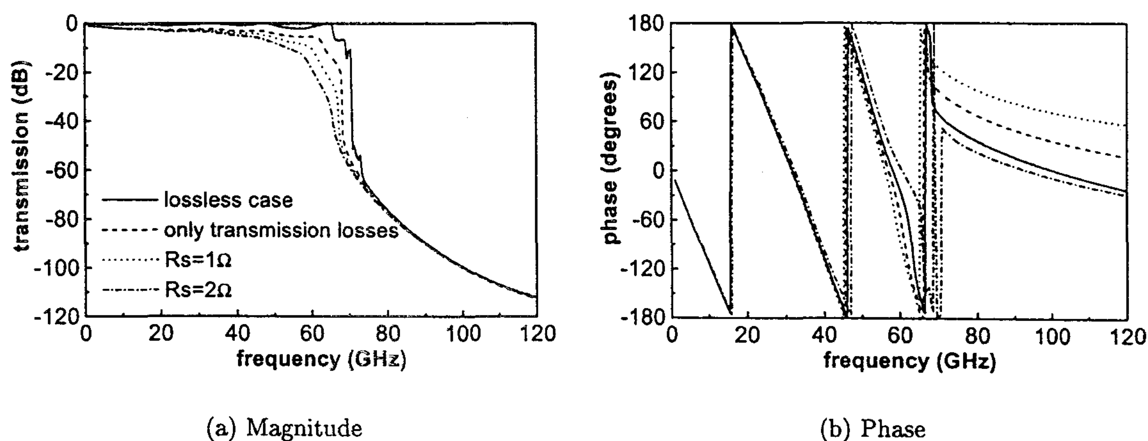

(a) Magnitude (b) Phase

Figure IV.2: Large signal S_{21} parameter as a function of the frequency for different losses

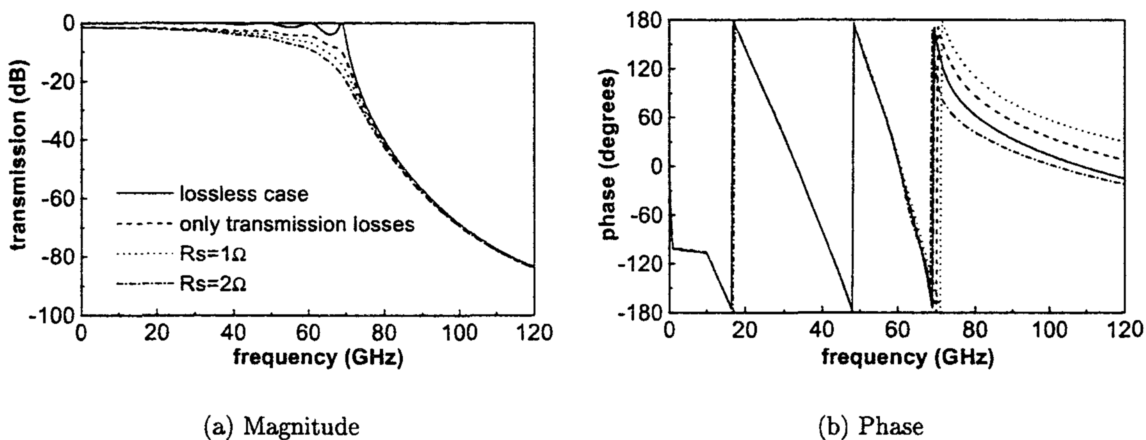

(a) Magnitude (b) Phase

Figure IV.3: Small signal S_{21} parameter as a function of the frequency for different losses

IV.4 Influence of the Diode C-V Characteristics on the Transmission Behavior of the Line

IV.4.1 Influence of the Area of the Diodes

In the HBV model used in the simulations, the area of the diodes is one of the design parameters of the NLTL. The behavior of the capacitance varying the diode area is shown in figure IV.4(c). Figure IV.4 shows the large signal S_{21} parameter for different areas of the diode, the input power being still fixed to $20dBm$. As the area of the diode fixes the average value of capacitance, it can be seen in figure IV.4(a) how the Bragg frequency shifts to smaller values as the area of the diode is increased. The phase is plotted in figure IV.4(b).

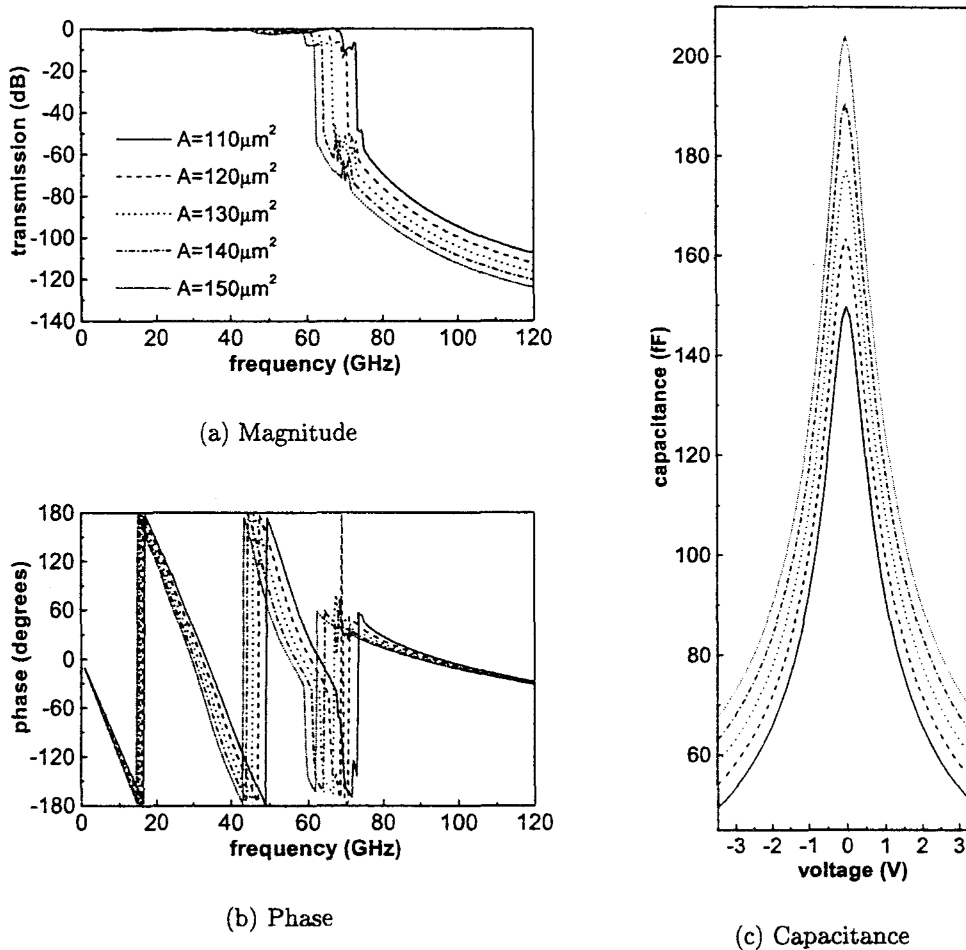

(a) Magnitude

(b) Phase

(c) Capacitance

Figure IV.4: Large signal S_{21} parameter ($P_{input} = 20dBm$) as a function of the frequency varying the diode area

IV.4.2 Influence of the Input Power

As expected and shown in figure IV.5, a similar shift effect is obtained by varying the input power applied to the NLTL, although by contrast the behavior at high frequencies differs from the previous case. Note that since the C-V characteristic is the same in each simulation, by varying the input power C_{ls} is modified. The use of the same nonlinear device presumably leads to the same asymptotic behavior at high frequencies, different from simply varying the C_{ls} value of the design.

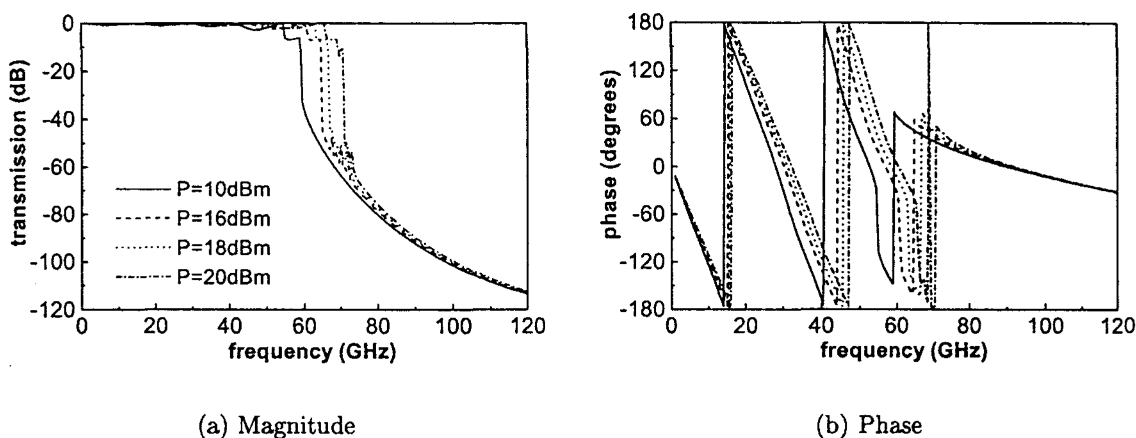

(a) Magnitude

(b) Phase

Figure IV.5: Large signal S_{21} parameter as a function of the frequency varying the input power

IV.4.3 Influence of the Number of Sections

In order to study the transition between the pass-band and the stop-band of the NLTL, a simulation has been performed varying the number of basic sections. As expected, by increasing the number of nonlinear devices, the transition becomes more abrupt, as shown in figure IV.6(a). This is analogous to the example of a low-pass filter, where increasing the number of sections leads to increasingly sharp pass-band/stop-band transitions. Figure IV.6(b) shows the phase of the large signal S_{21} parameter as a function of the frequency varying the number of basic sections.

Figure IV.7 shows the comparison between the large signal and small signal S_{21} parameter as a function of the frequency for different basic sections.

IV.4.4 The Abrupt Transition

As introduced before, once the number of diodes is fixed, the steepness of the transition is determined by the non linearity of the diode, the average capacitance only fixing the value of the Bragg frequency.

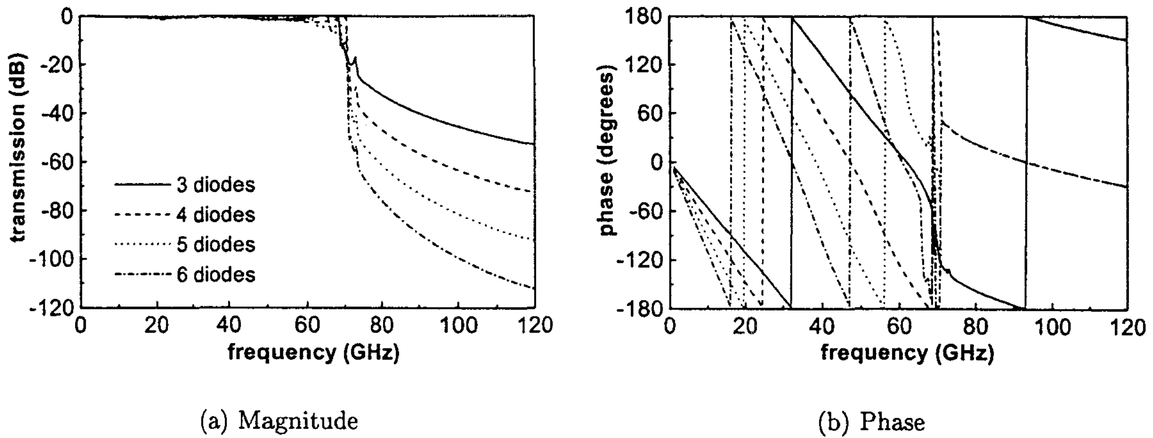

(a) Magnitude

(b) Phase

Figure IV.6: Large signal S_{21} parameter ($P_{input} = 20dBm$) as a function of the frequency varying the number of basic sections

This is proved in the following simulations where three different parabolic C-V relationships have been chosen, while keeping the average capacitance constant. An equation based-nonlinear device has been used to simulate the nonlinear capacitor by introducing a list of coefficients that describes a polynomial. In this case, $C_d(V) = 125 - 7.2V^2$, $C_d(V) = 135 - 12V^2$ and $C_d(V) = 145 - 16.8V^2$, stated in fF, correspond to the three parabolic C-V relationships used in the simulation and shown in figure IV.8(c). They all exhibit the same average capacitance. The input power has been set to $18dBm$ and the number of sections to 4 due to convergence problems of the simulator. The results in figure IV.8(a) show that the average capacitance fixes the value of the Bragg frequency and the more nonlinear the diode is (the first coefficient in the C-V relationship expressing the non linearity degree), the steeper the transition is. The phase is plotted in figure IV.8(b). This result reinforces the validity of the Large Signal S Parameter simulation in the frequency filtering analysis of an NLTL.

In comparison with the small signal analysis which is able to give us only the Bragg frequency, the large signal analysis gives information about the effects associated with the non linearity of the diode.

IV.4.5 Influence of the Diode C-V Relationship

Further to these results, additional simulations have been performed in order to gain an insight into the influence of the diode capacitance-voltage characteristics in the transmission behavior of the NLTL. It is well known that the fractional change in the diode capacitance affects the power transferred to higher order harmonics. The same conditions have been imposed for these simulations.

In 1997, Dillner *et al.* [DSK97] performed an analysis of symmetric varactor frequency multipliers. They investigated how the shape of the C-V characteristic influences the maximum multiplier efficiency and finally stated that the best efficiency is obtained for a C-V characteristic with large nonlinearity at zero volt bias.

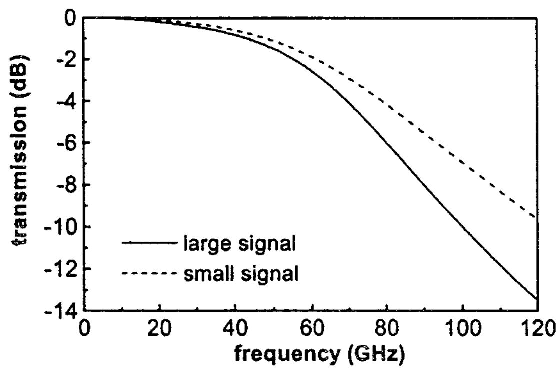

(a) One diode

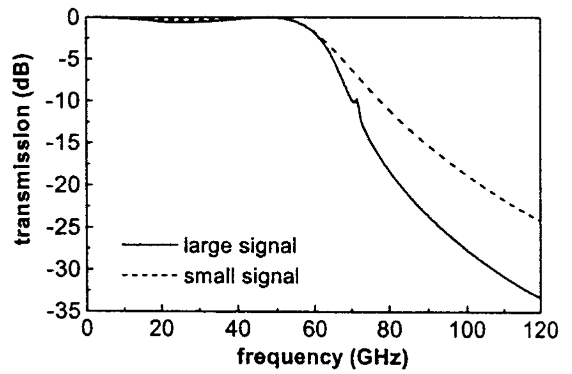

(b) Two diodes

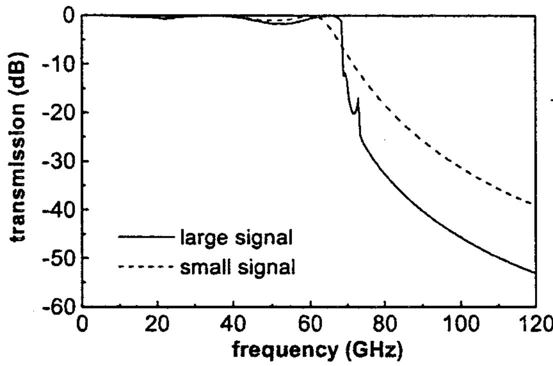

(c) Three diodes

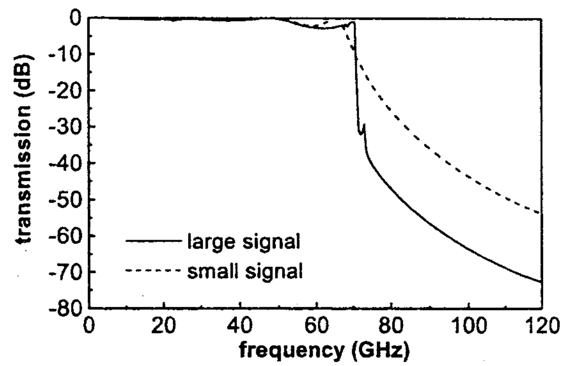

(d) Four diodes

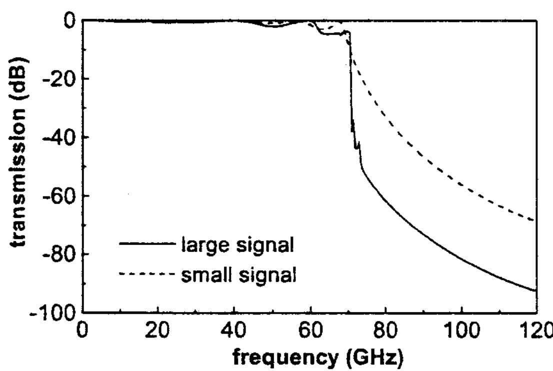

(e) Five diodes

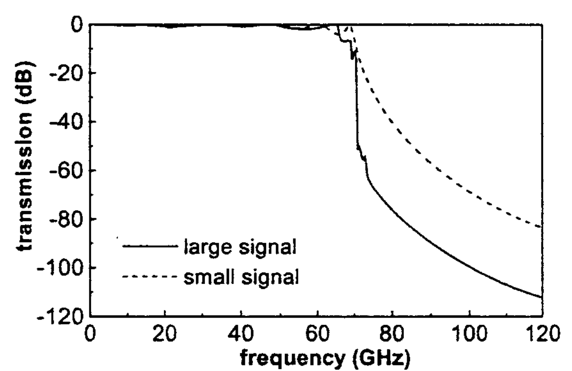

(f) Six diodes

Figure IV.7: Magnitude of the large signal and small signal S_{21} parameter as a function of the frequency for different basic sections

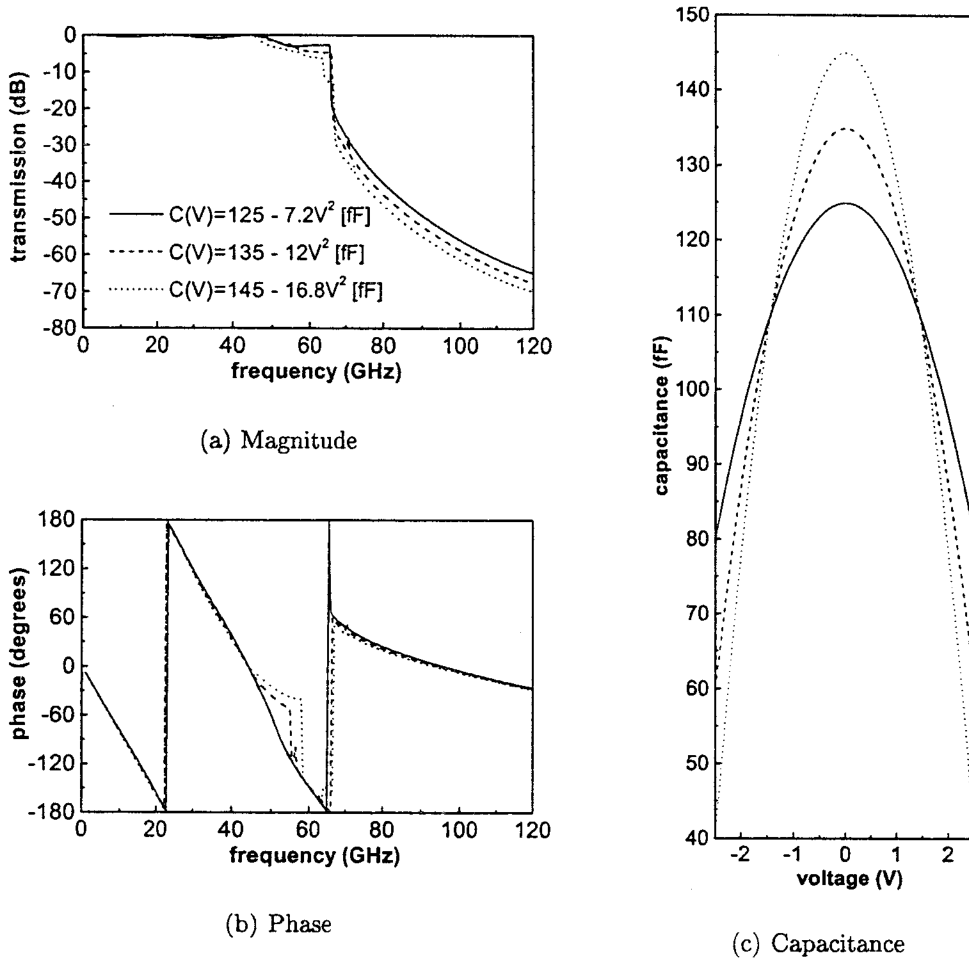

Figure IV.8: Large signal S_{21} parameter ($P_{input} = 18dBm$) as a function of the frequency varying the non linearity of the diode

Later, Salameh and Linton [SL99b] studied the effect of various parameters on NLTL performance. Schottky diode capacitance-voltage characteristics were computed using a physical simulator for different doping profiles, which were used as a parameter in the NLTL design, and their effect on NLTL performance was investigated. The doping profile of the Schottky diode is an important parameter in the diode design. Even though hyperabrupt doping profiles increase the reflection loss, the hyperabrupt doping always provides better performance than the uniform doping, as proved in reference [MMR+89]. In reference [SL99c], Salameh and Linton performed a detail study of the relation between doping profiles and diode C-V characteristics.

In 1994, Van Der Weide [Wei94] already stated that a more drastic change in the C-V characteristic should result in a similar change in the propagation velocity, resulting in its turn in an improvement in compression efficiency. Thus, he proposed delta-doped Schottky diodes better than hyperabrupt diodes as, over the central bias range, the delta-doped Schottky diode offers a greater velocity modulation than the hyperabrupt varactor.

Finally, Martín studied the effects of device nonlinearity on soliton formation and propagation. In reference [Mar00], it was demonstrated that a faster separation of the input signal into solitons is achieved for a C-V characteristic with large nonlinearity.

IV.4.5.1 By Keeping $Cmax$ Constant

First of all, a simulation has been performed selecting three different parabolic C-V relationships with the same $Cmax$ equal to $145fF$, corresponding to the following equations: $C_d(V) = 145 - 16.8V^2$, $C_d(V) = 145 - 12.8V^2$ and $C_d(V) = 145 - 8.8V^2$ in fF. Different from using the same nonlinear device and simply varying the input power, actually $Cmin$, in this example only $Cmax$ is kept constant as shown in figure IV.9(c). However, the same asymptotic behavior at high frequencies is observed in figure IV.9(a). The phase plot IV.9(b) is also similar to the one showing the phase of the large signal S_{21} parameter as a function of the frequency varying the input power.

IV.4.5.2 By Keeping $Cmin$ Constant

Then, the following simulation is performed keeping $Cmin$ constant and equal to $80fF$ for four different parabolic C-V relationships, expressed in fF as $C_d(V) = 112.5-5.2V^2$, $C_d(V) = 125 - 7.2V^2$, $C_d(V) = 137.5 - 9.2V^2$ and $C_d(V) = 150 - 11.2V^2$ and shown in figure IV.10(c). The magnitude of the large signal S_{21} parameter as a function of the frequency varying the non linearity of the diode is shown in figure IV.10(a), the phase in figure IV.10(b). Note that the magnitude graphic is similar to the one where the magnitude of the large signal S_{21} parameter is plotted as a function of the frequency varying the diode area. Nevertheless, the difference between these two simulations can be observed in the phase graphics.

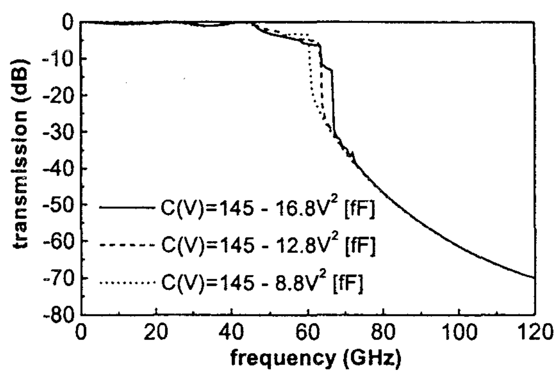

(a) Magnitude

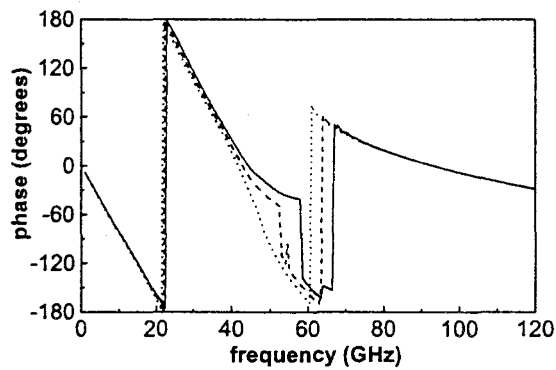

(b) Phase

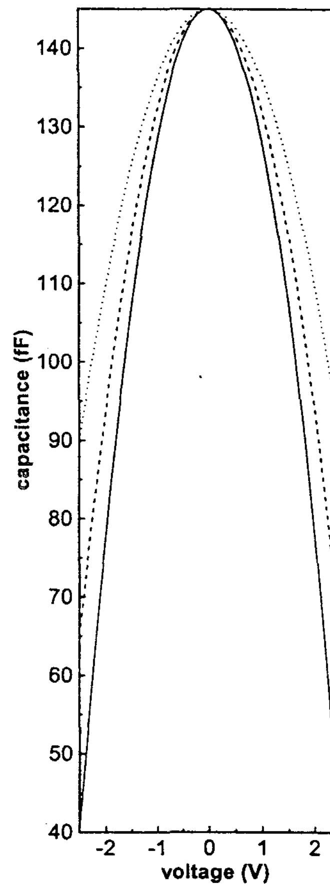

(c) Capacitance

Figure IV.9: Large signal S_{21} parameter ($P_{input} = 18dBm$) as a function of the frequency varying the non linearity of the diode by keeping $Cmax$ constant

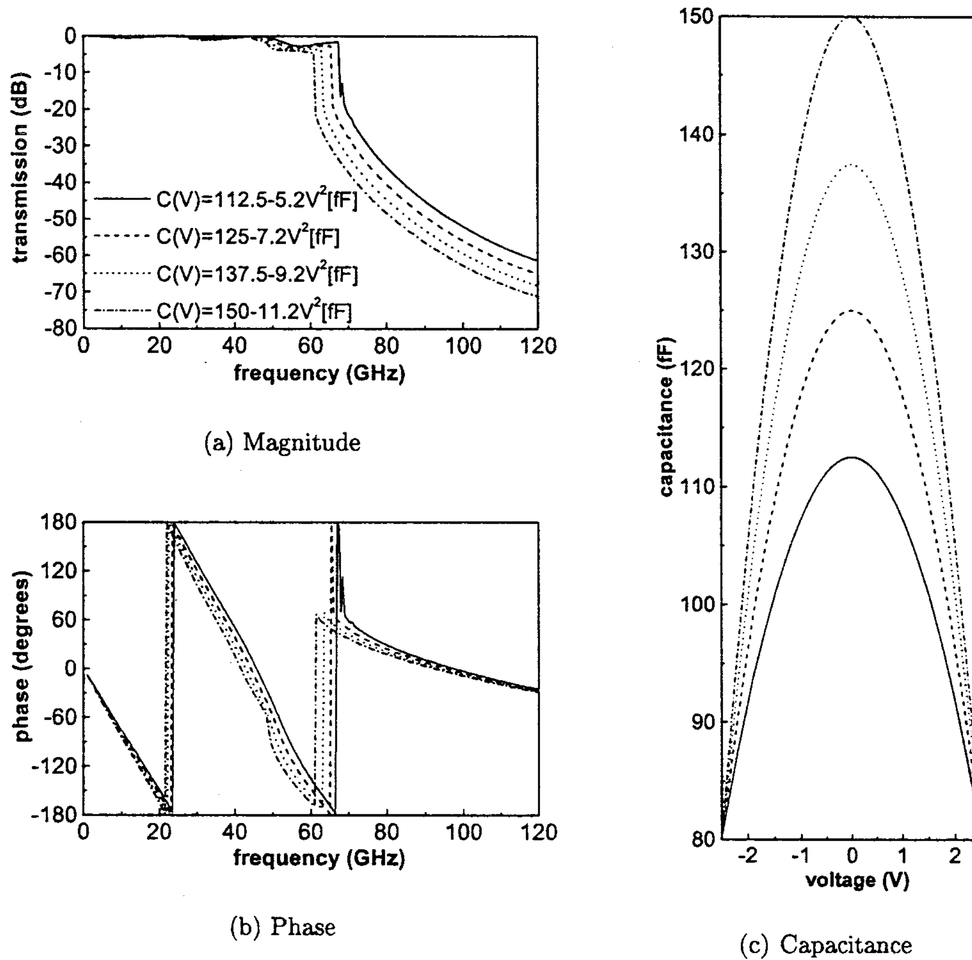

(a) Magnitude

(b) Phase

(c) Capacitance

Figure IV.10: Large signal S_{21} parameter ($P_{input} = 18dBm$) as a function of the frequency varying the non linearity of the diode by keeping $Cmin$ constant

IV.4.5.3 By Keeping both *Cmax* and *Cmin* Constant

Finally, combining the both previous results, a simulation has been carried out keeping *Cmax* and *Cmin* constant. In order to keep *Cmax* and *Cmin* constant, the degree of the polynomial equations representing the diode capacitance-voltage characteristics had to be increased up to 4. The resulting equations, expressed in fF, $C_d(V) = 150 - 21.33333V^2 + 1.36533V^4$, $C_d(V) = 150 - 8.53333V^2 - 0.68267V^4$ and $C_d(V) = 150 - 2.048V^4$ lead to $Cmax = 150fF$ and $Cmin = 70fF$ and are shown in figure IV.11(c). The magnitude of the large signal S_{21} parameter is plotted as a function of the frequency in figure IV.11(a). The behavior observed recalls the one in figure IV.9(a), where *Cmax* was kept constant. It can be noted from these simulations that the fact of fixing *Cmax* leads to the same asymptotic behavior at high frequencies, different from the other cases. Therefore, the difference arises from the phase graphics. Figure IV.11(b) shows the phase of the large signal S_{21} parameter as a function of the frequency. By simply comparing figures IV.11(b) and IV.9(b), it can be easily deduced that the simulation parameters referring the diode capacitance-voltage characteristics must be different.

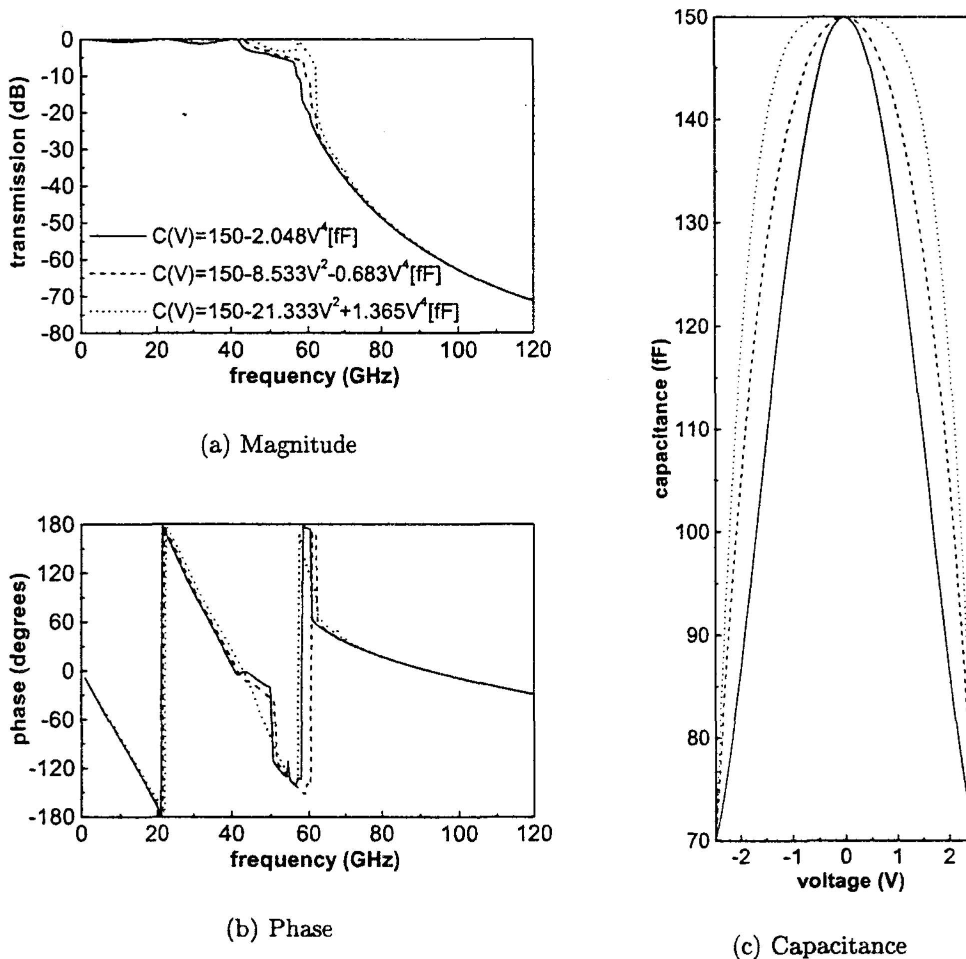

(a) Magnitude

(b) Phase

(c) Capacitance

Figure IV.11: Large signal S_{21} parameter ($P_{input} = 18dBm$) as a function of the frequency varying the non linearity of the diode by keeping both *Cmax* and *Cmin* constant

IV.5 Large Signal S Parameter and Harmonic Balance Simulations

As it has been already proved for harmonic balance applications in reference [SZD+95], by adjusting the f_{in}/f_B ratio the highest conversion efficiency for a specific harmonic can be obtained.

A harmonic balance simulation has been performed in order to study the conversion efficiency to the third harmonic by scanning the frequency of the input sine-wave. The SDD has been adopted again for these simulations. In the example of figure IV.12, the area of the diodes is set to $140\mu m^2$. A maximum conversion efficiency can be observed at $60GHz$, while the Bragg frequency fixed by the abrupt transition is a few GHz higher ($64GHz$). Actually, the fluctuating behavior between $61.5GHz$ and the transition may explain the margin taken between $3f_{in}$ and f_B. Even in the lossless case, this margin must be considered in the NLTL design.

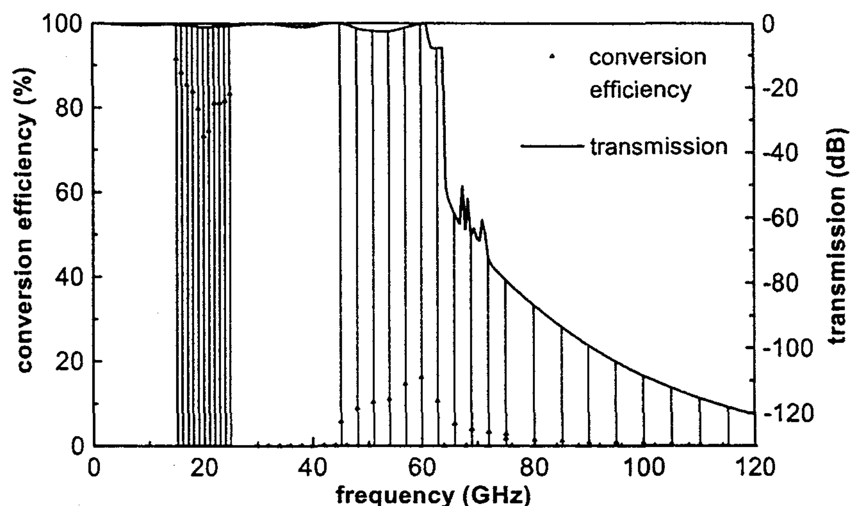

Figure IV.12: Large signal S_{21} parameter ($P_{input} = 20dBm$) and conversion efficiency as a function of the frequency in the lossless case

Four more examples in figure IV.13 (on pages 98 and 99) illustrate the justification of the safeguard taken, even in the lossless case, in the specification of the optimum ratio between the Bragg frequency and the input frequency. These examples correspond to different areas of the diode, $110\mu m^2$, $120\mu m^2$, $130\mu m^2$ and $150\mu m^2$. In this way, it can be stated that the magnitude of the large signal S_{21} parameter gives implicitly information about the conversion efficiency. In fact, besides the transmission information supplied by this parameter, its shape also announces the optimum conversion efficiency harmonic.

In presence of losses, the Bragg frequency shifts to lower values as it was observed in figure IV.2(a). In this example, the transmission losses and a series resistance of $Rs = 2\Omega$ have been considered. Even if a shift occurs in both large and small signal simulations,

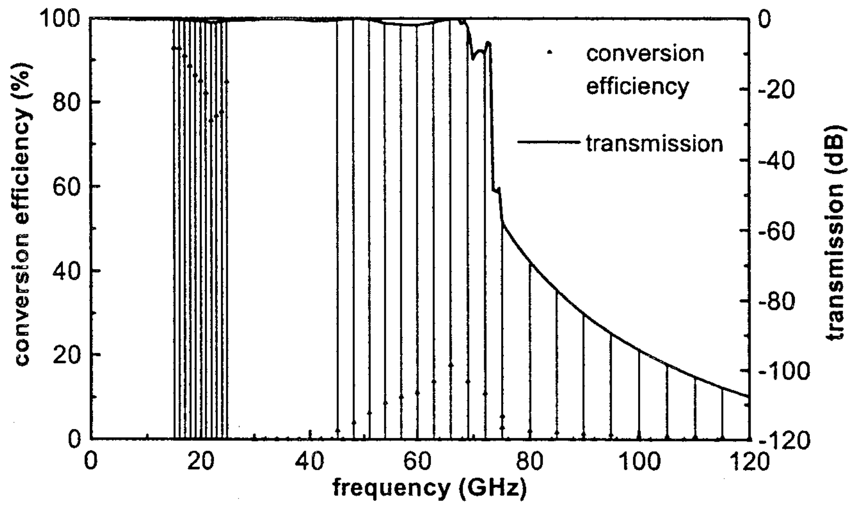

(a) $A = 110\mu m^2$

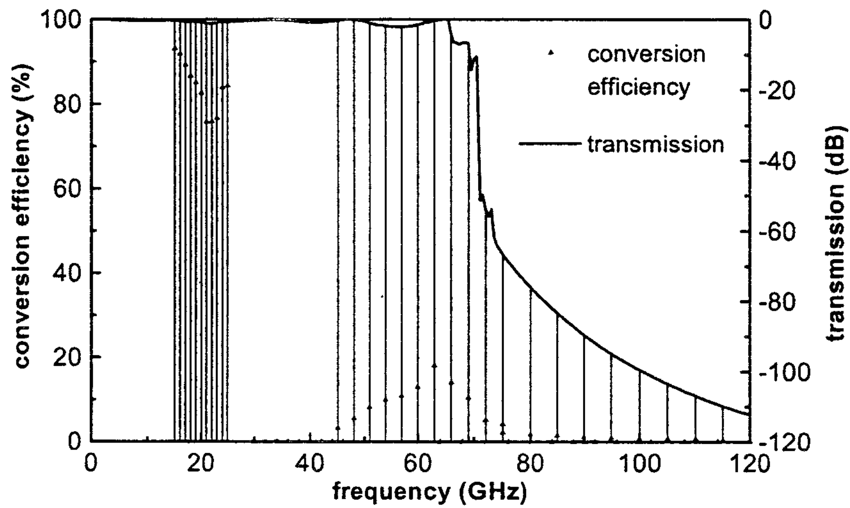

(b) $A = 120\mu m^2$

Figure IV.13: More examples of the large signal S_{21} parameter and the conversion efficiency in the lossless case

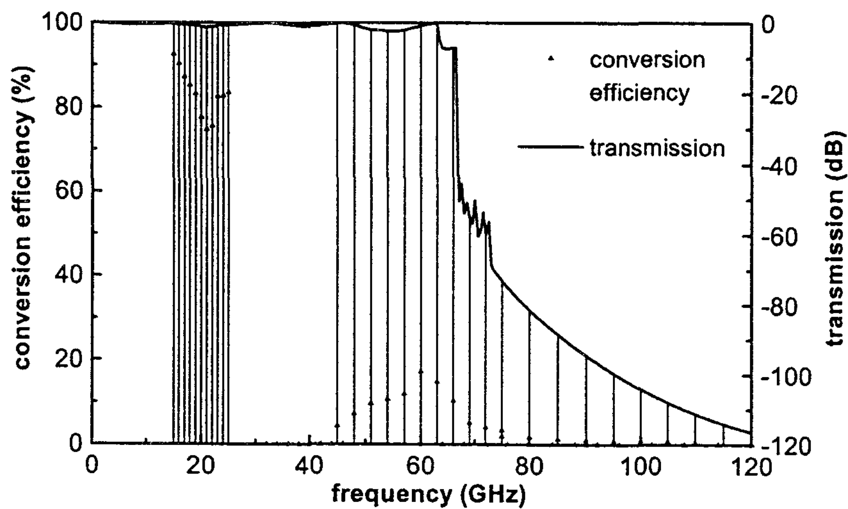

(c) $A = 130\mu m^2$

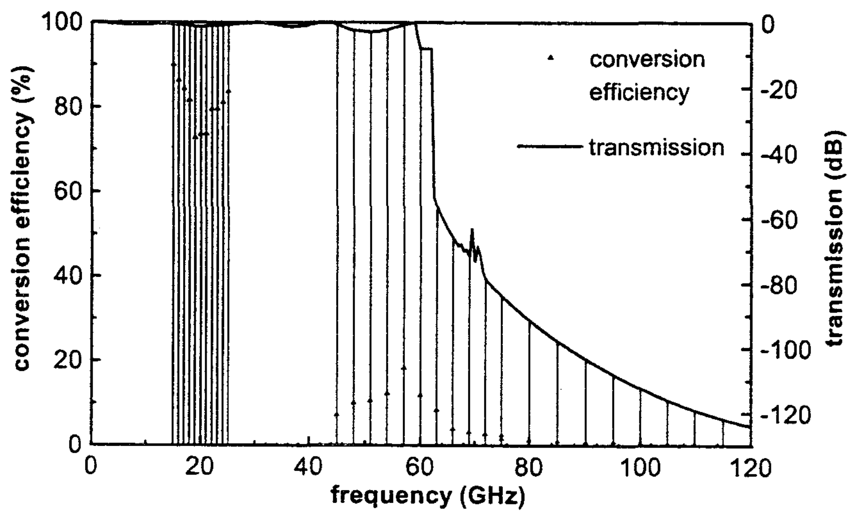

(d) $A = 150\mu m^2$

Figure IV.13: (continued)

figure IV.14(a) shows an important quantitative difference in this shift between the large and small signal S_{21} parameter. In the presence of loss, the Bragg frequency for the large signal simulation is considerably smaller. Note that in the lossless case (figure IV.1(a)), both large signal and small signal Bragg frequency are identical. As the Bragg frequency shifts to smaller values, the frequency margin to be taken becomes greater if the Bragg frequency considered is the lossless one. The phase of the S_{21} parameter is plotted in figure IV.14(b) as a function of the frequency performing a Large Signal S Parameter and a Small Signal S Parameter simulations.

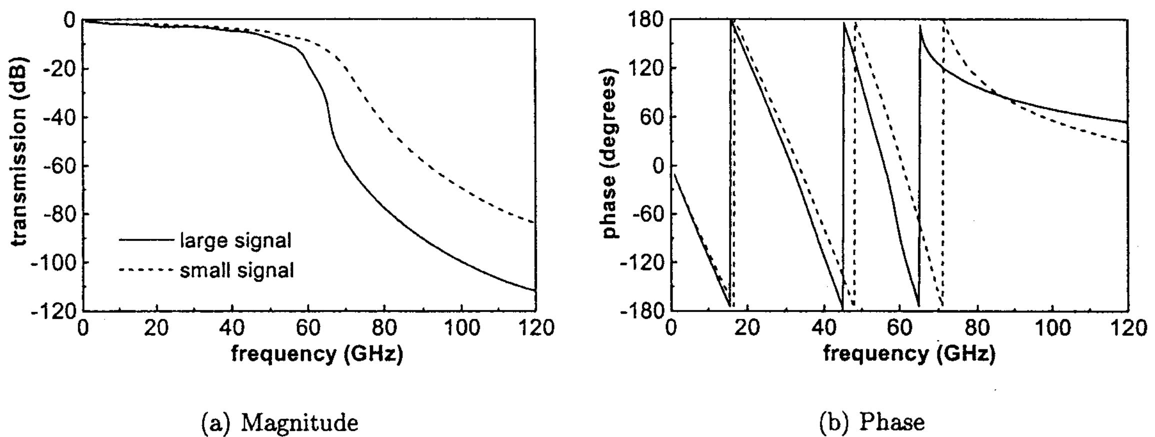

(a) Magnitude

(b) Phase

Figure IV.14: Large signal and small signal S_{21} parameter ($P_{input} = 20dBm$) as a function of the frequency in the presence of loss

The results reported may give information leading to the specification of the optimum ratio between the Bragg frequency and the input frequency.

IV.6 The S_{12} Parameter

As discussed before, in order to calculate the Large Signal S Parameters, the simulator performs basically the same steps followed in a Small Signal S Parameter simulation. Nevertheless, note the peculiarity in the calculation of the S_{12} and S_{22} parameters. The first step consists in terminating port one with the complex conjugate of its reference impedance and applying a signal of power $P_2 = |S_{21}|P_1$ at port two, using a source which impedance equals the complex conjugate of the reference impedance of port two. Then, using a harmonic balance simulation, the currents and voltages at ports one and two are calculated. This information is used to calculate the S_{12} and S_{22} parameters.

Different from the Small Signal S Parameters, even in a reciprocal and physically symmetrical network, $S_{21} \neq S_{12}$ and $S_{11} \neq S_{22}$ for the Large Signal S Parameters due to the injection of power at port two as a function of the magnitude of the S_{12} parameter ($P_2 = |S_{21}|P_1$). This can be observed in figure IV.15, where the magnitude of the large signal S_{21} and S_{12} parameters is plotted as a function of the frequency. In this example, the area of the diodes is set to $120\mu m^2$. Note the shift of the transition to smaller values of frequency for the S_{12} parameter.

Actually, the important fluctuation behavior preceding the transition for the S_{21} parameter has been saved, the current transition been precisely located at the very beginning of this previous fluctuation effect. In this case, no safeguard should be taken in the specification of the optimum ratio between the Bragg frequency and the input frequency.

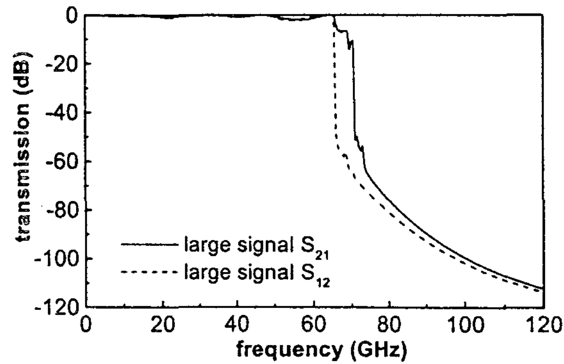

Figure IV.15: Magnitude of the large signal S_{21} and S_{12} parameters ($P_{input} = 20dBm$) as a function of the frequency in the lossless case

IV.7 Conclusion

In this chapter, a Large Signal S Parameter simulation has been performed for the analysis of NLTLs. This is the first work to our knowledge applying this powerful simulation tool in the study of the frequency filtering aspects of NLTLs. The results clearly show in this approach that the Bragg frequency is fixed by the value of the average capacitance and the more nonlinear the capacitance, the more abrupt the transition.

Furthermore, the Large Signal S Parameters proved to be important for optimum matching conditions and for the location of the input frequency in relation with the Bragg frequency.

Also, the behavior of the S_{21} parameter near the Bragg frequency gives additional information to complement a harmonic balance simulation concerning the prediction of the conversion efficiency.

This approach certainly represents a more accurate treatment of the effect of the degree of non linearity on the conversion efficiency.

Chapter V

Technology and Characterization of the CPW NLTL

Chapter V

Technology and Characterization of the CPW NLTL

V.1 Introduction

The aim of this chapter is the description of the process steps involved in the fabrication of the CoPlanar Waveguide (CPW) NonLinear Transmission Line (NLTL) which was designed in section III.3. A second part is devoted to the characterization under small signal and large signal conditions of the CPW NLTLs manufactured.

Globally, CPW NLTLs can be fabricated using as few as four masks. Note that the NLTLs were fabricated on semi-insulating InP epitaxial wafer.

The fabrication of the CPW NLTLs follows the processes used in any InP Monolithic Microwave Integrated Circuit (MMIC). The fabrication technologies for InP MMICs are largely discussed in reference [Kat92]. The book written by Williams [Wil84] remains basic in spite of dealing with GaAs technology. However, the process developed for the NLTLs has overcome a series of difficulties intrinsically related with its configuration and the active epitaxial structure employed.

The processing procedure will be described in detail in the following sections. It represents the latest process undertaken. However, earlier processes have been necessary in order to implement the final refinements, which could be improved in future processes.

V.2 Technology of the CPW NLTL

V.2.1 Active Epitaxial Structure

The active epitaxial structure depicted in figure V.1 corresponds to a double barrier InP-based Heterostructure Barrier Varactor (HBV) diode.

InGaAs	$1 \times 10^{19} cm^{-3}$	$5000 \AA$
InGaAs	$1 \times 10^{17} cm^{-3}$	$3000 \AA$
InGaAs	undoped	$50 \AA$
InAlAs	undoped	$50 \AA$
AlAs	undoped	$30 \AA$
InAlAs	undoped	$50 \AA$
InGaAs	undoped	$50 \AA$
InGaAs	$1 \times 10^{17} cm^{-3}$	$3000 \AA$
InGaAs	undoped	$50 \AA$
InAlAs	undoped	$50 \AA$
AlAs	undoped	$30 \AA$
InAlAs	undoped	$50 \AA$
InGaAs	undoped	$50 \AA$
InGaAs	$1 \times 10^{17} cm^{-3}$	$3000 \AA$
InGaAs	$1 \times 10^{19} cm^{-3}$	$1 \mu m$
InP substrate		

Figure V.1: Double barrier InP-based HBV epitaxial structure

This active epilayer structure consists in two blocking step-like InAlAs/AlAs/InAlAs multilayers, the $30 \AA$ thick intermediate semiconductor layer being surrounded by two $50 \AA$ thick InAlAs layers. Poor blocking of the barrier is alleviated both by making use of the $30 \AA$ thick AlAs layer grown under pseudomorphic conditions and by taking advantage of two barriers series integrated. The $50 \AA$ thick InGaAs spacer layers prevent the diffusion of dopant species into the barrier, stemming from three cladding layers ($3000 \AA$ thick) doped to $1 \times 10^{17} cm^{-3}$,

where the capacitance modulation takes place. At last, the highly doped ($1 \times 10^{19} cm^{-3}$) capping ($0.5\mu m$) and buried ($1\mu m$) InGaAs layers enable the implementation of low resistance ohmic contacts.

The epilayers were grown in a Gas Source-Molecular Beam Epitaxy machine (GS-MBE). The growth was performed without interruption on InP substrate, typically $400\mu m$ thick, at 520^oC.

Apart from the NLTL configuration itself, the active epitaxial structure raises a series of difficulties in its technological processing. First of all, a multilayer, as deep as $1.5\mu m$, must be etched. This step is aggravated by the preferencial polymer deposition which takes place on the Al-containing materials, namely the InAlAs/AlAs/InAlAs barrier. Secondly, the thickness of the capping and buried highly doped layers has been demonstrated to be necessary for the implementation of lower resistance ohmic contacts. The $1\mu m$ thick buried layer already involves an epitaxial growth on the leading edge of technology, with a relatively thick ternary layer lattice matched to the substrate. However, this should emphasize the difficulty in obtaining deeply etched structures. Finally, note that one is faced with a non-planar technology after the etch process.

V.2.2 Mask Set

On the basis of the work presented in section III.3, the mask set shown in figure V.2 was designed. It includes several line geometries resulting from the variation of the main parameters. Note that each NLTL follows the configuration proposed in the top view diagram of figure III.13 (on page 68). The various parameters were varied independently, taking as starting values the following:

- line length or diode number: 8 and 12 diodes
- center strip width: $w = 5\mu m$
- slot width: $s = 20\mu m$
- diode spacing: $d = 290\mu m$
- diode area: $A = 200\mu m^2$
- series resistance parameters: $r_1 = 40\mu m$ and $r_2 = 80\mu m$

Next, the parameter variation intended to observe the effect on NLTL performance is specified:

- line length or diode number: 5, 8, 10, 12 and 15 diodes
- center strip width: $w = 3\mu m$, $w = 4\mu m$ and $w = 5\mu m$
- slot width: $s = 15\mu m$, $s = 20\mu m$ and $s = 25\mu m$

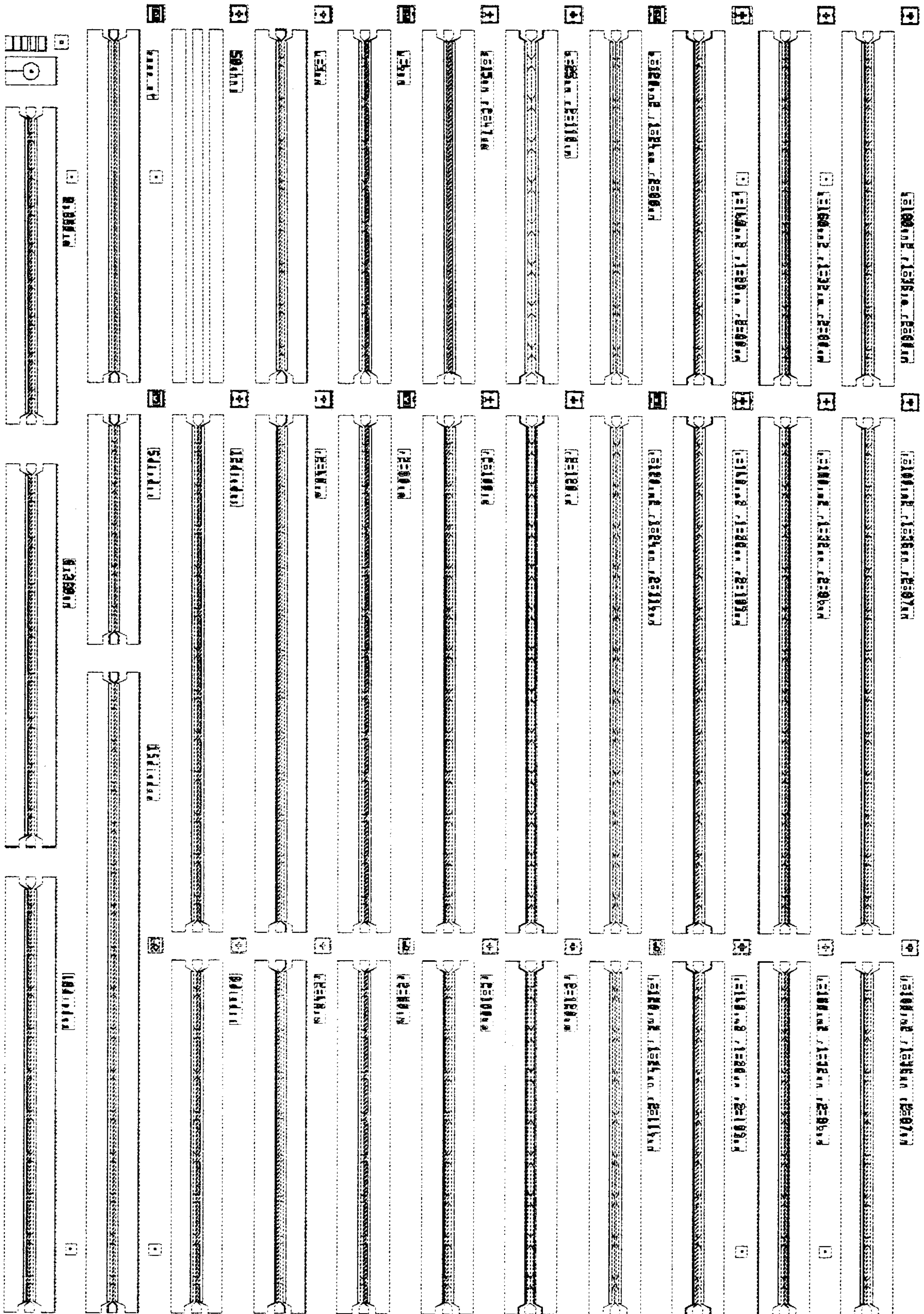

Figure V.2: Mask set general view

- diode spacing: $d = 260\mu m$, $d = 290\mu m$ and $d = 320\mu m$
- diode area: $A = 120\mu m^2$, $A = 140\mu m^2$, $A = 160\mu m^2$, $A = 180\mu m^2$ and $A = 200\mu m^2$
- series resistance parameter r_1: $r_1 = 24\mu m$, $r_1 = 28\mu m$, $r_1 = 32\mu m$, $r_1 = 36\mu m$ and $r_1 = 40\mu m$
- series resistance parameter r_2: $r_2 = 40\mu m$, $r_2 = 60\mu m$, $r_2 = 80\mu m$, $r_2 = 100\mu m$ and $r_2 = 120\mu m$

The diodes are simply positioned within the center strip by means of trapezoidal-shaped access areas realized in the highly doped n^+ lower layer. Note that the diode series resistance depends mainly on the parameters r_1 and r_2 depicted in figure III.13(a). The resistance of a trapezoidal-shaped conductor can be expressed as:

$$Rs = \rho \frac{s}{h(r_2 - r_1)} \ln(\frac{r_2}{r_1}) \tag{V.2.1}$$

where s is the slot width, ρ is the resistivity of the highly doped InGaAs layer and h its thickness.

Note that:

$$lim_{r_2 \to r_1} \rho \frac{s}{h(r_2 - r_1)} \ln(\frac{r_2}{r_1}) = \rho \frac{s}{hr_1} \tag{V.2.2}$$

which corresponds to the resistance of a rectangular-shaped conductor.

In the case where $r_1 = 40\mu m$ and $r_2 = 80\mu m$ and assuming the following $\rho = 3.1 \cdot 10^{-6}\Omega m$ and $h = 0.8\mu m$, the series resistance of the diodes results in a value of 0.7Ω, considering that the two trapezoidal-shaped access areas are in parallel.

This mask set includes four levels: the upper ohmic contact, lower ohmic contact, ground plane formation and isolation. Note the alignment difficulty in most of the steps, inherent to the requirements of the mask set.

In addition to the NLTLs, four special patterns are included in the left upper corner of the mask set, which will be now justified.

A diode ring-shaped configuration was contemplated in order to permit a quick assessment of the epilayer quality. The diodes, thus manufactured, can be characterized by positioning directly radio-frequency probes onto the top and side contacts. By this means, the intrinsic parameters can be measured without the need of de-embedding techniques.

The layout includes a Transmission Line Model (TLM) pattern implemented on the highly doped n^+ lower layer, which consists in four rectangular pads separated by different lengths. The TLM is the most widely used method for determining the ohmic contact resistance, the resistance being measured as a function of the gap spacing between the linear array of contacts.

There are also two test structures for reference purpose: a transmission line pattern following the NLTL configuration except from the trapezoidal-shaped access areas, which have been removed, and a second linear CPW observing the dimensions of the 50Ω access line. These patterns can provide information about the transmission line performance inclusive of all parasitics associated with the NLTL configuration itself.

V.2.3 Device Fabrication

The epitaxial structure has to undergo various processes. First, let us consider the fabrication sequence illustrated in figure V.3 (on pages 109, 110 and 111).

The first step is the deposition of the upper ohmic contact which will constitute the CPW center strip. Then, one must etch through the diode multilayer in order to reach the highly doped n^+ lower layer, where the deposition of the lower ohmic contacts is made in a third step. Next, a metallic overlay on the lower ohmic contacts will make up the ground planes. Finally, a wet chemical etch is used in order to render most of the wafer semi-insulating. Also in this step, in order to separate one diode from the other, the excess of highly doped n^+ is removed by a severe under-etching effect.

This brief description gives an overview of the technological steps. In the following sections, each processing step will be discussed in turn. Only photolithography has been required in all process.

V.2.3.1 Upper Ohmic Contact

Ohmic contacts are defined as a metal-semiconductor contact when the ratio of the potential drop across the contact versus the current flowing through the contact is linear or near-linear with a constant R_c. The contact resistance depends greatly on the doping level in the semiconductor, barrier height of the metal-semiconductor contact, carrier effective mass, dielectric constant and temperature. The review by Shen *et al.* [SGM92] presents a discussion of the recent and important research activities concerning ohmic contacts for III-V compound semiconductors.

A multilayer of Ni (150Å), Ge (195Å) and Au (390Å) is deposited by evaporation on the InGaAs layer. A layer of 500Å of Ti is then deposited on top of the Ni/Ge/Au trilayer and plays an important role in the isolation between the gold of the proper ohmic contact metallurgy and the overlay of 8000Å of Au. Finally, a layer of 150Å of Ti is evaporated to insure protection to the gold overlay during the reactive ion etching process. Indeed, the 150Å of Ti act as a surface protection layer or removable mask, as it will be removed during the plasma bombardment. Note that the Au layer can be removed more easily and this Au overlay is critical in the determination of the transmission line losses.

Rapid Thermal Annealing (RTA) is the last stage of the ohmic contact step. However, it will be done after the deposition of the second ohmic contact metallurgy.

Metal deposition follows the lift-off photolithography procedure. A common photoresist,

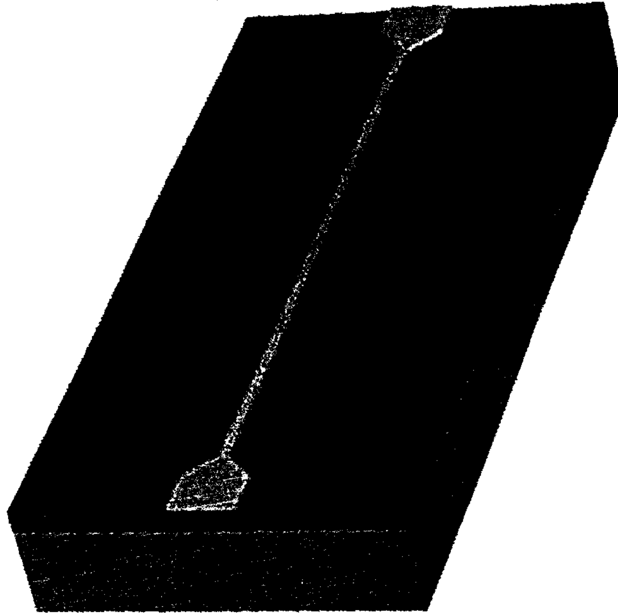

(a) Upper ohmic contact

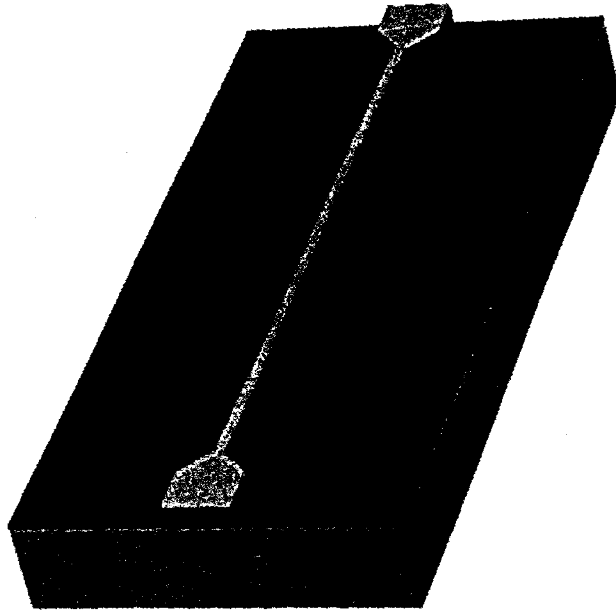

(b) Reactive ion etching

Figure V.3: CPW NLTL fabrication sequence

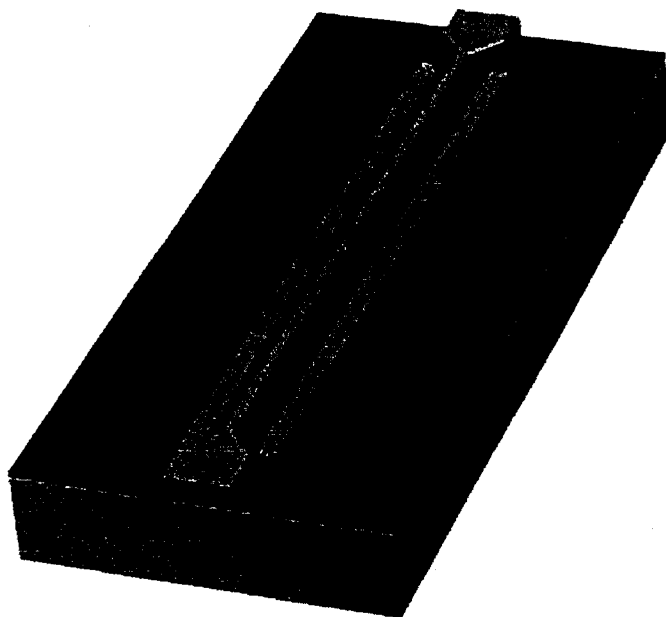

(c) Lower ohmic contact

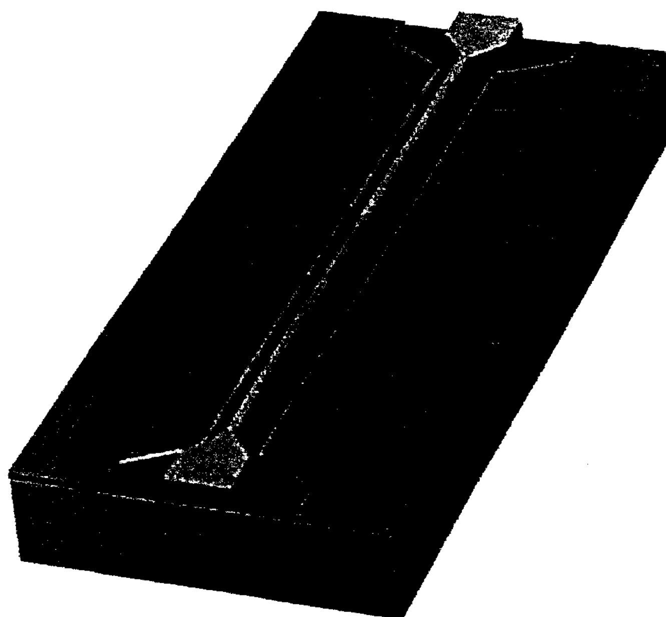

(d) Ground plane formation

Figure V.3: (continued)

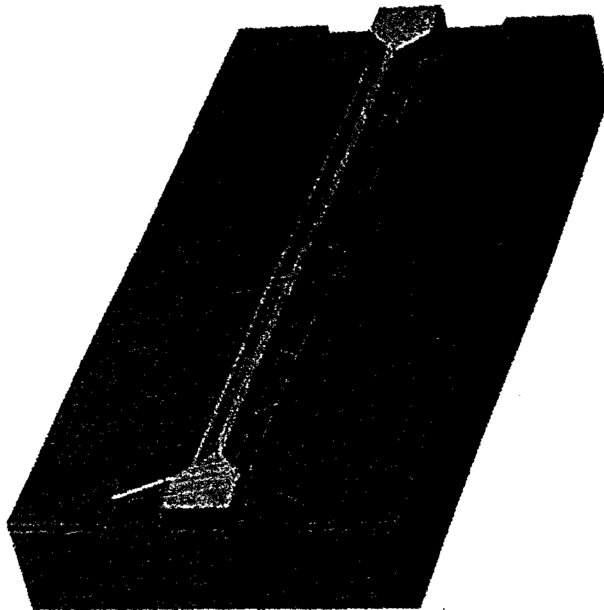

(e) Mesa isolation

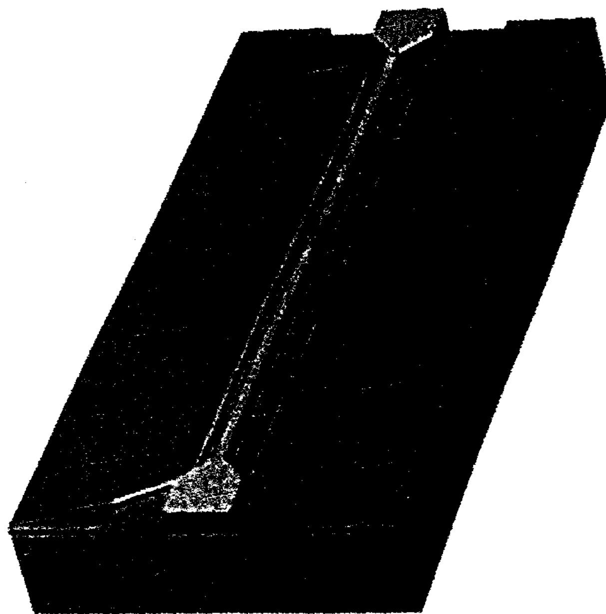

(f) Diode isolation

Figure V.3: (continued)

the $AZ-1518$ resist (Hoescht), is applied. Imparting a $5000rpm/s$ (acceleration) spin at $6000rpm$ (velocity) to the resist during $60s$, the film thickness expected is $1.5\mu m$, permitting reliable lift-off of the Au film. This thick metal layer is produced by a single lift-off without subsequent electroplating, which would result really hard considering the dimensions contemplated. The wafer is then pre-exposure baked at 110^oC during $1min30s$. At this point, the resist is surface treated by a plunge into a solution of $AZ-326$ during $30s$ (in order to harden the surface), rinsing next the wafer in distilled water (DI water) during $1min$.

Once the wafer has been exposed during $4s$ in the exposure aligner operating at $400nm$, it is then baked at 120^oC during $1min30s$ and developed in $AZ-400$ developer during $40s$. Previously, the $AZ-400$ developer has been three times diluted in distilled water. During the development process, adjustments are made in the exposure time.

At this point, note that the photoresist treatment used produces edges with negative slope, forming the so-called lift-off profile. Metal deposition will then result in a discontinuous film over the resist edges. By rinsing the wafer in acetone, the undesired metal is removed by dissolution of the resist, leaving only the metal which was deposited on the substrate.

Two optical views of the upper ohmic contact deposited on the substrate are shown in figure V.4.

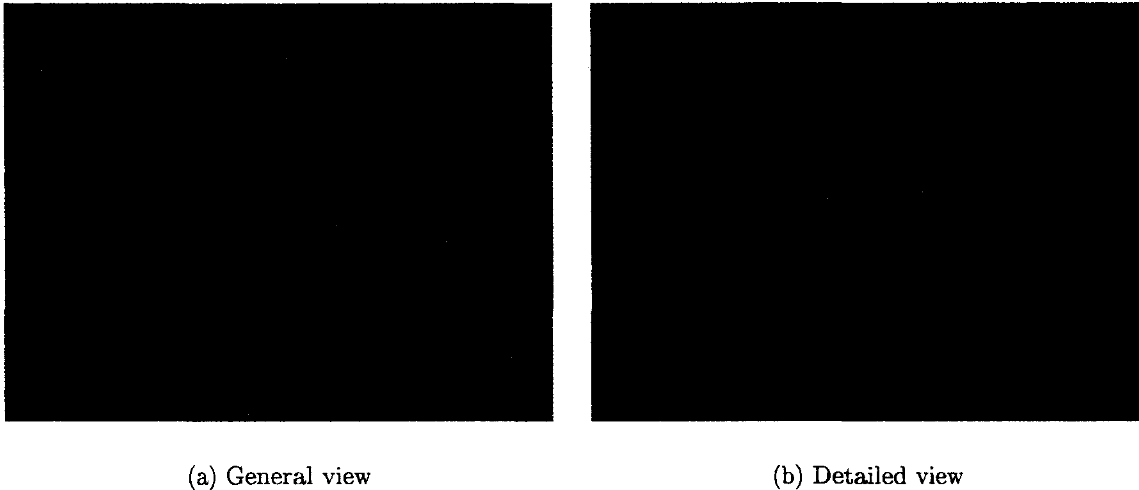

(a) General view (b) Detailed view

Figure V.4: Optical views of the upper ohmic contact

V.2.3.2 Reactive Ion Etching

In order to reach the highly doped n^+ lower layer, one must etch through the diode multilayer.

Reactive Ion Etching (RIE) consists in an anisotropic etching process produced by a positive ion bombardment of the substrate. The ion bombardment initiates or enhances fundamental reactions at the surface of the substrate, which leads to higher etch rates in the vertical direction than in the horizontal one. Wafers can be exposed to RIE plasmas of different gas mixtures.

RIE using Methane/Hydrogen/Argon (MHA) based plasma has been proved to be useful for smooth morphologies and anisotropic etches in InP-based materials. However, in deeply etched structures, the etch time is limited by polymer growth directly resulting of the MHA RIE. Furthermore, the Al-containing materials have been proved to be specially critical in the production of polymer. Indeed, in reference [SHM+93], Schramm *et al.* described a highly selective MHA RIE process that edged through InGaAs and which effectively terminated on an AlAs etch-stop layer, only $30\AA$ thick, or on an InAlAs Schottky contact layer.

A cyclical process, in which the Methane/Hydrogen/Argon RIE processes alternate with oxygen RIE, has then been chosen. In fact, the addition of oxygen is beneficial for polymer removal, which deposition constrains the achievement of deeply etched structures. Schramm *et al.* [SBH+97] investigated the various ways in which the oxygen may be incorporated into MHA RIE of deep (greater than $5\mu m$) InGaAsP/InP multilayers.

In this technique, the etching consists of alternating cycles of MHA etching and O_2 polymer removal cycles. Concerning the MHA RIE, the pressure was set to $65mTorr$, the self-bias voltage to $410V$, the power to $225W$ and the gas flows were $6sccm\ CH_4$, $50sccm\ H_2$ and $10sccm\ Ar$. The following oxygen plasma conditions were established: $100mTorr$, $220V$, $100W$ and $50sccm\ O_2$.

Let us precise now that the ohmic contact metallurgy acts as a metallic mask in the plasma etch process. The technique used has demonstrated to be capable of producing a clean anisotropic edge down to a $1.5\mu m$ depth, with line widths as small as $3\mu m$. The additional deposition of polymer has been overcome forcing more O_2 polymer removal cycles during the etch of the two InAlAs/AlAs/InAlAs barriers, which were monitored by a laser reflectometer. The change in the materials composing the wafer surface, namely the material interface, can be detected in the laser reflectometer plot of figure V.5. The crack observed in the last cycle announces the barrier.

In the Scanning Electron Microscope (SEM) photographs of figure V.6, the mesa obtained was $1.6\mu m$ deep, which results in an average etch rate of $123\AA/min$. Figure V.7 shows the relationship between the etch depth and the etch time.

Note that the wafer was efficiently bombarded during $135min$. However, one must also consider the time dedicated to the O_2 polymer removal cycles. In addition, cleaning processes are absolutely necessary during a large number of cycles and these clean-up cycles require a lot of time. In short, RIE results usually in a very long process.

Finally, as it has been already said, the $150\AA$ of Ti act as a removable mask, insuring protection to the gold overlay, because of its better resistance to MHA RIE. At the end of the plasma bombardment, it should be completely removed what can not be ensured. Thus, this lack of precision, joined to the inhomogeneity (typically $2000\AA$) introduced during the RIE process by the presence of polymer, results in a difficult determination of the etch depth. This imprecision in etch depth is critical and requires a compromise between the certainty that the highly doped n^+ lower layer has been reached everywhere but not attacked itself. In other terms, the deposition of the lower ohmic contact must be done on the buried n^+ layer. Also, the higher this layer, the lower the series resistance results. An average of $8600\AA$ of buried n^+ layer has been estimated after the RIE process.

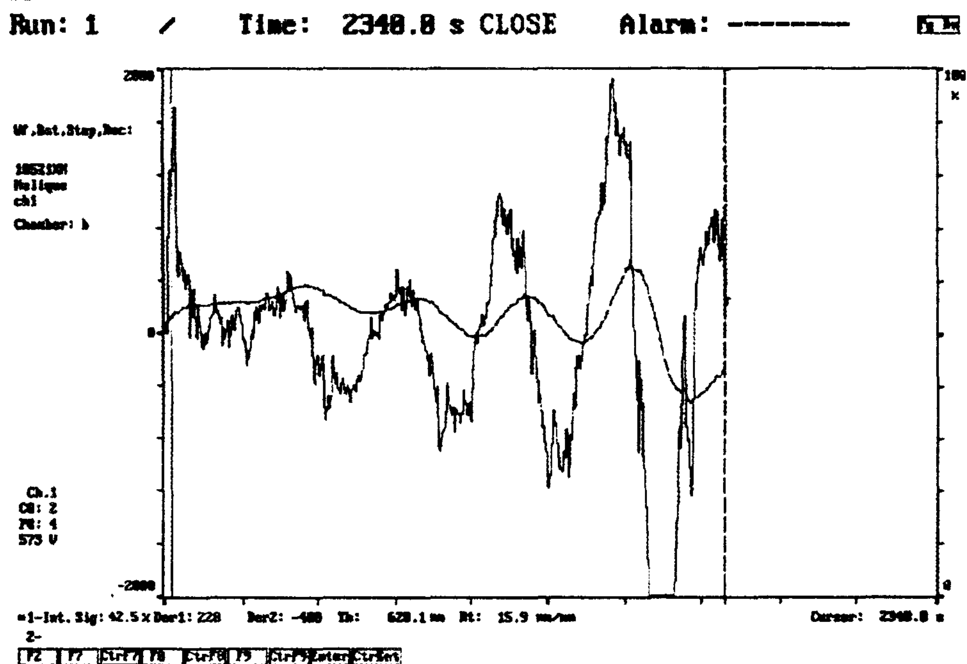

Figure V.5: Laser reflectometer plot announcing the barrier

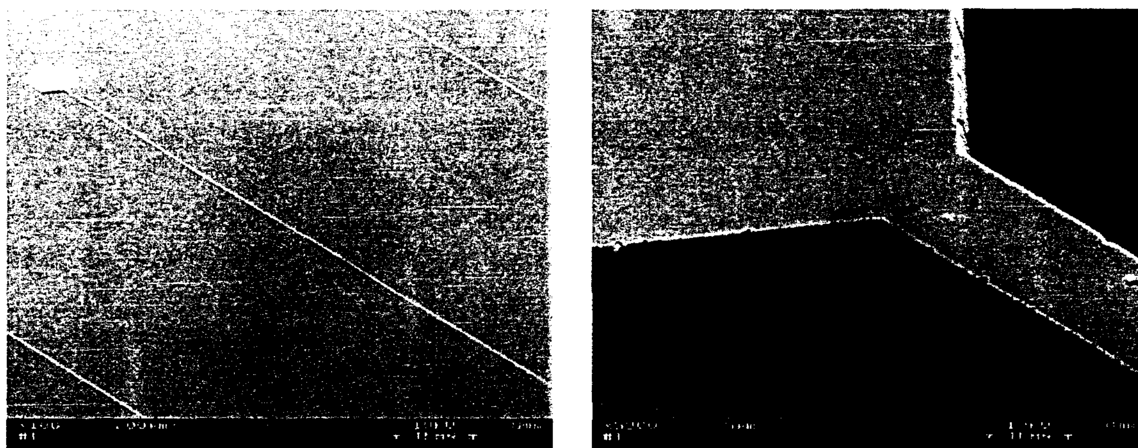

(a) General view

(b) Detailed view

Figure V.6: SEM photographs after the RIE process

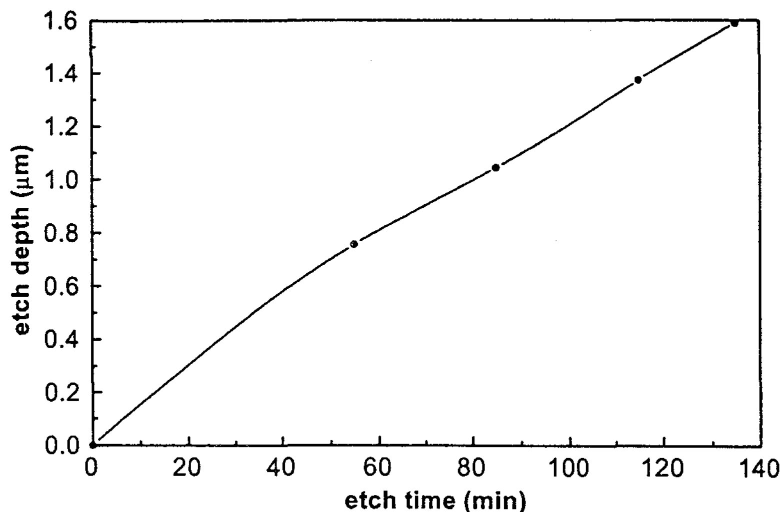

Figure V.7: Etch depth as a function of etch time

V.2.3.3 Lower Ohmic Contact

The second ohmic contact lies on the buried n^+ layer. The ohmic contacts to the buried n^+ layer form the diode cathode connections. This step of the process requires a second mask.

A Ni/Ge/Au/Ti/Au n-type metallization is deposited. The proper ohmic contact metallurgy is followed as well by $500\AA$ of Ti before deposition of the $2000\AA$ of Au.

Note that the contacts are patterned with a photoresist treated to outline the areas to be metallized. The same lift-off lithography technique used in the upper ohmic contact process is used here, except for a few differences. A $1.2\mu m$ resist thickness is obtained by a spin coating at $4500rpm$ and $5000rpm/s$ of the resist for $10s$. According to this film thickness, the wafer is pre-exposure and post-exposure baked during $1min$, half a minute less.

The lift-off is followed by a Rapid Thermal Annealing (RTA) at 400^oC in a H_2/N_2 gas flow. This treatment consists of rapidly raising the wafer temperature, holding this temperature for $40s$ and then reducing it back to room temperature. Under these conditions, the Ge and Au combine to form the eutectic mixture, the ohmic contact being formed when it diffuses into the upper part of the n^+ layer.

V.2.3.4 Ground Plane Formation

A third mask is used to pattern the ground planes. The lift-off lithography used is exactly the same than that described in section V.2.3.3. Here, a Ti $(1000\AA)$/Au $(4000\AA)$ metallic overlay fills up the areas to be metallized. After this step, no more metallic deposition will be required in the process.

V.2.3.5 Isolation

The process ends with an isolation treatment, which is carried out in two stages, by means of a negative mask.

V.2.3.5.1 Mesa Isolation

In order to render most of the wafer semi-insulating, one must etch through the buried highly doped n^+ layer. A wet etch is used here.

The $AZ-5214$ resist (Hoescht) has been used in this lithography. Applying a $4000rpm/s$ spin at $3000rpm$ to the photoresist during $60s$, the film thickness expected is $1.3\mu m$. The wafer is then pre-exposure baked at 120^oC during $2min30s$, after what it is exposed during $10s$ and developed in $MIF-726$ developer during $20s$. These standard parameters yield quasi-vertical edges at $400nm$ exposure. In order to increase the adhesion of the resist to the surface of the semiconductor, the wafer is baked again at 120^oC during $2min30s$.

In figure V.8, a SEM photograph shows the resist which remains on the wafer once it has been developed.

Figure V.8: $AZ-5214$ resist on the wafer once developed

At this point, the wafer is deoxidized by a dip, during $1min$, into a solution composed by one part of dilute NH_4OH (30%) and ten parts of H_2O. The wafer is then etched using a $H_3PO_4/H_2O_2/H_2O$ solution in the proportions 3 : 1 : 20. The mix etchant has been previously agitated using a magnetic stirrer bar.

The average etch rate is evaluated to $0.2\mu m/min$. The use of a H_3PO_4 etching solution yields a high selectivity between InGaAs and InP, ensuring a total control of the etch depth.

At this stage, each NLTL is isolated from the others and the trapezoidal-shaped access areas, realized in the highly doped n^+ lower layer, are already defined.

The four optical views of figure V.9 reveal the precision of the alignment, which is particularly critical in this technological step as the center strip must be preserved.

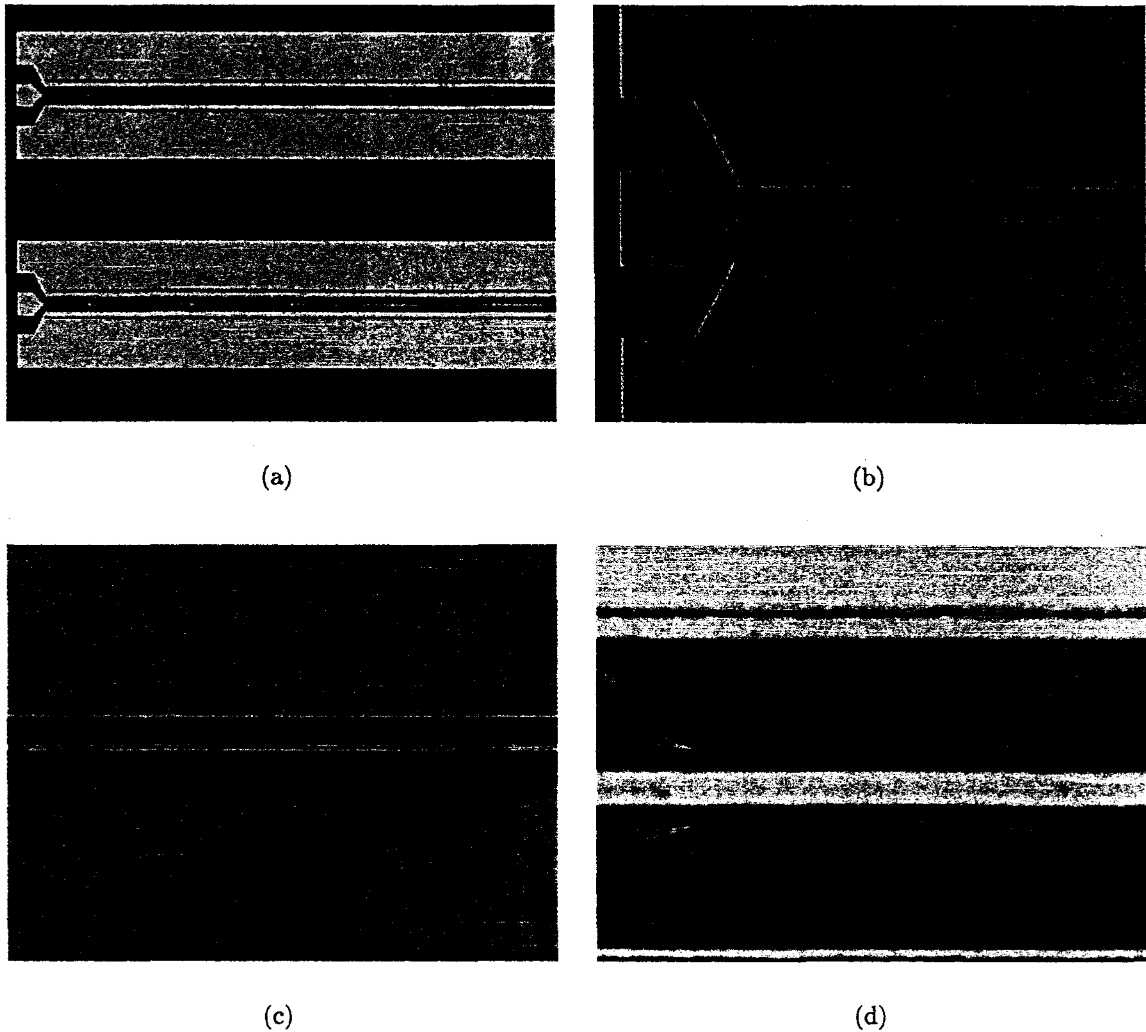

(a) (b)

(c) (d)

Figure V.9: Optical views of an NLTL

V.2.3.5.2 Diode Isolation

In order to separate one diode from the other, the excess of highly doped n^+ is removed, as well, by wet chemical etching. A severe under-etching effect promoted by the high selectivity between InGaAs and InP gives air gaps under the center strip of the CPW. In fact, the $4min$ etch has been prolonged two more minutes. Note that the vertical etch rate seems to be significantly higher than the horizontal one.

Finally, the resist is removed by rinsing the wafer in acetone. Thus, the isolation of the diodes is now insured and the device fabrication completed.

Figure V.10 shows two SEM photographs of a final NLTL. The air gaps under the center strip can be seen in figure V.11.

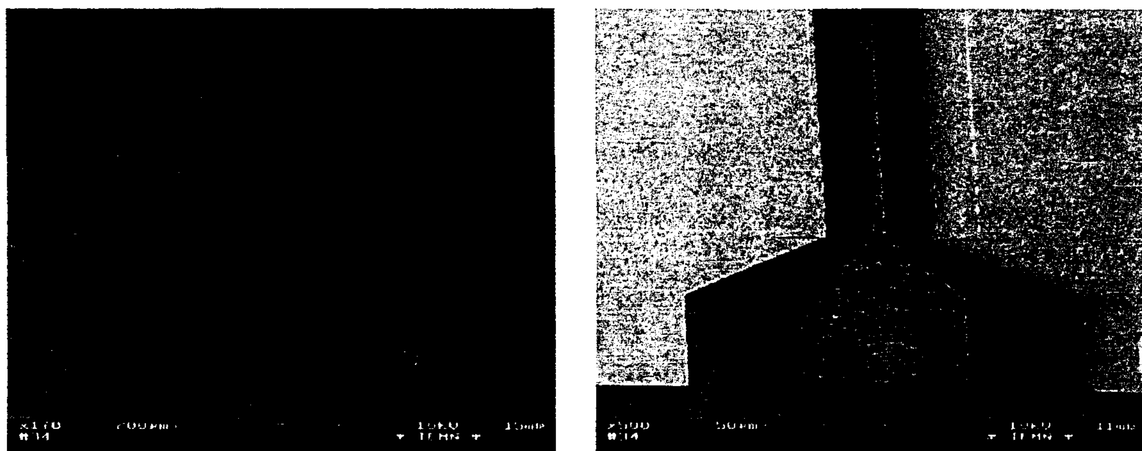

(a) General view (b) Detailed view

Figure V.10: SEM photographs of an NLTL

Figure V.11: Visible air gaps under the center strip in a SEM photograph

V.3 Characterization of the CPW NLTL

V.3.1 Linear Regime

V.3.1.1 Nonlinear Device Assessment

As it has been seen in section V.2.2, a diode ring-shaped configuration allows us a quick assessment of the epilayer quality, as the diodes, thus manufactured, can be characterized by positioning directly radio-frequency probes onto the top and side contacts. The intrinsic parameters typically obtained are presented in this section.

Figures V.12(a) and V.12(b) show respectively the C-V and I-V normalized characteristics of a double barrier InP-based HBV diode. However, the measurements are referred to a $20\mu m$ anode diameter diode, the distance between the concentric pads being $50\mu m$.

The measurements were performed by means of an $HP-8510C$ network analyzer. In particular, the C-V characteristic has been estimated at a frequency of $500MHz$. Note that this characteristic was proved to remain unchanged with frequency at least up to $85GHz$.

The double barrier HBV diode exhibits a normalized capacitance of $1fF/\mu m^2$ at zero volt bias and a capacitance ratio of 5 : 1, the saturation capacitance value being close to $0.2fF/\mu m^2$. In terms of current-voltage characteristic, the threshold conduction voltage is as high as $10V$ with a current density below $40A/cm^2$.

The ohmic contact resistance, epilayer resistance and spreading resistance are the main contributions to the series resistance of the device. The ohmic contact resistance was assessed experimentally at $2\cdot10^{-7}\Omega cm^2$ by TLM measurements. A theoretical study of this contribution is reported in reference [BGMS92]. From the three contributions, the spreading resistance is the most important. Moreover, it strongly depends on the geometry of the device, which makes its assessment more difficult. The spreading resistance was studied by Dickens in reference [Dic67]. In addition to this way of determining the series resistance, it can also be estimated globally from the S_{ij} parameters, by comparison with an equivalent circuit model in the frequency range $250MHz-40GHz$. After a comprehensive study, the series resistance has been found to be contained between 1Ω and 5Ω.

V.3.1.2 Unloaded Transmission Line Assessment

The mask set also includes two test structures designed for reference purpose only. In fact, these structures can provide information about all parasitics associated with the NLTL configuration itself.

At first, a CPW observing the dimensions of the 50Ω access line has been characterized. The measurements were made using a $37397C$ Anritsu vector network analyzer, which operating range is $40MHz-65GHz$. A transmission line pattern which dimensions are similar to the NLTL ones, but without the interconnecting trapezoidal-shaped areas, has also been considered. The S parameters of both transmission lines are shown in figures V.13 and V.14.

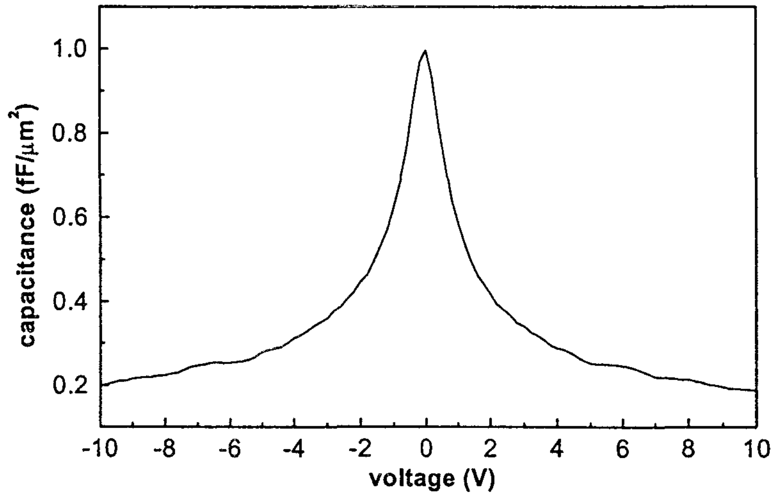

(a) C-V characteristic

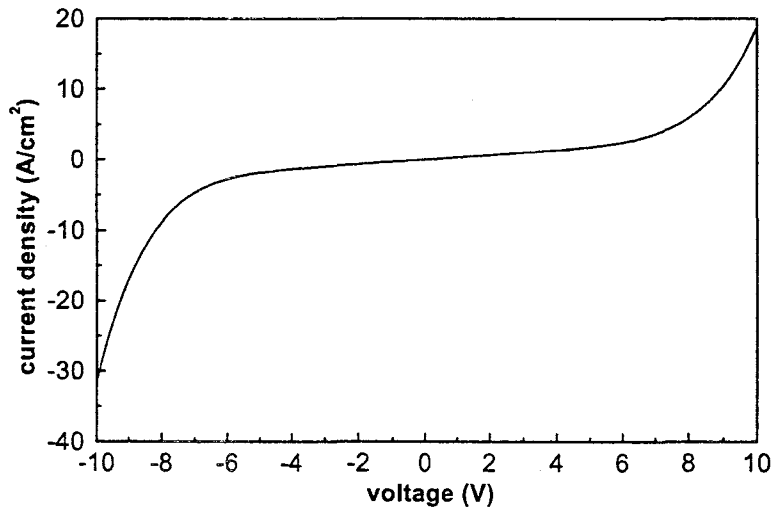

(b) I-V characteristic

Figure V.12: Measured capacitance-voltage and current-voltage characteristics of a double barrier InP-based HBV diode

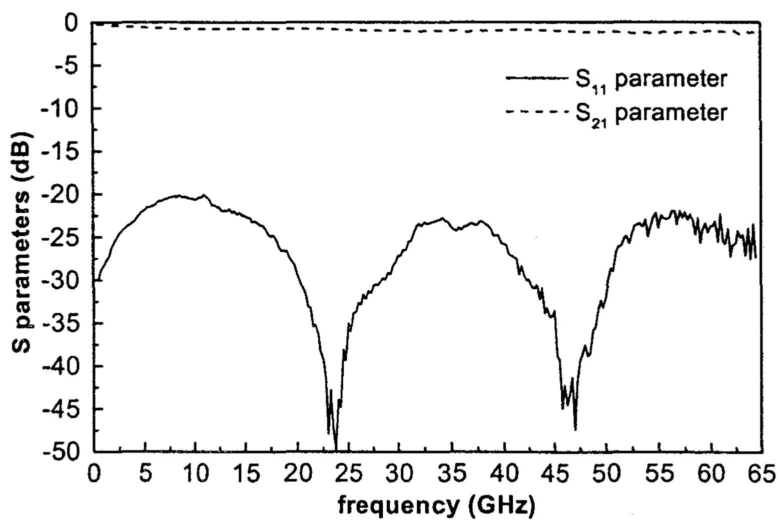

Figure V.13: S parameters as a function of the frequency for the access line

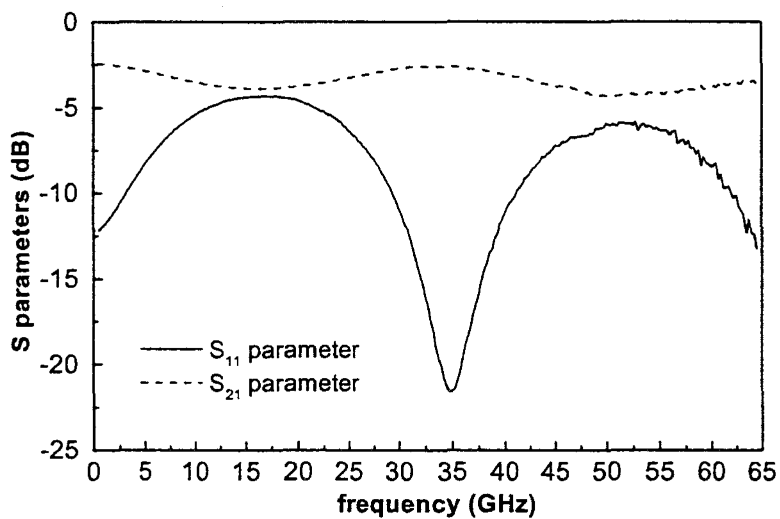

Figure V.14: S parameters as a function of the frequency for the non-loaded transmission line

Figures V.15(a) and V.15(b) show respectively the comparison between the S_{11} and S_{21} parameters of both transmission lines in a Smith chart representation.

The point on the right-hand side of the chart corresponds to the open-circuit position. Concerning the 50Ω access line, at low frequencies the S_{21} parameter begins at this point and moves clockwise with frequency following a spiral (lossy transmission line) through the angle $\phi = 2\pi/\lambda l$. Thus, the parameter l can be calculated and successfully compared with the length of the transmission line. Furthermore, the resonance frequency in figure V.13 has been proved to correspond to $l = \lambda/2$.

Note that the center point of the Smith chart represents a matching condition. The slight impedance mismatch, evidenced by the frequency dependent S_{11} locus, results from the special transmission line configuration, where the center strip is built on the active epitaxial structure. From the S_{11} parameter at $500MHz$ in figure V.15(a), a characteristic impedance of 53Ω can be easily calculated. This result is in good agreement with the High-Frequency Structure Simulator (HFSS) simulated value. In this same way, the non-loaded transmission line, following the NLTL configuration, has been proved to present a 82Ω characteristic impedance.

Finally, the losses as a function of the frequency are plotted in figure V.16 for both configurations. Even though in the tapered transition the characteristic impedance varies continuously in a smooth way from 50Ω to that of the non-loaded transmission line, physically it is difficult to couple a signal into a $5\mu m$ width CPW center strip, which could explain the additional losses. Of course, the transmission line center conductor width must be large in order to reduce losses. The difference between a $5\mu m$ and a $70\mu m$ width center strip is sufficient to observe an important gap in the transmission loss term.

V.3.1.3 NLTL Assessment

Finally, the 8-diode NLTLs were characterized in the linear regime before a comprehensive study in the nonlinear regime.

First of all, figures V.17(a) and V.17(b) show the C-V and I-V characteristics respectively.

The C-V characteristic results from the measurement of the S_{11} parameter at $500MHz$ under a dipole-type configuration. In this way, the result obtained corresponds to the equivalent capacitance of 8 diodes in parallel, the output being open-circuited. However, the last technological step, consisting in under-etching the center strip, is critical in the determination of the areas of the different diodes along the transmission line. It appears, moreover, that this technological step introduces a significant imprecision, which results in an inaccurate normalization of the capacitance versus the area. This should be taken into account at the time of interpreting figure V.17(a).

In short, these measurements have been carried in order to demonstrate the capacitance-voltage variation along the NLTL, as well as the presence of limited leakage current. As far as possible, a special attention has been paid in order to preserve to the utmost the NLTLs for characterization in the nonlinear regime. This explains the narrow voltage range in figures V.17(a) and V.17(b).

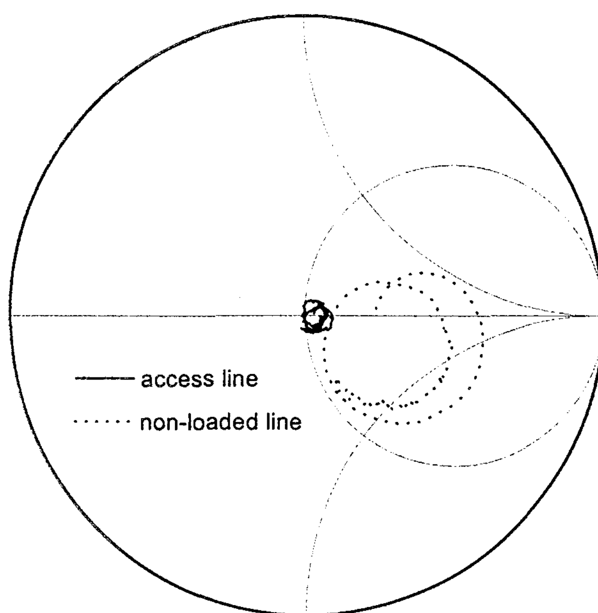

(a) S_{11} parameter

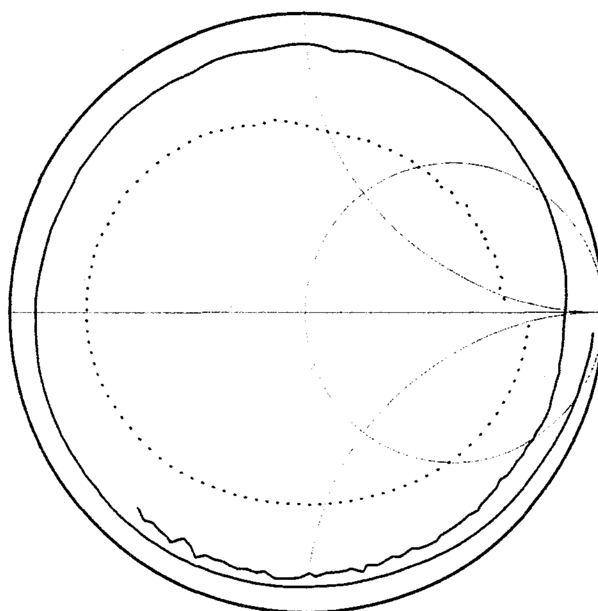

(b) S_{21} parameter

Figure V.15: Smith chart representation of the S parameters as a function of the frequency ($500MHz - 64.5GHz$) for the access line and the non-loaded transmission line

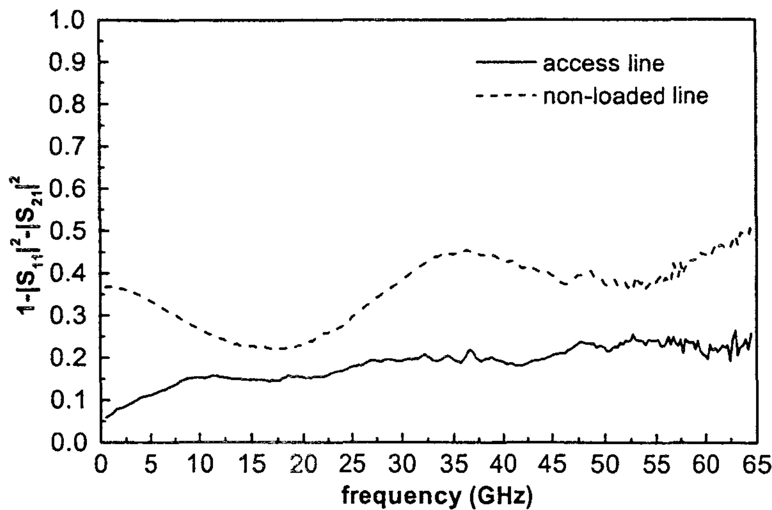

Figure V.16: Losses as a function of the frequency for the access line and the non-loaded transmission line

At this stage, the S_{21} parameter corresponding to an NLTL has been plotted in figure V.18 as a function of the frequency for different bias points. This has been possible thanks to an $HP-4142B$ modular DC source. The results obtained in the range $500MHz-64.5GHz$ seem to be in good agreement with the behavior already observed in figure IV.3(a) (on page 87), where in presence of losses the S_{21} parameter presents a slight slope up to the Bragg frequency. In addition, a more abrupt slope announces a smaller Bragg frequency. Indeed, figure V.18 shows that the slope becomes less abrupt with polarization, namely the Bragg frequency will be higher as expected. On the other hand, the transmission at $3V$ bias is better than at $0V$ bias, since the fabricated NLTL is optimized for impedance matched under large signal conditions.

V.3.2 Nonlinear Regime

V.3.2.1 Experimental Set-Up

Figure V.19 depicts the schematic of the large signal experimental set-up implemented. The corresponding photograph is shown in figure V.20.

An $HP-8360B$ series swept signal generator, operating between $10MHz$ and $50GHz$, was used as the pump source. The primary signal from the generator served to feed a medium power microwave amplifier. This $HP-8349B$ microwave amplifier, operating between $2GHz$ and $20GHz$, was able to deliver a maximum power of $24dBm$. Above $20GHz$, a roll-off of the delivered power is measured, so that only moderate power measurements can be conducted. For the measurements of the return loss magnitude, a $10dB$ directional coupler was mounted in a back configuration. The incident and reflected powers were recorded by means of an $HP-436A$ power meter preceded by an $HP-8485A$ power sensor calibrated at K-band.

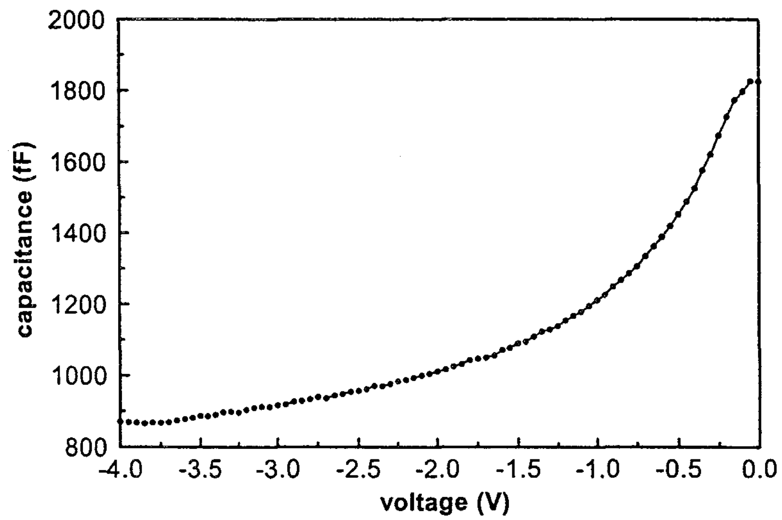

(a) C-V characteristic

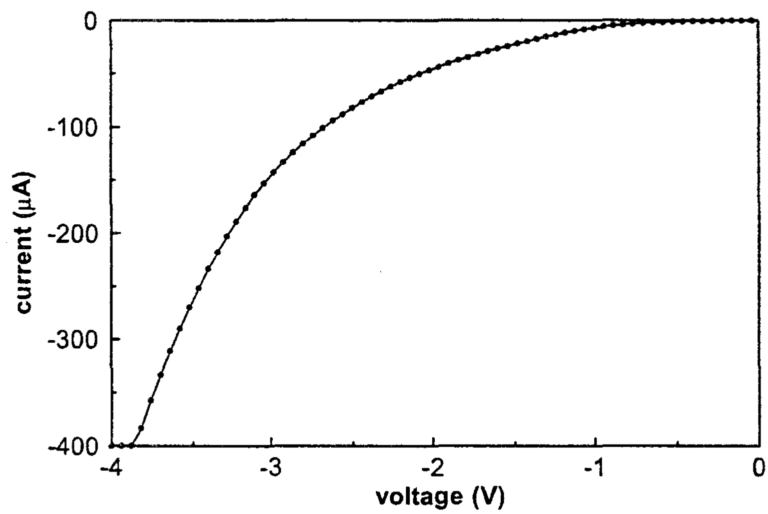

(b) I-V characteristic

Figure V.17: Measured capacitance-voltage and current-voltage characteristics of an NLTL

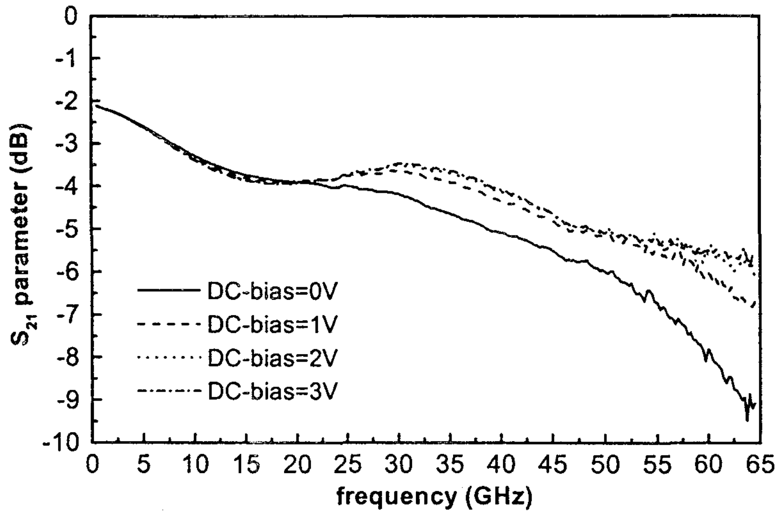

Figure V.18: S_{21} parameter as a function of the frequency for an NLTL varying the bias point of the diodes

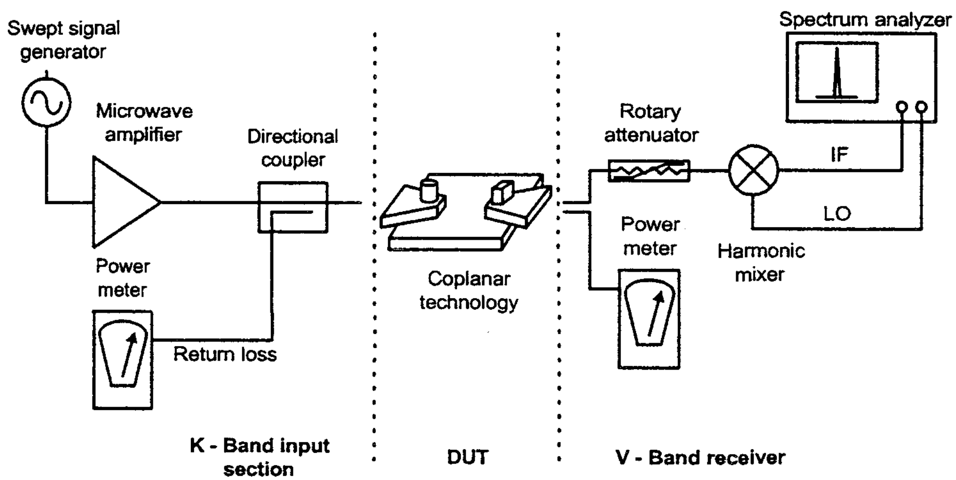

Figure V.19: Schematic of the large signal experimental set-up

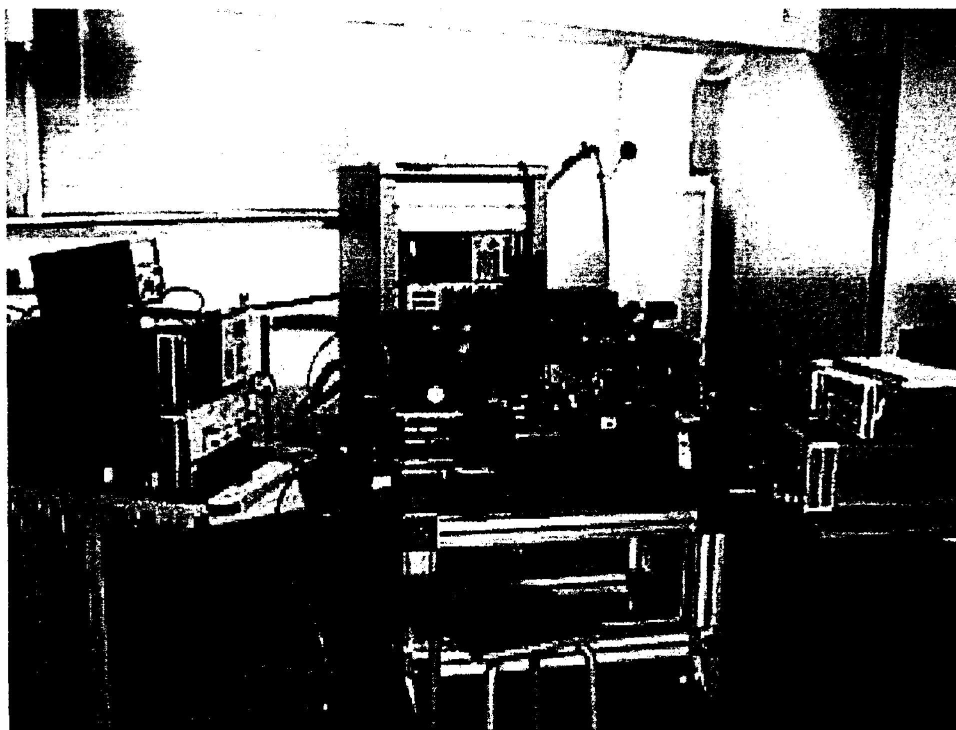

Figure V.20: Photograph of the large signal experimental set-up

The interface between the coaxial technology of the input section just described and the waveguide technology of the output one, via the uniplanar configuration of the Device Under Test (DUT), was carried out through radio-frequency probes.

The output section was mainly devoted to the heterodyne detection of the up-converted signal using a spectrum analyzer, from which the $HP - 70907A$ external mixer interface was used. A special attention was paid to avoid the saturation of the $HP - 11970V$ harmonic mixer, which explains the presence of the rotary attenuator. The analysis in the band of major concern was carried out through a $WR15$ waveguide, operating between $50GHz$ and $75GHz$ (V-band). For the power measurements, a calibrated bolometric head was used just as in the input section, followed by an $HP - 432A$ power meter.

Figure V.21 shows a photograph including the probe station equipped with a high performance microscope. A zoom in view on the radio-frequency probes and the DUT is presented in figure V.22.

Figure V.23 shows a photograph of the $HP - 70000$ spectrum analyzer system composed by three sections, an Intermediate Frequency (IF) section, a local oscillator and an external mixer interface. As already mentioned, this latter section was the one used in the large signal experimental set-up. The spectrum analysis is presented on an $HP - 70206A$ system graphics display.

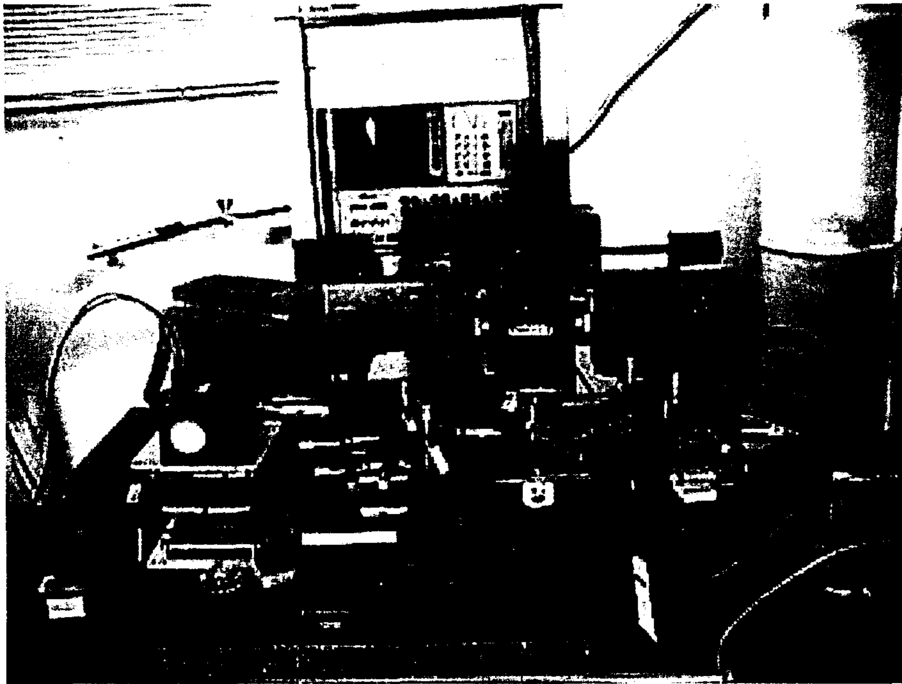

Figure V.21: Photograph of the probe station

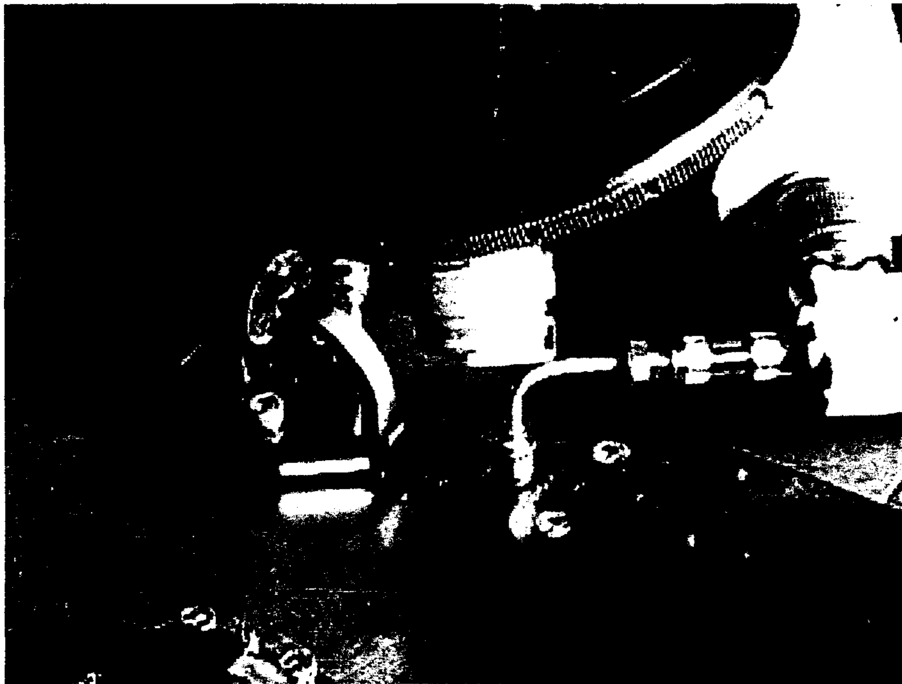

Figure V.22: Photograph of the radio-frequency probes

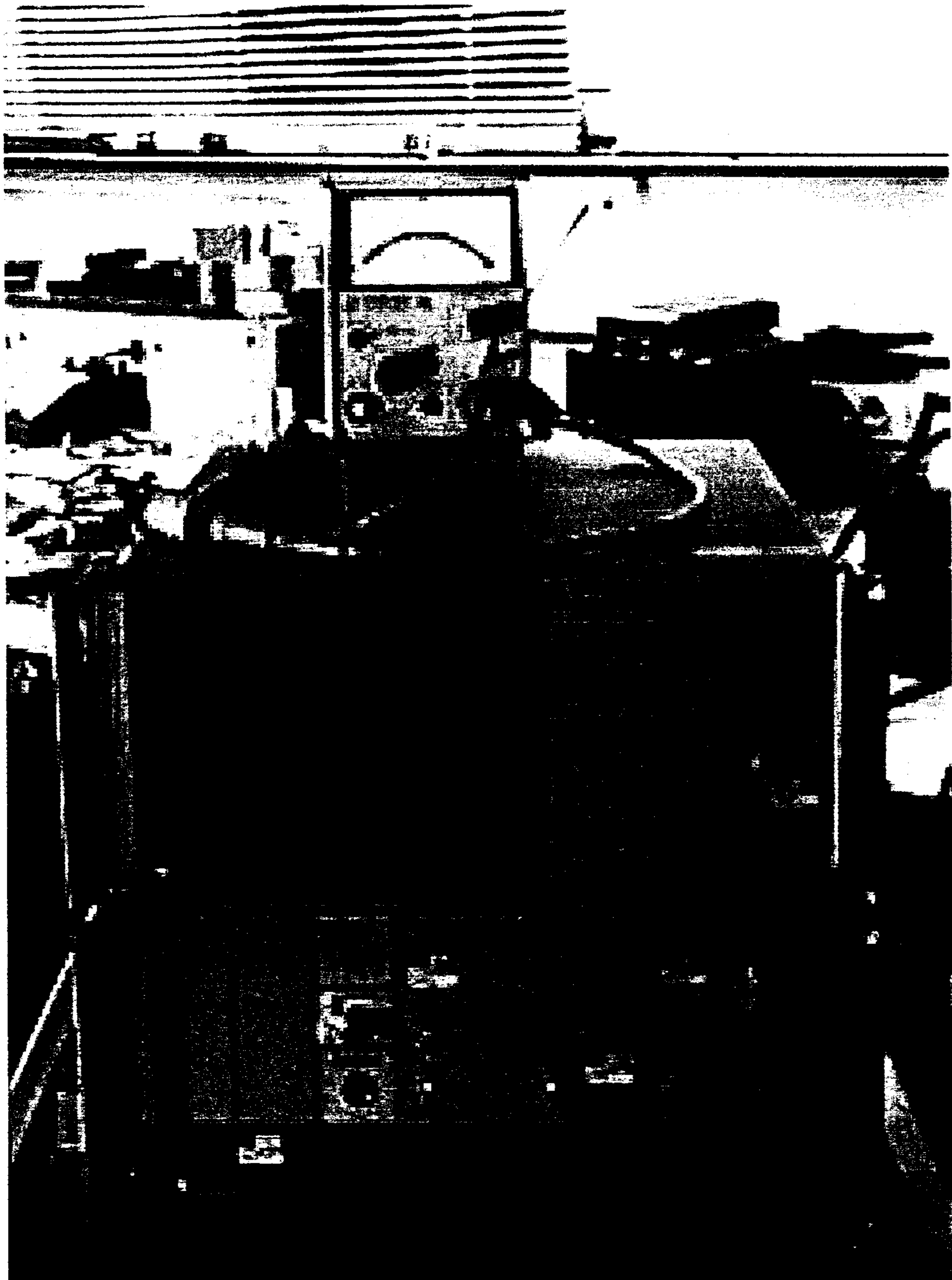

Figure V.23: Photograph of the spectrum analyzer system

V.3.2.2 Multiplier Performance

In this section, large signal measurements have been carried out under moderate pump conditions thanks to the experimental set-up just described. Different aspects concerning the NLTL performance will be presented, to be more specific, the number of sections, the broad-band behavior and the input power of an NLTL.

V.3.2.2.1 Number of Sections

First of all, a series of measurements were performed in order to determine the number of sections for an optimum performance in terms of conversion efficiency. Figure V.24 shows the conversion efficiency to the third harmonic as a function of the number of sections. In this particular case, the input frequency was set to $20GHz$ and the available input power to $10dBm$. The results of figure V.24 confirm what was already predicted by simulation in section III.3.5. An NLTL of 8 diodes seems to be a good trade-off between the length necessary to obtain a sufficient distortion and the subsequent transmission line losses.

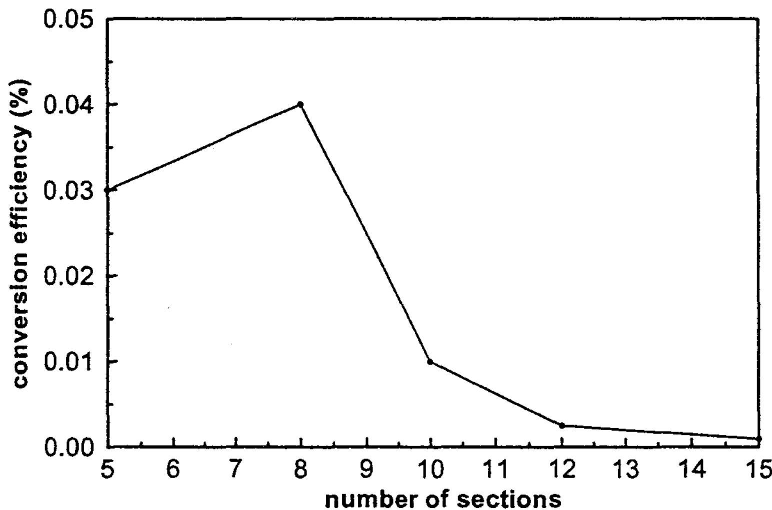

Figure V.24: Measured conversion efficiency as a function of the number of sections

In the following, the measurements will focus on the radio-frequency assessment of an 8-diode prototype.

V.3.2.2.2 Broad-Band Behavior

In order to determine the broad-band behavior of the NLTLs, measurements at $10dBm$ have been conducted varying the input frequency in the range $17GHz - 23GHz$. Figure V.25 has then been obtained.

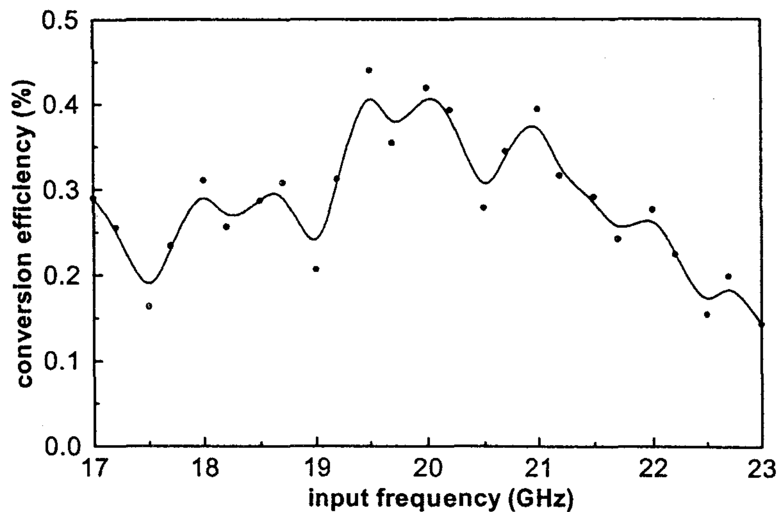

Figure V.25: Measured conversion efficiency as a function of the input frequency

The results confirmed that the line was properly designed for a $20 \times 3GHz$ operation, as the maximum conversion efficiency was achieved around $20GHz$. The corresponding conversion efficiency peak observed at the spectrum analyzer is shown in figure V.26(a). The peak in figure V.26(b) has been plotted in a narrower frequency scale. Note that the up-converted signal peak is well centered at $60GHz$.

Additional spectrum analyses were performed at Q-band (second harmonic) and W-band (fourth and fifth harmonics). The frequency tripler showed an effective rejection of odd harmonics owing to the capacitance-voltage symmetry, as well as of the fifth harmonic due to the Bragg reflection.

Figure V.27 shows the conversion efficiency to the fifth harmonic as a function of the input power, the input frequency being fixed to $12GHz$. Figure V.28 illustrates the spectrum recorded in the case of an available input power of $10dBm$ for the $12 \times 5GHz$ operation.

V.3.2.2.3 Input Power

The last series of measurements concerned the up-converted efficiency at $20GHz$ for an 8-diode structure. The study of the conversion efficiency as a function of the input power did not show a saturation effect, as shown in figure V.29. In fact, there is still room for conversion efficiency improvement.

About 1% conversion efficiency to the third harmonic was the highest achieved for $20dBm$ of available power source. It can be shown that these moderate pump conditions do not allow to pump the diodes over the full voltage range, typically a $20V$ peak-to-peak value for proper operation. Further improvements in terms of conversion efficiency are expected under harder pump conditions, as it implies larger nonlinearity and better large signal matching.

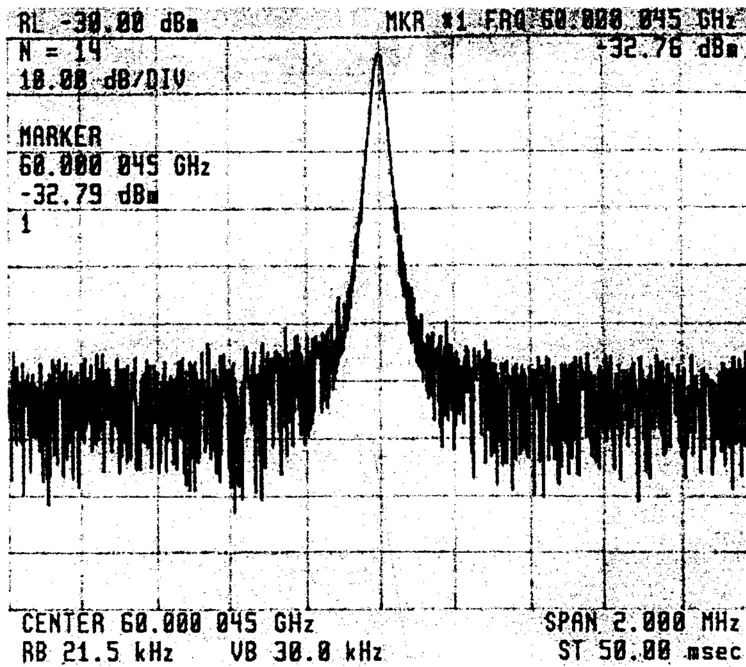

(a) In a larger frequency scale

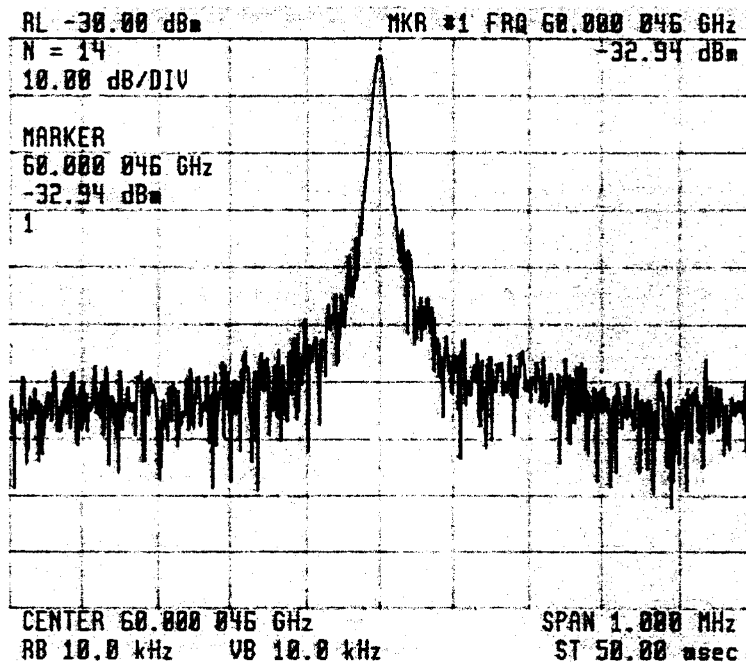

(b) In a narrower frequency scale

Figure V.26: Conversion efficiency peak shown at the spectrum analyzer

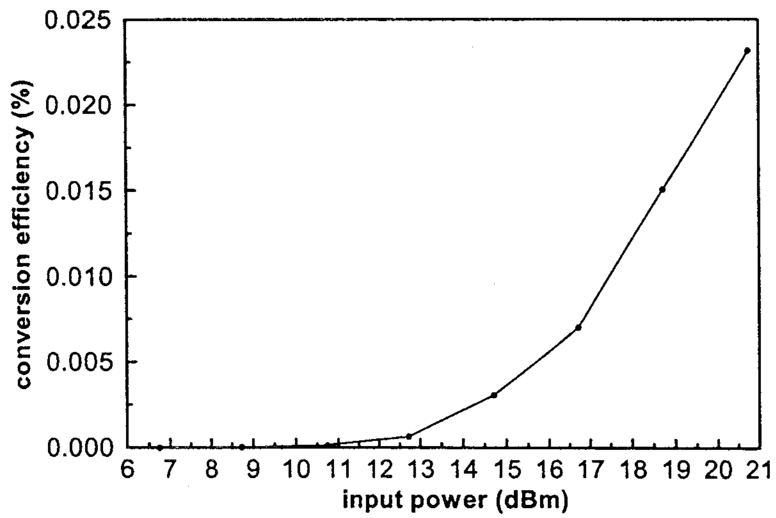

Figure V.27: Measured conversion efficiency to the fifth harmonic as a function of the input power

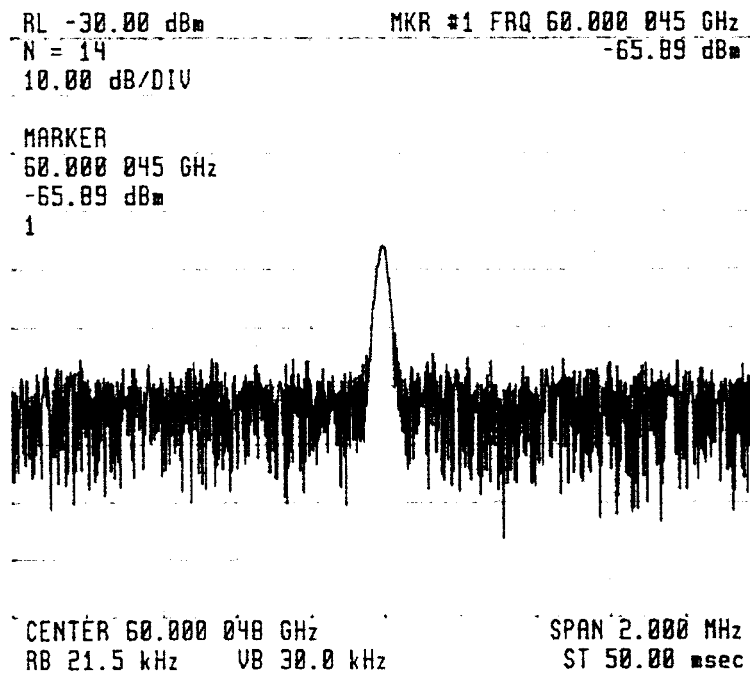

Figure V.28: Conversion efficiency peak of the fifth harmonic shown at the spectrum analyzer

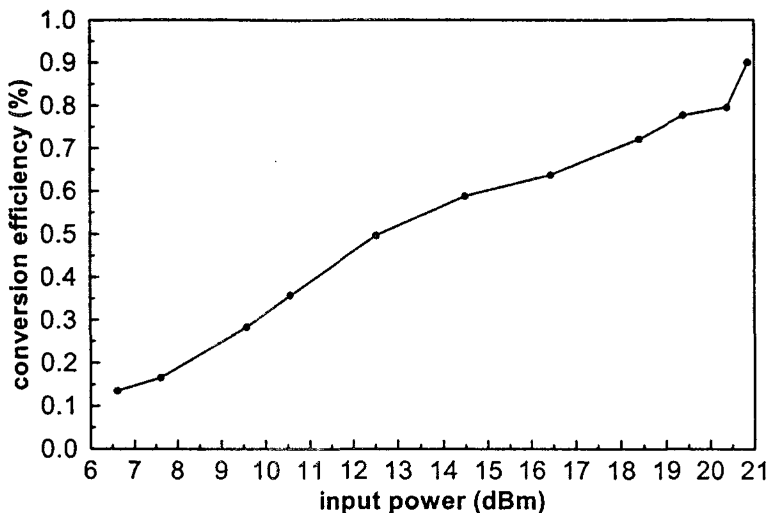

Figure V.29: Measured conversion efficiency as a function of the input power

V.4 Conclusion

NLTLs loaded by high-quality HBV diodes have been fabricated in a monolithic coplanar technology for the first time to our knowledge. The devices were designed for a $60GHz$ output frequency tripler. The double barrier HBV diodes exhibited a capacitance ratio of 5 : 1, a normalized capacitance of $1fF/\mu m^2$ at zero volt bias and an avalanche breakdown voltage in excess of $10V$. Under moderate pump conditions ($20dBm$), a tripling operation with a 30% bandwidth was demonstrated. An unsaturated 1% conversion efficiency was obtained for an 8-HBV prototype.

The preliminary experimental results are in agreement with the small and large signal regime analysis and, in this way, open up new horizons through harder pump conditions and optimized technology. In fact, transmission line and diode losses, which are determinant in these distributed approaches, could be further optimized by thicker metallic overlays, digited metallic contact pads and an airbridge technology. The transfer onto quartz of discrete devices, recently demonstrated in reference [ADM$^+$00], could be interesting for this distributed technology.

Finally, note that the interpretation of the measurements was quite difficult. The imprecision introduced by the severe under-etching effect, which was required for diode isolation, was the main cause. In addition, only one process has been completed successfully for the time being. Given that this involves few NLTLs, the systematic study of the parameter variation, which was planned at the beginning in order to observe the effect on NLTL performance (section V.2.2), has not been possible. After these preliminary results, measurements under harder pump conditions are at the moment in progress. In addition, an hybrid version which would alleviate the difficulties of fabrication encountered in a full monolithic approach is considered at present.

Conclusion and Prospects

For the last three decades, NonLinear Transmission Lines (NLTLs) have been widely studied. Nowadays, NLTLs are used in a large variety of applications. From the main three NLTL applications described in chapter I, harmonic generation is the one developed in this thesis.

The work presented here mainly concerned the design and fabrication of InP-based Heterostructure Barrier Varactor (HBV) NLTLs. For the first time to our knowledge, NLTLs loaded by high-quality HBV diodes have been fabricated in a monolithic coplanar technology. The novelty arises from the use of HBV diodes grown on InP substrate to be the nonlinear elements of our NLTLs. This choice was motivated by the record performances in terms of output power and conversion efficiency obtained in our group. In chapter II, the most common transmission lines loaded with the most common varactor diodes are reviewed.

In particular, the NLTLs were designed for a $60GHz$ output frequency tripler. Chapter III provides the design rules for NLTL harmonic generation ending up at a monolithic integrated coplanar prototype. Under moderate pump conditions ($20dBm$), an unsaturated 1% conversion efficiency was obtained. Through harder pump conditions, further improvements in terms of conversion efficiency are expected. Since the first attempt has already provided experimental results in agreement with the small and large signal regime analysis, it is therefore not surprising that an optimized technology would alleviate the difficulties described in chapter V, helping the conversion efficiency ratio.

Large Signal S Parameter analysis was discussed in chapter IV. The large signal technique enables us to simulate the NLTL globally, namely including all nonlinear effects. In this way, the determination of the large signal Bragg frequency is possible while the transmission behavior of the NLTL provides a better understanding of the frequency filtering aspect.

It is well known that harmonic generation in NLTLs is based on soliton-like propagation. For that reason, a description of soliton-like propagation in terms of NLTL characteristics was addressed in reference [Mar00], where an approximate equation was derived from the lumped equivalent circuit model. This model is based on the decomposition of a broad input pulse into a train of solitons. Since frequency multipliers rely on the interaction between two or more solitons, the understanding of NLTL harmonic generation in terms of soliton-like propagation does not seem straightforward. However, it is believed that such an approach could help towards millimeter wave NLTL multiplier design.

Still from the simulation side, tapered NLTLs for frequency multiplier applications suffer from less development than tapered NLTLs for shock wave generation. In this case, even a systematic method for the design of tapered NLTLs was developed in reference [JFF+98].

Recently, a special effort was paid to the design of tapered NLTLs for frequency multiplier applications. Preliminary simulations have already demonstrated the accuracy required in the determination of the different Bragg frequencies in order to enhance a specific harmonic. The use of tapered NLTLs could be the most efficient solution for higher order harmonic generation.

In these distributed approaches, transmission line and diode losses are determinant. In this sense, from the fabrication side, the NLTL losses could be further reduced by an airbridge technology.

The use of an air bridge as the CoPlanar Waveguide (CPW) center conductor appears as an efficient alternative to the under-etching effect chosen in this thesis. Here, a wet chemical etch is used to isolate the different lines and to define the periodic bottom diode connections, the under-etching effect enabling to fully define the diodes in the longitudinal dimension. Thus, our prototype could be considered in between a fully distributed approach and a periodically loaded approach. Indeed, the under-etching effect preserves the active layers, only removing the excess of highly doped n^+ lower layer. As the center conductor still lays on the active layers over the whole length, the transmission takes place partly in the semiconducting medium, which has not been semi-insulating, with the subsequent degradation in terms of losses. In this way, an airbridge technology avoids the excess of active material which introduces significant losses. Note that the main reason for this choice was to alleviate the technological difficulty for the first attempt. However, the airbridge inter-connection technology is mature in our group for the integration of HBV diodes in coplanar transmission lines, and hence airbridge-based NLTLs could be developed at short term.

Airbridge-based NLTLs have been already demonstrated in reference [BAR95] for a GaAs elevated CPW. This technique is opposed to a proton implantation process used in references [Rod87, Cas93]. It is well known that a planar processing is usually preferred. However, implant isolation is not always possible. An additional problem stems from the depth of the layers to be isolated. As an alternative to using a comparable process to implant isolation on GaAs, a fully elevated CPW on silicon substrate, with diode pillars supporting both the center conductor and ground conductor air bridges, was addressed in reference [BKW+98]. The advantages of this technology are to minimize the capacitance per unit length and the substrate effects of the waveguide.

Another technology, implemented in our group and reported in references [SDH+96, DCM+99], concerns the fabrication of micromachined or membrane transmission lines. Therefore, NLTLs could be manufactured on thin GaAs membranes, with the advantages demonstrated by simulation in reference [SBM+97]. The velocity would approach that of free space as in the case of an elevated CPW-based NLTL.

Other possibility consists of improving the NLTL performance with higher performance diodes. Important advances have been demonstrated in reference [ADM+00] on the basis of the transfer of InP-based HBV diodes onto quartz. In particular, this technology can dramatically reduce both the parasitic resistance and capacitance. The use of a transfer-substrate process can avoid conventional planar side contacts through the buried highly doped layer, which introduces the so-called spreading resistance. Indeed, a new configuration incorporating a Buried Metal Layer (BML), which directly contacts the back side of the mesa, has demonstrated further performances in terms of series resistance.

NLTLs have been used for a wide variety of applications. Even if only nonlinear applications have been extensively detailed in chapter I, the small signal characteristics of the NLTL can also be exploited. When used in the linear regime, an NLTL can be designed as a broad-band time delay/phase shift element capable of producing a continuously variable phase shift. On one hand, the phase velocity is controlled by the applied bias and independent for frequencies well below the Bragg frequency, on the other hand.

In 1996, an NLTL-based broad-band phased antenna array was fabricated in reference [ZHL+96]. Indeed, a phased antenna array consists of multiple antenna elements which include those time delay/phase shift devices. When used in phased array antennas, NLTL-based broad-band time delay/phase shift devices emerge as an efficient alternative to switched sections of transmission lines. The main advantage is that the phase can be continuously varied. Thus, fine tuning of the phase provides a more accurate beam control. Also, only one control line is needed to bias the varactor diodes.

In reference [NY99], a GaAs monolithic version of a distributed analog phase-shifter circuit was presented, consisting of a CPW periodically loaded with varactor diodes operating at $20GHz$. An alternative Ka-band phase-shifter circuit fabricated on high-resistivity silicon was reported in reference [ENL+00], relying on thin film ferroelectric material parallel plate capacitors.

In reference [BR98] was proposed the fabrication of distributed MicroElectroMechanical Systems (MEMS) transmission lines operating up to $60GHz$. By applying a single analog control voltage to the center conductor of the CPW, one can vary the height of the MEMS bridges, loading the transmission line with a pull-down voltage dependent parallel capacitance. Thus, it results in a broad-band time delay phase-shifter.

Finally, note that in 1987, a broad-band phase modulation of carriers from DC to millimeter wave frequencies, based in the broad-band voltage-controlled linear phase-shifter, was already proposed in reference [RBA87].

An NLTL is basically a CPW periodically loaded with varactor diodes. In the literature, NLTLs have also used ferroelectric material capacitors [WTS91, IOY+97, ENL+00] as the nonlinear elements.

Other type of CPW structures periodically loaded are reported in references [SWY+91, BR98, GKA98]. In reference [SWY+91], a CPW was capacitively coupled to periodically spaced sampling channels, which opens up new possibilities in broad-band optoelectronic time division demultiplexing.

As it has been just mentioned, the CPW loaded with MEMS bridges was proposed in reference [BR98], resulting in a broad-band time delay phase-shifter. In addition, it can result in a broad-band switch when the MEMS are pulled down.

Finally, a capacitively loaded CPW resonator was studied in reference [GKA98], in particular the interdigited capacitor and slot-loaded CPW resonator. These resonators have a smaller size and a higher performance as compared to the conventional half-wavelength CPW resonator. Besides, the interdigited-loaded CPW has a higher dispersion than the slot-loaded CPW resonator.

The distributed characteristic inherent in NLTLs is responsible for frequency dispersion,

which causes frequencies close to the Bragg frequency to propagate more slowly than other frequencies.

In this sense, namely filtering aspects, there is a striking analogy with Photonic Band Gap (PBG) materials. PBGs are crystalline-type artificial structures which exhibit bands of frequencies where the electromagnetic waves are not able to propagate. Indeed, localization effects inside these periodic structures can be explained in terms of Bragg reflection and Fabry-Perot resonance effects, as in reference [CVL97].

One of the reasons for the interest in PBGs arises from the possible application of these materials as antenna substrates. In the photonic band gap, the energy is fully reflected and the PBG material acts as a reflector if irradiated by an antenna. The equivalent plane reflector method was described in reference [Fer98]. Preferential directions can be pointed out depending on the position of the antenna with respect to the artificial reflector. Thus, PBGs have the peculiar quality of enhancing or tailoring the antenna radiation pattern. On the other hand, a modal analysis of guiding structures patterned in a metallic photonic crystal was carried out in reference [DCF+98].

More recently, with the analysis of three dimensional PBG structures, the attachment of nonlinear devices to PBGs has been demonstrated in reference [DVL99] as an emerging technology for applications at microwave and millimeter wave frequencies.

Bibliography

[ADM+00] S. Arscott, T. David, X. Mélique, P. Mounaix, O. Vanbésien, and D. Lippens, *Transferred-Substrate InP-Based Heterostructure Barrier Varactor Diodes on Quartz*, IEEE Microwave and Guided Wave Letters **10** (2000), no. 11, 472–474.

[BAR95] U. Bhattacharya, S. T. Allen, and M. J. W. Rodwell, *DC-725 GHz Sampling Circuits and Subpicosecond Nonlinear Transmission Lines using Elevated Coplanar Waveguide*, IEEE Microwave and Guided Wave Letters **5** (1995), no. 2, 50–52.

[BGMS92] K. Bhaumik, B. Gelmont, R. J. Mattauch, and M. Shur, *Series Impedance of GaAs Planar Schottky Diodes Operated to 500GHz*, IEEE Transactions on Microwave Theory and Techniques **40** (1992), no. 5, 880–885.

[BHJ+93] R. J. Baker, D. J. Hodder, B. P. Johnson, P. C. Subedi, and D. C. Williams, *Generation of Kilovolt-Subnanosecond Pulses using a Nonlinear Transmission Line*, Measurement Science and Technology **4** (1993), no. 8, 893–895.

[BK98] A. M. Belyantsev and A. B. Kozyrev, *Generation of High-Frequency Oscillations by Electromagnetic Shock Wave at its Synchronism with Backward Harmonic of Periodic Transmission Line Based on a Multilayer Heterostructure*, International Journal of Infrared and Millimeter Waves **19** (1998), no. 11, 1571–1586.

[BKE97] R. F. Bradley, A. R. Kerr, and N. R. Erickson, *Why Don't Back-to-Back Abrupt Junction Frequency Triplers Work?*, Proceedings of the 8th International Symposium on Space Terahertz Technology (1997).

[BKW+98] M. Birk, H. Kibbel, C. Warns, A. Trasser, and H. Schumacher, *Efficient Transient Compression using an All-Silicon Nonlinear Transmission Line*, IEEE Microwave and Guided Wave Letters **8** (1998), no. 5, 196–198.

[BL65] F. A. Benson and J. D. Last, *Nonlinear-Transmission-Line Harmonic Generator*, Proceedings of the IEEE **112** (1965), no. 4, 635–643.

[BLG+00] M. Birk, L. M. Lunardi, A. H. Gnauck, H. Schumacher, and D. Behammer, *10-Gbit/s RZ Pulses using an All-Silicon Nonlinear Transmission Line Integrated Circuit*, Proceedings of the Optical Fiber Communication Conference **1** (2000), 248–250.

[BR98] N. S. Barker and G. M. Rebeiz, *Distributed MEMS True-Time Delay Phase Shifters and Wide-Band Switches*, IEEE Transactions on Microwave Theory and Techniques **46** (1998), no. 11, 1881–1890.

[Bur95] J. R. Burger, *Modeling Solitary Waves on Nonlinear Transmission Lines*, IEEE Transactions on Circuits and Systems-I: Fundamental Theory and Applications **42** (1995), no. 1, 34–36.

[Cas93] M. G. Case, *Nonlinear Transmission Lines for Picosecond Pulse, Impulse and Millimeter-Wave Harmonic Generation*, PhD in Electrical and Computer Engineering, University of California, Santa Barbara, July 1993.

[CCK+92] E. Carman, M. Case, M. Kamegawa, R. Yu, K. Giboney, and M. J. W. Rodwell, *V-Band and W-Band Broad-Band Monolithic Distributed Frequency Multipliers*, IEEE Microwave and Guided Wave Letters **2** (1992), no. 6, 253–254.

[CGC+91] E. Carman, K. Giboney, M. Case, M. Kamegawa, R. Yu, K. Abe, M. J. W. Rodwell, and J. Franklin, *28-39 GHz Distributed Harmonic Generation on a Soliton Nonlinear Transmission Line*, IEEE Microwave and Guided Wave Letters **1** (1991), no. 2, 28–31.

[CGJB+98] D. Cai, N. Grønbech-Jensen, A. R. Bishop, A. T. Findikoglu, and D. Reagor, *A Perturbed Toda Lattice Model for Low Loss Nonlinear Transmission Lines*, Physica D **123** (1998), 291–300.

[CKY+91] M. Case, M. Kamegawa, R. Yu, M. J. W. Rodwell, and J. Franklin, *Impulse Compression using Soliton Effects in a Monolithic GaAs Circuit*, Applied Physics Letters **58** (1991), no. 2, 173–175.

[Col92] R. E. Collin, *Foundations for Microwave Engineering*, second ed., Electrical Engineering Series, McGraw-Hill, New York, 1992.

[CS86] K. S. Champlin and D. R. Singh, *Small-Signal Second-Harmonic Generation by a Nonlinear Transmission Line*, IEEE Transactions on Microwave Theory and Techniques **34** (1986), no. 3, 351–353.

[CSS+95] D. Choudhury, P. H. Siegel, R. P. Smith, A. V. Räisänen, S. C. Martin, and M. A. Frerking, *Integrated Back to Back Barrier-N-N+ Varactor Diode Tripler using a Split-Waveguide Block*, IEEE Transactions on Microwave Theory and Techniques **43** (1995), no. 4, 948–954.

[CVL97] J. Carbonell, O. Vanbésien, and D. Lippens, *Electric Field Patterns in Finite Two-Dimensional Wire Photonic Lattices*, Superlattices and Microstructures **22** (1997), no. 4, 597–605.

[DCF+98] J. Danglot, J. Carbonell, M. Fernández, O. Vanbésien, and D. Lippens, *Modal Analysis of Guiding Structures Patterned in a Metallic Photonic Crystal*, Applied Physics Letters **73** (1998), no. 19, 2712–2714.

[DCM+99] O. Dupuis, J. Carbonell, P. Mounaix, O. Vanbésien, and D. Lippens, *Micromachined Coplanar Transmission Lines in a GaAs Technology*, Microwave and Optical Technology Letters **20** (1999), no. 2, 106–110.

[DFF+01] J. M. Duchamp, M. Fernández, P. Ferrari, X. Mélique, J. W. Tao, and D. Lippens, *Comparaison des Lignes Non Linéaires Distribuées et Périodiques pour la Multiplication de Fréquence*, Proceedings of the 12th Journées Nationales Microondes, Poitiers, France (2001).

[DGA+01] T. David, M. Guillon, S. Arscott, A. Maestrini, T. Akalin, B. Lecomte, J. Carbonell, M. Chaubet, P. Mounaix, G. Beaudin, and D. Lippens, *A 5mW-290GHz Heterostructure Barrier Tripler in a Waveguide Configuration*, IEEE MTT-S International Microwave Symposium Digest (2001).

[DHK+91] N. I. Dib, W. P. Harokopus, P. B. Katehi, C. C. Ling, and G. M. Rebeiz, *Study of a Novel Planar Transmission Line*, IEEE MTT-S International Microwave Symposium Digest **2** (1991), 623–626.

[Dic67] L. E. Dickens, *Spreading Resistance as a Function of Frequency*, IEEE Transactions on Microwave Theory and Techniques **15** (1967), no. 2, 101–109.

[Dil97] L. Dillner, *Heterostructure Barrier Varactor*, PhD in Electrical and Computer Engineering, Chalmers University of Technology, December 1997.

[DMV+98] V. Duez, X. Mélique, O. Vanbésien, P. Mounaix, F. Mollot, and D. Lippens, *High Capacitance Ratio with GaAs/InGaAs/AlAs Heterostructure Quantum Well-Barrier Varactors*, Electronics Letters **34** (1998), no. 19, 1860–1861.

[DSK97] L. Dillner, J. Stake, and E. L. Kollberg, *Analysis of Symmetric Varactor Frequency Multipliers*, Microwave and Optical Technology Letters **15** (1997), no. 1, 26–29.

[DVL99] J. Danglot, O. Vanbésien, and D. Lippens, *Active Waveguides Patterned in Mixed 2D-3D Metallic Photonic Crystal*, Electronics Letters **35** (1999), no. 6, 475–477.

[EBJ77] K. Everszumrode, B. Brockmann, and D. Jäger, *Efficiency of Harmonic Frequency Generation along Schottky Contact Microstrip Lines*, AEÜ International Journal of Electronics and Communications **31** (1977), no. 5, 212–215.

[ENL+00] E. G. Erker, A. S. Nagra, Y. Liu, P. Periaswamy, T. R. Taylor, J. Speck, and R. A. York, *Monolithic Ka-Band Phase Shifter using Voltage Tunable BaSrTiO3 Parallel Plate Capacitors*, IEEE Microwave and Guided Wave Letters **10** (2000), no. 1, 10–12.

[FDM+01] M. Fernández, J. M. Duchamp, X. Mélique, P. Ferrari, S. Arscott, T. Mao, and D. Lippens, *Fabrication et Caractérisation de Lignes de Transmission Non Linéaires Chargées par des Heterostructure Barrier Varactors*, Proceedings of the 12th Journées Nationales Microondes, Poitiers, France (2001).

[Fer98] M. Fernández, *Modeling and Characterization of Metallic Photonic Band Gap*, Training Report, Université des Sciences et Technologies de Lille, March 1998.

[FI82] Y. Fukuoka and T. Itoh, *Analysis of Slow-Wave Phenomena in Coplanar Waveguide on a Semiconductor Substrate*, Electronics Letters **18** (1982), no. 14, 589–590.

[FK77] R. H. Freeman and A. E. Karbowiak, *An Investigation of Nonlinear Transmission Lines and Shock Waves*, Journal of Physics D: Applied Physics **10** (1977), 633–643.

[GGBB96] K. C. Gupta, R. Garg, I. Bahl, and P. Bhartia, *Microstrip Lines and Slotlines*, second ed., Artech House, Boston-London, 1996.

[GKA98] A. Görür, C. Karpuz, and M. Alkan, *Characteristics of Periodically Loaded CPW Structures*, IEEE Microwave and Guided Wave Letters **8** (1998), no. 8, 278–280.

[GV73] U. Günther and E. Voges, *Variable Capacitance MIS Microstrip Lines*, AEÜ International Journal of Electronics and Communications **27** (1973), no. 3, 131–139.

[Hei93] W. Heinrich, *Quasi-TEM Description of MMIC Coplanar Lines Including Conductor-Loss Effects*, IEEE Transactions on Microwave Theory and Techniques **41** (1993), no. 1, 45–52.

[HLV+98] R. Havart, E. Lheurette, O. Vanbésien, P. Mounaix, F. Mollot, and D. Lippens, *Step-Like Heterostructure Barrier Varactor*, IEEE Transactions on Electron Devices **45** (1998), no. 11, 2291–2297.

[HS73] R. Hirota and K. Suzuki, *Theoretical and Experimental Studies of Lattice Solitons in Nonlinear Lumped Networks*, Proceedings of the IEEE **61** (1973), no. 10, 1483–1491.

[HS92] R. J. Hwu and L. P. Sadwick, *Limitations of the Back-to-Back Barrier-Intrinsic-n^+ (BIN) Diode Frequency Tripler*, IEEE Transactions on Electron Devices **39** (1992), no. 8, 1805–1810.

[HSD+00] S. Hollung, J. Stake, L. Dillner, M. Ingvarson, and E. Kollberg, *A Distributed Heterostructure Barrier Varactor Frequency Tripler*, IEEE Microwave and Guided Wave Letters **10** (2000), no. 1, 24–26.

[HW96] S. Hofschen and I. Wolff, *Simulation of an Elevated Coplanar Waveguide using 2-D FDTD*, IEEE Microwave and Guided Wave Letters **6** (1996), no. 1, 28–30.

[IOY+97] S. Ibuka, M. Ohnishi, T. Yamada, K. Yasuoka, S. Ishii, and K. C. Ko, *Voltage Amplification Effect of Nonlinear Transmission Lines for Fast High Voltage Pulse*

Generation, Proceedings of the 11th IEEE International Pulsed Power Conference **2** (1997), 1548–1553.

[IWW+88] H. Ikezi, S. S. Wojtowicz, R. E. Waltz, J. S. deGrassie, and D. R. Baker, *High-Power Soliton Generation at Microwave Frequencies*, Journal of Applied Physics **64** (1988), no. 6, 3277–3281.

[Jäg76] D. Jäger, *Slow-Wave Propagation along Variable Schottky-Contact Microstrip Line*, IEEE Transactions on Microwave Theory and Techniques **24** (1976), no. 9, 566–573.

[Jäg78] D. Jäger, *Soliton Propagation along Periodic-Loaded Transmission Line*, Applied Physics **16** (1978), 35–38.

[Jäg85] D. Jäger, *Characteristics of Travelling Waves along the Non-Linear Transmission Lines for Monolithic Integrated Circuits: a Review*, International Journal of Electronics **58** (1985), no. 4, 649–669.

[JB77] D. Jäger and J. P. Becker, *Distributed Variable-Capacitance Microstrip Lines for Microwave Applications*, Applied Physics **12** (1977), no. 2, 203–207.

[JFF+98] A. Jrad, P. Ferrari, C. Fuchs, A. Dominjon, J. W. Tao, B. Fléchet, and G. Angénieux, *A Simple and Systematic Method for the Design of Tapered Nonlinear Transmission Lines*, IEEE MTT-S International Microwave Symposium Digest (1998), 1627–1630.

[JFT+99] A. Jrad, P. Ferrari, J. W. Tao, C. Fuchs, A. Dominjon, G. Angénieux, and J. L. Coutaz, *Choice of CPW Characteristic Impedance for Lossy Nonlinear Transmission Lines Synthesis*, Electronics Letters **35** (1999), no. 12, 985–986.

[JJT94] J. R. Jones, S. H. Jones, and G. B. Tait, *GaAs/InGaAs/AlGaAs Heterostructure Barrier Varactors for Frequency Tripling*, Proceedings of the 5th International Symposium on Space Terahertz Technology (1994), 497–513.

[Jra99] A. Jrad, *Etude des Lignes Non Linéaires pour la Génération et la Propagation d'Impulsions Ultra-Courtes*, PhD in Electronics, Université de Savoie, July 1999.

[JT78] D. Jäger and F. J. Tegude, *Nonlinear Wave Propagation along Periodic-Loaded Transmission Line*, Applied Physics **15** (1978), 393–397.

[JTFT00] A. Jrad, W. Thiel, P. Ferrari, and J. W. Tao, *Comparison of FDTD and SPICE Simulations for Lossy and Dispersive Nonlinear Transmission Lines*, Electronics Letters **36** (2000), no. 9, 797–798.

[Kat92] A. Katz, *Indium Phosphide and Related Materials: Processing, Technology, and Devices*, Artech House, Boston-London, 1992.

[KG91] N. Katzenellenbogen and D. Grischkowsky, *Efficient Generation of 380 fs Pulses of THz Radiation by Ultrafast Laser Pulse Excitation of a Biased Metal-Semiconductor Interface*, Applied Physics Letters **58** (1991), no. 3, 222–224.

[KGK+91] M. Kamegawa, K. Giboney, J. Karin, S. Allen, M. Case, R. Yu, M. J. W. Rodwell, and J. E. Bowers, *Picosecond GaAs Monolithic Optoelectronic Sampling Circuit*, IEEE Photonics Technology Letters **3** (1991), no. 6, 567–569.

[KKC+92] Y. Konishi, M. Kamegawa, M. Case, R. Yu, M. J. W. Rodwell, R. A. York, and D. B. Rutledge, *Picosecond Electrical Spectroscopy using Monolithic GaAs Circuits*, Applied Physics Letters **61** (1992), no. 23, 2829–2831.

[KNH94] K. Krishnamurthi, S. M. Nilsen, and R. G. Harrison, *GaAs Single-Barrier Varactors for Millimeter-Wave Triplers: Guidelines for Enhanced Performance*, IEEE Transactions on Microwave Theory and Techniques **42** (1994), no. 12, 2512–2516.

[KR89] E. Kollberg and A. Rydberg, *Quantum-Barrier-Varactor Diodes for High-Efficiency Millimeter-Wave Multipliers*, Electronics Letters **25** (1989), no. 25, 1696–1698.

[Lan60] R. Landauer, *Parametric Amplification along Nonlinear Transmission Lines*, Journal of Applied Physics **31** (1960), no. 3, 479–484.

[LFM+99] E. Lheurette, M. Fernández, X. Mélique, P. Mounaix, O. Vanbésien, and D. Lippens, *Non Linear Transmission Line Quintupler Loaded by Heterostructure Barrier Varactors*, Proceedings of the 29th European Microwave Conference **2** (1999), 217–220.

[LH98] M. Li and R. G. Harrison, *A Fully-Distributed Heterostructure-Barrier-Varactor Nonlinear-Transmission-Line Frequency Tripler*, IEEE MTT-S International Microwave Symposium Digest (1998), 1639–1642.

[LKH98] M. Li, K. Krishnamurthi, and R. G. Harrison, *A Fully Distributed Heterostructure-Barrier Varactor Nonlinear Transmission-Line Frequency Multiplier and Pulse Sharpener*, IEEE Transactions on Microwave Theory and Techniques **46** (1998), no. 12, 2295–2301.

[LMM+98] E. Lheurette, X. Mélique, P. Mounaix, F. Mollot, O. Vanbésien, and D. Lippens, *Capacitance Engineering for InP-Based Heterostructure Barrier Varactor*, IEEE Electron Device Letters **19** (1998), no. 9, 338–340.

[LMS+96] E. Lheurette, P. Mounaix, P. Salzenstein, F. Mollot, and D. Lippens, *High Performance InP-Based Heterostructure Barrier Varactors in Single and Stack Configuration*, Electronics Letters **32** (1996), no. 15, 1417–1418.

[LTFM92] U. Lieneweg, T. J. Tolmunen, M. A. Frerking, and J. Maserjian, *Modeling of Planar Varactor Frequency Multiplier Devices with Blocking Barriers*, IEEE Transactions on Microwave Theory and Techniques **40** (1992), no. 5, 839–845.

[Mar00] F. Martín, *Modeling Soliton Pulses in Nonlinear Transmission Lines for Millimeter Wave Generation*, Proceedings of the 30th European Microwave Conference **3** (2000), 181–184.

[MCH+98] X. Mélique, J. Carbonell, R. Havart, P. Mounaix, O. Vanbésien, and D. Lippens, *InGaAs/InAlAs/AlAs Heterostructure Barrier Varactors for Harmonic Multiplication*, IEEE Microwave and Guided Wave Letters **8** (1998), no. 7, 254–256.

[Mei73] P. J. Meier, *Equivalent Relative Permittivity and Unloaded Q Factor of Integrated Finline*, Electronics Letters **9** (1973), no. 7, 162–163.

[Mél99] X. Mélique, *Tripleur de Fréquence utilisant des Diodes Varactors à Hétérostructures en Gamme Millimétrique*, PhD in Electronics, Université des Sciences et Technologies de Lille, November 1999.

[MFO+01] F. Martín, M. Fernández, X. Oriols, O. Vanbésien, and D. Lippens, *Simulation of Nonlinear Transmission Lines for Millimeter Wave Generation: A Comparison between Distributed and Lumped Element Models*, Proceedings of the 31th European Microwave Conference (2001).

[MMF+00] X. Mélique, A. Maestrini, R. Farré, P. Mounaix, M. Favreau, O. Vanbésien, J. M. Goutoule, F. Mollot, G. Beaudin, T. Närhi, and D. Lippens, *Fabrication and Performance of InP-Based Heterostructure Barrier Varactors in a 250-GHz Waveguide Tripler*, IEEE Transactions on Microwave Theory and Techniques **48** (2000), no. 6, 1000–1005.

[MMM+98] X. Mélique, C. Mann, P. Mounaix, J. Thornton, O. Vanbésien, F. Mollot, and D. Lippens, *5-mW and 5InP-Based Heterostructure Barrier Varactor Tripler*, IEEE Microwave and Guided Wave Letters **8** (1998), no. 11, 384–386.

[MMM+99] X. Mélique, A. Maestrini, P. Mounaix, M. Favreau, O. Vanbésien, J. M. Goutoule, G. Beaudin, T. Närhi, and D. Lippens, *Record Performance of a 250-GHz InP-Based Heterostructure Barrier Varactor Tripler*, Electronics Letters **35** (1999), no. 11, 938–939.

[MMR+89] C. J. Madden, R. A. Marsland, M. J. W. Rodwell, D. M. Bloom, and Y. C. Pao, *Hyperabrupt-Doped GaAs Nonlinear Transmission Line for Picosecond Shock-Wave Generation*, Applied Physics Letters **54** (1989), no. 11, 1019–1021.

[MMW+90] R. A. Marsland, C. J. Madden, D. W. Van Der Weide, M. S. Shakouri, and D. M. Bloom, *Monolithic Integrated Circuits for Millimeter-Wave Instrumentation*, Proceedings of the IEEE GaAs IC Symposium (1990), 19–22.

[MR56] J. M. Manley and H. E. Rowe, *Some General Properties of Nonlinear Elements. Part I. General Energy Relations*, Proceedings of the Institute of Radio Engineers (1956), 904–913.

[MSB90] R. A. Marsland, M. S. Shakouri, and D. M. Bloom, *Millimeter-Wave Second Harmonic Generation on a Nonlinear Transmission Line*, Electronics Letters **26** (1990), no. 16, 1235–1237.

[MVM+89] R. A. Marsland, V. Valdivia, C. J. Madden, M. J. W. Rodwell, and D. M. Bloom, *130 GHz GaAs Monolithic Integrated Circuit Sampling Head*, Applied Physics Letters **55** (1989), no. 6, 592–594.

[MW81] K. Muroya and S. Watanabe, *Experiment on Soliton in Inhomogeneous Electric Circuit. I. Dissipative Case*, Journal of the Physical Society of Japan **50** (1981), no. 9, 3159–3165.

[NA78] H. Nagashima and Y. Amagishi, *Experiment on the Toda Lattice using Nonlinear Transmission Lines*, Journal of the Physical Society of Japan **45** (1978), no. 2, 680–688.

[NY99] A. S. Nagra and R. A. York, *Distributed Analog Phase Shifters with Low Insertion Loss*, IEEE Transactions on Microwave Theory and Techniques **47** (1999), no. 9, 1705–1711.

[OLB91] E. Özbay, K. D. Li, and D. M. Bloom, *2.0 ps, 150 GHz GaAs Monolithic Photodiode and All-Electronic Sampler*, IEEE Photonics Technology Letters **3** (1991), no. 6, 570–572.

[Pag58] C. H. Page, *Harmonic Generation with Ideal Rectifiers*, Proceedings of the Institute of Radio Engineers **46** (1958), 1738–1740.

[PBAR96] R. Pullela, U. Bhattacharya, S. T. Allen, and M. J. W. Rodwell, *Multiplexer-Demultiplexer IC Technology for 100 Gb/s Fiber-Optic Transmission*, IEEE Journal of Solid-State Circuits **31** (1996), no. 5, 740–743.

[Ram95] J. I. Ramos, *Asymptotic Methods for the Analysis of Wave Propagation in Nonlinear, Lossless Transmission Lines and Equivalent Circuits*, Microwave and Optical Technology Letters **8** (1995), no. 4, 186–193.

[RAY+94] M. J. W. Rodwell, S. T. Allen, R. Y. Yu, M. G. Case, U. Bhattacharya, M. Reddy, E. Carman, M. Kamegawa, Y. Konishi, J. Pusl, and R. Pullela, *Active and Nonlinear Wave Propagation Devices in Ultrafast Electronics and Optoelectronics*, Proceedings of the IEEE **82** (1994), no. 7, 1037–1059.

[RBA87] M. J. W. Rodwell, D. M. Bloom, and B. A. Auld, *Nonlinear Transmission Line for Picosecond Pulse Compression and Broadband Phase Modulation*, Electronics Letters **23** (1987), no. 3, 109–110.

[RKY+91] M. J. W. Rodwell, M. Kamegawa, R. Yu, M. Case, E. Carman, and K. S. Giboney, *GaAs Nonlinear Transmission Lines for Picosecond Pulse Generation and Millimeter-Wave Sampling*, IEEE Transactions on Microwave Theory and Techniques **39** (1991), no. 7, 1194–1204.

[Rod87] M. J. W. Rodwell, *Picosecond Electrical Wavefront Generation and Picosecond Optoelectronic Instrumentation*, PhD in Electrical Engineering, Stanford University, December 1987.

[RW98] A. Reichelt and I. Wolff, *New Coplanar-Like Transmission Lines for Application in Monolithic Integrated Millimeter-Wave and Submillimeter-Wave Circuits*, IEEE MTT-S International Microwave Symposium Digest (1998), 99–102.

[SBAB93] M. S. Shakouri, A. Black, B. A. Auld, and D. M. Bloom, *500 GHz GaAs MMIC Sampling Wafer Probe*, Electronics Letters **29** (1993), no. 6, 557–558.

[SBH+97] J. E. Schramm, D. I. Babic, E. L. Hu, J. E. Bowers, and J. L. Merz, *Fabrication of High-Aspect-Ratio InP-Based Vertical-Cavity Laser Mirrors using* $CH_4/H_2/O_2/Ar$ *Reactive Ion Etching*, Journal of Vacuum Science and Technology **B15** (1997), no. 6, 2031–2036.

[SBM+97] S. Simion, G. Bartolucci, R. Marcelli, A. Müller, B. Szentpali, and F. Riesz, *Nonlinear Transmission Lines on GaAs Membranes for Picosecond and Large Amplitude Shockwaves Generation*, Proceedings of the International Semiconductor Conference **2** (1997), 353–356.

[SCM73] A. C. Scott, F. Y. F. Chu, and D. W. McLaughlin, *The soliton: A New Concept in Applied Science*, Proceedings of the IEEE **61** (1973), no. 10, 1443–1483.

[SDH+96] P. Salzenstein, O. Dupuis, M. Hélal, E. Lheurette, O. Vanbésien, P. Mounaix, and D. Lippens, *Coplanar Waveguides on Dielectric Membranes Micromachined on a GaAs Substrate*, Electronics Letters **32** (1996), no. 9, 821–822.

[SDJ+98] J. Stake, L. Dillner, S. H. Jones, C. Mann, J. Thornton, J. R. Jones, W. L. Bishop, and E. L. Kollberg, *Effects of Self-Heating on Planar Heterostructure Barrier Varactor Diodes*, IEEE Transactions on Electron Devices **45** (1998), no. 11, 2298–2303.

[SGM92] T. C. Shen, G. B. Gao, and H. Morkoç, *Recent Developments in Ohmic Contacts for III-V Compound Semiconductors*, Journal of Vacuum Science and Technology **B10** (1992), no. 5, 2113–2132.

[SHM+93] J. E. Schramm, E. L. Hu, J. L. Merz, J. J. Brown, M. A. Melendes, M. A. Thompson, and A. S. Brown, *Highly Selective Reactive Ion Etch Process for InP-Based Device Fabrication using Methane/Hydrogen/Argon*, Journal of Vacuum Science and Technology **B11** (1993), no. 6, 2280–2283.

[SL99a] D. Salameh and D. Linton, *Microstrip GaAs Nonlinear Transmission-Line (NLTL) Harmonic Pulse Generators*, IEEE Transactions on Microwave Theory and Techniques **47** (1999), no. 7, 1118–1122.

[SL99b] D. Salameh and D. Linton, *Study of the Effect of Various Parameters on Nonlinear Transmission-Line (NLTL) Performance*, IEEE Transactions on Microwave Theory and Techniques **47** (1999), no. 3, 358–353.

[SL99c] D. Salameh and D. Linton, *Study of the Relation between Doping Profile and Diode CV Characteristics*, IEEE Transactions on Microwave Theory and Techniques **47** (1999), no. 4, 506–509.

[SLS84] R. Sorrentino, G. Leuzzi, and A. Silbermann, *Characteristics of Metal-Insulator-Semiconductor Coplanar Waveguides for Monolithic Microwave Circuits*, IEEE Transactions on Microwave Theory and Techniques **32** (1984), no. 4, 410–416.

[SWY+91] C. Shu, X. Wu, E. S. Yang, X. C. Zhang, and D. H. Auston, *Propagation Characteristics of Picosecond Electrical Pulses on a Periodically Loaded Coplanar Waveguide*, IEEE Transactions on Microwave Theory and Techniques **39** (1991), no. 6, 930–936.

[SZD+95] H. Shi, W. M. Zhang, C. W. Domier, N. C. Luhmann, L. B. Sjogren, and H. X. L. Liu, *Novel Concepts for Improved Nonlinear Transmission Line Performance*, IEEE Transactions on Microwave Theory and Techniques **43** (1995), no. 4, 780–788.

[TBMA00] W. Thiel, M. Birk, W. Menzel, and P. Abele, *A Global Finite Difference Time Domain Analysis of a Silicon Nonlinear Transmission Line*, IEEE MTT-S International Microwave Symposium Digest (2000), 371–374.

[TBS91] M. M. Turner, G. Branch, and P. W. Smith, *Methods of Theoretical Analysis and Computer Modeling of the Shaping of Electrical Pulses by Nonlinear Transmission

Lines and Lumped-Element Delay Lines, IEEE Transactions on Electron Devices **38** (1991), no. 4, 810–816.

[Tho99] J. R. Thorpe, *Non-Linear Transmission Line Frequency Multipliers for Millimeter and Submillimeter-Wave Applications*, PhD in Electronic and Electrical Engineering, University of Leeds, 1999.

[TSA88] M. Tan, C. Y. Su, and W. J. Anklam, 7× *Electrical Pulse Compression on an Inhomogeneous Nonlinear Transmission Line*, Electronics Letters **24** (1988), no. 4, 213–215.

[TSM98] J. R. Thorpe, P. Steenson, and R. E. Miles, *Non-Linear Transmission Lines for Millimeter-Wave Frequency Multiplier Applications*, Proceedings of the 6th IEEE International Terahertz Electronics Conference (1998), 54–57.

[Tsu89] T. Tsuboi, *Phase Shift in the Collision of Two Solitons Propagating in a Nonlinear Transmission Line*, Physical Review A **40** (1989), no. 5, 2753–2755.

[Tsu90] T. Tsuboi, *Formation Process of Solitons in a Nonlinear Transmission Line: Experimental Study*, Physical Review A **41** (1990), no. 8, 4534–4537.

[WAP+98] O. Wohlgemuth, B. Agarwal, R. Pullela, D. Mensa, Q. Lee, J. Guthrie, M. J. W. Rodwell, R. Reuter, J. Braunstein, M. Schlechtweg, and K. Köhler, *A NLTL-Based Integrated Circuit for a 70-200 GHz VNA System*, Proceedings of the 28th European Microwave Conference **1** (1998), 104–107.

[Wat82] S. Watanabe, *Solitons in Nonlinear Transmission Line*, Journal of the Physical Society of Japan **51** (1982), no. 3, 1030–1036.

[WBAB93] D. W. Van Der Weide, J. S. Bostak, B. A. Auld, and D. M. Bloom, *All-Electronic Generation of 880 fs, 3.5 V Shockwaves and their Application to a 3 THz Free-Space Signal Generation System*, Applied Physics Letters **62** (1993), no. 1, 22–24.

[Wei93] D. W. Van Der Weide, *A YIG-Tuned Nonlinear Transmission Line Multiplier*, IEEE MTT-S International Microwave Symposium Digest **2** (1993), 557–560.

[Wei94] D. W. Van Der Weide, *Delta-Doped Schottky Diode Nonlinear Transmission Lines for 480-fs, 3.5-V Transients*, Applied Physics Letters **65** (1994), no. 7, 881–883.

[Wen69] C. P. Wen, *Coplanar Waveguide: A Surface Strip Transmission Line Suitable for Nonreciprocal Gyromagnetic Device Applications*, IEEE Transactions on Microwave Theory and Techniques **17** (1969), no. 12, 1087–1088.

[WH99] X. Wang and R. J. Hwu, *Theoretical Analysis and FDTD Simulation of GaAs Nonlinear Transmission Lines*, IEEE Transactions on Microwave Theory and Techniques **47** (1999), no. 7, 1083–1091.

[Wil84] R. E. Williams, *Gallium Arsenide Processing Techniques*, Artech House, Boston-London, 1984.

[WJ81] B. Wedding and D. Jäger, *Phase-Matched Second Harmonic Generation and Parametric Mixing on Nonlinear Transmission Lines*, Electronics Letters **17** (1981), no. 2, 76–77.

[WRR+99] O. Wohlgemuth, M. J. W. Rodwell, R. Reuter, J. Braunstein, and M. Schlechtweg, *Active Probes for 2-Port Network Analysis within 70-230 GHz*, IEEE MTT-S International Microwave Symposium Digest **4** (1999), 1635–1638.

[WTS91] C. R. Wilson, M. M. Turner, and P. W. Smith, *Pulse Sharpening in a Uniform LC Ladder Network Containing Nonlinear Ferroelectric Capacitors*, IEEE Transactions on Electron Devices **38** (1991), no. 4, 767–771.

[WY84] S. Watanabe and N. Yajima, *K-dV Soliton in Inhomogeneous System*, Journal of the Physical Society of Japan **53** (1984), no. 10, 3325–3334.

[YCK+90] R. Y. Yu, M. Case, M. Kamegawa, M. Sundaram, M. J. W. Rodwell, and A. W. Gossard, *275 GHz 3-Mask Integrated GaAs Sampling Circuit*, Electronics Letters **26** (1990), no. 13, 949–951.

[YKC+91] R. Y. Yu, M. Kamegawa, M. Case, M. J. W. Rodwell, and J. Franklin, *A 2.3-ps Time-Domain Reflectometer for Millimeter-Wave Network Analysis*, IEEE Microwave and Guided Wave Letters **1** (1991), no. 11, 334–336.

[YPK+92] R. Y. Yu, J. Pusl, Y. Konishi, M. Case, M. Kamegawa, and M. J. W. Rodwell, *A Time-Domain Millimeter-Wave Vector Network Analyzer*, IEEE Microwave and Guided Wave Letters **2** (1992), no. 8, 319–321.

[YRP+95] R. Y. Yu, M. Reddy, J. Pusl, S. T. Allen, M. Case, and M. J. W. Rodwell, *Millimeter-Wave On-Wafer Waveform and Network Measurements using Active Probes*, IEEE Transactions on Microwave Theory and Techniques **43** (1995), no. 4, 721–729.

[ZHL+96] W. M. Zhang, R. P. Hsia, C. Liang, G. Song, C. W. Domier, and N. C. Luhmann, *Novel Low-Loss Delay Line for Broadband Phased Antenna Array Applications*, IEEE Microwave and Guided Wave Letters **6** (1996), no. 11, 395–397.

Summary

The nonlinear charge-voltage characteristic of a varactor diode is used for many applications in electronics, frequency multiplication being the most immediate. At high frequencies, one of the most widely used device in frequency multiplication is the Schottky diode. However, Heterostructure Barrier Varactor (HBV) diodes have emerged as a promising alternative. If the diode is instead incorporated somehow into a transmission line, the resulting structure takes the form of a NonLinear Transmission Line (NLTL). The advantage of NLTLs over discrete devices is a high frequency operation over a wider bandwidth, the NLTL being self matched.

In this context, this work describes the design considerations, fabrication and measurements of NLTLs periodically loaded with InP-based HBV diodes. The design focused on a V-band frequency multiplier operating at $60GHz$. Also, a special effort was paid to the determination of the large signal Bragg frequency and the transmission behavior of the NLTL by means of a Large Signal S Parameter analysis, providing a better understanding of the frequency filtering aspect.

Concerning the fabrication, NLTLs loaded with high-quality HBV diodes have been manufactured in a monolithic coplanar technology for the first time to our knowledge. As an alternative to implant isolation, the under-etching effect required for diode isolation has provided a prototype which could be considered in between a fully distributed and periodically loaded approach.

Finally, the preliminary experimental results under moderate pump conditions are in agreement with the small and large signal regime analysis. In this way, through harder pump conditions, further improvements in terms of conversion efficiency are expected.

Keywords:

- Nonlinear Transmission Line
- Heterostructure Barrier Varactor
- Harmonic Generation
- Monolithic Microwave Integrated Circuit
- Coplanar Waveguide
- Large Signal S Parameters